AFIT/DS/ENG/96-16

Electromagnetic Scattering from a Cavity

in a Ground Plane: Theory and Experiment

DISSERTATION
William D. Wood, Jr.
Captain, USAF

AFIT/DS/ENG/96-16

DTIC QUALITY INSPECTED 2

The views expressed in this dissertation are those of the author and do not reflect the official policy or position of the Department of Defense or the United States Government.

AFIT/DS/ENG/96-16

Electromagnetic Scattering from a Cavity in a Ground Plane: Theory and Experiment

DISSERTATION

Presented to the Faculty of the School of Engineering

of the Air Force Institute of Technology

Air University

In Partial Fulfillment of the

Requirements for the Degree of

Doctor of Philosophy

William D. Wood, Jr., B.S.E.E., M.S.E.E.

Captain, USAF

March 1997

Electromagnetic Scattering from a Cavity in a Ground Plane: Theory and Experiment

William D. Wood, Jr., B.S.E.E., M.S.E.E.

Captain, USAF

Approved:

Vittal P Pyati   *16 Apr 97*

Dr. Vittal P. Pyati   Date
Chairman, Advisory Committee

Will. P. Bak   *13 Mar 97*

Dr. William P. Baker   Date
Member, Advisory Committee

J. Paul Sk   *8 APR 97*

Dr. J. Paul Skinner, Major, USAF   Date
Member, Advisory Committee

Krishna Naishadham   *April 15, 97*

Dr. Krishna Naishadham   Date
Member, Advisory Committee

B. N. Naj   *13 Mar 97*

Dr. Brahamanand N. Nagarsenker   Date
Dean's Representative

Robert A. Calico, Jr.
Dean

Table of Contents

List of Tables

x

AFIT/DS/ENG/96-16

Abstract

We examine the electromagnetic scattering from an arbitrarily shaped open cavity embedded in a perfectly conducting, infinite ground plane. The cavity is filled with an arbitrary linear, isotropic, homogeneous, lossy material. The field everywhere in the cavity interior and above the ground plane are expressed in terms of the tangential fields on the cavity surface and aperture. We develop a coupled set of three integral equations to determine the tangential electromagnetic fields on the aperture and cavity surface. The integral equations are based on fundamental mathematical laws obeyed by the fields rather than on the usual surface or volume equivalence principles. The unknown functions are the tangential electric and magnetic fields on the cavity aperture, and the tangential magnetic field on the cavity surface. The support of the unknown tangential fields is finite.

We design a moment-method based algorithm to find an approximate solution to the integral equations for plane wave illumination, and implement it on a digital computer. The algorithm is specialized for the case of axisymmetric cavities, and uses the same basis functions as are used in traditional body-of-revolution scattering codes. The unknown tangential fields are expanded using piecewise-linear functions in the elevation plane and complex exponentials in the azimuth plane. Orthogonality of the complex exponentials is exploited to reduce the size of the moment method matrix.

The algorithm yields a well-conditioned numerical solution for the tangential fields. The tangential fields obey the edge condition at the aperture rim. The integral equations are uniquely solvable at frequencies where other integral equation-based techniques admit spurious solutions. Radar cross section calculations are compared to experimental measurements of full-scale physical models. Results show that an open cavity can serve as an effective RCS enhancement device.

Electromagnetic Scattering from a Cavity in a Ground Plane: Theory and Experiment

I. **Introduction**

1.1   Motivation

Methods of radar cross section (RCS) reduction have been extensively investigated over the past several decades and have reached a state of maturity sufficient to find many practical applications. On the other hand methods of RCS enhancement have received only limited attention. An example of RCS enhancement is the use of a string of corner reflectors to locate runways by approaching aircraft in bad weather. A similar example, albeit in the optical regime, is the placement of cat's eye lane demarkers on highways to help motorists at night. Such aids represent "brute force" approaches employing already existing technology, and are not constrained by other factors such as the requirement to minimize size or weight. As such, they do not constitute the product of a serious, comprehensive study of RCS enhancement techniques. Hence it would appear that an investigation of RCS enhancement techniques is warranted. Before one begins to undertake such studies, it is worthwhile to identify a few practical applications to justify any such efforts.

- RPV Tracking: Remotely piloted vehicles (RPVs) are an inexpensive means of gathering intelligence data and are routinely used in tactical scenarios. It goes without saying that the user must maintain constant contact with the RPV. Since the operation is supposed to be clandestine, the use of tracking beacons is ill-advised. To enhance the ability to track the RPV by radar, RCS enhancement without compromising flying qualities appears attractive. Corner reflectors or Luneberg lenses are devices that can enhance RPV RCS, but such devices invariably increase the drag of an otherwise streamlined air vehicle. The answer obviously lies in working from the inside with suitable coupling to the outside by means of RF windows which blend smoothly with the skin of the RPV.

- UAV Decoys: Unmanned air vehicles (UAVs) can serve as an inexpensive decoy. Such decoys might be launched in large numbers to saturate enemy air defenses, thus increasing the survivability of friendly aircraft. A small, inexpensive UAV would typically have a smaller

RCS than that of a fighter-size aircraft, thereby providing an adversary with a way to discriminate between the two. An effective decoy should mimic the strike aircraft in as many ways as possible, so we desire a method to increase the decoy's RCS to the level of the strike aircraft. In this way, the effectiveness of a UAV decoy could be considerably increased.

- Camouflage of Stealthy Aircraft: As low-RCS aircraft enter the inventory, the need to controllably increase their RCS has become evident. In many cases, a stealthy aircraft's low RCS might impair its capability, especially in a peacetime training environment. For instance, air traffic control radars must be able to detect low-RCS aircraft in their areas of responsibility to ensure air safety; and reliance on a transponder may introduce safety-of-flight issues. Additionally, one may wish to protect knowledge of a low-RCS aircraft's true radar signature, so the ability to increase it in a controlled manner may prevent the compromise of vital operational capabilities.

- Identification: Current non-cooperative target recognition (NCTR) research efforts exploit target RCS signatures, so it is conceivable that controllable, distinctive RCS enhancement could be used as a means to identify friendly aircraft. Currently, friendly aircraft are normally identified via Identification Friend or Foe (IFF) transponders (which require an aircraft to broadcast its presence using coded signals over specific frequencies) or through non-cooperative techniques that fail at some aspect angles. An RCS enhancement device may create an RCS signature that is distinctive enough to make an unerring friendly identification at all aspect angles possible.

Several techniques have been considered to accomplish effective RCS enhancement. Impedance loading has been investigated to control RCS [55], although most research in impedance loading techniques has been focused on RCS reduction and, furthermore, the technique has been found to be effective only over fairly narrow bandwidths. RCS enhancement has traditionally been accomplished using corner reflectors, bicones, or dielectric lenses [12, Chap 8]. These devices are effective RCS enhancement devices because they scatter strongly over large bandwidths, broad aspect angles, and varied polarizations. However, when applied to an air vehicle, they exhibit the following drawbacks:

- Decreased aerodynamic performance through increased drag,
- Additional parasitic weight, and

2

- Lack of in-flight switching capability

    It would be useful if an alternative method of RCS enhancement could be found to mitigate these drawbacks, while effectively increasing RCS.
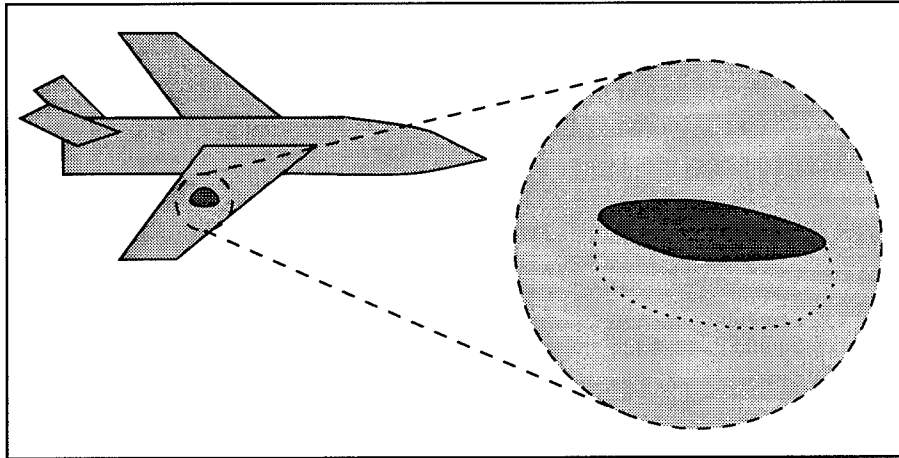
Figure 1   An open cavity embedded in the wing of a UAV

1.1.1   A Viable Candidate for RCS Enhancement.   A potentially viable candidate design for an RCS enhancement device consists of one or more open cavities embedded behind the air vehicle's exterior skin. Figure 1 shows a possible location of an open cavity on an unmanned air vehicle (UAV) – on the upper surface of its wing. Here, the open cavity would provide RCS enhancement for aspects above the waterline of the UAV; RCS enhancement below the waterline could be accomplished by a similar open cavity mounted on the wing's underside. Unlike an external radar reflector, an open cavity would not extend into the airstream and create additional aerodynamic drag. The additional weight to the air vehicle is negligible. An open cavity could conceivably be turned on or off by electrically controlling the conductivity of a membrane covering its aperture thus providing an in-flight switching capability ([52, 66]). [1] Additionally, it is anticipated that an open cavity would be an effective RCS enhancement device, scattering strongly

---

[1]In the "off" state, the membrane's conductivity would be very high, blending the aperture of the open cavity into the conducting skin of the aircraft and effectively isolating the open cavity from the incident field. In this state, the open cavity would not affect the normal RCS of the air vehicle. In the "on" state, the membrane's conductivity would be very low, and the membrane would be nearly transparent to the incident field. In this state, the open cavity would scatter strongly, overriding the natural RCS of the aircraft.

over a large bandwidth, broad range of aspect angles, and arbitrary polarization; it is the goal of this dissertation to characterize its scattering characteristics.

1.1.2 Open Cavity RCS Enhancement Device. For the purposes of this dissertation, we define an open cavity RCS enhancement device (OCRED) to consist of an open box or enclosure whose mouth or aperture is set in a perfectly conducting plane. A "shoebox" shaped example of this geometry is shown in Figure 3(a). The interior of the open cavity couples to the half space above via an opening ("aperture") in the ground plane. The ground plane is perfectly conducting, as are the walls of the open cavity, and the interior of the open cavity is filled with a homogeneous, isotropic, linear dielectric material. The half-space above the ground plane is a free-space region. The scattering properties of an OCRED can be studied using analytical methods complemented by experimental measurements. There is a woeful lack of experimental data in the open literature, and each analytical/computational method in common use is limited in some way.

In the context of this document, the OCRED is a canonical problem of the more complex situation in the real world. For example, in the real world the OCRED would be mounted on a finite-sized air vehicle rather than in an infinite ground plane, and the cavity walls and surrounding air vehicle skin may not be perfectly conducting. We will deal here with the idealized, canonical problem as a means to gain insight into the real world one.

1.1.2.1 Analytical Predictions. Predicting the scattering characteristics of the OCRED is a challenging problem in electromagnetic theory, especially in the resonance regime. In the low-frequency and high-frequency limits, certain approximations can be made to make the problem more tractable, but when the dimensions of the OCRED are on the order of a wavelength, these approximations generally fail. Most current general-purpose RCS prediction codes are based on either high-frequency asymptotic methods, or the method of moments. High-frequency asymptotic methods include physical optics (PO), the physical theory of diffraction (PTD), geometrical optics (GO), and the uniform theory of diffraction (UTD), and view scattering as a phenomenon dependent only on the incident field and local geometry. But in a cavity, the scattering is a complex function of the interactions between the aperture, the cavity interior, and the ground plane. For this reason, high-frequency asymptotic methods do not predict OCRED scattering accurately. The conventional, general-purpose integral equation approach has the inherent capability to predict OC-

4

RED scattering, but the need to model the equivalent currents on the infinite ground plane makes it impractical. (An important variation, the generalized network formulation, will be discussed in Chapter II.)

1.1.2.2 Experimental Measurements. Building and measuring an OCRED model has the advantage of providing high-quality data and is easily within the capabilities of today's fabrication technology and RCS measurement ranges. Unfortunately, it is not cost-effective to build and measure many such models with the aim of obtaining insight into the viability or design of an effective OCRED, and there is a surprising lack of measured data in the open literature.

1.2 Organization

This dissertation represents an attempt to understand the electromagnetic scattering characteristics of the OCRED geometry. In Chapter II, we summarize the pertinent related work that has appeared in the open literature. In Chapter III, we develop a new set of integral equations to predict the scattering from an arbitrary OCRED geometry. In Chapter IV, we develop an algorithm to find an approximate solution to these integral equations for the case of axially symmetric (body of revolution) geometries. In Chapter V we present the results of implementing the numerical algorithm and making experimental measurements of several physical models. In Chapter VI, we conclude the dissertation with a brief summary of the findings and recommendations for further research.

II. Related Work

The OCRED geometry consists of two canonical geometries: an open cavity and an aperture in a ground plane. Each of these forms has been investigated extensively, but the composite problem has received far less attention.

2.1 Open Cavities

A large body of work exists dealing with the problem of scattering from an open, perfectly conducting cavity in free space [17, 27, 38, 58]. Most of this work makes use of Harrington and Mautz' generalized network formulation [23]. This method partitions the problem into an exterior problem and an interior problem, as shown in Figure 2. Each (simpler) problem is treated individually, and the composite problem is solved by enforcing tangential field continuity across the aperture. If there are no sources present, the electric field for the interior problem will satisfy the homogeneous vector wave equation and the perfect electrical conductor (PEC) boundary condition. For an arbitrarily shaped interior problem, it can be shown [11, 68] that the interior fields are not uniquely determinable at a countably infinite set of discrete, resonant frequencies. At these frequencies, the generalized network formulation fails to provide a unique solution for the fields in the cavity interior and surface [35]. This is a very serious limitation, especially for cavities of arbitrary shape, since it is very difficult to find the resonant frequencies. Only for a limited number of simple geometries (such as rectangular boxes, spheres, and circular cylinders) one can analytically determine the resonant frequencies. It is therefore not apparent whether the generalized network
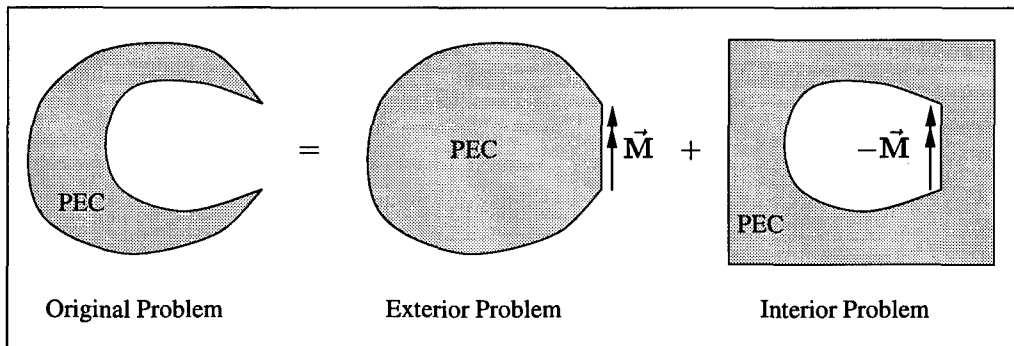
Figure 2   Partitioning of an open cavity problem into an exterior problem and an interior problem, showing equivalent magnetic current $\vec{M}$.

6

formulation will break down for a particular frequency of interest. The resonance phenomenon exhibited by the interior problem does *not* mean that the OCRED fields are not uniquely solvable at all frequencies. The *source-free* interior problem artificially enforces a vanishing tangential electric field across the aperture, whereas the complete OCRED problem implies no such requirement. It is this "spurious resonance" that motivates us to find an alternate method to the generalized network formulation technique.

A related problem is that of scattering by perfectly conducting finite obstacles in free space. This problem is typically solved using the equivalence principle [21] which involves determining equivalent electric currents on the boundary, satisfying an integral equation. Typically, the integral equation is either the electric field integral equation (EFIE) or the magnetic field integral equation (MFIE) [40]. Neither formulation is uniquely solvable at interior resonant frequencies [57]. The root of the problem is the failure of the EFIE and MFIE to enforce proper boundary conditions on the scatterer at resonance [51, 68]. This results in a nontrivial solution to the homogeneous (source-free) problem, which contaminates the true solution. More complicated formulations have been proposed to "fix" the EFIE and MFIE [42,43,67,68]. Unfortunately, none of these approaches apply to the interior problem because the resonances of the interior cavity are real.

Despite its problems with "spurious resonances," the generalized network formulation has been successfully used by many investigators (see, for example, [63]). In all these cases, particular care is taken to stay away from frequencies corresponding to known internal resonances.

2.1.1 Open Spherical Shells. A particular canonical open cavity which can be analyzed without resorting to the generalized network formulation is the open, infinitesimally thin, conducting spherical shell [5, 56, 58, 69]. Because this geometry is separable, it can be analyzed by expanding the exterior and interior fields using spherical vector wave functions [47]. The resulting infinite series is typically truncated, and a linear system of equations solved to determine the unknown coefficients. Unfortunately, this technique applies only to geometries natural to the spherical coordinate system.

2.2 Apertures in a Ground Plane

Scattering by and transmission through an arbitrary aperture in a ground plane has been extensively investigated. An excellent review of techniques developed through the late 1970s can be found in Butler *et al* [8]. More recently, investigators have explored other techniques. Luebbers [39] uses the finite-difference time domain (FDTD) method to find the scattering from an infinite slot in a thick ground plane. This method can be extended to three-dimensional apertures, but the geometry must be approximated by a rectangular grid. The finite element method (FEM) has become popular [16, 26, 28, 29], but requires modeling the interior of the computational domain and matching the solution to a boundary integral equation that implicitly contains the radiation condition. Several authors [10, 13] have considered the problem of electrically small apertures and expressed the solution as a power series in frequency. When the frequency is sufficiently small the first term of the series yields reasonably accurate results.

2.3 Open Cavity in a Ground Plane

The composite OCRED problem represents a combination of an open cavity and an aperture in a ground plane. The analogous two-dimensional problem of scattering by an infinite trough in a ground plane has been treated by several investigators [3,14,20,24,25]. The approaches which have been taken can be broadly categorized as low-frequency, high-frequency, and resonant-frequency techniques, based on the assumed value of kd where k is the wavenumber and d is a characteristic linear dimension of the cavity or aperture.

2.3.1 Low-Frequency Techniques, $kd \ll 1$.

Hansen and Yaghjian [20] examine the two-dimensional trough in a ground plane, using a truncated power series in kd. This represents a perturbation of the corresponding electrostatic problem. Kempel and Senior [32] model an OCRED as an impedance disk on a ground plane. This technique can only be applied, however, to cavity geometries that can be modeled as sections of waveguides. Since the size of the cavity is assumed to be small compared to the wavelength, low-frequency techniques are primarily useful for finding the scattering from imperfections such as cracks, gaps, and rivet-holes in the skins of aircraft. For larger cavities, low-frequency techniques are not useful.

2.3.2 High-Frequency Techniques, $kd \gg 1$. Nearly all high frequency techniques may be grouped under the term "ray" techniques, because they take the viewpoint that electromagnetic waves propagate like rays of optical light. Ray techniques are valid if scattering is a local phenomenon and physically distant portions of the geometry do not significantly interact. Many investigators have used ray techniques and in several instances merged them with modal methods when the cavity has properties of a waveguide [7, 9, 15, 36, 37, 49]. High-frequency techniques have application in the prediction of scattering from jet engine inlet ducts. When the cavity is not electrically large, interactions between the aperture and cavity termination become important and the accuracy of high-frequency techniques is questionable.

2.3.3 Resonant-Frequency Techniques, $kd = \mathcal{O}(1)$. Resonant-frequency techniques employ the finite element, finite-difference time domain, modal, or integral equation method, or some hybridization of them. These are discussed below.

Hybrid Finite Element Method. The finite element method (FEM) has been combined with the boundary integral equation method to solve OCRED-like problems [3]. It has been used to model arbitrary geometries [27]. However, "penalty functions" [53] must be introduced into the three-dimensional FEM variational equations to suppress spurious solutions. Sun *et al* show that these spurious solutions are caused by an incorrect component of the solution associated with the static electric potential (*i.e.*, the null space of the curl operator), rather than "the nonsolenoidal nature of finite-element-approximation procedures" [60]. Webb [64] uses special basis functions to model field behavior at edges, increasing the complexity of the method.

Finite-Difference Time Domain (FDTD) Method. The FDTD method has been employed to predict the scattering from open cavities. Penney and Luebbers [50] use FDTD to analyze cavity-backed antennas, while Lee *et al* [34] apply it to find the scattering from a jet engine inlet duct. A single FDTD simulation can generate broadband scattering data, but only for a single angle of incidence. Additionally, FDTD meshes are restricted to be rectangular, and special absorbing boundary conditions must be used to approximate the radiation condition for the scattered fields.

Modal Methods. For rectangular geometries, the fields in the OCRED cavity can be expanded in waveguide modes [4]. Large field magnitudes in the aperture have been observed when the aperture is electrically small and the frequency is near a resonant frequency for the interior

problem [35]. Modal methods are restricted to the narrow class of geometries for which analytical expressions for the modes are available.

Integral Equation Methods. Most integral equation approaches to the OCRED scattering problem employ the generalized network formulation, as described in Section 2.1, and are not uniquely solvable at some discrete frequencies. An interesting and very promising boundary integral equation approach was recently proposed by Asvestas & Kleinman [2]. Their method requires solving for surface currents on the open cavity surface, and the authors claim that the integral equations are uniquely solvable at all frequencies, but provide no substantiation. Additionally, the formulation only applies to empty cavities and the theory must be extended to account for material-filled cavities. Recently, the method was extended to handle a dyadic impedance boundary condition imposed on the cavity surface, though the ground plane is still perfectly conducting [1].

To select an appropriate technique to model OCRED scattering, we look at three desirable attributes. First, the technique must be valid for cavities that are neither electrically large nor electrically small. Second, the technique should not suffer from the problem of spurious resonances. Third, the technique should minimize the computational domain so that computational resources are conserved. The technique that best satisfies these three attributes is the Asvestas boundary integral equation technique, which will be further explored in the remainder of this dissertation.

III. Theory

In this chapter, we will cast the problem of scattering from an open cavity embedded in a perfectly conducting ground plane in terms of integral equations. We shall first define the specific geometry for the field components. Following the approach of Asvestas and Kleinman [2], we shall then obtain the final integral equations.

In Section 3.1, we introduce the OCRED geometry. In Section 3.2, we define the electromagnetic fields for the OCRED problem, along with the partial differential equations and boundary conditions they satisfy. In Section 3.3, we introduce several scalar and dyadic functions and define their properties. In Section 3.4, we develop radiation integrals that define the electromagnetic fields everywhere in the OCRED domain in terms of the tangential field components on the cavity surface and aperture. Finally, in Section 3.5, we transform the radiation integrals into a set of three coupled surface integral equations involving these tangential field components alone.

3.1 Geometry

The general OCRED geometry is shown in Figure 3. The entire xy-plane is partitioned into
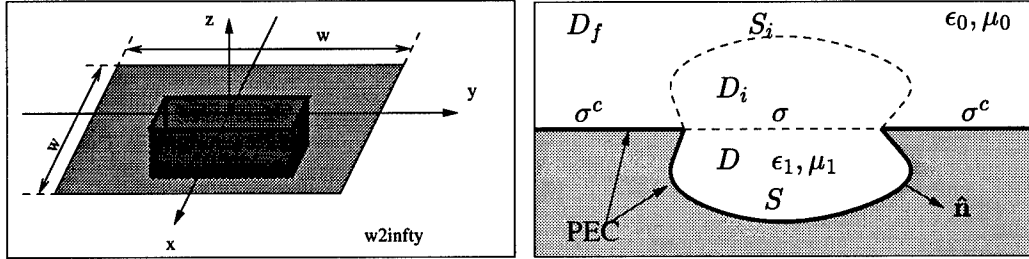
(a) A shoebox-shaped OCRED in a finite ground plane. For an infinite ground plane, let $w \to \infty$.

(b) Cross-sectional view of an OCRED.

Figure 3   The geometry of an OCRED. Figure 3(a) shows a three-dimensional representation. Figure 3(b) shows a two-dimensional view, with regions and surfaces defined.

two regions: a bounded, simply-connected region, σ, and its complement in the xy-plane, σ^c. The cavity volume, D, is bounded by the closed regular surface ∂D, which is composed of σ and the open regular surface, S. In the following development, we shall assume the following:

- The cavity surface S and the aperture complement σ^c are perfect electric conductors.

11

- The boundary of σ (*i.e.* the rim of the aperture), $\partial\sigma$, is a closed, bounded, piecewise smooth curve in the xy-plane.

- The cavity surface S does not extend into the upper half space, and intersects the xy-plane only at $\partial\sigma$.

- The unit normal vector, $\hat{n}$, is defined almost everywhere (except for a finite number of edges, corners, or tips) on S and is oriented away from D.

- The cavity volume D is filled with a homogeneous, isotropic, linear material characterized by its permittivity ϵ_1 and permeability μ_1, one or both of which may be complex.

- The upper half space is filled with free space.

Before proceeding further, we should clarify that the symbol $\vec{r}$ will be used to denote either the position vector $x\hat{x} + y\hat{y} + z\hat{z}$ or the corresponding point (x, y, z). The distinction will be clear from the context in which $\vec{r}$ is used.
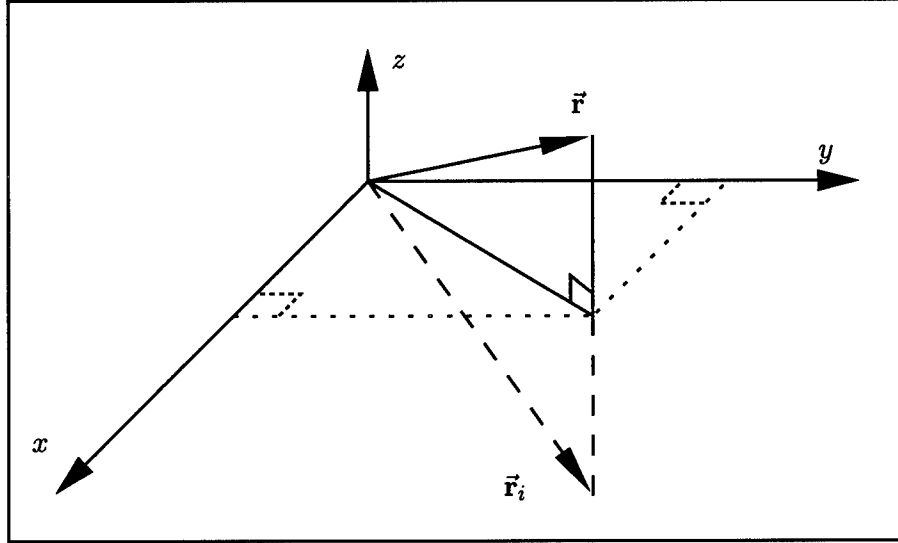
Figure 4   Position vector, $\vec{r}$, and its image, $\vec{r}_i$

In what follows we shall make extensive use of image theory. We define the image of $\vec{r}$ with respect to the xy-plane, as $\vec{r}_i = x\hat{x} + y\hat{y} - z\hat{z} = \vec{r} \cdot \overline{\overline{I}}_i$, where $\overline{\overline{I}}_i = \hat{x}\hat{x} + \hat{y}\hat{y} - \hat{z}\hat{z}$ is the image dyadic. Similarly for a field vector $\vec{A}(\vec{r}) = A_x(\vec{r})\hat{x} + A_y(\vec{r})\hat{y} + A_z(\vec{r})\hat{z}$, we have the image $\vec{A}_i(\vec{r}) = A_x(\vec{r})\hat{x} + A_y(\vec{r})\hat{y} - A_z(\vec{r})\hat{z} = \vec{A}(\vec{r}) \cdot \overline{\overline{I}}_i$. To summarize, the image of any vector, be it a position vector or a field vector function, is simply that vector dotted into the image dyadic.

Image surfaces and image volumes are defined analogously to image vectors: the image of the cavity surface S is denoted S_i and defined as $S_i = \{\vec{r} : \vec{r}_i \in S\}$, while the image of the cavity

12

volume D is denoted D_i and is defined as $D_i = \{\vec{r} : \vec{r}_i \in D\}$, The portion of the upper half space less those points that are not contained in either volume D_i or surface S_i is denoted D_f.

3.2 Fields

We restrict all impressed sources to exist only in D_f so that the total fields in D and D_i satisfy the following Maxwell's equations for homogeneous, linear, isotropic, source-free media ($e^{\jmath\omega t}$ time convention) [21]:

$$\nabla \times \vec{\mathbf{E}} = -\jmath\omega\mu\vec{\mathbf{H}} \qquad (1a)$$

$$\nabla \times \vec{\mathbf{H}} = \jmath\omega\epsilon\vec{\mathbf{E}} \qquad (1b)$$

$$\nabla \cdot \vec{\mathbf{E}} = 0 \qquad (1c)$$

$$\nabla \cdot \vec{\mathbf{H}} = 0 \qquad (1d)$$

where $\vec{\mathbf{E}} \equiv \vec{\mathbf{E}}(\vec{r})$ is the electric field intensity in volts/meter, and $\vec{\mathbf{H}} \equiv \vec{\mathbf{H}}(\vec{r})$ is the magnetic field intensity in Amperes/meter. ω is the frequency in radians/second, μ is the permeability of the medium in Henrys/meter, ϵ is the permittivity of the medium in Farads/meter, and $\jmath = \sqrt{-1}$. Taking the curl of equations (1a) and (1b) and combining them, we see that both $\vec{\mathbf{E}}$ and $\vec{\mathbf{H}}$ satisfy the homogeneous wave equation [59]

$$\nabla \times \nabla \times \vec{\mathbf{E}}(\vec{r}) - k^2\vec{\mathbf{E}}(\vec{r}) = 0 \qquad (2a)$$

$$\nabla \times \nabla \times \vec{\mathbf{H}}(\vec{r}) - k^2\vec{\mathbf{H}}(\vec{r}) = 0 \qquad (2b)$$

where $k = \omega\sqrt{\mu\epsilon}$ is the propagation constant of the medium in inverse meters. We assume that the known incident fields, $\vec{\mathbf{E}}^{\text{inc}}$ and $\vec{\mathbf{H}}^{\text{inc}}$, impinge on the open cavity, giving rise to the reflected fields, $\vec{\mathbf{E}}^{\text{ref}}$ and $\vec{\mathbf{H}}^{\text{ref}}$, and the diffracted or scattered fields, $\vec{\mathbf{E}}^{\text{scat}}$ and $\vec{\mathbf{H}}^{\text{scat}}$. The given incident fields are defined to be those that exist in unbounded free space. The reflected fields are defined to be those scattered by an unbroken, perfectly-conducting ground plane located at $z = 0$. The scattered fields represent a perturbation due to the presence of the cavity, and are defined as the remainders: $\vec{\mathbf{E}}^{\text{scat}} \equiv \vec{\mathbf{E}} - \vec{\mathbf{E}}^{\text{inc}} - \vec{\mathbf{E}}^{\text{ref}}$ and $\vec{\mathbf{H}}^{\text{scat}} \equiv \vec{\mathbf{H}} - \vec{\mathbf{H}}^{\text{inc}} - \vec{\mathbf{H}}^{\text{ref}}$.

In addition to equations (1) and (2), the fields must also satisfy certain boundary conditions. The tangential component of the total electric field must vanish on σ^c and S:

$$\hat{\mathbf{n}} \times \vec{\mathbf{E}}(\vec{\mathbf{r}}) = 0 \qquad \text{for } \vec{\mathbf{r}} \in S \qquad (3a)$$

$$\hat{\mathbf{z}} \times \vec{\mathbf{E}}(\vec{\mathbf{r}}) = 0 \qquad \text{for } \vec{\mathbf{r}} \in \sigma^c \qquad (3b)$$

The tangential components of the total electric and magnetic fields must be continuous across the aperture σ:

$$\lim_{\delta \to 0} \left[\hat{\mathbf{z}} \times \vec{\mathbf{E}}(\vec{\mathbf{r}} + \delta \, \hat{\mathbf{z}}) - \hat{\mathbf{z}} \times \vec{\mathbf{E}}(\vec{\mathbf{r}} - \delta \, \hat{\mathbf{z}}) \right] = 0 \qquad \text{for } \vec{\mathbf{r}} \in \sigma \qquad (4a)$$

$$\lim_{\delta \to 0} \left[\hat{\mathbf{z}} \times \vec{\mathbf{H}}(\vec{\mathbf{r}} + \delta \, \hat{\mathbf{z}}) - \hat{\mathbf{z}} \times \vec{\mathbf{H}}(\vec{\mathbf{r}} - \delta \, \hat{\mathbf{z}}) \right] = 0 \qquad \text{for } \vec{\mathbf{r}} \in \sigma \qquad (4b)$$

Finally, the scattered fields must satisfy the Sommerfeld's radiation conditions at infinity ([59, pp. 485-6] and [31, p. 56])

$$\lim_{|\vec{\mathbf{r}}| \to \infty} \left[\vec{\mathbf{r}} \cdot \nabla \vec{\mathbf{E}}^{\text{scat}}(\vec{\mathbf{r}}) + \jmath k |\vec{\mathbf{r}}| \vec{\mathbf{E}}^{\text{scat}}(\vec{\mathbf{r}}) \right] = 0 \qquad (5a)$$

$$\lim_{|\vec{\mathbf{r}}| \to \infty} \left[\vec{\mathbf{r}} \cdot \nabla \vec{\mathbf{H}}^{\text{scat}}(\vec{\mathbf{r}}) + \jmath k |\vec{\mathbf{r}}| \vec{\mathbf{H}}^{\text{scat}}(\vec{\mathbf{r}}) \right] = 0 \qquad (5b)$$

as well as the regularity conditions [59, pp. 485-6]

$$\lim_{|\vec{\mathbf{r}}| \to \infty} |\vec{\mathbf{r}}| \vec{\mathbf{E}}^{\text{scat}}(\vec{\mathbf{r}}) = 0 \qquad (6a)$$

$$\lim_{|\vec{\mathbf{r}}| \to \infty} |\vec{\mathbf{r}}| \vec{\mathbf{H}}^{\text{scat}}(\vec{\mathbf{r}}) = 0 \qquad (6b)$$

3.3 Green's Functions

We introduce the scalar Green's function

$$G(k; \vec{\mathbf{r}}, \vec{\mathbf{r}}') = \frac{e^{-\jmath k R}}{4 \pi R}$$
$$R = |\vec{\mathbf{r}} - \vec{\mathbf{r}}'| \qquad (7)$$

where $\vec{\mathbf{r}} = x\hat{\mathbf{x}} + y\hat{\mathbf{y}} + z\hat{\mathbf{z}}$ and $\vec{\mathbf{r}}' = x'\hat{\mathbf{x}} + y'\hat{\mathbf{y}} + z'\hat{\mathbf{z}}$ are position vectors in unprimed and primed coordinates, respectively. The scalar Green's function satisfies the distributional differential

14

equation

$$\nabla^2 G + k^2 G = -\delta(\vec{r} - \vec{r}')$$
$$= -\delta(x - x')\,\delta(y - y')\,\delta(z - z') \tag{8}$$

as well as the scalar analogues of the radiation and regularity conditions expressed by equations (5) and (6). For readability, we will suppress the dependence of $G(k; \vec{r}, \vec{r}')$ on k, $\vec{r}$, and $\vec{r}'$ where their presence is clearly implied.

For convenience we define the auxiliary scalar functions

$$G_D(k; \vec{r}, \vec{r}') = G(k; \vec{r}, \vec{r}') - G(k; \vec{r}, \vec{r}_i') \tag{9a}$$

$$G_N(k; \vec{r}, \vec{r}') = G(k; \vec{r}, \vec{r}') + G(k; \vec{r}, \vec{r}_i') \tag{9b}$$

It is easy to verify that G_D and G_N satisfy the homogeneous boundary conditions

$$G_D(k; \vec{r}, \vec{r}') = 0 \qquad \text{for } z = 0 \tag{10a}$$

$$\frac{\partial}{\partial z} G_N(k; \vec{r}, \vec{r}') = 0 \qquad \text{for } z = 0 \tag{10b}$$

We shall refer to G_D as the Dirichlet scalar half-space Green's function, and G_N as the Neumann scalar half-space Green's function. We recognize G_D as the Green's function for a horizontal electric dipole over a ground plane, and G_N as the Green's function for a vertical electric dipole over a ground plane [62, page 404]. Next, we introduce the dyadic function

$$\overline{\overline{\Gamma}}(k; \vec{r}, \vec{r}') = -\jmath k \nabla G(k; \vec{r}, \vec{r}') \times \overline{\overline{I}} \tag{11}$$

where $\overline{\overline{I}} = \hat{x}\hat{x} + \hat{y}\hat{y} + \hat{z}\hat{z}$ is the idemfactor. One can show that $\overline{\overline{\Gamma}}$ satisfies the distributional differential equation (Appendix A)

$$\nabla \times \nabla \times \overline{\overline{\Gamma}} - k^2 \overline{\overline{\Gamma}} = -\jmath k \nabla \delta(\vec{r} - \vec{r}') \times \overline{\overline{I}} \tag{12}$$

15

The curl of $\overline{\overline{\Gamma}}$ can be expressed in the alternate forms

$$\nabla \times \overline{\overline{\Gamma}}(k; \vec{r}, \vec{r}') = -\jmath k \left[k^2 G(k; \vec{r}, \vec{r}') + \nabla\nabla G(k; \vec{r}, \vec{r}') \right]$$

$$= -\jmath k \left\{ \left[3 + 3\jmath kR + (\jmath kR)^2 \right] \hat{\mathbf{R}}\hat{\mathbf{R}} \right.$$

$$\left. - \left[1 + \jmath kR + (\jmath kR)^2 \right] \overline{\overline{\mathbf{I}}} \right\} \frac{G(k; \vec{r}, \vec{r}')}{R^2} \tag{13}$$

where $\hat{\mathbf{R}} = (\vec{r} - \vec{r}')/R$. Similarly, we define the auxiliary dyadic functions

$$\overline{\overline{\Gamma}}_1 = -\jmath k \left(\nabla G_N \times \overline{\overline{\mathbf{I}}}_t + \nabla G_D \times \hat{\mathbf{z}}\hat{\mathbf{z}} \right) \tag{14a}$$

$$\overline{\overline{\Gamma}}_2 = -\jmath k \left(\nabla G_D \times \overline{\overline{\mathbf{I}}}_t + \nabla G_N \times \hat{\mathbf{z}}\hat{\mathbf{z}} \right) \tag{14b}$$

where $\overline{\overline{\mathbf{I}}}_t = \hat{\mathbf{x}}\hat{\mathbf{x}} + \hat{\mathbf{y}}\hat{\mathbf{y}}$ is the transverse idemfactor. It is easy to show that the auxiliary dyadic functions satisfy the homogeneous boundary conditions

$$\hat{\mathbf{z}} \times \overline{\overline{\Gamma}}_1 = 0 \qquad\qquad \text{for } z = 0 \tag{15a}$$

$$\hat{\mathbf{z}} \times \nabla \times \overline{\overline{\Gamma}}_2 = 0 \qquad\qquad \text{for } z = 0 \tag{15b}$$

as well as the equations

$$\hat{\mathbf{z}} \cdot \left[\vec{\mathbf{A}}(\vec{r}) \times \nabla \times \overline{\overline{\Gamma}}_1(k; \vec{r}, \vec{r}') \right] = 2\hat{\mathbf{z}} \cdot \left[\vec{\mathbf{A}}(\vec{r}) \times \nabla \times \overline{\overline{\Gamma}}(k; \vec{r}, \vec{r}') \right] \qquad \text{for } z = 0 \tag{16a}$$

$$\hat{\mathbf{z}} \cdot \left[\vec{\mathbf{A}}(\vec{r}) \times \overline{\overline{\Gamma}}_2(k; \vec{r}, \vec{r}') \right] = 2\hat{\mathbf{z}} \cdot \left[\vec{\mathbf{A}}(\vec{r}) \times \overline{\overline{\Gamma}}(k; \vec{r}, \vec{r}') \right] \qquad \text{for } z = 0 \tag{16b}$$

where $\vec{\mathbf{A}}(\vec{r})$ is any vector function of position.

3.4 Radiation Integrals

The scalar and dyadic functions defined in the previous section provide the building blocks for three theorems which are fundamental to the development of the integral equations of our problem. All of these theorems are presented in [2] and proved in Appendix A. We state them here.

Theorem 1 *Let V be a homogeneous region with regular boundary ∂V, $\hat{\mathbf{n}}$ be the outward unit normal vector on ∂V, and $\overline{\overline{\Gamma}} \equiv \overline{\overline{\Gamma}}(k; \mathbf{r}, \mathbf{r}')$ be defined by equation (11). If $\vec{A} \equiv \vec{A}(\vec{r})$ satisfies $\nabla \times \nabla \times \vec{A} - k^2 \vec{A} = \vec{0} \quad \forall \quad \vec{r} \in V$, then*

$$
\int_{\partial V} \hat{\mathbf{n}} \cdot \left\{ \vec{A} \times \left[\nabla \times \overline{\overline{\Gamma}} \right] + \left[\nabla \times \vec{A} \right] \times \overline{\overline{\Gamma}} \right\} ds = \begin{cases} jk\nabla' \times \vec{A}(\vec{r}') & \text{for } \vec{r}' \in V \\ 0 & \text{for } \vec{r}' \notin \overline{V} \end{cases} \tag{17}
$$

where $\overline{V}$ is the closure of V; that is, the union of V and its boundary.

Theorem 2 *Let V, $\overline{V}$, ∂V, $\hat{\mathbf{n}}$, and $\vec{A}$ be defined as in Theorem 1. Let $\overline{\overline{\Gamma}}_1$ be defined by equation (14a), V_i be the image of V with respect to the xy-plane, and $\overline{V}_i$ be the closure of V_i. Then*

$$
\int_{\partial V} \hat{\mathbf{n}} \cdot \left\{ \vec{A} \times \left[\nabla \times \overline{\overline{\Gamma}}_1 \right] + \left[\nabla \times \vec{A} \right] \times \overline{\overline{\Gamma}}_1 \right\} ds = \begin{cases} jk\nabla' \times \vec{A}(\vec{r}') & \text{for } \vec{r}' \in V \\ jk \left[\nabla'_i \times \vec{A}(\vec{r}_i') \right]_i & \text{for } \vec{r}' \in V_i \\ 0 & \text{for } \vec{r}' \notin \overline{V} \cup \overline{V}_i \end{cases}
$$

$$\tag{18}$$

Theorem 3 *Let V, $\overline{V}$, ∂V, V_i, $\overline{V}_i$, $\hat{\mathbf{n}}$, and $\vec{A}$ be defined as in Theorem 2. Let $\overline{\overline{\Gamma}}_2$ be defined by equation (14b). Then*

$$
\int_{\partial V} \hat{\mathbf{n}} \cdot \left\{ \vec{A} \times \left[\nabla \times \overline{\overline{\Gamma}}_2 \right] + \left[\nabla \times \vec{A} \right] \times \overline{\overline{\Gamma}}_2 \right\} ds = \begin{cases} jk\nabla' \times \vec{A}(\vec{r}') & \text{for } \vec{r}' \in V \\ -jk \left[\nabla'_i \times \vec{A}(\vec{r}_i') \right]_i & \text{for } \vec{r}' \in V_i \\ 0 & \text{for } \vec{r}' \notin \overline{V} \cup \overline{V}_i \end{cases}
$$

$$\tag{19}$$

The operator ∇ differentiates with respect to unprimed coordinates, while ∇' differentiates with respect to primed coordinates. The differential operator ∇'_i is the same as ∇' except that $\frac{\partial}{\partial z'}$ is replaced by $\frac{-\partial}{\partial z'}$. Theorems 1–3 do not apply when $\vec{r}'$ lies exactly on ∂V, but are valid as $\vec{r}'$ approaches ∂V from either the interior or exterior of V.

Much like the source-free form of the Stratton–Chu equations [59], Theorems 1–3 relate a vector function evaluated at a point to an integral over a closed surface. We may think of $\vec{A}$ and

17

$\nabla \times \vec{A}$ on the surface as effective sources giving rise to $\nabla \times \vec{A}$ in the volume interior, and, in the case of Theorems 2 and 3, $\nabla \times \vec{A}$ in the image of the volume interior. However, Theorems 1–3 are stated in general terms; the only requirements are that the vector function $\vec{A}(\vec{r})$ satisfy the homogeneous wave equation (2) and that the outward unit normal $\hat{n}$ be defined almost everywhere on ∂V. In this section, we will specialize Theorems 1–3 to the OCRED scattering problem shown in Figure 3 by associating $\vec{A}(\vec{r})$ with various OCRED field components and associating V with either the cavity volume D or the upper half space, $z > 0$.

A notational distinction arises when the cavity volume D is filled with a material whose constitutive parameters differ from those of free space. When we associate V with D, the wavenumber for the cavity medium appears in the wave equation and the scalar and dyadic Green's functions; that is, $k = k_1 = \omega\sqrt{\mu_1\epsilon_1}$. When we associate V with the upper half space, the wavenumber is the free space wavenumber, $k = k_0 = \omega\sqrt{\mu_0\epsilon_0}$.

An exhaustive list of the possible equations arising from the application of Theorems 1–3 to the OCRED problem appears in Appendix B. Here, we will only present those results which directly contribute to the final integral equations of Section 3.5.

Application 1. Let $V = D$, $\vec{A} = \vec{H}$, and $\vec{r}' \in D$ in Theorem 1. Making use of equations (1b) and (3a), we obtain

$$k_1^2 Y_1 \vec{E}(\vec{r}') = -\int_{\partial D} \left[\hat{n} \times \vec{H}(\vec{r})\right] \cdot \nabla \times \overline{\overline{\Gamma}}(k_1; \vec{r}, \vec{r}') \, ds$$
$$- jk_1 Y_1 \int_\sigma \left[\hat{z} \times \vec{E}(\vec{r})\right] \cdot \overline{\overline{\Gamma}}(k_1; \vec{r}, \vec{r}') \, d\sigma \qquad \text{for } \vec{r}' \in D \qquad (20)$$

where $Y_1 = \sqrt{\epsilon_1/\mu_1}$ is the intrinsic admittance of the cavity material. Equation (20) shows that the total electric field at any point in the cavity volume is a function of the tangential electric and magnetic fields on the cavity surface and aperture.

Application 2. Let $V = D$, $\vec{A} = \vec{E}$, and $\vec{r}' \in D$ in Theorem 1. Making use of equations (1a) and (3a), we obtain

$$k_1^2 Z_1 \vec{H}(\vec{r}') = \int_\sigma \left[\hat{z} \times \vec{E}(\vec{r}) \right] \cdot \nabla \times \overline{\overline{\Gamma}}(k_1; \vec{r}, \vec{r}') \, ds$$

$$- jk_1 Z_1 \int_{\partial D} \left[\hat{n} \times \vec{H}(\vec{r}) \right] \cdot \overline{\overline{\Gamma}}(k_1; \vec{r}, \vec{r}') \, d\sigma \qquad \text{for } \vec{r}' \in D \qquad (21)$$

where $Z_1 = \sqrt{\mu_1/\epsilon_1}$ is the intrinsic impedance of the cavity material. Equation (21) shows that the total magnetic field at any point in the cavity volume is a function of the tangential electric and magnetic fields on the cavity surface and aperture.

Application 3. Let V be the upper half space, $\vec{A} = \vec{E}^{\text{scat}}$, and $z' > 0$ in Theorem 2. Making use of equations (1a), (3b), (15a), and (16a), we obtain

$$\frac{-k_0^2 Z_0}{2} \vec{H}^{\text{scat}}(\vec{r}') = \int_\sigma \hat{z} \times \vec{E}(\vec{r}) \cdot \nabla \times \overline{\overline{\Gamma}}(k_0; \vec{r}, \vec{r}') \, d\sigma \qquad \text{for } z' > 0 \qquad (22)$$

Equation (22) shows that the scattered magnetic field at any point in the upper half space is a function of the tangential electric field on the cavity aperture.

Application 4. Let $V = D$, $\vec{A} = \vec{E}$, and $\vec{r}' \in D$ in Theorem 3. Making use of equations (1a), (3a), (15b), and (16b), we obtain

$$jk_1 \vec{H}(\vec{r}') = 2 \int_\sigma \left[\hat{z} \times \vec{H}(\vec{r}) \right] \cdot \overline{\overline{\Gamma}}(k_1; \vec{r}, \vec{r}') \, d\sigma$$

$$+ \int_S \left[\hat{n} \times \vec{H}(\vec{r}) \right] \cdot \overline{\overline{\Gamma}}_2(k_1; \vec{r}, \vec{r}') \, ds \qquad \text{for } \vec{r}' \in D \qquad (23)$$

Equation (23) shows that the total magnetic field at any point in the cavity volume is a function of the tangential magnetic field on the cavity surface and aperture.

Application 5. Let V be the upper half space, $\vec{A} = \vec{H}^{\text{scat}}$, and $z' > 0$ in Theorem 3. Making use of equations (1b), (3b), (15b), and (16b), we obtain

$$\frac{-jk_0}{2} \vec{E}^{\text{scat}}(\vec{r}') = \int_\sigma \hat{z} \times \vec{E}(\vec{r}) \cdot \overline{\overline{\Gamma}}(k_0; \vec{r}, \vec{r}') \, d\sigma \qquad \text{for } z' > 0 \qquad (24)$$

Equation (24) shows that the scattered electric field at any point in the upper half space is a function of the tangential electric field on the cavity aperture. This equation serves as the overall radiation integral for the OCRED scattering problem. Once $\hat{z} \times \vec{E}$ on σ is known, equation (24) allows us to calculate the OCRED echo area A_e (also known as radar cross section) using the well-known definition [21, page 116]

$$A_e = \lim_{|\vec{r}'| \to \infty} 4\pi \left| \vec{r}' \right|^2 \left| \vec{E}^{\text{scat}}(\vec{r}') \right|^2 \tag{25}$$

where the incident field is a uniform plane wave having unit amplitude.

3.5 Surface Integral Equations

Equations (20)–(24) define the total fields in the cavity volume and the scattered fields in the upper half space in terms of the tangential field components on the cavity surface and aperture. Thus it is sufficient to find these tangential field components to solve the entire OCRED scattering problem. In this section, we develop surface integral equations which may be used to find these tangential field components.

We notice that the left and right sides of equations (20)–(23) involve different types of field quantities. Specifically, we see that the right sides of equations (20)–(23) involve the tangential components of $\vec{E}$ and $\vec{H}$ evaluated on ∂D, but that the left sides of these equations involve $\vec{E}$ and $\vec{H}$ evaluated at points away from ∂D.

To make equations (20)–(23) more useful, we will let $\vec{r}'$ approach ∂D, and then "sift out" the tangential component of the result. First, we fix a point $\vec{r}$ on ∂D, so that $\hat{n}$ is the outward unit normal vector at $\vec{r}$, as shown in Figure 5. Second, we cross multiply the equations by $\hat{n}$. Finally, we let $\vec{r}' = \vec{r} + \delta \, \hat{n}$ and evaluate the limit as $\delta \to 0$. In so doing, we make use of the following theorem ([2], [30, p. 334], [62, p. 354], [48, p. 205]):

Theorem 4 *Let V be a volume with regular boundary ∂V, $\vec{r}$ be a fixed point on ∂V, $\hat{n}$ be the outward unit normal vector at $\vec{r}$, and $\overline{\overline{\Gamma}}(k; \vec{r}, \vec{r}')$ be defined by equation (11). If $\vec{A}(\vec{r})$ is continuous*
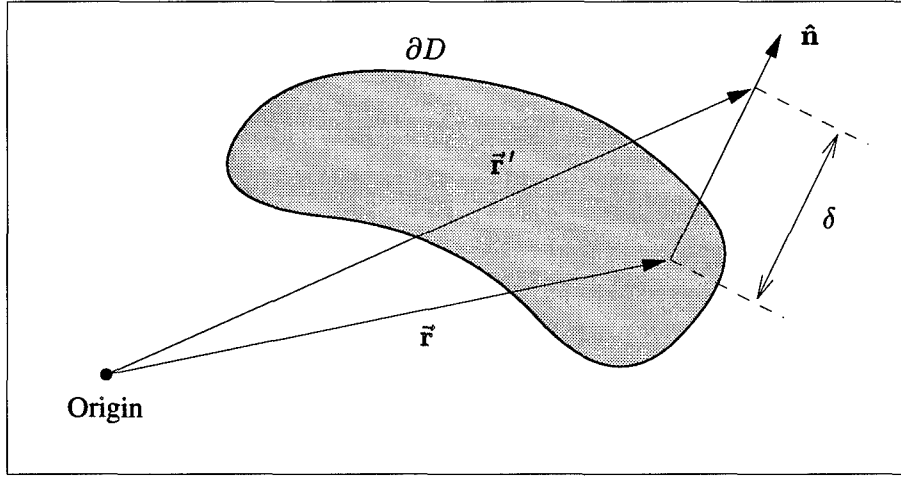
Figure 5   A portion of ∂D in the neighborhood of $\vec{r}$. The point $\vec{r}'$ approaches $\vec{r}$ along $\hat{n}$ such that $\vec{r}' - \vec{r} = \delta\,\hat{n}$.

on ∂V, then

$$\lim_{\vec{r}' \to \vec{r}} \hat{n} \times \int_{\partial V} \vec{A}(\vec{r}'') \cdot \overline{\overline{\Gamma}}(k; \vec{r}'', \vec{r}')\, ds''$$

$$= \mp \frac{jk}{2}\vec{A}(\vec{r}) + \hat{n} \times \int_{\partial V} \vec{A}(\vec{r}'') \cdot \overline{\overline{\Gamma}}(k; \vec{r}'', \vec{r}')\, ds'' \qquad (26)$$

where the upper sign is taken if $\vec{r}' \to \vec{r}$ from the exterior of V, and the lower sign is taken if $\vec{r}' \to \vec{r}$ from the interior of V.

Theorem 4 provides a means to treat the limit of the integrals involving the dyadic kernel $\overline{\overline{\Gamma}}$ as $\vec{r}'$ approaches ∂D; the limit as $\vec{r}' \to \partial D$ is different from the evaluation of such integrals with $\vec{r}' \in \partial D$. In contrast, integrals involving the dyadic kernel $\nabla \times \overline{\overline{\Gamma}}$ exhibit no such discontinuity and behave as

$$\lim_{\vec{r}' \to \vec{r}} \hat{n} \times \int_{\partial V} \vec{A}(\vec{r}'') \cdot \nabla \times \overline{\overline{\Gamma}}(k; \vec{r}'', \vec{r}')\, ds'' = \hat{n} \times \int_{\partial V} \vec{A}(\vec{r}'') \cdot \nabla \times \overline{\overline{\Gamma}}(k; \vec{r}'', \vec{r}')\, ds'' \qquad (27)$$

where V, ∂V, $\vec{r}$, $\hat{n}$, $\overline{\overline{\Gamma}}$, and $\vec{A}$ are defined as in Theorem 4. Furthermore, we note that the total tangential fields are continuous across σ, as shown in equations (4a) and (4b).

We now apply the procedure outlined earlier in this section to each of equations (20)–(23).

21

Application to equation (20). Fix $\vec{r} \in \sigma$ so that $\hat{n} = \hat{z}$, and set $\vec{r}' = \vec{r} - \delta\,\hat{z}$, with $\delta > 0$. We cross multiply equation (20) by $\hat{z}$ and take the limit as $\delta \to 0$. Applying Theorem 4, we obtain

$$\frac{-k_1^2 Y_1}{2}\hat{z} \times \vec{E}(\vec{r}') = \hat{z} \times \int_{\partial D} \left[\hat{n} \times \vec{H}(\vec{r})\right] \cdot \nabla \times \overline{\overline{\Gamma}}(k_1; \vec{r}, \vec{r}')\, ds$$

$$+ \jmath k_1 Y_1 \hat{z} \times \int_{\sigma} \left[\hat{z} \times \vec{E}(\vec{r})\right] \cdot \overline{\overline{\Gamma}}(k_1; \vec{r}, \vec{r}')\, d\sigma \qquad \text{for } \vec{r}' \in \sigma \qquad (28)$$

It is easy to show that $\hat{z} \times \left\{ \left[\hat{z} \times \vec{E}(\vec{r})\right] \cdot \overline{\overline{\Gamma}}(k_1; \vec{r}, \vec{r}') \right\} = 0$ when $\vec{r} \in \sigma$ and $\vec{r}' \in \sigma$. Thus the second integral in equation (28) vanishes and we are left with

$$\frac{-k_1^2 Y_1}{2}\hat{z} \times \vec{E}(\vec{r}') = \hat{z} \times \int_{\partial D} \left[\hat{n} \times \vec{H}(\vec{r})\right] \cdot \nabla \times \overline{\overline{\Gamma}}(k_1; \vec{r}, \vec{r}')\, ds \qquad \text{for } \vec{r}' \in \sigma \qquad (29)$$

Equation (29) shows that the tangential electric field on σ can be expressed as a function of the tangential magnetic field on ∂D.

Application to equation (21). Fix $\vec{r} \in \sigma$ so that $\hat{n} = \hat{z}$, and set $\vec{r}' = \vec{r} - \delta\,\hat{z}$, with $\delta > 0$. We cross multiply equation (21) by $\hat{z}$ and take the limit as $\delta \to 0$. Applying Theorem 4, we obtain

$$\frac{k_1^2 Z_1}{2}\hat{z} \times \vec{H}(\vec{r}') = \hat{z} \times \int_{\sigma} \left[\hat{z} \times \vec{E}(\vec{r})\right] \cdot \nabla \times \overline{\overline{\Gamma}}(k_1; \vec{r}, \vec{r}')\, ds$$

$$- \jmath k_1 Z_1 \hat{z} \times \int_{S} \left[\hat{n} \times \vec{H}(\vec{r})\right] \cdot \overline{\overline{\Gamma}}(k_1; \vec{r}, \vec{r}')\, ds \qquad \text{for } \vec{r}' \in \sigma \qquad (30)$$

Equation (30) shows that the tangential magnetic field on σ can be expressed as a function of the tangential magnetic field on S and the tangential electric field on σ.

Application to equation (22). Fix $\vec{r} \in \sigma$ so that $\hat{n} = \hat{z}$, and set $\vec{r}' = \vec{r} + \delta\,\hat{z}$, with $\delta > 0$. We cross multiply equation (22) by $\hat{z}$ and take the limit as $\delta \to 0$. Applying Theorem 4, we obtain

$$\frac{-k_0^2 Z_0}{2}\hat{z} \times \vec{H}^{\text{scat}}(\vec{r}') = \hat{z} \times \int_{\sigma} \hat{z} \times \vec{E}(\vec{r}) \cdot \nabla \times \overline{\overline{\Gamma}}(k_0; \vec{r}, \vec{r}')\, d\sigma \qquad \text{for } \vec{r}' \in \sigma \qquad (31)$$

Noting that $\vec{H}^{scat} = \vec{H} - \vec{H}^{inc} - \vec{H}^{ref}$ and that $\hat{z} \times \vec{H}^{ref} = \hat{z} \times \vec{H}^{inc}$ on σ, this becomes

$$\frac{-k_0^2 Z_0}{2} \hat{z} \times \left[\vec{H}(\vec{r}') - 2\vec{H}^{inc}(\vec{r}') \right] =$$
$$\hat{z} \times \int_\sigma \hat{z} \times \vec{E}(\vec{r}) \cdot \nabla \times \overline{\overline{\Gamma}}(k_0; \vec{r}, \vec{r}') \, d\sigma \qquad \text{for } \vec{r}' \in \sigma \qquad (32)$$

Equation (32) shows that the tangential magnetic field on σ can be expressed as a function of the tangential electric field on σ and the tangential incident magnetic field on σ.

Application to equation (23). Fix $\vec{r} \in S$ and set $\vec{r}' = \vec{r} - \delta \, \hat{n}$, with $\delta > 0$. We cross multiply equation (23) by $\hat{n}$ and take the limit as $\delta \to 0$. Applying Theorem 4, we obtain

$$\frac{jk_1}{2} \hat{n}' \times \vec{H}(\vec{r}') = 2\hat{n}' \times \int_\sigma \left[\hat{z} \times \vec{H}(\vec{r}) \right] \cdot \overline{\overline{\Gamma}}(k_1; \vec{r}, \vec{r}') \, d\sigma$$
$$+ \hat{n}' \times \int_S \left[\hat{n} \times \vec{H}(\vec{r}) \right] \cdot \overline{\overline{\Gamma}}_2(k_1; \vec{r}, \vec{r}') \, ds \qquad \text{for } \vec{r}' \in S \qquad (33)$$

Equation (33) shows that the tangential magnetic field on S satisfies a second-kind integral equation because the unknown function $\hat{n} \times \vec{H}$ appears both within the integral and outside it.

Equations (29), (30), (32), and (33) are coupled integral equations involving four functions: the tangential magnetic field on S, the tangential electric field on σ, the tangential magnetic field on σ, and the incident tangential magnetic field on σ. The last of these functions is known while the first three are not known *a priori*. We associate these tangential field components with equivalent current densities as follows:

$$\vec{J}_S(\vec{r}) \equiv \hat{n} \times \vec{H}(\vec{r}) \qquad\qquad \text{for } \vec{r} \in S \qquad (34a)$$

$$\vec{J}_\sigma(\vec{r}) \equiv \hat{z} \times \vec{H}(\vec{r}) \qquad\qquad \text{for } \vec{r} \in \sigma \qquad (34b)$$

$$\vec{M}_\sigma(\vec{r}) \equiv -\hat{z} \times \vec{E}(\vec{r}) \qquad\qquad \text{for } \vec{r} \in \sigma \qquad (34c)$$

$$\vec{J}^0(\vec{r}) \equiv 2\hat{z} \times \vec{H}^{inc}(\vec{r}) \qquad\qquad \text{for } \vec{r} \in \sigma \qquad (34d)$$

We call $\vec{J}_S$ and $\vec{J}_\sigma$ "equivalent electric current densities" and $\vec{M}_\sigma$ the "equivalent magnetic current density." $\vec{J}^0$ is the familiar "physical optics" electric current density that exists on an unbroken ground plane. With these definitions, equations (29), (30), (32), and (33) become integral equations involving three unknown current densities ($\vec{J}_S$, $\vec{J}_\sigma$, and $\vec{M}_\sigma$), along with one known one ($\vec{J}^0$). We

will find it convenient to combine equations (30) and (32) by dividing equation (30) by $-jk_1$, dividing equation (32) by $-jk_0$, and forming the difference of the result. Then, equations (29), (30), (32), and (33) become

$$\hat{\mathbf{z}} \times \int_{\sigma} \vec{\mathbf{J}}_{\sigma}(\vec{\mathbf{r}}) \cdot \nabla \times \overline{\overline{\Gamma}}(k_1; \vec{\mathbf{r}}, \vec{\mathbf{r}}') \, d\sigma + \hat{\mathbf{z}} \times \int_{S} \vec{\mathbf{J}}_S(\vec{\mathbf{r}}) \cdot \nabla \times \overline{\overline{\Gamma}}(k_1; \vec{\mathbf{r}}, \vec{\mathbf{r}}') \, ds$$
$$= \frac{k_1^2 Y_1}{2} \vec{\mathbf{M}}_{\sigma}(\vec{\mathbf{r}}') \qquad \text{for } \vec{\mathbf{r}}' \in \sigma \qquad (35)$$

$$\hat{\mathbf{z}} \times \int_{\sigma} \vec{\mathbf{M}}_{\sigma}(\vec{\mathbf{r}}) \cdot \left\{ \frac{\nabla \times \overline{\overline{\Gamma}}(k_1; \vec{\mathbf{r}}, \vec{\mathbf{r}}')}{-jk_1} - \frac{\nabla \times \overline{\overline{\Gamma}}(k_0; \vec{\mathbf{r}}, \vec{\mathbf{r}}')}{-jk_0} \right\} \, d\sigma$$
$$+ \frac{jk_1 Z_1 + jk_0 Z_0}{2} \vec{\mathbf{J}}_{\sigma}(\vec{\mathbf{r}}') - Z_1 \hat{\mathbf{z}} \times \int_{S} \vec{\mathbf{J}}_S(\vec{\mathbf{r}}) \cdot \overline{\overline{\Gamma}}(k_1; \vec{\mathbf{r}}, \vec{\mathbf{r}}') \, ds$$
$$= \frac{jk_0 Z_0}{2} \vec{\mathbf{J}}^0(\vec{\mathbf{r}}') \qquad \text{for } \vec{\mathbf{r}}' \in \sigma \qquad (36)$$

$$2\hat{\mathbf{n}}_0 \times \int_{\sigma} \vec{\mathbf{J}}_{\sigma}(\vec{\mathbf{r}}) \cdot \overline{\overline{\Gamma}}(k_1; \vec{\mathbf{r}}, \vec{\mathbf{r}}') \, d\sigma + \hat{\mathbf{n}}_0 \times \int_{S} \vec{\mathbf{J}}_S(\vec{\mathbf{r}}) \cdot \overline{\overline{\Gamma}}_2(k_1; \vec{\mathbf{r}}, \vec{\mathbf{r}}') \, ds$$
$$= \frac{jk_1}{2} \vec{\mathbf{J}}_S(\vec{\mathbf{r}}') \qquad \text{for } \vec{\mathbf{r}}' \in S \qquad (37)$$

Equations (35), (36), and (37) constitute a system of three coupled integral equations involving three unknown functions: $\vec{\mathbf{J}}_S$, $\vec{\mathbf{J}}_{\sigma}$, and $\vec{\mathbf{M}}_{\sigma}$. When this system is solved and the equivalent current densities $\vec{\mathbf{J}}_S$, $\vec{\mathbf{J}}_{\sigma}$, and $\vec{\mathbf{M}}_{\sigma}$ are found, then equations (20)–(24) can be used to find the fields everywhere in the cavity volume and in the upper half space.

We note that equation (35) may be considered to be an explicit definition of $\vec{\mathbf{M}}_{\sigma}$ in terms of $\vec{\mathbf{J}}_{\sigma}$ and $\vec{\mathbf{J}}_S$, which may be used in equations (36) and (37) to eliminate $\vec{\mathbf{M}}_{\sigma}$ as an unknown. Similarly, we note that equation (36) may be considered to be an explicit definition of $\vec{\mathbf{J}}_{\sigma}$ in terms of $\vec{\mathbf{M}}_{\sigma}$ and $\vec{\mathbf{J}}_S$, which may be used in equations (35) and (37) to eliminate $\vec{\mathbf{J}}_{\sigma}$ as an unknown. While these may seem appealing because they reduce the number of unknown functions from three to two, this comes at the price of much more complicated integral equations involving iterated

24

surface integrals. [1] We choose to keep the equations as simple as possible, and thus we will work with all three integral equations for the remainder of this document.

3.6 The Degenerate Case

We define the degenerate case to be that in which the cavity is filled with free space. In this case, $k = k_1 = k_0$, $Y = Y_1 = Y_0$, and $Z = Z_1 = Z_0$, and examination of equation (36) reveals that the dyadic kernel of the integral involving $\vec{M}_\sigma$ vanishes, so that equation (36) involves the electric current densities $\vec{J}_\sigma$ and $\vec{J}_S$ alone. In other words, the electric current densities $\vec{J}_\sigma$ and $\vec{J}_S$ effectively decouple from the magnetic current density $\vec{M}_\sigma$. With $\vec{M}_\sigma$ eliminated, equations (36) and (37) form a system of equations independent of equation (35). We note that this reduced set of equations is identical to those developed by Asvestas and Kleinman [2].

In the degenerate case, it is possible to express the scattered electric field in D_f in terms of $\vec{J}_S$. To see this, we combine equations (178) and (180) to get

$$\vec{H}^{\text{scat}}(\vec{r}') = \frac{1}{jk} \int_S \vec{J}_S(\vec{r}) \cdot \overline{\overline{\Gamma}}_1(k; \vec{r}, \vec{r}') \, ds \qquad \text{for } \vec{r}' \in D_f \qquad (38)$$

Then by equation (1b),

$$\vec{E}^{\text{scat}}(\vec{r}') = \frac{1}{k^2 Y} \nabla \times \int_S \vec{J}_S(\vec{r}) \cdot \overline{\overline{\Gamma}}_1(k; \vec{r}, \vec{r}') \, ds \qquad \text{for } \vec{r}' \in D_f \qquad (39)$$

Equations (36), (37), and (39) are all that are needed to solve the degenerate scattering OCRED problem.

3.7 Summary

In this chapter, we have defined the OCRED geometry along with the characteristics of the electromagnetic fields for the OCRED scattering problem. We have introduced dyadic functions which form the kernels of several integral equations defining the electromagnetic fields everywhere in terms of the equivalent electric and magnetic current densities on the cavity surface and aperture.

---

[1]Such a reduction may be attractive when dealing with very large geometries where matrix solve time dominates the overall solution time, but in this effort we will limit ourselves to smaller OCREDs.

We have transformed these integral equations into a set of three coupled surface integral equations that are satisfied by the equivalent current densities. We have shown that this set is a generalization of the set developed by Asvestas and Kleinman.

IV. Numerical Solution of the Integral Equations

The set of three coupled integral equations (35)–(37) cannot be solved analytically for arbitrary cavity shapes. However, we can approximate the solution to an acceptable level of accuracy by using the method of moments [22]. The method of moments involves approximating the integral equations by a system of linear equations, and then solving the system to find the unknown functions. Provided it is implemented judiciously, the approximate solution produced by the method of moments approaches the exact solution if the latter is available.

To start with the method of moments involves approximating the unknown function as a linear combination of a known set of functions, called basis functions. Usually, the basis functions are of the subdomain type, which means they are non-zero over only a small portion of the domain of the unknown function. This allows great flexibility in approximating the unknown function, but at the expense of needing to find a large number of coefficients. One useful choice of basis functions [54] uses triangular subdomains to model the unknown function over arbitrary three-dimensional surfaces. These triangles are typically 0.1λ on a side (where λ is the wavelength), so that one square wavelength of surface requires on the order of 100 basis functions. It is easy to see that the problem rapidly becomes unmanageable as the domain of the unknown function increases in area expressed in square wavelengths.

The remainder of this chapter is organized as follows. The geometry of a special class of OCRED geometry is defined in Section 4.1. The basis functions to be employed in the method of moments are introduced in Section 4.2, while the testing functions and inner product are discussed in Section 4.3. The details of calculating the elements of the moment method matrix are given in Section 4.4. The system excitation, or forcing function, is given in Section 4.5, and some computational savings reaped by exploiting symmetry properties are shown in Section 4.6.

4.1 Body of Revolution OCRED

Since the backscatter pattern of an effective OCRED is relatively insensitive to small changes in aspect angle, we will restrict our attention to those geometries having a backscatter pattern that is independent of azimuth angle. Such OCREDs are symmetric with respect to the z axis, and

27

are termed "body of revolution," or BOR, OCREDs. We shall see also that this restriction greatly reduces the labor of modeling the OCRED backscattering problem.
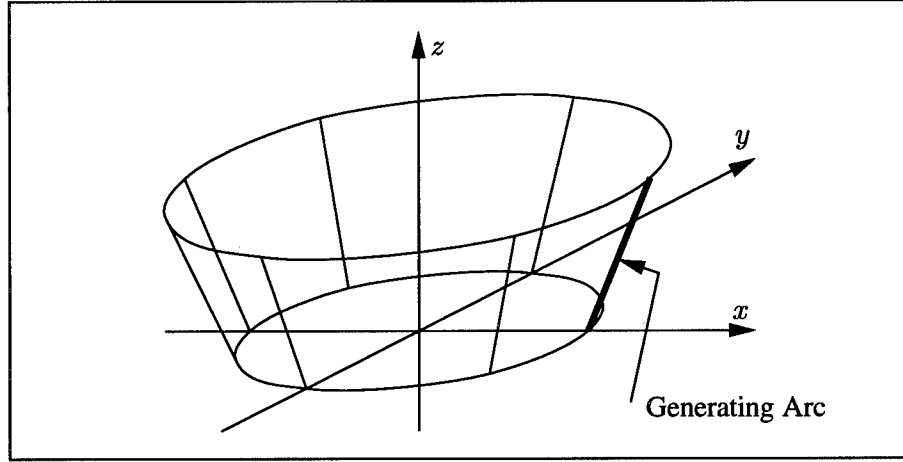
Figure 6   A cone frustum generated by revolving a line segment about the z axis.

Consider a simple, open curve that lies in the xz plane and does not intersect the z axis. If we revolve this curve about the z axis, we generate an open surface that is rotationally symmetric about the z axis. Such a surface is called a surface of revolution, and the curve is called the generating arc. If the curve is a straight line segment, then the corresponding surface of revolution is a cone frustum, as shown in Figure 6. If we let the endpoints, and only the endpoints, of the curve lie on the z axis, then the corresponding surface of revolution becomes a closed surface, and the region enclosed by the surface is called a body of revolution. If the OCRED cavity interior D is a body of revolution, we call the OCRED a BOR OCRED.

The generating arc for the BOR OCRED is a bounded, piecewise-smooth plane curve which begins at the origin and ends on the z-axis somewhere below the origin. The BOR OCRED generating arc is shown in Figure 7. It does not intersect the z-axis except at the endpoints, and, without loss of generality, we restrict the generating arc to lie in the xz-plane. We parameterize the generating arc by its arc length ℓ such that $\ell = 0$ corresponds to its endpoint at the origin and $\ell = L$, where L is the length of the generating arc, corresponds to its endpoint on the negative z axis.

If $\vec{r}(\ell)$ is a point on the generating arc, then we see that $\vec{r}(\ell)$ is uniquely determined by its coordinates in the xz plane; that is, $\vec{r}(\ell) = \hat{x}\,\rho(\ell) + \hat{z}\,z(\ell)$, as shown in Figure 7. Since, for the
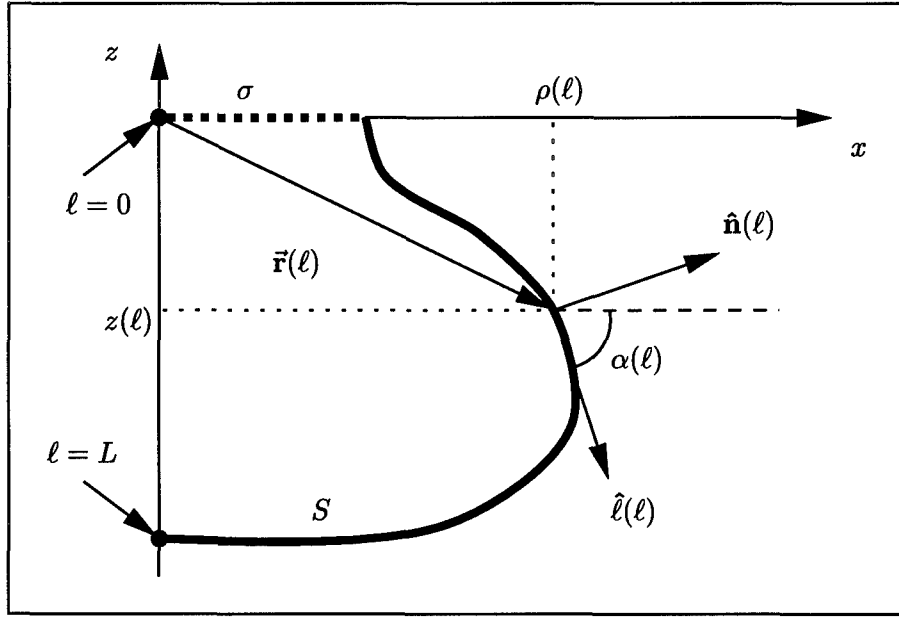
Figure 7 The generating arc of a body of revolution (BOR) OCRED. The dashed portion generates the aperture σ while the solid portion generates the cavity surface S. The arc length variable ℓ increases from 0 to L. The position vector $\vec{r}(\ell)$ defines a point on the generating arc, with normal vector $\hat{n}(\ell)$ and tangent vector $\hat{\ell}(\ell)$. The angle $\alpha(\ell)$ defines the orientation of $\hat{\ell}(\ell)$.

BOR OCRED geometry, no part of the generating arc lies above the z axis or to the left of the x axis, we see that $\rho(\ell) \geq 0$ and $z(\ell) \leq 0$ for $0 \leq \ell \leq L$.

If we now allow $\vec{r}(\ell)$ to rotate about the z axis by an amount ϕ in the positive sense, then we see that every point on the surface of revolution is specified by the chosen values of ℓ and ϕ in the ranges $0 \leq \ell \leq L$ and $0 \leq \phi < 2\pi$. For arbitrary ℓ and ϕ, the corresponding point on the surface of revolution is then given by

$$\vec{r}(\ell, \phi) = \hat{x}\,\rho(\ell)\,\cos\phi + \hat{y}\,\rho(\ell)\,\sin\phi + \hat{z}\,z(\ell) \tag{40}$$

It is obvious that ρ, ϕ, and z are the coordinates of the circular cylindrical coordinate system.

We have established that the coordinates ℓ and ϕ uniquely determine a point $\vec{r}(\ell, \phi)$ on the surface of revolution. In addition, they also determine several vector quantities of interest. Specifically, we define $\hat{\ell}(\ell)$ to be the unit vector in the direction of increasing ℓ, $\hat{\phi}(\phi)$ to be the unit vector in the direction of increasing ϕ, and $\hat{n}(\ell, \phi)$ to be the unit vector normal to the surface, pointing away from the interior volume. It is easy to see that $\hat{\ell}$, $\hat{\phi}$, and $\hat{n}$ are mutually orthogonal.

29

Thus, $\hat{\ell}$ and $\hat{\phi}$ are tangent to the surface at $\vec{r}(\ell, \phi)$. The angle $\alpha(\ell)$ describes the orientation of $\hat{\ell}$ and $\hat{n}$ in the xz-plane, such that $\hat{\ell} = \hat{x} \cos\alpha - \hat{y} \sin\alpha$ and $\hat{n} = \hat{x} \sin\alpha + \hat{y} \cos\alpha$. The radius $\rho(\ell)$ is the magnitude of the projection of $\vec{r}(\ell)$ onto the xy-plane and is given by $\rho(\ell) = \left| \vec{r}(\ell) \cdot \overline{\overline{\mathbf{I}}}_t \right|$.

The generating arc for a BOR OCRED can have any amount of curvature so long as it generates a valid BOR OCRED. To make the analysis more tractable, however, we shall require the generating arc to be piecewise linear. This is not too great a restriction since we expect an arbitrary curved generating arc may be well approximated by a piecewise linear one, especially if the line segments are small compared to a wavelength.

Consider a piecewise linear BOR OCRED generating arc consisting of N segments joining $N + 1$ nodes. We number the nodes in ascending order such that each node corresponds to a progressively larger value of the arc length variable ℓ. Then we may write the relation

$$0 = \ell_0 < \ell_1 < \ell_2 < \cdots < \ell_{N+1} = L \tag{41}$$

The number of segments that generate the aperture σ is N_a and the number of segments that generate the cavity surface S is N_s, such that $N = N_a + N_s$. Now suppose $\vec{r}(\ell)$ is a point on the nth segment; that is, $\ell_{n-1} < \ell < \ell_n$. Let $\rho_n = \rho(\ell_n)$ and $z_n = z(\ell_n)$. Then any point $\vec{r}(\ell)$ on the nth segment is fully characterized by the linear relations

$$\rho(\ell) = \frac{\rho_{n-1}(\ell_n - \ell) + \rho_n(\ell - \ell_{n-1})}{\ell_n - \ell_{n-1}} \qquad \text{for } \ell_{n-1} < \ell < \ell_n \tag{42a}$$

$$z(\ell) = \frac{z_{n-1}(\ell_n - \ell) + z_n(\ell - \ell_{n-1})}{\ell_n - \ell_{n-1}} \qquad \text{for } \ell_{n-1} < \ell < \ell_n \tag{42b}$$

The orientation angle $\alpha(\ell)$ is constant on the nth segment and is given by

$$\begin{aligned} \alpha(\ell) &= \alpha_n \\ &= \arctan \frac{z_{n-1} - z_n}{\rho_n - \rho_{n-1}} \qquad \text{for } \ell_{n-1} < \ell < \ell_n \end{aligned} \tag{43}$$

30
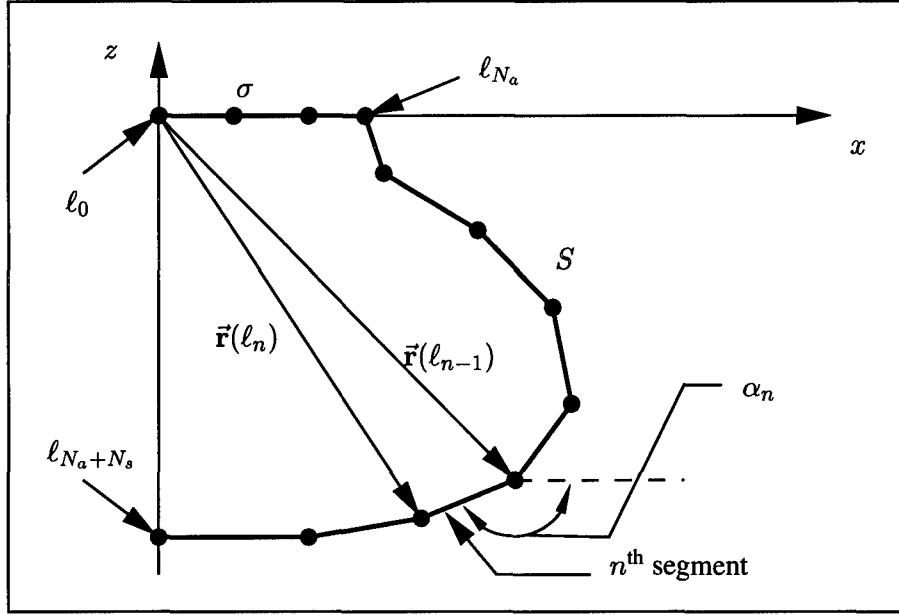
Figure 8   A piecewise-linear generating arc. N_a segments generate the aperture σ and N_s segments generate the cavity surface S. The nth segment falls between $\vec{r}(\ell_{n-1})$ and $\vec{r}(\ell_n)$.

4.2   Basis Functions

The first step in the method of moments is to define a set of basis functions capable of accurately approximating the unknown functions. Referring to equations (35)–(37), we see that the unknown functions we wish to approximate are $\vec{M}_\sigma(\vec{r})$ and $\vec{J}_\sigma(\vec{r})$ for $\vec{r} \in \sigma$ and $\vec{J}_S(\vec{r})$ for $\vec{r} \in S$. The basis functions we will use here are the same as those used by Mautz & Harrington [41] and Medgyesi-Mitschang & Putnam [44]. These basis functions have a piecewise smooth variation with ℓ and complex exponential (Fourier) variation in ϕ. We define the basis functions formally as

$$\vec{\psi}^\ell_{mn}(\ell, \phi) = e^{jm\phi}\, \frac{T_n(\ell)}{\rho(\ell)}\, \hat{\ell} \tag{44a}$$

$$\vec{\psi}^\phi_{mn}(\ell, \phi) = e^{jm\phi}\, \frac{T_n(\ell)}{\rho(\ell)}\, \hat{\phi} \tag{44b}$$

where $\hat{\ell} = \hat{x}\,\cos\alpha(\ell)\,\cos\phi + \hat{y}\,\cos\alpha(\ell)\,\sin\phi - \hat{z}\,\sin\alpha(\ell)$, $\hat{\phi} = -\hat{x}\,\sin\phi + \hat{y}\,\cos\phi$, and $T_n(\ell)$ is a "triangle" function as shown in Figure 9 and given by the equation
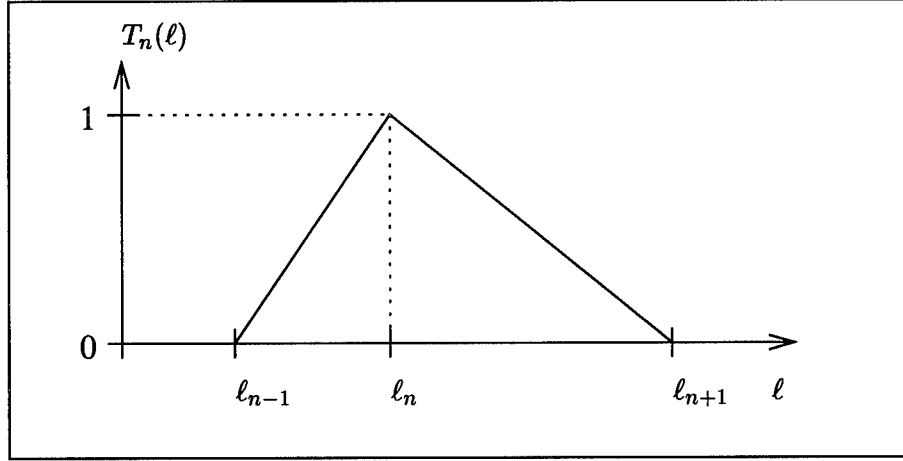
Figure 9   Triangle function, $T_n(\ell)$. $T_n(\ell)$ is the piecewise linear function having unit amplitude at ℓ_n and vanishing at all other nodes on the generating arc.

$$T_n(\ell) = \begin{cases} \frac{\ell - \ell_{n-1}}{\ell_n - \ell_{n-1}} & \text{for } \ell_{n-1} < \ell < \ell_n \\[2mm] \frac{\ell_{n+1} - \ell}{\ell_{n+1} - \ell_n} & \text{for } \ell_n < \ell < \ell_{n+1} \\[2mm] 0 & \text{otherwise} \end{cases} \tag{45}$$

When $n = N_a$, we will treat $T_n(\ell)$ to be either the left half-triangle or the right half-triangle, depending on whether $T_n(\ell)$ is being used in a basis function with support on the aperture or the cavity surface, respectively. This is necessary to allow for the possible discontinuity of the electric and magnetic current densities in the neighborhood of the aperture rim. Using the basis functions of equation (44), we approximate the unknown functions by

$$\vec{\mathbf{M}}_\sigma(\ell, \phi) \approx Z_0 \sum_{m=-M}^{M} \sum_{n=1}^{N_a} \left[A_{mn}^\ell \, \vec{\psi}_{mn}^\ell(\ell, \phi) + A_{mn}^\phi \, \vec{\psi}_{mn}^\phi(\ell, \phi) \right] \tag{46}$$

$$\vec{\mathbf{J}}_\sigma(\ell, \phi) \approx \sum_{m=-M}^{M} \sum_{n=1}^{N_a} \left[B_{mn}^\ell \, \vec{\psi}_{mn}^\ell(\ell, \phi) + B_{mn}^\phi \, \vec{\psi}_{mn}^\phi(\ell, \phi) \right] \tag{47}$$

$$\vec{\mathbf{J}}_s(\ell, \phi) \approx \sum_{m=-M}^{M} \sum_{n=N_a}^{N_a + N_s - 1} \left[C_{mn}^\ell \, \vec{\psi}_{mn}^\ell(\ell, \phi) + C_{mn}^\phi \, \vec{\psi}_{mn}^\phi(\ell, \phi) \right] \tag{48}$$

where M is the highest-order Fourier mode to be included and $A_{mn}^{\ell,\phi}$, $B_{mn}^{\ell,\phi}$, and $C_{mn}^{\ell,\phi}$ are complex coefficients to be determined. The choice of M will be discussed in Section 5.4.3, but it should be proportional to the electrical size of the aperture, that is $M \propto \ell_{N_a}/\lambda$. Likewise, N_a and N_s will

increase linearly with frequency. In equations (46) and (47), $0 < \ell < \ell_{N_a}$ and $0 \leq \phi < 2\pi$, while in equation (48), $\ell_{N_a} < \ell < \ell_{N_a+N_s}$ and $0 \leq \phi < 2\pi$. To enhance numerical stability, we scale the expansion of $\vec{\mathbf{M}}_\sigma$ by Z_0 so that all expansion coefficients will be of similar orders of magnitude.

The behavior of the fields near the rim of the aperture provides valuable information. As-suming that the radius of the aperture rim is not too small, the electric and magnetic fields near the aperture rim obey the same conditions as the fields near the tip of a two-dimensional PEC wedge, as shown in Figure 10. In the two-dimensional wedge geometry, ϱ measures the distance from the wedge tip and φ measures the angle from one of the wedge faces. This geometry is studied
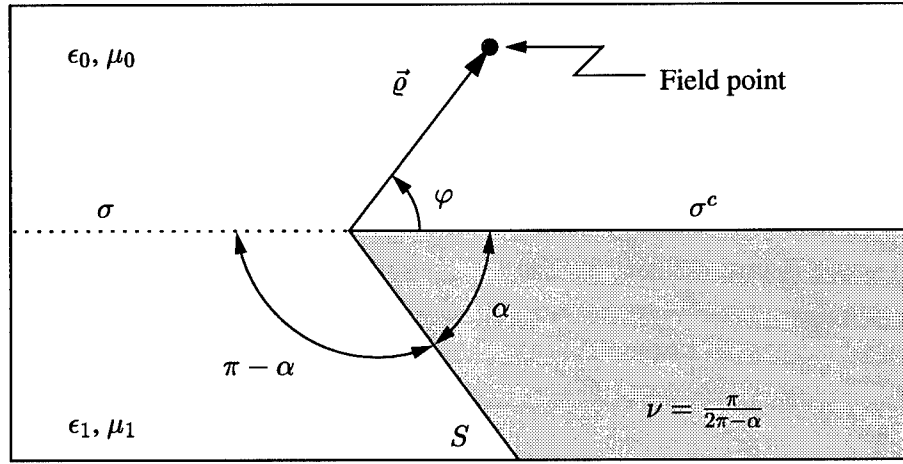
Figure 10   Two-dimensional wedge geometry corresponding to the aperture rim. ϱ measures distance from the wedge tip. φ measures angle counterclockwise from σ^c. The region $0 < \varphi < \pi$ is the upper half space; the surface $\varphi = \pi$ is the aperture σ; the region $\pi < \varphi < 2\pi - \alpha$ is the cavity volume D; and the surface $\varphi = 2\pi - \alpha$ is the cavity surface S.

by Meixner [45], who shows that the total magnetic field parallel to the wedge tip is finite and invariant with φ as $\varrho \to 0$. Then by the relations $\vec{\mathbf{J}}_\sigma = \hat{\mathbf{z}} \times \vec{\mathbf{H}}$ and $\vec{\mathbf{J}}_S = \hat{\mathbf{n}} \times \vec{\mathbf{H}}$, we see that

$$\lim_{\ell \to \ell_{N_a}} \vec{\mathbf{J}}_\sigma \cdot \hat{\ell} = \lim_{\ell \to \ell_{N_a}} \vec{\mathbf{J}}_S \cdot \hat{\ell};$$ that is, the $\hat{\ell}$ component of the electric current density on $S \cup \sigma$ is continuous and finite in the neighborhood of the aperture rim. In contrast, the magnetic field per-pendicular to the wedge tip is unbounded and varies with φ as $\varrho \to 0$, so that $\lim\limits_{\ell \to \ell_{N_a}} \left| \vec{\mathbf{J}}_\sigma \cdot \hat{\phi} \right|$ and $\lim\limits_{\ell \to \ell_{N_a}} \left| \vec{\mathbf{J}}_S \cdot \hat{\phi} \right|$ are unbounded and, in general, not equal. Turning our attention to the electric field, we find that the electric field parallel to the wedge tip vanishes as $\varrho \to 0$, while the electric field perpendicular to the wedge tip is unbounded and varies with φ as $\varrho \to 0$. Then using the relation $\vec{\mathbf{M}}_\sigma = -\hat{\mathbf{z}} \times \vec{\mathbf{E}}$, we see that $\lim\limits_{\ell \to \ell_{N_a}} \left| \vec{\mathbf{M}}_\sigma \cdot \hat{\ell} \right|$ vanishes, while $\lim\limits_{\ell \to \ell_{N_a}} \left| \vec{\mathbf{M}}_\sigma \cdot \hat{\phi} \right|$ is unbounded. This a

33

priori knowledge of the behavior of $\vec{\mathbf{J}}_\sigma$, $\vec{\mathbf{J}}_S$, and $\vec{\mathbf{M}}_\sigma$ in the neighborhood of the aperture rim will be extremely valuable in later calculations (specifically, Sections 4.4.2 and 4.4.3).

4.3 Testing Functions and Inner Product

The second step in the method of moments is to define a set of testing functions and an appropriate inner product. In accordance with Galerkin's procedure, we will use testing functions $\vec{\gamma}$ that are of the same form as the basis functions.

$$\vec{\gamma}^\ell_{m'n'}(\ell', \phi') = e^{jm'\phi'} \frac{T_{n'}(\ell')}{\rho(\ell')} \, \hat{\ell}' \tag{49a}$$

$$\vec{\gamma}^\phi_{m'n'}(\ell', \phi') = e^{jm'\phi'} \frac{T_{n'}(\ell')}{\rho(\ell')} \, \hat{\phi}' \tag{49b}$$

where $\hat{\ell}' = \hat{\mathbf{x}} \cos \alpha(\ell') \cos \phi' + \hat{\mathbf{y}} \cos \alpha(\ell') \sin \phi' - \hat{\mathbf{z}} \sin \alpha(\ell')$ and $\hat{\phi}' = -\hat{\mathbf{x}} \sin \phi' + \hat{\mathbf{y}} \cos \phi'$. As an inner product, we will choose the following:

$$\langle \vec{\mathbf{A}}, \vec{\mathbf{B}} \rangle = \int_{S \cup \sigma} \vec{\mathbf{A}}(\vec{\mathbf{r}}') \cdot \vec{\mathbf{B}}^*(\vec{\mathbf{r}}') \, ds' \tag{50}$$

where $\vec{\mathbf{B}}^*$ denotes the complex conjugate of $\vec{\mathbf{B}}$ and $S \cup \sigma = \partial D$ is the boundary of the cavity interior. This choice of testing function and inner product allows us to realize the major advantage of the BOR symmetry [41]. Since $\int_0^{2\pi} e^{jm\phi} e^{-jm'\phi} d\phi = 0$ for $m \neq m'$, we see that the basis and testing functions are orthogonal with respect to the inner product when their Fourier indices are different. In other words, the different Fourier modes do not influence each other and effectively decouple. This will allow us to consider each Fourier mode separately.

Applying our choices of basis function, testing function, and inner product to the coupled integral equations (35)–(37) results in a system of linear equations which can be expressed compactly in matrix form as

$$\begin{bmatrix} \frac{-jk_1 Y_1}{2Y_0} \langle \vec{\psi}, \vec{\gamma} \rangle & \langle \mathcal{L}_1 \vec{\psi}, \vec{\gamma} \rangle & \langle \mathcal{L}_2 \vec{\psi}, \vec{\gamma} \rangle \\ Z_0 \langle \mathcal{L}_3 \vec{\psi}, \vec{\gamma} \rangle & \frac{jk_1 Z_1 + jk_0 Z_0}{2} \langle \vec{\psi}, \vec{\gamma} \rangle & -Z_1 \langle \mathcal{L}_4 \vec{\psi}, \vec{\gamma} \rangle \\ 0 & 2\langle \mathcal{L}_5 \vec{\psi}, \vec{\gamma} \rangle & \langle \mathcal{L}_6 \vec{\psi}, \vec{\gamma} \rangle \end{bmatrix} \begin{bmatrix} A \\ B \\ C \end{bmatrix} = \begin{bmatrix} 0 \\ \frac{jk_0 Z_0}{2} \langle \vec{\mathbf{J}}^0, \vec{\gamma} \rangle \\ 0 \end{bmatrix} \tag{51}$$

where

$$\mathcal{L}_1 \vec{\psi} = \hat{\mathbf{z}} \times \int_\sigma \vec{\psi}(\vec{r}) \cdot \frac{\nabla \times \overline{\overline{\Gamma}}(k_1; \vec{r}, \vec{r}')}{-jk_1} \, d\sigma \qquad\qquad \text{for } \vec{r}' \in \sigma \qquad (52)$$

$$\mathcal{L}_2 \vec{\psi} = \hat{\mathbf{z}} \times \int_S \vec{\psi}(\vec{r}) \cdot \frac{\nabla \times \overline{\overline{\Gamma}}(k_1; \vec{r}, \vec{r}')}{-jk_1} \, ds \qquad\qquad \text{for } \vec{r}' \in \sigma \qquad (53)$$

$$\mathcal{L}_3 \vec{\psi} = \hat{\mathbf{z}} \times \int_\sigma \vec{\psi}(\vec{r}) \cdot \left\{ \frac{\nabla \times \overline{\overline{\Gamma}}(k_1; \vec{r}, \vec{r}')}{-jk_1} - \frac{\nabla \times \overline{\overline{\Gamma}}(k_0; \vec{r}, \vec{r}')}{-jk_0} \right\} \, d\sigma \qquad \text{for } \vec{r}' \in \sigma \qquad (54)$$

$$\mathcal{L}_4 \vec{\psi} = \hat{\mathbf{z}} \times \int_S \vec{\psi}(\vec{r}) \cdot \overline{\overline{\Gamma}}(k_1; \vec{r}, \vec{r}') \, ds \qquad\qquad \text{for } \vec{r}' \in \sigma \qquad (55)$$

$$\mathcal{L}_5 \vec{\psi} = \hat{\mathbf{n}}' \times \int_\sigma \vec{\psi}(\vec{r}) \cdot \overline{\overline{\Gamma}}_2(k_1; \vec{r}, \vec{r}') \, d\sigma \qquad\qquad \text{for } \vec{r}' \in S \qquad (56)$$

$$\mathcal{L}_6 \vec{\psi} = \hat{\mathbf{n}}' \times \int_S \vec{\psi}(\vec{r}) \cdot \overline{\overline{\Gamma}}_2(k_1; \vec{r}, \vec{r}') \, ds - \frac{jk_1}{2} \vec{\psi}(\vec{r}') \qquad\qquad \text{for } \vec{r}' \in S \qquad (57)$$

Equation (51) is often written in compact form as $ZI = V$, where Z is called the generalized impedance matrix, I is a column vector containing the desired expansion coefficients, and V is a column vector containing the system excitation. The dimensionality of Z is $2(2M + 1)(2N_a + N_s)$, which is equal to the total number of unknown coefficients. However, by exploiting the Fourier orthogonality, equation (51) is equivalent to $2M + 1$ smaller systems ($Z_m I_m = V_m$, $m = 0, \pm 1 \ldots \pm M$), each corresponding to a different Fourier index m and having dimension $2(2N_a + N_s)$. This decomposition reduces the numerical complexity of the problem in two ways. First, the number of matrix elements that must be computed is reduced by a factor of $2M + 1$. Second, under the assumption that the computer time required to solve a system of N linear equations using Gaussian elimination is $\mathcal{O}(N^3)$ [6], solving the $(2M + 1)$ smaller systems can be accomplished $(2M + 1)^2$ times faster than the equivalent larger system. Thus, exploiting symmetry allows us to solve the BOR OCRED scattering problem $(2M + 1)^3$ times faster than solving a non-BOR OCRED scattering problem of equivalent size.

4.4 Calculating Elements of Z_m

Each element of Z_m corresponds to the coupling between a basis function and a testing function. Typically, this involves calculating an iterated surface integral where the dyadic kernel is $\nabla \times \overline{\overline{\Gamma}}(k; \vec{r}, \vec{r}')$, $\overline{\overline{\Gamma}}(k; \vec{r}, \vec{r}')$, or $\overline{\overline{\Gamma}}_2(k; \vec{r}, \vec{r}')$. It is convenient to partition Z_m into 9 block sub-

matrices:

$$Z_m = \begin{bmatrix} Z_m^{11} & Z_m^{12} & Z_m^{13} \\ Z_m^{21} & Z_m^{22} & Z_m^{23} \\ Z_m^{31} & Z_m^{32} & Z_m^{33} \end{bmatrix} \tag{58}$$

where Z_m^{ij} denote the elements of Z_m that come from testing equation (35), (36), or (37) ($i = 1, 2, 3$ respectively) and expanding $\vec{M}_\sigma$, $\vec{J}_\sigma$, or $\vec{J}_s$ ($j = 1, 2, 3$ respectively). Examination of equation (51) reveals that the elements comprising Z_m^{31} vanish identically. The other eight submatrices are treated individually in the following sections.
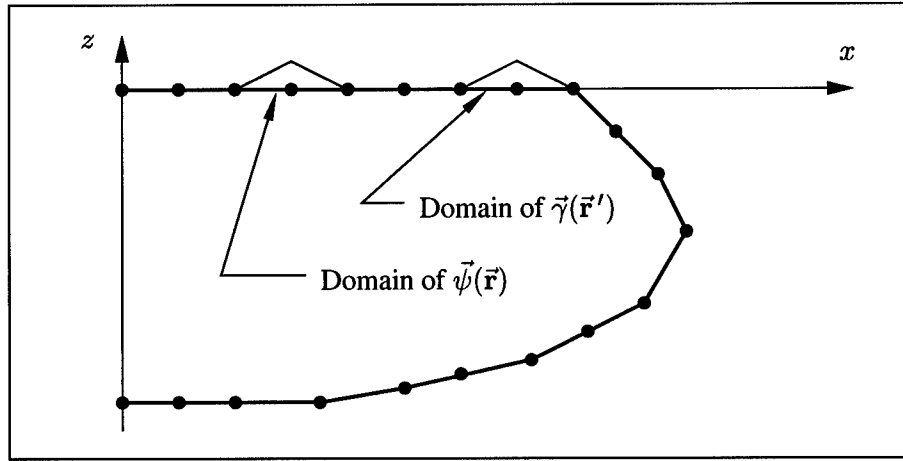
Figure 11   Domains of $\vec{\psi}(\vec{r})$ and $\vec{\gamma}(\vec{r}')$ for Z_m^{11}, Z_m^{12}, Z_m^{21}, and Z_m^{22}. Both $\vec{r}$ and $\vec{r}'$ are defined on annuli in the xy-plane formed by revolving a portion of the aperture generating arc about the z-axis.

4.4.1 Z_m^{11}. Z_m^{11} is the $2N_a \times 2N_a$ submatrix associated with the testing of equation (35) and the expansion of $\vec{M}_\sigma$. As shown in Figure 11, the domain of both the basis and testing functions is confined to the aperture σ. The elements of Z_m^{11} are found from the inner product

$$\langle \vec{\psi}_{mn}^{\ell,\phi}, \vec{\gamma}_{mn'}^{\ell,\phi} \rangle = \int_\sigma \vec{\psi}_{mn}^{\ell,\phi}(\vec{r}') \cdot \vec{\gamma}_{mn'}^{\ell,\phi\,*}(\vec{r}') \, d\sigma', \tag{59}$$

36

where $m = 0, \pm1, \pm2 \ldots, \pm M$, $1 \le n \le N_a$, and $1 \le n' \le N_a$, Since $\hat{\ell}' \perp \hat{\phi}'$, the "cross terms" $\langle \vec{\psi}_{mn}^{\phi}, \vec{\gamma}_{mn'}^{\ell} \rangle$ and $\langle \vec{\psi}_{mn}^{\ell}, \vec{\gamma}_{mn'}^{\phi} \rangle$ vanish. We are left with

$$
\begin{aligned}
\langle \vec{\psi}_{mn}^{\ell}, \vec{\gamma}_{mn'}^{\ell} \rangle &= \langle \vec{\psi}_{mn}^{\phi}, \vec{\gamma}_{mn'}^{\phi} \rangle \\
&= \int_0^{2\pi} \int_0^{\ell_{N_a}} \left[e^{\jmath m \phi'} \frac{T_n(\ell')}{\rho(\ell')} \right] \left[e^{-\jmath m \phi'} \frac{T_{n'}(\ell')}{\rho(\ell')} \right] \rho(\ell')\, d\ell'\, d\phi' \qquad (60) \\
&= 2\pi \int_0^{\ell_{N_a}} \frac{T_n(\ell') T_{n'}(\ell')}{\rho(\ell')}\, d\ell'
\end{aligned}
$$

We note that $\rho(\ell') = \ell'$ for $0 < \ell' < \ell_{N_a}$ so that the integrand of equation (60) is a rational function of polynomials in ℓ' and the integral can be solved in closed form. We look at three cases depending on the values of n and n'. If n and n' differ by two or more, the last integral vanishes because the product of the two triangle functions is zero when their respective supports do not overlap. If $|n' - n| = 1$, then we have

$$
\begin{aligned}
\langle \vec{\psi}_{mn}^{\ell}, \vec{\gamma}_{mn'}^{\ell} \rangle &= \langle \vec{\psi}_{mn}^{\phi}, \vec{\gamma}_{mn'}^{\phi} \rangle \\
&= \frac{2\pi}{(\ell_{n'} - \ell_n)^2} \int_{\ell_n}^{\ell_{n'}} \frac{(\ell_{n'} - \ell')(\ell' - \ell_n)}{\ell'}\, d\ell' \qquad (61) \\
&= \frac{2\pi}{(\ell_{n'} - \ell_n)^2} \left| \frac{\ell_{n'}^2 - \ell_n^2}{2} + \ell_n \ell_{n'} \ln \frac{\ell_n}{\ell_{n'}} \right| \qquad \text{for } |n' - n| = 1
\end{aligned}
$$

If $n' = n$, then we have

$$
\begin{aligned}
\langle \vec{\psi}_{mn}^{\ell}, \vec{\gamma}_{mn'}^{\ell} \rangle &= \langle \vec{\psi}_{mn}^{\phi}, \vec{\gamma}_{mn'}^{\phi} \rangle \\
&= 2\pi \left\{ \int_{\ell_{n-1}}^{\ell_n} \frac{(\ell' - \ell_{n-1})^2}{\ell'(\ell_n - \ell_{n-1})^2}\, d\ell' + \int_{\ell_n}^{\ell_{n+1}} \frac{(\ell_{n+1} - \ell')^2}{\ell'(\ell_{n+1} - \ell_n)^2}\, d\ell' \right\} \\
&= 2\pi \left\{ \frac{\ell_n - 3\ell_{n-1}}{2(\ell_n - \ell_{n-1})} + \left[\frac{\ell_{n-1}}{\ell_n - \ell_{n-1}} \right]^2 \ln \frac{\ell_n}{\ell_{n-1}} \right. \qquad (62) \\
&\quad \left. + \frac{\ell_n - 3\ell_{n+1}}{2(\ell_{n+1} - \ell_n)} + \left[\frac{\ell_{n+1}}{\ell_{n+1} - \ell_n} \right]^2 \ln \frac{\ell_{n+1}}{\ell_n} \right\} \qquad \text{for } n' = n
\end{aligned}
$$

In equation (62), the following special cases must be examined. First, if $n = 1$, then we must evaluate equation (62) in the limit as $\ell_0 \to 0$ to avoid taking the logarithm of infinity. Second, if $n = 1$, then we ignore the terms involving ℓ_{n+1} due to the half-triangle function used in the basis and testing functions at the aperture rim.

37

4.4.2 Z_m^{12}. Z_m^{12} is the $2N_a \times 2N_a$ submatrix associated with the testing of equation (35) and the expansion of $\vec{\mathbf{J}}_\sigma$. As shown in Figure 11, the domain of both the basis and testing functions is confined to the aperture σ. From equation (13) we have $\nabla \times \overline{\overline{\Gamma}}(k_1; \vec{r}, \vec{r}') = -jk_1 \left(k_1^2 \overline{\overline{\mathbf{I}}} + \nabla\nabla \right) G(k_1; \vec{r}, \vec{r}')$, the elements of Z_m^{12} can be found from the inner product

$$
\langle \mathcal{L}_1 \vec{\psi}_{mn}^{\ell,\phi}, \vec{\gamma}_{mn'}^{\ell,\phi} \rangle = k_1^2 \int_\sigma \int_\sigma \left\{ \vec{\gamma}_{mn'}^{\ell,\phi\,*}(\vec{r}') \cdot \left[\hat{\mathbf{z}} \times \vec{\psi}_{mn}^{\ell,\phi}(\vec{r}) \right] \right\} G(k_1; \vec{r}, \vec{r}') \, d\sigma \, d\sigma'
$$

$$
+ \int_\sigma \int_\sigma \vec{\gamma}_{mn'}^{\ell,\phi\,*}(\vec{r}') \cdot \left\{ \hat{\mathbf{z}} \times \left[\vec{\psi}_{mn}^{\ell,\phi}(\vec{r}) \cdot \nabla\nabla G(k_1; \vec{r}, \vec{r}') \right] \right\} \, d\sigma \, d\sigma' \qquad (63)
$$

where $m = 0, \pm 1, \pm 2 \ldots \pm M$, $1 \leq n \leq N_a$, and $1 \leq n' \leq N_a$. The first integral in equation (63) is a convergent integral, though improper due to the R^{-1} singularity of the scalar Green's function at $\vec{r} = \vec{r}'$. The second integral, however, does not converge in the classical sense due to the R^{-3} singularity of $\nabla\nabla G$ at $\vec{r} = \vec{r}'$, and must be interpreted as a two dimensional Cauchy principal value (CPV) integral [46]. However, this interpretation is troublesome when $\vec{r}$ lies on the boundary of σ because the CPV concept requires the division of σ into two parts, one of which is a disk centered at $\vec{r}$ with radius $\delta > 0$. To give meaning to the second integral, we regularize it by using the following theorem (proved in Appendix C).

Theorem 5 *Let $\vec{\mathbf{A}}(\vec{r})$ and $\vec{\mathbf{B}}(\vec{r})$ be continuous, piecewise differentiable vector functions defined on the regular surfaces S_1 and S_2, respectively, such that $\hat{\mathbf{n}}' \cdot \vec{\mathbf{A}} = 0$ on S_1 and $\hat{\mathbf{n}} \cdot \vec{\mathbf{B}} = 0$ on S_2 where $\hat{\mathbf{n}}'$ is the unit normal on S_1 and $\hat{\mathbf{n}}$ is the unit normal on S_2. Then*

$$
\int_{S_1} \int_{S_2} \vec{\mathbf{A}}(\vec{r}') \cdot \hat{\mathbf{n}}' \times \left[\vec{\mathbf{B}}(\vec{r}) \cdot \nabla\nabla G(k; \vec{r}, \vec{r}') \right] \, ds \, ds' =
$$

$$
\int_{S_1} \int_{S_2} G(k; \vec{r}, \vec{r}') \left[\nabla_s \cdot \vec{\mathbf{B}}(\vec{r}) \right] \left\{ \nabla_s' \cdot \left[\hat{\mathbf{n}}' \times \vec{\mathbf{A}}(\vec{r}') \right] \right\} \, ds \, ds'
$$

$$
+ \int_{S_2} \oint_{\partial S_1} G(k; \vec{r}, \vec{r}') \left[\nabla_s \cdot \vec{\mathbf{B}}(\vec{r}) \right] \vec{\mathbf{A}}(\vec{r}') \cdot d\vec{c}' \, ds \qquad (64)
$$

$$
+ \int_{S_1} \oint_{\partial S_2} G(k; \vec{r}, \vec{r}') \left\{ \nabla_s' \cdot \left[\hat{\mathbf{n}}' \times \vec{\mathbf{A}}(\vec{r}') \right] \right\} \left[\vec{\mathbf{B}}(\vec{r}) \times \hat{\mathbf{n}} \right] \cdot d\vec{c} \, ds'
$$

$$
+ \oint_{\partial S_1} \oint_{\partial S_2} G(k; \vec{r}, \vec{r}') \left[\vec{\mathbf{B}}(\vec{r}) \times \hat{\mathbf{n}} \right] \cdot d\vec{c} \, \vec{\mathbf{A}}(\vec{r}') \cdot d\vec{c}'
$$

where the line integrals are traversed in the positive sense with respect to the normal vectors.

Theorem 5 is valid for any regular surfaces S_1 and S_2, even those that overlap. In particular, Theorem 5 is valid when $S_1 = S_2$. If we associate both S_1 and S_2 with σ, and let $\vec{A}(\vec{r}') = \vec{\gamma}_{mn'}^{\ell,\phi\,*}(\vec{r}')$ and $\vec{B}(\vec{r}) = \vec{\psi}_{mn}^{\ell,\phi}(\vec{r})$, then equation (63) becomes

$$
\begin{aligned}
\langle \mathcal{L}_1 \vec{\psi}_{mn}^{\ell,\phi}, \vec{\gamma}_{mn'}^{\ell,\phi} \rangle =\ & k_1^2 \int_\sigma \int_\sigma \left\{ \vec{\gamma}_{mn'}^{\ell,\phi\,*}(\vec{r}') \cdot \left[\hat{z} \times \vec{\psi}_{mn}^{\ell,\phi}(\vec{r}) \right] \right\} \, G(k_1; \vec{r}, \vec{r}') \, d\sigma \, d\sigma' \\
&+ \int_\sigma \int_\sigma \left[\nabla_s \cdot \vec{\psi}_{mn}^{\ell,\phi}(\vec{r}) \right] \left\{ \nabla_s' \cdot \left[\hat{z} \times \vec{\gamma}_{mn'}^{\ell,\phi\,*}(\vec{r}') \right] \right\} \, G(k; \vec{r}, \vec{r}') \, d\sigma \, d\sigma' \\
&+ \int_\sigma \oint_{\partial\sigma} \left[\nabla_s \cdot \vec{\psi}_{mn}^{\ell,\phi}(\vec{r}) \right] \, G(k; \vec{r}, \vec{r}') \, \vec{\gamma}_{mn'}^{\ell,\phi\,*}(\vec{r}') \cdot d\vec{c}' \, d\sigma \\
&+ \int_\sigma \oint_{\partial\sigma} \left\{ \nabla_s' \cdot \left[\hat{z} \times \vec{\gamma}_{mn'}^{\ell,\phi\,*}(\vec{r}') \right] \right\} \, G(k; \vec{r}, \vec{r}') \left[\vec{\psi}_{mn}^{\ell,\phi}(\vec{r}) \times \hat{z} \right] \cdot d\vec{c} \, d\sigma' \\
&+ \oint_{\partial\sigma} \oint_{\partial\sigma} G(k; \vec{r}, \vec{r}') \left[\vec{\psi}_{mn}^{\ell,\phi}(\vec{r}) \times \hat{z} \right] \cdot d\vec{c} \, \vec{\gamma}_{mn'}^{\ell,\phi\,*}(\vec{r}') \cdot d\vec{c}'
\end{aligned}
\tag{65}
$$

where both $d\vec{c}$ and $d\vec{c}'$ are differential vectors along the aperture rim, pointing in the direction of increasing ϕ. We note that, with $S_1 = \sigma$ and $S_2 = \sigma$,

$$
d\vec{c} = \hat{\phi}\, \ell_{N_a}\, d\phi \qquad\qquad\qquad d\vec{c}' = \hat{\phi}'\, \ell_{N_a}\, d\phi'
\tag{66}
$$

$$
d\sigma = \ell\, d\ell\, d\phi \qquad\qquad\qquad d\sigma' = \ell'\, d\ell'\, d\phi'
\tag{67}
$$

we can write equation (65) as

$$
\begin{aligned}
\langle \mathcal{L}_1 \vec{\psi}_{mn}^{\ell,\phi}, \vec{\gamma}_{mn'}^{\ell,\phi} \rangle =\ & \\
k_1^2 \int_0^{2\pi}\!\! \int_0^{\ell_{N_a}}\!\! \int_0^{2\pi}\!\! \int_0^{\ell_{N_a}} & \left\{ \vec{\gamma}^*(\ell', \phi') \cdot \left[\hat{z} \times \vec{\psi}(\ell, \phi) \right] \right\} \, G\, \ell\, d\ell\, d\phi\, \ell'\, d\ell'\, d\phi' \\
+ \int_0^{2\pi}\!\! \int_0^{\ell_{N_a}}\!\! \int_0^{2\pi}\!\! \int_0^{\ell_{N_a}} & \left[\nabla_s \cdot \vec{\psi}(\ell, \phi) \right] \left\{ \nabla_s' \cdot \left[\hat{z} \times \vec{\gamma}^*(\ell', \phi') \right] \right\} G\, \ell\, d\ell\, d\phi\, \ell'\, d\ell'\, d\phi' \\
+ \ell_{N_a} \int_0^{2\pi}\!\! \int_0^{\ell_{N_a}}\!\! \int_0^{2\pi} & \left[\nabla_s \cdot \vec{\psi}(\ell, \phi) \right] \, G\, \vec{\gamma}^*(\ell_{N_a}, \phi') \cdot \hat{\phi}'\, d\phi'\, \ell\, d\ell\, d\phi \\
+ \ell_{N_a} \int_0^{2\pi}\!\! \int_0^{\ell_{N_a}}\!\! \int_0^{2\pi} & \left\{ \nabla_s' \cdot \left[\hat{z} \times \vec{\gamma}^*(\ell', \phi') \right] \right\} \, G\, \left[\vec{\psi}(\ell_{N_a}, \phi) \times \hat{z} \right] \cdot \hat{\phi}\, d\phi\, \ell'\, d\ell'\, d\phi' \\
+ \ell_{N_a}^2 \int_0^{2\pi}\!\! \int_0^{2\pi} & G\, \left[\vec{\psi}(\ell, \phi) \times \hat{z} \right] \cdot \hat{\phi}\, d\phi\, \vec{\gamma}^*(\ell_{N_a}, \phi') \cdot \hat{\phi}'\, d\phi'
\end{aligned}
\tag{68}
$$

where $\vec{\psi} \equiv \vec{\psi}_{mn}^{\ell,\phi}$, $\vec{\gamma}^* \equiv \vec{\gamma}_{mn'}^{\ell,\phi\,*}$, and $G \equiv G(k_1; \vec{r}, \vec{r}')$ have been introduced to improve the readability of the formula.

It is easy to see that all the integrands in equation (68) are functions of ℓ, ℓ', and $\phi - \phi'$. Employing the change of variables $\theta = \phi - \phi'$ and after some tedious algebraic manipulations, we can write equation (68) as

$$
\begin{aligned}
\langle \mathcal{L}_1 \vec{\psi}_{mn}^{\ell,\phi}, \vec{\gamma}_{mn'}^{\ell,\phi} \rangle = \\
k_1^2 \int_0^{\ell_{N_a}} \int_0^{2\pi} \int_0^{\ell_{N_a}} \frac{e^{-\jmath k_1 R}}{2R} \left\{ \vec{\gamma}^*(\ell',0) \cdot \left[\hat{\mathbf{z}} \times \vec{\psi}(\ell,\theta) \right] \right\} \ell \, d\ell \, d\theta \, \ell' \, d\ell' \\
+ \int_0^{\ell_{N_a}} \int_0^{2\pi} \int_0^{\ell_{N_a}} \frac{e^{-\jmath k_1 R}}{2R} \left[\nabla_s \cdot \vec{\psi}(\ell,\theta) \right] \left\{ \nabla_s' \cdot \left[\hat{\mathbf{z}} \times \vec{\gamma}^*(\ell',0) \right] \right\} \ell \, d\ell \, d\theta \, \ell' \, d\ell' \\
+ \ell_{N_a} \int_0^{\ell_{N_a}} \int_0^{2\pi} \frac{e^{-\jmath k_1 R}}{2R} \left[\nabla_s \cdot \vec{\psi}(\ell,\theta) \right] \vec{\gamma}^*(\ell_{N_a},0) \cdot \hat{\mathbf{y}} \, \ell \, d\ell \, d\theta \\
+ \ell_{N_a} \int_0^{\ell_{N_a}} \int_0^{2\pi} \frac{e^{-\jmath k_1 R}}{2R} \left\{ \nabla_s' \cdot \left[\hat{\mathbf{z}} \times \vec{\gamma}^*(\ell',0) \right] \right\} \left[\vec{\psi}(\ell_{N_a},\theta) \times \hat{\mathbf{z}} \right] \cdot \hat{\phi} \, \ell' \, d\theta \, d\ell' \\
+ \ell_{N_a}^2 \int_0^{2\pi} \frac{e^{-\jmath k_1 R}}{2R} \left[\vec{\psi}(\ell_{N_a},\theta) \times \hat{\mathbf{z}} \right] \cdot \hat{\phi} \, \vec{\gamma}^*(\ell_{N_a},0) \cdot \hat{\mathbf{y}} \, d\theta
\end{aligned}
\tag{69}
$$

where $R = R(\ell,\ell',\theta) = \sqrt{(\ell - \ell')^2 + 2\ell\ell' (1 - \cos\theta)}$, $\ell = \ell_{N_a}$ in the fourth and fifth integrals, and $\ell' = \ell_{N_a}$ in the third and fifth integrals. It will be shown in Section 4.4.3 that the last two integrals in equation (69) exactly cancel with two other integrals associated with Z_m^{13} and thus do not contribute to Z_m^{12}.

The weak singularity of the first two integrals in equation (69) can be extracted and integrated analytically using the relation [19]

$$
\frac{1}{2} \int_0^\pi \int_a^b \frac{\ell}{R} \, d\ell \, d\theta =
\begin{cases}
b \, E\left(\frac{\ell'}{b}\right) - a \, E\left(\frac{\ell'}{a}\right) & \ell' \leq a < b \\
b \, E\left(\frac{\ell'}{b}\right) - \ell' \, E\left(\frac{a}{\ell'}\right) + \frac{\ell'^2 - a^2}{\ell'} K\left(\frac{a}{\ell'}\right) & a < \ell' \leq b \\
\ell' \, E\left(\frac{b}{\ell'}\right) - \ell' \, E\left(\frac{a}{\ell'}\right) - \frac{\ell'^2 - b^2}{\ell'} K\left(\frac{b}{\ell'}\right) + \frac{\ell'^2 - a^2}{\ell'} K\left(\frac{a}{\ell'}\right) & a < b \leq \ell'
\end{cases}
\tag{70}
$$

where K and E are the complete elliptic integrals of the first and second kinds, respectively.
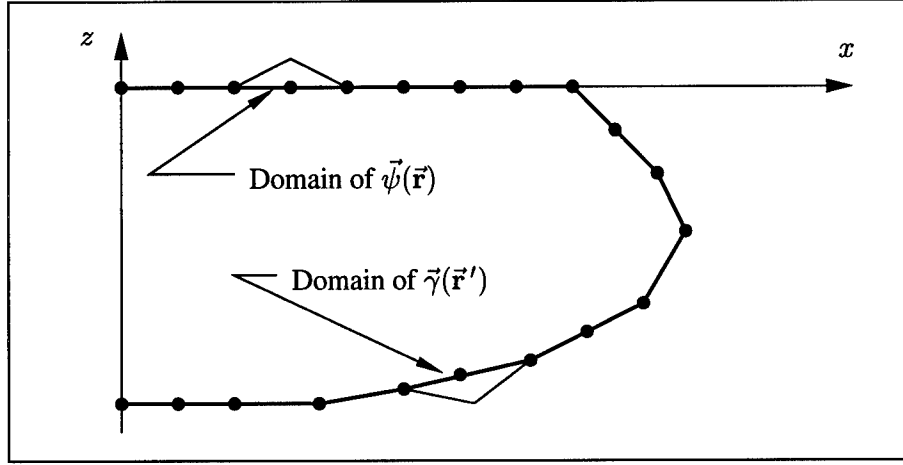
Figure 12   Domains of $\vec{\psi}(\vec{r})$ and $\vec{\gamma}(\vec{r}')$ for Z_m^{13} and Z_m^{23}. $\vec{r}$ is defined on an annulus in the xy-plane formed by revolving a portion of the aperture generating arc about the z-axis. $\vec{r}'$ is defined on a cone frustum formed by revolving a portion of the cavity surface generating arc about the z-axis.

4.4.3 Z_m^{13}.

Z_m^{13} is the $2N_a \times 2N_s$ submatrix associated with the testing of equation (35) and the expansion of $\vec{J}_S$. As shown in Figure 12, the domain of the basis functions is confined to the cavity surface S while the domain of the testing functions is confined to the aperture σ. From equation (13) we have $\nabla \times \overline{\overline{\Gamma}}(k_1; \vec{r}, \vec{r}') = -jk_1 \left(k_1^2 \overline{\overline{I}} + \nabla\nabla \right) G(k_1; \vec{r}, \vec{r}')$, the elements of Z_m^{13} can be found from the inner product

$$\langle \mathcal{L}_2 \vec{\psi}_{mn}^{\ell,\phi}, \vec{\gamma}_{mn'}^{\ell,\phi} \rangle = k_1^2 \int_\sigma \int_S \left\{ \vec{\gamma}_{mn'}^{\ell,\phi\,*}(\vec{r}') \cdot \left[\hat{z} \times \vec{\psi}_{mn}^{\ell,\phi}(\vec{r}) \right] \right\} G(k_1; \vec{r}, \vec{r}') \, ds \, d\sigma'$$

$$+ \int_\sigma \int_S \vec{\gamma}_{mn'}^{\ell,\phi\,*}(\vec{r}') \cdot \left\{ \hat{z} \times \left[\vec{\psi}_{mn}^{\ell,\phi}(\vec{r}) \cdot \nabla\nabla G(k_1; \vec{r}, \vec{r}') \right] \right\} \, ds \, d\sigma' \qquad (71)$$

where $m = 0, \pm 1, \pm 2 \ldots \pm M$, $N_a \leq n \leq N_a + N_s - 1$, and $1 \leq n' \leq N_a$. Employing the same regularization procedure as used to calculate the elements of Z_m^{12}, we obtain

41

$$\langle \mathcal{L}_2 \vec{\psi}_{mn}^{\ell,\phi}, \vec{\gamma}_{mn'}^{\ell,\phi} \rangle =$$

$$k_1^2 \int_\sigma \int_S \left\{ \vec{\gamma}_{mn'}^{\ell,\phi\,*}(\vec{r}') \cdot \left[\hat{\mathbf{z}} \times \vec{\psi}_{mn}^{\ell,\phi}(\vec{r}) \right] \right\} \, G(k_1; \vec{r}, \vec{r}') \, d\sigma \, d\sigma'$$

$$+ \int_\sigma \int_S \left[\nabla_s \cdot \vec{\psi}_{mn}^{\ell,\phi}(\vec{r}) \right] \left\{ \nabla_s' \cdot \left[\hat{\mathbf{z}} \times \vec{\gamma}_{mn'}^{\ell,\phi\,*}(\vec{r}') \right] \right\} \, G(k_1; \vec{r}, \vec{r}') \, d\sigma \, d\sigma'$$

$$+ \int_S \oint_{\partial\sigma} \left[\nabla_s \cdot \vec{\psi}_{mn}^{\ell,\phi}(\vec{r}) \right] \, G(k_1; \vec{r}, \vec{r}') \, \vec{\gamma}_{mn'}^{\ell,\phi\,*}(\vec{r}') \cdot d\vec{c}' \, ds$$

$$+ \int_\sigma \oint_{\partial S} \left\{ \nabla_s' \cdot \left[\hat{\mathbf{z}} \times \vec{\gamma}_{mn'}^{\ell,\phi\,*}(\vec{r}') \right] \right\} \, G(k_1; \vec{r}, \vec{r}') \left[\vec{\psi}_{mn}^{\ell,\phi}(\vec{r}) \times \hat{\mathbf{z}} \right] \cdot d\vec{c} \, d\sigma'$$

$$+ \oint_{\partial\sigma} \oint_{\partial S} G(k_1; \vec{r}, \vec{r}') \left[\vec{\psi}_{mn}^{\ell,\phi}(\vec{r}) \times \hat{\mathbf{z}} \right] \cdot d\vec{c} \, \vec{\gamma}_{mn'}^{\ell,\phi\,*}(\vec{r}') \cdot d\vec{c}'$$

(72)

where $d\vec{c}$ is a differential vector along the aperture rim, pointing in the direction of *decreasing* ϕ and $d\vec{c}'$ is a differential vector along the aperture rim, pointing in the direction of *increasing* ϕ. We note that, with $S_1 = \sigma$ and $S_2 = \sigma$,

$$d\vec{c} = -\hat{\phi} \, \ell_{N_a} \, d\phi \qquad\qquad d\vec{c}' = \hat{\phi}' \, \ell_{N_a} \, d\phi' \qquad (73)$$

$$d\sigma = \ell \, d\ell \, d\phi \qquad\qquad d\sigma' = \ell' \, d\ell' \, d\phi' \qquad (74)$$

we can write equation (72) as

$$\langle \mathcal{L}_1 \vec{\psi}_{mn}^{\ell,\phi}, \vec{\gamma}_{mn'}^{\ell,\phi} \rangle =$$

$$k_1^2 \int_0^{2\pi} \int_0^{\ell_{N_a}} \int_0^{2\pi} \int_{\ell_{N_a}}^{L} G \left\{ \vec{\gamma}^*(\ell', \phi') \cdot \left[\hat{\mathbf{z}} \times \vec{\psi}(\ell, \phi) \right] \right\} \ell \, d\ell \, d\phi \, \ell' \, d\ell' \, d\phi'$$

$$+ \int_0^{2\pi} \int_0^{\ell_{N_a}} \int_0^{2\pi} \int_{\ell_{N_a}}^{L} G \left[\nabla_s \cdot \vec{\psi}(\ell, \phi) \right] \left\{ \nabla_s' \cdot \left[\hat{\mathbf{z}} \times \vec{\gamma}^*(\ell', \phi') \right] \right\} \ell \, d\ell \, d\phi \, \ell' \, d\ell' \, d\phi'$$

(75)

$$+ \ell_{N_a} \int_0^{2\pi} \int_{\ell_{N_a}}^{L} \int_0^{2\pi} G \left[\nabla_s \cdot \vec{\psi}(\ell, \phi) \right] \vec{\gamma}^*(\ell_{N_a}, \phi') \cdot \hat{\phi}' \, d\phi' \, \ell \, d\ell \, d\phi$$

$$- \ell_{N_a} \int_0^{2\pi} \int_0^{\ell_{N_a}} \int_0^{2\pi} G \left\{ \nabla_s' \cdot \left[\hat{\mathbf{z}} \times \vec{\gamma}^*(\ell', \phi') \right] \right\} \left[\vec{\psi}(\ell_{N_a}, \phi) \times \hat{\mathbf{z}} \right] \cdot \hat{\phi} \, d\phi \, \ell' \, d\ell' \, d\phi'$$

$$- \ell_{N_a}^2 \int_0^{2\pi} \int_0^{2\pi} G \left[\vec{\psi}(\ell_{N_a}, \phi) \times \hat{\mathbf{z}} \right] \cdot \hat{\phi} \, d\phi \, \vec{\gamma}^*(\ell_{N_a}, \phi') \cdot \hat{\phi}' \, d\phi'$$

42

where $\vec{\psi} \equiv \vec{\psi}_{mn}^{\ell,\phi}$, $\vec{\gamma}^* \equiv \vec{\gamma}_{mn'}^{\ell,\phi\,*}$, and $G \equiv G(k_1; \mathbf{r}, \mathbf{r}')$ have been introduced to improve the readability of the formula.

Proceeding as in section 4.4.2, we make the change of variables $\theta = \phi - \phi'$ and write equation (75) as

$$
\langle \mathcal{L}_1 \vec{\psi}_{mn}^{\ell,\phi}, \vec{\gamma}_{mn'}^{\ell,\phi} \rangle =
$$

$$
k_1^2 \int_0^{\ell_{N_a}} \int_0^{2\pi} \int_{\ell_{N_a}}^{L} \frac{e^{-jk_1 R(\ell,\ell',\theta)}}{2R(\ell,\ell',\theta)} \left\{ \vec{\gamma}^*(\ell',0) \cdot \left[\hat{\mathbf{z}} \times \vec{\psi}(\ell,\theta) \right] \right\} \ell \, d\ell \, d\theta \, \ell' \, d\ell'
$$

$$
+ \int_0^{\ell_{N_a}} \int_0^{2\pi} \int_{\ell_{N_a}}^{L} \frac{e^{-jk_1 R(\ell,\ell',\theta)}}{2R(\ell,\ell',\theta)} \left[\nabla_s \cdot \vec{\psi}(\ell,\theta) \right] \left\{ \nabla_s' \cdot \left[\hat{\mathbf{z}} \times \vec{\gamma}^*(\ell',0) \right] \right\} \ell \, d\ell \, d\theta \, \ell' \, d\ell'
$$

$$
+ \ell_{N_a} \int_{\ell_{N_a}}^{L} \int_0^{2\pi} \frac{e^{-jk_1 R(\ell,\ell_{N_a},\theta)}}{2R(\ell,\ell_{N_a},\theta)} \left[\nabla_s \cdot \vec{\psi}(\ell,\theta) \right] \vec{\gamma}^*(\ell_{N_a},0) \cdot \hat{\mathbf{y}} \, \ell \, d\ell \, d\theta \tag{76}
$$

$$
- \ell_{N_a} \int_0^{\ell_{N_a}} \int_0^{2\pi} \frac{e^{-jk_1 R(\ell_{N_a},\ell',\theta)}}{2R(\ell_{N_a},\ell',\theta)} \left\{ \nabla_s' \cdot \left[\hat{\mathbf{z}} \times \vec{\gamma}^*(\ell',0) \right] \right\} \left[\vec{\psi}(\ell_{N_a},\theta) \times \hat{\mathbf{z}} \right] \cdot \hat{\phi} \, \ell' \, d\theta \, d\ell'
$$

$$
- \ell_{N_a}^2 \int_0^{2\pi} \frac{e^{-jk_1 R(\ell_{N_a},\ell_{N_a},\theta)}}{2R(\ell_{N_a},\ell_{N_a},\theta)} \left[\vec{\psi}(\ell_{N_a},\theta) \times \hat{\mathbf{z}} \right] \cdot \hat{\phi} \, \vec{\gamma}^*(\ell_{N_a},0) \cdot \hat{\mathbf{y}} \, d\theta
$$

where $R(\ell,\ell',\theta) = \sqrt{[\rho(\ell) - \ell']^2 + 2\rho(\ell)\ell'(1 - \cos\theta) + z(\ell)^2}$.

Because of the continuity of $\vec{J} \cdot \hat{\ell}$ in the neighborhood of ℓ_{N_a} we see that the last two integrals of equation (69) and equation (76) exactly cancel, and so never need be calculated. In fact, the presence of these integrals in the first place is an artifact of the separation of $\vec{J}$ into $\vec{J}_\sigma$ and $\vec{J}_S$. This separation is justified because of the discontinuity of $\vec{J} \cdot \hat{\phi}$ across the aperture rim, but $\vec{J} \cdot \hat{\ell}$ could easily be modeled as a single continuous function from $0 < \ell < L$.

4.4.4 Z_m^{21}.

Z_m^{21} is the $2N_a \times 2N_a$ submatrix associated with the testing of equation (36) and the expansion of $\vec{\mathbf{M}}_\sigma$. This case dictates that the domain of both the basis and testing functions

is σ. The elements of Z_m^{21} can be found from the inner product

$$\langle \mathcal{L}_3 \vec{\psi}_{mn}^{\ell,\phi}, \vec{\gamma}_{mn'}^{\ell,\phi} \rangle =$$
$$\int_\sigma \int_\sigma \vec{\gamma}_{mn'}^{\ell,\phi\,*}(\vec{r}') \cdot \left[\hat{\mathbf{z}} \times \left\{ \vec{\psi}_{mn}^{\ell,\phi}(\vec{r}) \cdot \left[\frac{\nabla \times \overline{\overline{\Gamma}}(k_1; \vec{r}, \vec{r}')}{-jk_1} - \frac{\nabla \times \overline{\overline{\Gamma}}(k_0; \vec{r}, \vec{r}')}{-jk_0} \right] \right\} \right] d\sigma\, d\sigma' \quad (77)$$

where $m = 0, \pm 1, \pm 2 \ldots \pm M$, $N_a \le n \le N_a + N_s$, and $1 \le n' \le N_a$.

From equation (13), $\nabla \times \overline{\overline{\Gamma}}(k; \vec{r}, \vec{r}')/(-jk)$ can be written

$$\frac{\nabla \times \overline{\overline{\Gamma}}(k; \vec{r}, \vec{r}')}{-jk} = \left\{ \left[3 + 3jkR + (jkR)^2 \right] \hat{\mathbf{R}}\hat{\mathbf{R}} \right.$$
$$\left. - \left[1 + jkR + (jkR)^2 \right] \overline{\overline{\mathbf{I}}} \right\} \frac{G(k; \vec{r}, \vec{r}')}{R^2} \quad (78)$$

where $\hat{\mathbf{R}} = (\vec{r} - \vec{r}')/R$. Then the dyadic kernel of equation (77) can be written as

$$\frac{\nabla \times \overline{\overline{\Gamma}}(k_1; \vec{r}, \vec{r}')}{-jk_1} - \frac{\nabla \times \overline{\overline{\Gamma}}(k_0; \vec{r}, \vec{r}')}{-jk_0} =$$
$$\left\{ \frac{\left[3 + 3jk_1R + (jk_1R)^2 \right] e^{-jk_1R} - \left[3 + 3jk_0R + (jk_0R)^2 \right] e^{-jk_0R}}{4\pi R^3} \right\} \hat{\mathbf{R}}\hat{\mathbf{R}}$$
$$\left\{ \frac{\left[1 + jk_1R + (jk_1R)^2 \right] e^{-jk_1R} - \left[1 + jk_0R + (jk_0R)^2 \right] e^{-jk_0R}}{4\pi R^3} \right\} \overline{\overline{\mathbf{I}}} \quad (79)$$

Expanding the complex exponential in a Taylor series about $R = 0$,

$$e^{-jkR} = 1 - jkR + \mathcal{O}(R^2), \qquad R \to 0 \quad (80)$$

we find that

$$\left| \vec{A} \cdot \left\{ \frac{\nabla \times \overline{\overline{\Gamma}}(k_1; \vec{r}, \vec{r}')}{-jk_1} - \frac{\nabla \times \overline{\overline{\Gamma}}(k_0; \vec{r}, \vec{r}')}{-jk_0} \right\} \cdot \vec{B} \right| = \mathcal{O}(R^{-1}), \qquad R \to 0 \quad (81)$$

for arbitrary vectors $\vec{A}$ and $\vec{B}$. As a consequence we see that, although each of the dyadic functions $\nabla \times \overline{\overline{\Gamma}}(k_1; \vec{r}, \vec{r}')/(-jk_1)$ and $\nabla \times \overline{\overline{\Gamma}}(k_0; \vec{r}, \vec{r}')/(-jk_0)$ has a R^{-3} singularity at $\vec{r} = \vec{r}'$, their difference has only a R^{-1} singularity there. Thus the integral in equation (78) is merely weakly

44

singular and can be handled numerically using the extraction procedure outlined at the end of Section 4.4.2. Of course, in the degenerate case of an unfilled OCRED cavity, $k_1 = k_0$ and the dyadic kernel identically vanishes.

4.4.5 Z_m^{22}.

Z_m^{22} is the $2N_a \times 2N_a$ submatrix associated with the testing of equation (36) and the expansion of $\vec{J}_\sigma$. This case dictates that the domain of both the basis and testing functions is confined to the aperture σ. The elements of Z_m^{22} are found from the inner product $\langle \vec{\psi}_{mn}^{\ell,\phi}, \vec{\gamma}_{mn'}^{\ell,\phi\,*} \rangle$ where $m = 0, \pm 1, \pm 2 \ldots \pm M$, $1 \leq n \leq N_a$, and $1 \leq n' \leq N_a$. This inner product is given in Section 4.4.1, and we simply restate it here for completeness.

$$\langle \vec{\psi}_{mn}^{\phi}, \vec{\gamma}_{mn'}^{\ell} \rangle = \langle \vec{\psi}_{mn}^{\ell}, \vec{\gamma}_{mn'}^{\phi} \rangle = 0 \tag{82a}$$

$$\langle \vec{\psi}_{mn}^{\ell}, \vec{\gamma}_{mn'}^{\ell} \rangle = \langle \vec{\psi}_{mn}^{\phi}, \vec{\gamma}_{mn'}^{\phi} \rangle$$

$$= \begin{cases} 2\pi \left\{ \begin{array}{l} \dfrac{\ell_n - 3\ell_{n-1}}{2(\ell_n - \ell_{n-1})} + \left[\dfrac{\ell_{n-1}}{\ell_n - \ell_{n-1}} \right]^2 \ln \dfrac{\ell_n}{\ell_{n-1}} \\[2mm] + \dfrac{\ell_n - 3\ell_{n+1}}{2(\ell_{n+1} - \ell_n)} + \left[\dfrac{\ell_{n+1}}{\ell_{n+1} - \ell_n} \right]^2 \ln \dfrac{\ell_{n+1}}{\ell_n} \end{array} \right\} & n' = n \\[6mm] \dfrac{2\pi}{(\ell_{n'} - \ell_n)^2} \left| \dfrac{\ell_{n'}^2 - \ell_n^2}{2} + \ell_n \ell_{n'} \ln \dfrac{\ell_n}{\ell_{n'}} \right| & |n' - n| = 1 \\[4mm] 0 & |n' - n| > 1 \end{cases} \tag{82b}$$

If $n = n' = 1$ in equation (82b) then the term involving $\ln[\ell_n/\ell_{n-1}]$ is ignored, while if $n = n' = N_a$ then the terms involving ℓ_{n+1} are ignored, for the same reasons as given in Section 4.4.1.

4.4.6 Z_m^{23}.

Z_m^{23} is the $2N_a \times 2N_s$ submatrix associated with the testing of equation (36) and the expansion of $\vec{J}_\sigma$. This case dictates that the domain of the basis functions is confined to the cavity surface S while the domain of the testing functions is confined to the aperture σ, as shown in Figure 12. The elements of Z_m^{23} are found from the inner product

$$\langle \mathcal{L}_4 \vec{\psi}_{mn}^{\ell,\phi}, \vec{\gamma}_{mn'}^{\ell,\phi} \rangle = \int_\sigma \int_S \vec{\gamma}_{mn'}^{\ell,\phi\,*}(\vec{r}') \cdot \left\{ \hat{z} \times \left[\vec{\psi}_{mn}^{\ell,\phi}(\vec{r}) \cdot \overline{\overline{\Gamma}}(k_1; \vec{r}, \vec{r}') \right] \right\} ds\, d\sigma' \tag{83}$$

where $m = 0, \pm 1, \pm 2 \ldots \pm M$, $N_a \leq n \leq N_a + N_s - 1$, and $1 \leq n' \leq N_a$. Writing $\overline{\overline{\Gamma}}(k; \vec{r}, \vec{r}') = -\jmath k \, \nabla G(k; \vec{r}, \vec{r}') \times \overline{\overline{\mathbf{I}}}$, we obtain

$$
\begin{aligned}
\vec{\psi}_{mn}^{\ell,\phi}(\vec{r}) \cdot \overline{\overline{\Gamma}}(k_1; \vec{r}, \vec{r}') &= -\jmath k \, \vec{\psi}_{mn}^{\ell,\phi}(\vec{r}) \cdot \left[\nabla G(k; \vec{r}, \vec{r}') \times \overline{\overline{\mathbf{I}}} \right] \\
&= -\jmath k \, \vec{\psi}_{mn}^{\ell,\phi}(\vec{r}) \times \nabla G(k; \vec{r}, \vec{r}')
\end{aligned}
\tag{84}
$$

where we have used the identity $\vec{A} \cdot \left(\vec{B} \times \overline{\overline{\mathbf{C}}} \right) = \left(\vec{A} \times \vec{B} \right) \cdot \overline{\overline{\mathbf{C}}}$. Explicitly writing

$$
\nabla G(k; \vec{r}, \vec{r}') = (-\jmath k R - 1) \frac{e^{-\jmath k R}}{4 \pi R^3} \vec{R}
\tag{85}
$$

$$
= (-\jmath k R - 1) \frac{G(k; \vec{r}, \vec{r}')}{R^2} \vec{R}
\tag{86}
$$

where $\vec{R} = \vec{r} - \vec{r}'$, equation (83) becomes

$$
\langle \mathcal{L}_4 \vec{\psi}_{mn}^{\ell,\phi}, \vec{\gamma}_{mn'}^{\ell,\phi} \rangle = -\jmath k \int_\sigma \int_S \left\{ \vec{\gamma}_{mn'}^{\ell,\phi \, *}(\vec{r}') \cdot \left[\hat{\mathbf{z}} \times \left\{ \vec{\psi}_{mn}^{\ell,\phi}(\vec{r}) \times \vec{R} \right\} \right] \right\} \times
$$
$$
(-\jmath k R - 1) \frac{G(k; \vec{r}, \vec{r}')}{R^2} \, ds \, d\sigma'
\tag{87}
$$

Although the integrand in equation (87) has a $\mathcal{O}(R^{-2})$ singularity at $\vec{r} = \vec{r}'$, since the cavity surface S and aperture σ do not overlap, the integral converges. We now calculate each of the four permutations of the vector portion of the integrand of equation (87). We have

$$
\hat{\ell} = \hat{\mathbf{x}} \cos \alpha \cos \phi + \hat{\mathbf{y}} \cos \alpha \sin \phi - \hat{\mathbf{z}} \sin \alpha
\tag{88a}
$$

$$
\hat{\phi} = -\hat{\mathbf{x}} \sin \phi + \hat{\mathbf{y}} \cos \phi
\tag{88b}
$$

$$
\hat{\ell}' = \hat{\mathbf{x}} \cos \phi' + \hat{\mathbf{y}} \sin \phi'
\tag{88c}
$$

$$
\hat{\phi}' = -\hat{\mathbf{x}} \sin \phi' + \hat{\mathbf{y}} \cos \phi'
\tag{88d}
$$

$$
\vec{R} = \hat{\mathbf{x}} \left(\rho \cos \phi - \rho' \cos \phi' \right) + \hat{\mathbf{y}} \left(\rho \sin \phi - \rho' \sin \phi' \right) - \hat{\mathbf{z}} z
\tag{88e}
$$

from which we find

$$\hat{\ell}' \cdot \hat{z} \times \left(\hat{\ell} \times \vec{R} \right) = \left[\rho \cos(\phi - \phi') - \rho' \right] \sin \alpha + z \cos \alpha \cos(\phi - \phi') \tag{89a}$$

$$\hat{\phi}' \cdot \hat{z} \times \left(\hat{\ell} \times \vec{R} \right) = \left[\rho \sin \alpha + z \cos \alpha \right] \sin(\phi - \phi') \tag{89b}$$

$$\hat{\ell}' \cdot \hat{z} \times \left(\hat{\phi} \times \vec{R} \right) = -z \sin(\phi - \phi') \tag{89c}$$

$$\hat{\phi}' \cdot \hat{z} \times \left(\hat{\phi} \times \vec{R} \right) = z \cos(\phi - \phi') \tag{89d}$$
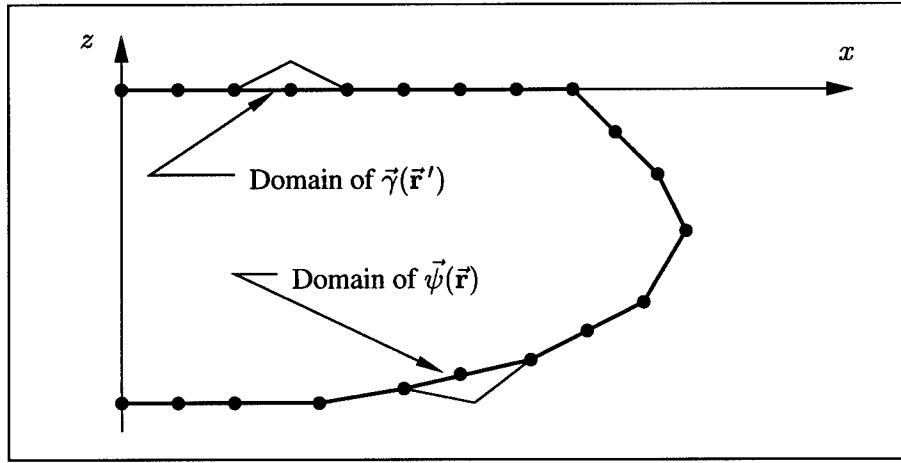
Figure 13   Domains of $\vec{\psi}(\vec{r})$ and $\vec{\gamma}(\vec{r}')$ for Z_m^{32}. $\vec{r}$ is defined on a cone frustum formed by revolving a portion of the cavity surface generating arc about the z-axis. $\vec{r}'$ is defined on an annulus in the xy-plane formed by revolving a portion of the aperture generating arc about the z-axis.

4.4.7 Z_m^{32}. Z_m^{32} is the $2N_s \times 2N_a$ submatrix associated with the testing of equation (37) and the expansion of $\vec{J}_\sigma$. As shown in Figure 13, the domain of the basis functions is the cavity surface S, while the domain of the testing functions is the aperture σ. The elements of Z_m^{32} are found from the inner product

$$\langle \mathcal{L}_5 \vec{\psi}_{mn}^{\ell,\phi}, \vec{\gamma}_{mn'}^{\ell,\phi *} \rangle = \int_S \int_\sigma \vec{\gamma}_{mn'}^{\ell,\phi *}(\vec{r}') \cdot \left\{ \hat{n}' \times \left[\vec{\psi}_{mn}^{\ell,\phi}(\vec{r}) \cdot \overline{\overline{\Gamma}}(k_1; \vec{r}, \vec{r}') \right] \right\} \, d\sigma \, ds' \tag{90}$$

where $m = 0, \pm 1, \pm 2, \ldots, \pm M$, $1 \leq n \leq N_a$, and $N_a \leq n' \leq N_a + N_s - 1$. Noting that $\overline{\overline{\Gamma}}(k; \vec{r}, \vec{r}')$ can be written as

$$\overline{\overline{\Gamma}}(k; \vec{r}, \vec{r}') = -\jmath k \nabla G(k; \vec{r}, \vec{r}') \times \overline{\overline{I}} \tag{91}$$

47

and using the identity $\vec{\mathbf{A}} \cdot \left(\vec{\mathbf{B}} \times \overline{\overline{\mathbf{C}}}\right) = \left[\vec{\mathbf{A}} \times \vec{\mathbf{B}}\right] \cdot \overline{\overline{\mathbf{C}}}$, we can write equation (90) as

$$\langle \mathcal{L}_5 \vec{\psi}_{mn}^{\ell,\phi}, \vec{\gamma}_{mn'}^{\ell,\phi \,*} \rangle = -\jmath k_1 \int_S \int_\sigma \vec{\gamma}_{mn'}^{\ell,\phi \,*}(\vec{\mathbf{r}}') \cdot \left\{ \hat{\mathbf{n}}' \times \left[\vec{\psi}_{mn}^{\ell,\phi}(\vec{\mathbf{r}}) \times \nabla G(k_1; \vec{\mathbf{r}}, \vec{\mathbf{r}}') \right] \right\} \, d\sigma \, ds' \quad (92)$$

Making use of equation (85) in equation (90) we obtain

$$\langle \mathcal{L}_5 \vec{\psi}_{mn}^{\ell,\phi}, \vec{\gamma}_{mn'}^{\ell,\phi \,*} \rangle = -\jmath k_1 \int_S \int_\sigma \vec{\gamma}_{mn'}^{\ell,\phi \,*}(\vec{\mathbf{r}}') \cdot \left\{ \hat{\mathbf{n}}' \times \left[\vec{\psi}_{mn}^{\ell,\phi}(\vec{\mathbf{r}}) \times \vec{\mathbf{R}} \right] \right\}$$
$$(-\jmath k R - 1) \frac{e^{-\jmath k R}}{4\pi R^3} \, d\sigma \, ds' \quad (93)$$

where $\vec{\mathbf{R}} = \vec{\mathbf{r}} - \vec{\mathbf{r}}'$. Although the integrand in equation (93) has a $\mathcal{O}(R^{-2})$ singularity at $\vec{\mathbf{r}} = \vec{\mathbf{r}}'$, since the aperture σ and cavity surface S do not overlap, the integral converges. We now calculate each of the four permutations of the vector portion of the integrand of equation (93). We define the relevant vectors as

$$\hat{\ell} = \hat{\mathbf{x}} \cos \phi + \hat{\mathbf{y}} \sin \phi \quad (94a)$$

$$\hat{\phi} = -\hat{\mathbf{x}} \sin \phi + \hat{\mathbf{y}} \cos \phi \quad (94b)$$

$$\hat{\ell}' = \hat{\mathbf{x}} \cos \alpha' \cos \phi' + \hat{\mathbf{y}} \cos \alpha' \sin \phi' - \hat{\mathbf{z}} \sin \alpha' \quad (94c)$$

$$\hat{\phi}' = -\hat{\mathbf{x}} \sin \phi' + \hat{\mathbf{y}} \cos \phi' \quad (94d)$$

$$\vec{\mathbf{R}} = \hat{\mathbf{x}} \left(\rho \cos \phi - \rho' \cos \phi'\right) + \hat{\mathbf{y}} \left(\rho \sin \phi - \rho' \sin \phi'\right) + \hat{\mathbf{z}} z' \quad (94e)$$

from which we find

$$\hat{\ell}' \cdot \hat{\mathbf{n}}' \times \left(\hat{\ell} \times \vec{\mathbf{R}}\right) = -z' \cos(\phi - \phi') \quad (95a)$$

$$\hat{\phi}' \cdot \hat{\mathbf{n}}' \times \left(\hat{\ell} \times \vec{\mathbf{R}}\right) = -\left(\rho' \sin \alpha' + z' \cos \alpha'\right) \sin(\phi - \phi') \quad (95b)$$

$$\hat{\ell}' \cdot \hat{\mathbf{n}}' \times \left(\hat{\phi} \times \vec{\mathbf{R}}\right) = z' \sin(\phi - \phi') \quad (95c)$$

$$\hat{\phi}' \cdot \hat{\mathbf{n}}' \times \left(\hat{\phi} \times \vec{\mathbf{R}}\right) = \left[\rho - \rho' \cos(\phi - \phi')\right] \sin \alpha' - z' \cos \alpha' \cos(\phi - \phi') \quad (95d)$$

4.4.8 Z_m^{33}.

Z_m^{33} is the $2N_s \times 2N_s$ submatrix associated with the testing of equation (37) and the expansion of $\vec{\mathbf{J}}_S$. As shown in figure 14, the domain of both the basis and testing functions
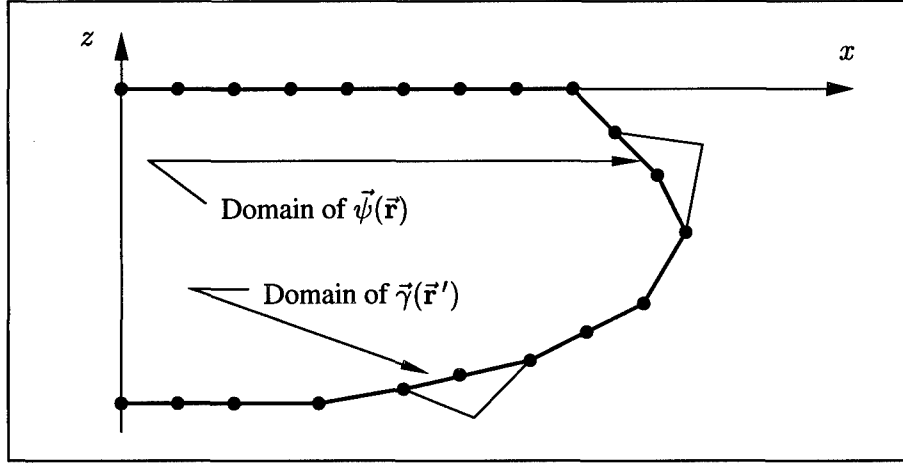
Figure 14   Domains of $\vec{\psi}(\vec{r})$ and $\vec{\gamma}(\vec{r}')$ for Z_m^{33}. Both $\vec{r}$ and $\vec{r}'$ are defined on cone frusta formed by revolving a portions of the cavity surface generating arc about the z-axis.

is the cavity surface S. The elements of Z_m^{33} are found from the inner product

$$\langle \mathcal{L}_6 \vec{\psi}_{mn}^{\ell,\phi}, \vec{\gamma}_{mn'}^{\ell,\phi} \rangle = \int_S \int_S \vec{\gamma}_{mn'}^{\ell,\phi\,*}(\vec{r}') \cdot \left\{ \hat{\mathbf{n}}' \times \left[\vec{\psi}_{mn}^{\ell,\phi}(\vec{r}) \cdot \overline{\overline{\Gamma}}_2(k_1; \vec{r}, \vec{r}') \right] \right\} \, ds \, ds'$$
$$- \frac{jk_1}{2} \int_S \vec{\psi}_{mn}^{\ell,\phi}(\vec{r}') \cdot \vec{\gamma}_{mn'}^{\ell,\phi\,*}(\vec{r}') \, ds' \qquad (96)$$

where $m = 0, \pm 1, \pm 2, \dots, \pm M$, $N_a \leq n \leq N_a + N_s - 1$, and $N_a \leq n' \leq N_a + N_s - 1$. Noting that $\overline{\overline{\Gamma}}_2(k; \vec{r}, \vec{r}')$ can be written

$$\overline{\overline{\Gamma}}_2(k; \vec{r}, \vec{r}') = -jk \left[\nabla G(k; \vec{r}, \vec{r}') \times \overline{\overline{\mathbf{I}}} - \nabla G(k; \vec{r}, \vec{r}_i') \times \overline{\overline{\mathbf{I}}}_i \right] \qquad (97)$$

and using the identity $\vec{A} \cdot \left[\vec{B} \times \overline{\overline{C}} \right] = \left[\vec{A} \times \vec{B} \right] \cdot \overline{\overline{C}}$, we can write equation (96) as

$$\langle \mathcal{L}_6 \vec{\psi}_{mn}^{\ell,\phi}, \vec{\gamma}_{mn'}^{\ell,\phi} \rangle = \int_S \int_S \vec{\gamma}_{mn'}^{\ell,\phi\,*}(\vec{r}') \cdot \left\{ \hat{\mathbf{n}}' \times \left[\vec{\psi}_{mn}^{\ell,\phi}(\vec{r}) \times \nabla G(k_1; \vec{r}, \vec{r}') \right] \right\} \, ds \, ds'$$
$$- \int_S \int_S \vec{\gamma}_{mn'}^{\ell,\phi\,*}(\vec{r}') \cdot \left\{ \hat{\mathbf{n}}' \times \left[\vec{\psi}_{mn}^{\ell,\phi}(\vec{r}) \times \nabla G(k_1; \vec{r}, \vec{r}_i') \right]_i \right\} \, ds \, ds' \qquad (98)$$
$$- \frac{jk_1}{2} \int_S \vec{\psi}_{mn}^{\ell,\phi}(\vec{r}') \cdot \vec{\gamma}_{mn'}^{\ell,\phi\,*}(\vec{r}') \, ds'$$

49

We may express the gradients of the scalar Green's functions as

$$\nabla G(k; \vec{r}, \vec{r}') = \left(-\jmath k \left|\vec{r} - \vec{r}'\right| - 1\right) \frac{\exp\left(-\jmath k \left|\vec{r} - \vec{r}'\right|\right)}{4\pi \left|\vec{r} - \vec{r}'\right|^3} \left(\vec{r} - \vec{r}'\right) \tag{99a}$$

$$\nabla G(k; \vec{r}, \vec{r}_i') = \left(-\jmath k \left|\vec{r} - \vec{r}_i'\right| - 1\right) \frac{\exp\left(-\jmath k \left|\vec{r} - \vec{r}_i'\right|\right)}{4\pi \left|\vec{r} - \vec{r}_i'\right|^3} \left(\vec{r} - \vec{r}_i'\right) \tag{99b}$$

We have defined $R = \left|\vec{r} - \vec{r}'\right|$ and $\vec{R} = \vec{r} - \vec{r}'$; we will now define $R_i = \left|\vec{r} - \vec{r}_i'\right|$ and $\vec{R}_i = \vec{r} - \vec{r}_i'$. *Note that this definition of* $\vec{R}_i$ *is a deviation from the convention that the subscript i on a vector indicates the image of that vector!* These quantities are shown in Figure 15. We rewrite
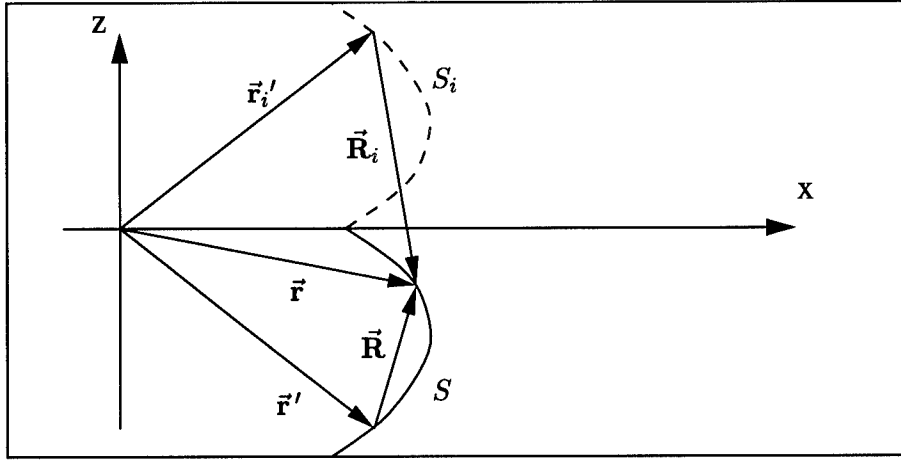
Figure 15   Definition of $\vec{R}_i$. $\vec{R}_i = \vec{r} - \vec{r}_i'$ where $\vec{r}$ denotes a point on S and $\vec{r}_i'$ denotes a point on S_i.

equation (98) as

$$\langle \mathcal{L}_6 \vec{\psi}_{mn}^{\ell,\phi}, \vec{\gamma}_{mn'}^{\ell,\phi} \rangle =$$

$$-\jmath k_1 \int_S \int_S \left\{ \vec{\gamma}_{mn'}^{\ell,\phi *}(\vec{r}') \cdot \left[\hat{n}' \times \left\{ \vec{\psi}_{mn}^{\ell,\phi}(\vec{r}) \times \vec{R} \right\} \right] \right\} (-\jmath k_1 R - 1) \frac{e^{-\jmath k_1 R}}{4\pi R^3} \, ds \, ds'$$

$$+\jmath k_1 \int_S \int_S \left\{ \vec{\gamma}_{mn'}^{\ell,\phi *}(\vec{r}') \cdot \left[\hat{n}' \times \left\{ \vec{\psi}_{mn}^{\ell,\phi}(\vec{r}) \times \vec{R}_i \right\}_i \right] \right\} (-\jmath k_1 R_i - 1) \frac{e^{-\jmath k_1 R_i}}{4\pi R_i^3} \, ds \, ds' \tag{100}$$

$$-\frac{\jmath k_1}{2} \int_S \vec{\psi}_{mn}^{\ell,\phi}(\vec{r}') \cdot \vec{\gamma}_{mn'}^{\ell,\phi *}(\vec{r}') \, ds'$$

Using elementary vector analysis, we may show that $\vec{A} \cdot \left(\vec{B} \times \vec{C}_i\right) = -\vec{A}_i \cdot \left(\vec{B}_i \times \vec{C}\right)$ so equation (100) becomes

$$
\begin{aligned}
\langle \mathcal{L}_6 \vec{\psi}_{mn}^{\ell,\phi}, \vec{\gamma}_{mn'}^{\ell,\phi} \rangle = \\
-jk_1 \int_S \int_S \left\{ \vec{\gamma}_{mn'}^{\ell,\phi\,*}(\vec{r}') \cdot \left[\hat{n}' \times \left\{ \vec{\psi}_{mn}^{\ell,\phi}(\vec{r}) \times \vec{R} \right\} \right] \right\} (-jk_1 R - 1) \frac{e^{-jk_1 R}}{4\pi R^3} \, ds \, ds' \\
-jk_1 \int_S \int_S \left\{ \left[\vec{\gamma}_{mn'}^{\ell,\phi\,*}(\vec{r}') \right]_i \cdot \left[\hat{n}_i' \times \left\{ \vec{\psi}_{mn}^{\ell,\phi}(\vec{r}) \times \vec{R}_i \right\} \right] \right\} (-jk_1 R - 1) \frac{e^{-jk_1 R}}{4\pi R^3} \, ds \, ds' \quad (101) \\
-\frac{jk_1}{2} \int_S \vec{\psi}_{mn}^{\ell,\phi}(\vec{r}') \cdot \vec{\gamma}_{mn'}^{\ell,\phi\,*}(\vec{r}') \, ds'
\end{aligned}
$$

The second integral in equation (101) converges because $R_i > 0$ for $\vec{r} \in S$ and $\vec{r}' \in S$. The third integral also converges since the integrand is bounded on the (finite) region of integration. The first integral in equation (101) must be handled carefully because of the (apparent) $\mathcal{O}(R^{-3})$ singularity of the integrand at $\vec{r} = \vec{r}'$. However, we can show that

$$
\left| \hat{\gamma}(\vec{r}') \cdot \left[\hat{n}' \times \left\{ \hat{\psi}(\vec{r}) \times \vec{R} \right\} \right] \right| = \mathcal{O}(R^2), \qquad \vec{r} \to \vec{r}', \tag{102}
$$

where $\hat{\gamma}(\vec{r}')$ is either $\hat{\ell}'$ or $\hat{\phi}'$ and $\hat{\psi}(\vec{r})$ is either $\hat{\ell}$ or $\hat{\phi}$. Thus the integrand of the first integral in equation (101) has only a weak $\mathcal{O}(R^{-1})$ singularity at $\vec{r} = \vec{r}'$ and, hence, the first integral converges.

4.5 Forcing Function

In the matrix equation $Z_m I_m = V_m$, the right side, V_m, contains the effect of the mth Fourier mode of the incident field. V_m is a column vector given by $[v_1 \; v_2 \; \ldots \; v_N]^T$, where $N = 4N_a + 2N_s$ is the system size. The elements of V_m correspond to the right sides of equations (35)–(37). The right side of equation (35) is zero, which causes the first $2N_a$ elements of V_m to identically vanish. Likewise, the right side of equation (37) is zero, causing the last $2N_s$ elements of V_m to vanish. Only the elements of V_m which correspond to the testing of equation (36) do not identically vanish; these are elements $i = 2N_a + 1$ through $i = 4N_a$. The effect of the incident field is manifested via the "physical optics" current density $\vec{J}^0(\vec{r}') = 2\hat{z} \times \vec{H}^{\text{inc}}(\vec{r}')$, $\vec{r}' \in \sigma$.

We assume that the system excitation is caused by a uniform plane wave having a propagation unit vector $\hat{\mathbf{k}}$, as shown in Figure 16. Without loss of generality, we restrict $\hat{\mathbf{k}}$ to lie in the
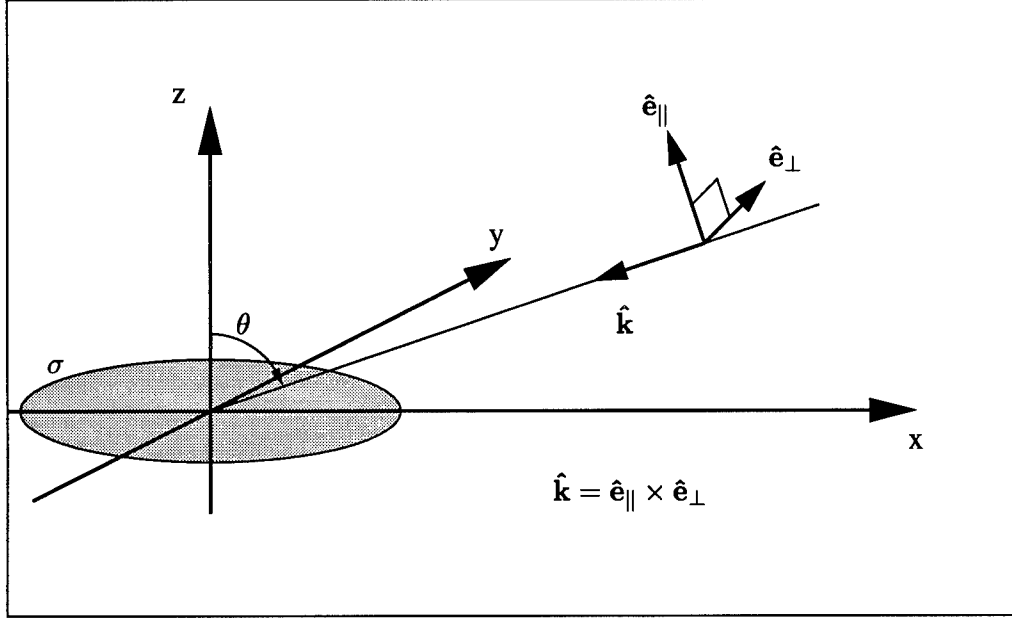
Figure 16   Parallel ($\parallel$) and perpendicular ($\perp$) polarized incident plane waves.

xz-plane, which we will call the plane of incidence. Then we define the unit vector $\hat{\mathbf{e}}_\perp$ to be perpendicular to the plane of incidence and the unit vector $\hat{\mathbf{e}}_\parallel$ to be parallel to the plane of incidence. Both $\hat{\mathbf{e}}_\perp$ and $\hat{\mathbf{e}}_\parallel$ are perpendicular to $\hat{\mathbf{k}}$, and satisfy the relation $\hat{\mathbf{k}} = \hat{\mathbf{e}}_\parallel \times \hat{\mathbf{e}}_\perp$. Defining θ as the angle between $\hat{\mathbf{z}}$ and $-\hat{\mathbf{k}}$, we find

$$\hat{\mathbf{k}} = -\hat{\mathbf{x}} \sin\theta - \hat{\mathbf{z}} \cos\theta \tag{103a}$$

$$\hat{\mathbf{e}}_\perp = \hat{\mathbf{y}} \tag{103b}$$

$$\hat{\mathbf{e}}_\parallel = -\hat{\mathbf{x}} \cos\theta + \hat{\mathbf{z}} \sin\theta \tag{103c}$$

We assume that the electric field vector $\vec{\mathbf{E}}^{\text{inc}}$ of the incident plane wave has unit amplitude and zero phase at the origin, and is either completely parallel to the plane of incidence ($\parallel$ polarization) or completely perpendicular to the plane of incidence ($\perp$ polarization):

$$\vec{\mathbf{E}}^{\text{inc}}(\vec{\mathbf{r}}') = \hat{\mathbf{e}} \, e^{jk_0(x' \sin\theta + z' \cos\theta)} \tag{104}$$

52

where $\hat{e} = \hat{e}_\parallel$ for parallel polarization and $\hat{e} = \hat{e}_\perp$ for perpendicular polarization. Then the incident magnetic field $\vec{H}^{inc} = Y_0 \hat{k} \times \vec{E}^{inc}$ can be written as

$$\vec{H}^{inc}(\vec{r}') = \hat{e} \, Y_0 \, e^{jk_0(x' \sin\theta + z' \cos\theta)} \tag{105}$$

where $\hat{e} = \hat{e}_\perp$ for parallel polarization and $\hat{e} = -\hat{e}_\parallel$ for perpendicular polarization. The "physical optics" current density $\vec{J}^0(\vec{r}') = 2\hat{z} \times \vec{H}^{inc}(\vec{r}')$, $z' = 0$, is given by

$$\vec{J}^0(\vec{r}') = 2 \, Y_0 \, e^{jk_0\rho' \sin\theta \cos\phi'} \begin{cases} -\hat{x} & \text{for} \parallel \text{Pol} \\[2mm] \hat{y} \cos\theta & \text{for} \perp \text{Pol} \end{cases} \tag{106}$$

where $\rho' = \sqrt{x'^2 + y'^2}$ and $\phi' = \arctan(y'/x')$.

To find v_i, $2N_a + 1 \leq i \leq 4N_a$, we calculate the inner product of $\vec{J}^0$ and corresponding testing function $\vec{\gamma}^{\ell,\phi}_{mn'}(\vec{r}')$:

$$\begin{aligned} v_i &= \frac{jk_0 Z_0}{2} \langle \vec{J}^0, \vec{\gamma}^{\ell,\phi}_{mn'} \rangle \\ &= \frac{jk_0 Z_0}{2} \int_\sigma \vec{J}^0(\vec{r}') \cdot \vec{\gamma}^{\ell,\phi *}_{mn'}(\vec{r}') \, d\sigma, \end{aligned} \tag{107}$$

where $1 \leq n' \leq N_a$. The testing function $\vec{\gamma}^{\ell,\phi}_{mn'}(\vec{r}')$ was introduced in Section 4.3; we repeat it here for convenience.

$$\vec{\gamma}^\ell_{mn'}(\vec{r}') = e^{jm\phi'} \frac{T_{n'}(\ell')}{\rho(\ell')} \hat{\ell}' \tag{108a}$$

$$\vec{\gamma}^\phi_{mn'}(\vec{r}') = e^{jm\phi'} \frac{T_{n'}(\ell')}{\rho(\ell')} \hat{\phi}' \tag{108b}$$

Since the testing functions that contribute to V are defined only for $\vec{r}' \in \sigma$, the arc-length variable ℓ' is equivalent to the polar radial variable $\rho(\ell')$, and we can write $\hat{\ell}' = \hat{x} \cos\phi' + \hat{y} \sin\phi'$ and $\hat{\phi} = -\hat{x} \sin\phi' + \hat{y} \cos\phi'$. Expressing the inner product as an integral in polar coordinates, we have

$$\langle \vec{J}^0, \vec{\gamma}^{\ell,\phi}_{mn'} \rangle = \int_0^{2\pi} \int_0^{\ell_{N_a}} f(\ell', \phi') \, g(\theta, \phi') \, d\ell' \, d\phi' \tag{109a}$$

53

where

$$f(\ell', \phi') = 2\,Y_0\;e^{jk_0\ell'\sin\theta\cos\phi'}\;T_{n'}(\ell')\;e^{-jm\phi'} \tag{109b}$$

$$g(\theta, \phi') = \begin{cases} -\cos\phi' & \text{for } \vec\gamma = \vec\gamma^\ell \text{ and } \parallel \text{Pol} \\[1.5ex] \sin\phi' & \text{for } \vec\gamma = \vec\gamma^\phi \text{ and } \parallel \text{Pol} \\[1.5ex] \cos\theta\sin\phi' & \text{for } \vec\gamma = \vec\gamma^\ell \text{ and } \perp \text{Pol} \\[1.5ex] \cos\theta\cos\phi' & \text{for } \vec\gamma = \vec\gamma^\phi \text{ and } \perp \text{Pol} \end{cases} \tag{109c}$$

Using basic trigonometric identities and the relation $J_n(z) = \dfrac{j^{-n}}{\pi}\displaystyle\int_0^\pi e^{jz\cos\phi}\,\cos(n\phi)\,d\phi$, where J_n is the Bessel function of the first kind of order n, we can write the inner product as

$$\langle \vec{\mathbf{J}}^0, \vec\gamma_{mn'}^{\ell,\phi} \rangle = 2\,\pi\,Y_0 \int_0^{\ell_{Na}} T_{n'}(\ell')\,f_m(\ell')\,d\ell' \tag{110a}$$

where

$$f_m(\ell') = \begin{cases} j\,g_m^{(-)}(\ell') & \text{for } \vec\gamma = \vec\gamma^\ell \text{ and } \parallel \text{Pol} \\[1.5ex] -g_m^{(+)}(\ell') & \text{for } \vec\gamma = \vec\gamma^\phi \text{ and } \parallel \text{Pol} \\[1.5ex] -\cos\theta\,g_m^{(+)}(\ell') & \text{for } \vec\gamma = \vec\gamma^\ell \text{ and } \perp \text{Pol} \\[1.5ex] -j\cos\theta\,g_m^{(-)}(\ell') & \text{for } \vec\gamma = \vec\gamma^\phi \text{ and } \perp \text{Pol} \end{cases} \tag{110b}$$

$$g_m^{(\pm)}(\ell') = j^m\left\{ J_{m-1}(k_0\ell'\sin\theta) \pm J_{m+1}(k_0\ell'\sin\theta) \right\} \tag{110c}$$

We note that $g_m^{(+)} = g_{-m}^{(+)}$ and $g_m^{(-)} = -g_{-m}^{(-)}$.

4.6 Symmetry

Up to this point, we have been working with the matrix equation $Z_m\,I_m = V_m$ where $m = 0, \pm 1, \ldots \pm M$. It so happens that we need only explicitly solve the matrix equation for $m = 0, 1, \ldots M$. The solution vector I_m for negative m can be found with no additional computation by exploiting the symmetry between $Z_m\,I_m = V_m$ and $Z_{-m}\,I_{-m} = V_{-m}$. We may symbolically

write the matrix equation $Z_m \, I_m = V_m$ as

$$
\begin{bmatrix}
\begin{pmatrix} Z_m^{11,\ell\ell} & Z_m^{11,\ell\phi} \\ Z_m^{11,\phi\ell} & Z_m^{11,\phi\phi} \end{pmatrix} & \begin{pmatrix} Z_m^{12,\ell\ell} & Z_m^{12,\ell\phi} \\ Z_m^{12,\phi\ell} & Z_m^{12,\phi\phi} \end{pmatrix} & \begin{pmatrix} Z_m^{13,\ell\ell} & Z_m^{13,\ell\phi} \\ Z_m^{13,\phi\ell} & Z_m^{13,\phi\phi} \end{pmatrix} \\[2em]
\begin{pmatrix} Z_m^{21,\ell\ell} & Z_m^{21,\ell\phi} \\ Z_m^{21,\phi\ell} & Z_m^{21,\phi\phi} \end{pmatrix} & \begin{pmatrix} Z_m^{22,\ell\ell} & Z_m^{22,\ell\phi} \\ Z_m^{22,\phi\ell} & Z_m^{22,\phi\phi} \end{pmatrix} & \begin{pmatrix} Z_m^{23,\ell\ell} & Z_m^{23,\ell\phi} \\ Z_m^{23,\phi\ell} & Z_m^{23,\phi\phi} \end{pmatrix} \\[2em]
\begin{pmatrix} Z_m^{31,\ell\ell} & Z_m^{31,\ell\phi} \\ Z_m^{31,\phi\ell} & Z_m^{31,\phi\phi} \end{pmatrix} & \begin{pmatrix} Z_m^{32,\ell\ell} & Z_m^{32,\ell\phi} \\ Z_m^{32,\phi\ell} & Z_m^{32,\phi\phi} \end{pmatrix} & \begin{pmatrix} Z_m^{33,\ell\ell} & Z_m^{33,\ell\phi} \\ Z_m^{33,\phi\ell} & Z_m^{33,\phi\phi} \end{pmatrix}
\end{bmatrix}
\begin{bmatrix} \begin{pmatrix} A_m^\ell \\ A_m^\phi \end{pmatrix} \\[2em] \begin{pmatrix} B_m^\ell \\ B_m^\phi \end{pmatrix} \\[2em] \begin{pmatrix} C_m^\ell \\ C_m^\phi \end{pmatrix} \end{bmatrix}
=
\begin{bmatrix} \begin{pmatrix} 0 \\ 0 \end{pmatrix} \\[2em] \begin{pmatrix} V_m^\ell \\ V_m^\phi \end{pmatrix} \\[2em] \begin{pmatrix} 0 \\ 0 \end{pmatrix} \end{bmatrix}
\tag{111}
$$

In equation (111), the block submatrix $Z_m^{11,\ell\phi}$ contains the elements of Z_m^{11} corresponding to ℓ-directed basis functions and ϕ-directed testing functions; the other block submatrices are defined analogously. The block subvector A_m^ℓ contains the expansion coefficients of equation (46) for ℓ-directed basis functions; the other subvectors of I_m are defined analogously. The block subvector V_m^ℓ contains the result of testing equation (36) with ℓ-directed testing functions; V_m^ϕ is defined analogously.

Each submatrix of Z_m is either odd or even with respect to the Fourier index m. By examining the formulations in Sections 4.4.1–4.4.8, we find that

$$
\begin{bmatrix}
\begin{pmatrix} E & \emptyset \\ \emptyset & E \end{pmatrix} & \begin{pmatrix} O & E \\ E & O \end{pmatrix} & \begin{pmatrix} O & E \\ E & O \end{pmatrix} \\[2em]
\begin{pmatrix} O & E \\ E & O \end{pmatrix} & \begin{pmatrix} E & O \\ O & E \end{pmatrix} & \begin{pmatrix} E & O \\ O & E \end{pmatrix} \\[2em]
\begin{pmatrix} \emptyset & \emptyset \\ \emptyset & \emptyset \end{pmatrix} & \begin{pmatrix} E & O \\ O & E \end{pmatrix} & \begin{pmatrix} E & O \\ O & E \end{pmatrix}
\end{bmatrix}
\begin{bmatrix} \begin{pmatrix} A_m^\ell \\ A_m^\phi \end{pmatrix} \\[2em] \begin{pmatrix} B_m^\ell \\ B_m^\phi \end{pmatrix} \\[2em] \begin{pmatrix} C_m^\ell \\ C_m^\phi \end{pmatrix} \end{bmatrix}
=
\begin{bmatrix} \begin{pmatrix} 0 \\ 0 \end{pmatrix} \\[2em] \begin{pmatrix} V_m^\ell \\ V_m^\phi \end{pmatrix} \\[2em] \begin{pmatrix} 0 \\ 0 \end{pmatrix} \end{bmatrix}
\tag{112}
$$

Equation (112) repeats equation (111) except that each submatrix of Z_m in equation (111) has been replaced with an "E" if it is even with respect to m, an "O" if it is odd with respect to m, and an "$\emptyset$" if it is identically zero. From section 4.5 we see that $V_m^\ell = V_{-m}^\ell$ and $V_m^\ell = -V_{-m}^\ell$ for parallel polarization, while $V_m^\ell = -V_{-m}^\ell$ and $V_m^\ell = V_{-m}^\ell$ for perpendicular polarization. From this we

may draw the following conclusions regarding the subvectors of I_m:

$$A_m^\ell = \mp A_{-m}^\ell \qquad A_m^\phi = \pm A_{-m}^\phi$$

$$B_m^\ell = \pm B_{-m}^\ell \qquad B_m^\phi = \mp B_{-m}^\phi \tag{113}$$

$$C_m^\ell = \pm C_{-m}^\ell \qquad C_m^\phi = \mp C_{-m}^\phi$$

where the top sign is taken for parallel polarization and the bottom sign is taken for perpendicular polarization. Exploiting the relations of equation (113), we may then re-write equations (46)–(48) to sum over only non-negative Fourier indices:

$$\vec{\mathbf{M}}_\sigma(\ell,\phi) \approx Z_0 \sum_{m=0}^{M} \epsilon_m \sum_{n=1}^{N_a} \frac{T_n(\ell)}{\rho(\ell)} \left\{ A_{mn}^\ell \, f(\phi) \, \hat{\ell} + A_{mn}^\phi \, g(\phi) \, \hat{\phi} \right\} \tag{114a}$$

$$\vec{\mathbf{J}}_\sigma(\ell,\phi) \approx \sum_{m=0}^{M} \epsilon_m \sum_{n=1}^{N_a} \frac{T_n(\ell)}{\rho(\ell)} \left\{ B_{mn}^\ell \, g(\phi) \, \hat{\ell} + B_{mn}^\phi \, f(\phi) \, \hat{\phi} \right\} \tag{114b}$$

$$\vec{\mathbf{J}}_s(\ell,\phi) \approx \sum_{m=0}^{M} \epsilon_m \sum_{n=N_a}^{N_a+N_s-1} \frac{T_n(\ell)}{\rho(\ell)} \left\{ C_{mn}^\ell \, g(\phi) \, \hat{\ell} + C_{mn}^\phi \, f(\phi) \, \hat{\phi} \right\} \tag{114c}$$

where $0 \le \phi < 2\pi$, $0 < \ell < \ell_{N_a}$ for $\vec{\mathbf{M}}_\sigma$ and $\vec{\mathbf{J}}_\sigma$, $\ell_{N_a} < \ell < \ell_{N_a+N_s}$ for $\vec{\mathbf{J}}_s$, and

$$f(\phi) = \jmath \, \sin(m\phi) \tag{115a}$$

$$g(\phi) = \cos(m\phi) \tag{115b}$$

$$\epsilon_m = \begin{cases} 1 & \text{for } m = 0 \\ 2 & \text{for } m \ne 0. \end{cases} \tag{115c}$$

56

V. Numerical and Experimental Results

A computer program was written to implement the method of moments solution outlined in Chapter IV for the BOR OCRED scattering problem. For simplicity, the program was written only for OCRED geometries in which the cavity volume is unfilled. As noted previously, when the cavity volume is unfilled, only the electric current density on the aperture ($\vec{J}_\sigma$) and the electric current density on the cavity surface ($\vec{J}_S$) need to be found. Once $\vec{J}_\sigma$ and $\vec{J}_S$ are determined, the program calculates the monostatic radar cross section for the user-supplied angle of incidence.

To validate the results generated by the program, several physical BOR OCRED models were fabricated and their radar cross sections measured. The measurements are discussed in the next section, and the results for each model are discussed in subsequent sections.

5.1 BOR OCRED Geometries

(a) Spherical OCRED. $\ell_0 = 0$, $\ell_1 = R_a$, $\ell_2 = R_a + R_s(\pi - \alpha)$.

(b) Cylindrical OCRED. $\ell_0 = 0$, $\ell_1 = R_a$, $\ell_2 = R_a + d$, $\ell_3 = 2R_a + d$. There are two cylindrical OCREDs, deep and shallow.

(c) Conical OCRED. $\ell_0 = 0$, $\ell_1 = R_a$, $\ell_2 = R_a + \sqrt{R_a^2 + d^2}$.
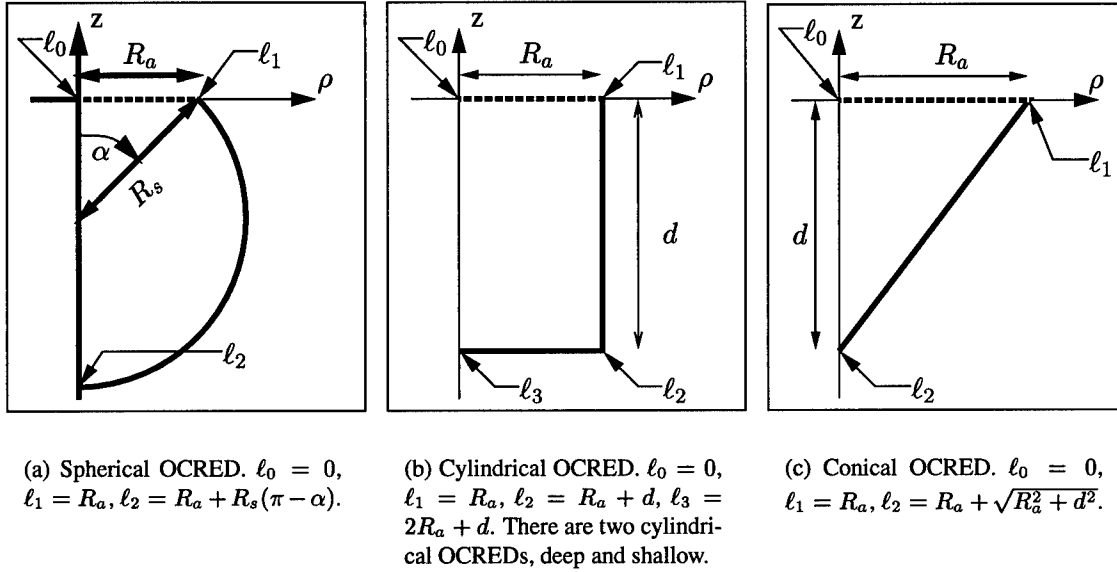
Figure 17   Generating arcs for the four BOR OCRED geometries investigated in this dissertation. The cavity volume D is carved out by rotating the generating arc about the z-axis. The dashed portion forms the aperture σ while the solid portion forms the cavity surface S.

Figure 17 shows the generating arcs for the four BOR OCRED geometries. Each BOR OCRED geometry is formed by revolving the generating arc about the z-axis. The portion of the

generating arc on the ρ-axis generates the OCRED aperture σ, while the portion below the ρ-axis generates the cavity surface S. The ground plane (the $z = 0$ plane less the aperture σ) is implied.

Each generating arc shown in Figure 17 can be mathematically defined in terms of the arc length parameter ℓ, which measures the distance along the generating arc, starting from the origin. We formally define each generating arc mathematically as follows.

Spherical OCRED. The generating arc for the spherical BOR OCRED is shown in Figure 17(a). The equations defining the generating arc are

$$\rho(\ell) = \begin{cases} \ell, & 0 \leq \ell < R_a \\ R_s \sin\left(\frac{\ell - R_a}{R_s} + \alpha\right), & R_a \leq \ell \leq R_a + R_s(\pi - \alpha) \end{cases} \tag{116}$$

$$z(\ell) = \begin{cases} 0, & 0 \leq \ell < R_a \\ R_s \cos\left(\frac{\ell - R_a}{R_s} + \alpha\right) - R_s \cos\alpha, & R_a \leq \ell \leq R_a + R_s(\pi - \alpha) \end{cases} \tag{117}$$

where $R_s = 7/8$ inches $= 0.022225$ meters is the radius of the spherical cavity, $R_a = 5/8$ inches $= 0.015875$ meters is the radius of the aperture, and $\alpha = \arcsin(R_a/R_s) \approx 45.6°$. The domain of $\rho(\ell)$ and $z(\ell)$ is $0 \leq \ell \leq R_a + R_s(\pi - \alpha)$.

Cylindrical OCREDs. The generating arc for the generic cylindrical BOR OCRED is shown in Figure 17(b). Two cylindrical BOR OCREDs are considered in this research, a shallow one and a deep one. The equations defining the generating arc are

$$\rho(\ell) = \begin{cases} \ell, & 0 \leq \ell < R_a \\ R_a, & R_a \leq \ell < R_a + d \\ 2R_a + d - \ell, & R_a + d \leq \ell \leq 2R_a + d \end{cases} \tag{118}$$

$$z(\ell) = \begin{cases} 0, & 0 \leq \ell < R_a \\ R_a - \ell, & R_a \leq \ell < R_a + d \\ -d, & R_a + d \leq \ell \leq 2R_a + d \end{cases} \tag{119}$$

58

where R_a = 5/8 inches = 0.015875 meters is the radius of the aperture, and d is the depth of the cylindrical cavity. For the deep cylindrical OCRED, d = 3 inches = 0.0762 meters, while for the shallow cylindrical OCRED, d = 1.5 inches = 0.0381 meters. The domain of $\rho(\ell)$ and $z(\ell)$ is $0 \leq \ell \leq 2R_a + d$.

Conical OCRED. The generating arc for the conical BOR OCRED is shown in Figure 17(c). The equations defining the generating arc are

$$\rho(\ell) = \begin{cases} \ell, & 0 \leq \ell < R_a \\ R_a \left(1 - \dfrac{\ell - R_a}{\sqrt{R_a^2 + d^2}} \right), & R_a \leq \ell \leq R_a + \sqrt{R_a^2 + d^2} \end{cases} \tag{120}$$

$$z(\ell) = \begin{cases} 0, & 0 \leq \ell < R_a \\ -d\dfrac{\ell - R_a}{\sqrt{R_a^2 + d^2}}, & R_a \leq \ell \leq R_a + \sqrt{R_a^2 + d^2} \end{cases} \tag{121}$$

where R_a = 1 inch = 0.0254 meters is the radius of the aperture, and d = 1.75 inches = 0.04445 meters is the depth of the conical cavity. The domain of $\rho(\ell)$ and $z(\ell)$ is $0 \leq \ell \leq R_a + \sqrt{R_a^2 + d^2}$.

5.2 Measurements

A physical model of each BOR OCRED geometry described in Section 5.1 was created for the purpose of measuring its RCS at various frequencies, polarizations, and aspects. Each BOR OCRED model was machined out of a solid block of aluminum and mounted in a square, 1/16 inch thick aluminum plate. The models are shown in Figure 18. While the conductivity of aluminum is not infinite, it is sufficiently high to model the ideal perfectly conducting nature of the OCRED cavity surface and ground plane.

Measurement Process. Each OCRED model was then mounted in a test fixture, as shown in Figure 19. A metallic adapter was used to transition from the 7-inch square OCRED model to the 30-inch diameter hole in the test fixture. Metallized tape was used to ensure electrical continuity between the adapter and the OCRED model, and between the adapter and the test fixture. The test fixture had a large, flat surface which was metallized to simulate an infinite conducting ground plane. and was specially shaped to minimize its monostatic radar cross section.
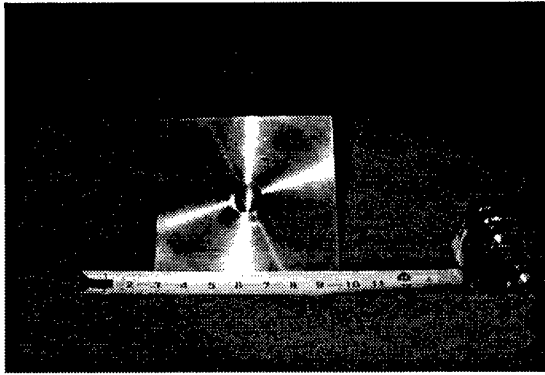
(a) Spherical OCRED model.
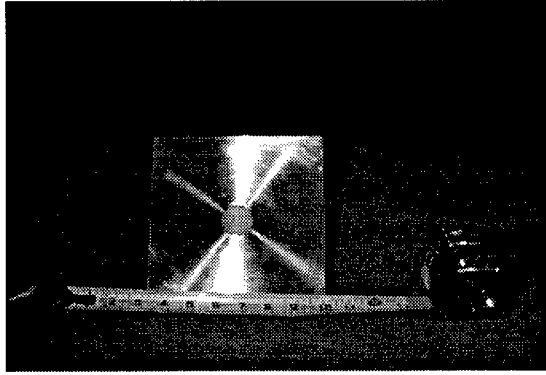
(b) Deep Cylindrical OCRED model.
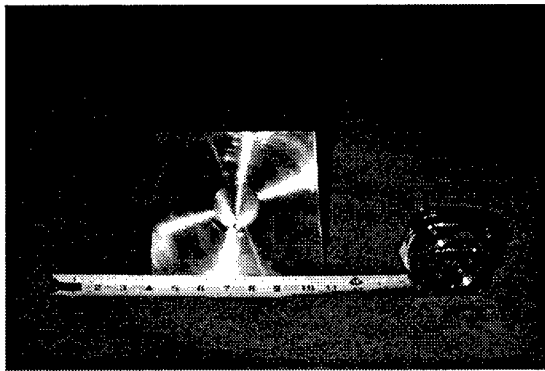
(c) Conical OCRED model.
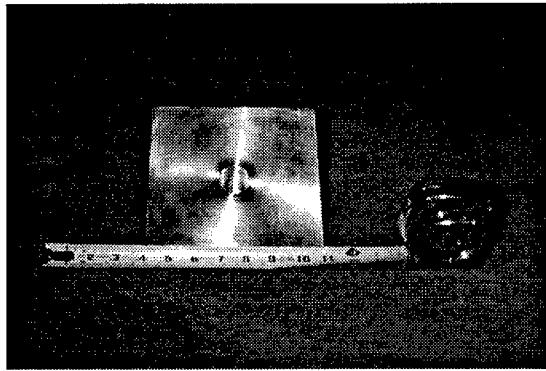
(d) Shallow Cylindrical OCRED model.

Figure 18   OCRED models.

The RCS of each OCRED model was measured in Wright Laboratory's Advanced Compact Range. Figure 20 shows the test fixture, with OCRED model installed, mounted on the target support pylon. The RCS of the OCRED model is measured using a coherent background subtraction technique [33]. This technique consists of measuring the far-zone scattered electric field under four separate configurations of the compact range. In the first configuration, the scattered electric field of the test fixture with the BOR OCRED model installed is measured ($E^{OCRED+TF}$); in the second configuration, the scattered electric field of the test fixture with the OCRED aperture replaced with a conductor is measured (E^{TF}); in the third configuration, the scattered electric field of a metal sphere is measured (E^{Sphere}); and in the fourth configuration, the scattered electric field

60

Figure 19   The test fixture with an OCRED model installed. The OCRED model is mounted in an adapter having a 30-inch diameter, which is in turn mounted in the test fixture. Metallic tape is used at the junctions to ensure electrical continuity.

Figure 20   The test fixture mounted on the support pylon in the Advanced Compact Range.
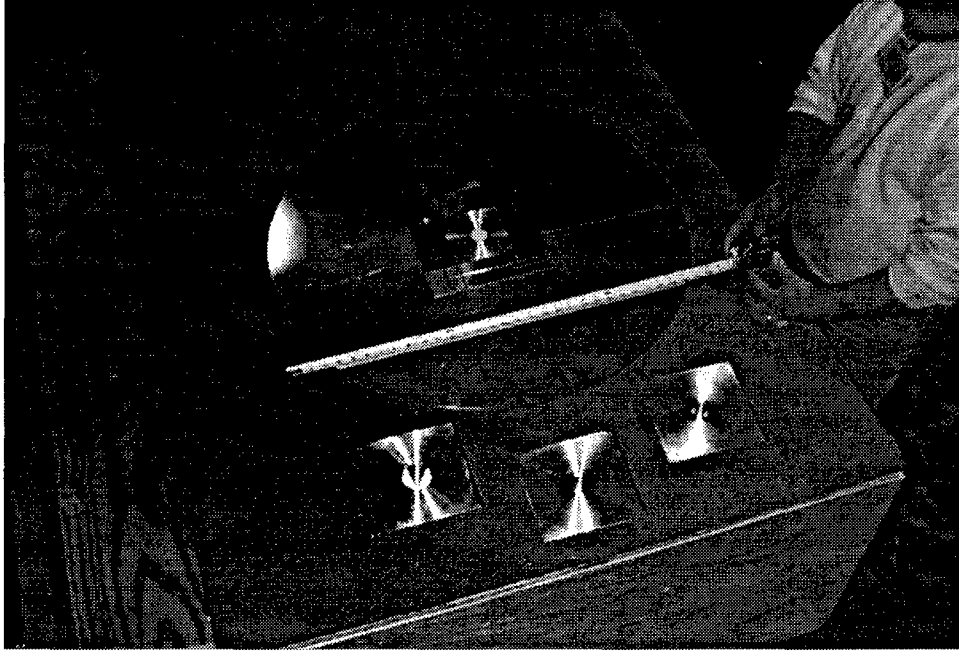
Figure 21   The adapter with one of the OCRED models installed. The other three models are shown in the foreground.

of the empty chamber is measured ($E^{\text{Empty Chamber}}$). Then the RCS of the OCRED is computed as

$$\sigma_{\text{OCRED}} = \left| \frac{E^{\text{OCRED+TF}} - E^{\text{TF}}}{E^{\text{Sphere}} - E^{\text{Empty Chamber}}} \right|^2 \sigma_{\text{Sphere}} \tag{122}$$

where σ_{Sphere} is the calculated RCS of the conducting sphere. The quantities in equation (122) are implicit functions of aspect angle, polarization, and frequency. The Advanced Compact Range measures these quantities to within 0.25 dB of their true values over the frequency range of 2-18 GHz. Neglecting the presence of noise in the receiver, this measurement technique is exact provided the OCRED and the test fixture do not interact, and its accuracy degrades as such interactions become more significant. The nature of this degradation is as follows.

Figure 22 illustrates how the background subtraction process works. E^{TF} and $E^{\text{OCRED+TF}}$ are the complex quantities (scattered electric fields) directly measured in the compact range, and their difference is $\tilde{E}^{\text{OCRED}}$. We would really like to measure $E^{\text{OCRED}} + E^{\text{TF}}$, so that we could find the true value $E^{\text{OCRED}} = (E^{\text{OCRED}} + E^{\text{TF}}) - E^{\text{TF}}$. $E^{\text{OCRED+TF}}$ differs from $E^{\text{OCRED}} + E^{\text{TF}}$ by an amount $E^{\text{interaction}}$, which is caused by the interactions between the test fixture and
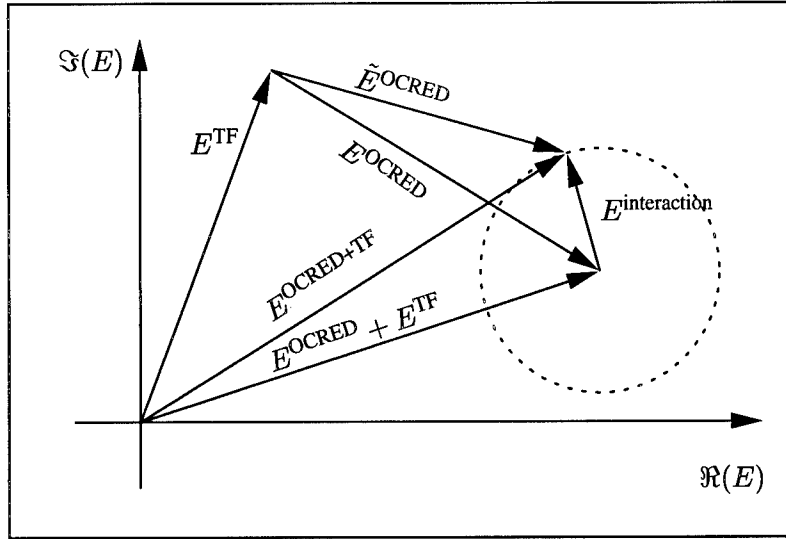
Figure 22   Complex (phasor) representation of the scattering from the OCRED model and the test fixture. E^{TF} is the scattered electric field from the test fixture; E^{OCRED} is the scattered electric field from the OCRED model; $E^{OCRED+TF}$ is the scattered electric field from the test fixture with the OCRED model installed; $E^{interaction}$ is the scattered electric field from the interactions between the test fixture and the OCRED model; and $\tilde{E}^{OCRED}$ is the difference between E^{TF} and $E^{OCRED+TF}$.

the OCRED model. It is generally not possible to directly measure the amplitude or phase of $E^{interaction}$. However, if $E^{interaction}$ is small relative to $E^{OCRED} + E^{TF}$, then $E^{OCRED} + E^{TF} \approx E^{OCRED+TF}$ and $\tilde{E}^{OCRED} \approx E^{OCRED}$. Generally, $E^{interaction}$ is largest near grazing incidence for parallel polarization.

A problem that can cause errors in the measurement of $\tilde{E}^{OCRED}$ occurs when E^{TF} is very much larger than E^{OCRED}. In this case, the calculation of $\tilde{E}^{OCRED} = E^{OCRED+TF} - E^{TF}$ becomes numerically sensitive, such that small uncertainties in measurement can produce large uncertainties in $\tilde{E}^{OCRED}$. Figure 23 shows the bounds on the uncertainty in calculating $\tilde{E}^{OCRED} = E^{OCRED+TF} - E^{TF}$ as a function of the relative magnitude of E^{OCRED} and E^{TF}. We see that even though E^{OCRED} and E^{TF} are measured to be within 0.25 dB of their true values, an uncertainty of 1.0 dB in $\tilde{E}^{OCRED}$ requires E^{TF} to be at least 3 dB below E^{OCRED}. This situation is encountered at near-normal incidence when scattering from the flat portion of the test fixture is very large.

5.2.1   The Spherical OCRED.   The first OCRED model to be considered is spherical in shape. Its generating arc is shown in Figure 17(a) and described in Section 5.1. Because the spherical OCRED bears a strong resemblance to a spherical cavity, we expect the frequency response of

63
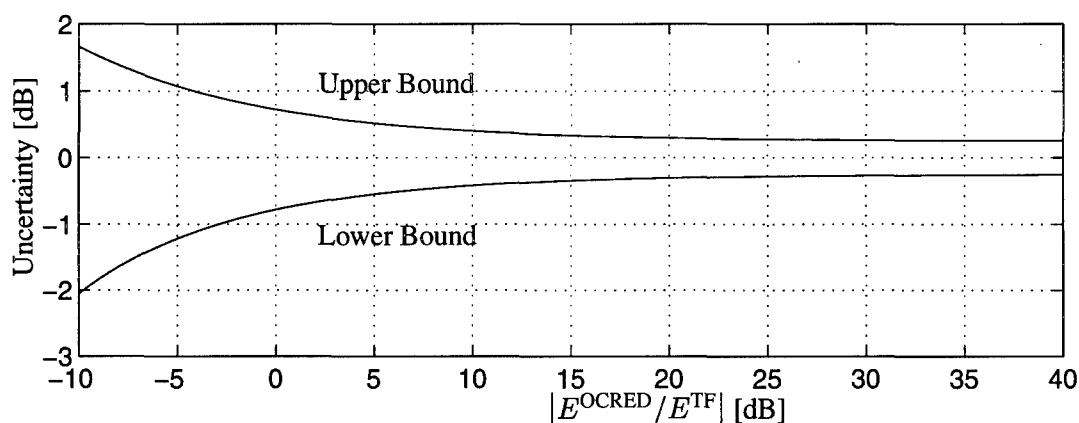
Figure 23   Uncertainty in estimating $\tilde{E}^{\mathrm{OCRED}}$ by $E^{\mathrm{OCRED+TF}} - E^{\mathrm{TF}}$. Uncertainty of $E^{\mathrm{OCRED+TF}}$ and E^{TF} is 0.25 dB.

the RCS of the spherical OCRED to exhibit singular behavior near the resonant frequencies of a spherical cavity of the same radius. Indeed, we can think of the spherical OCRED as a spherical cavity with an aperture that serves to reduce the Q (quality factor) of the cavity. Using a classical separation of variables approach, the lowest resonant frequencies of a spherical cavity having a 0.875 inch radius can be determined [21, page 271]. These frequencies, and their corresponding modes, are shown in Table 1. (The triply subscripted modes, e.g. TM$_{pqr}$, are defined by the rth zero of the spherical Bessel function (TE) or its derivative (TM) of order q, along with the associated Legendre function P_q^p.)

Table 1   Lowest resonant frequencies of a perfectly conducting spherical cavity with radius of 7/8 inch. Each resonant frequency is associated with multiple modes, each associated with a particular value of p, which is allowed to vary from 0 to the value of the second index.

Modes	TM$_{p11}$	TM$_{p21}$	TE$_{p11}$	TM$_{p31}$
Resonant Frequency [GHz]	5.89	8.31	9.65	10.7

The measured RCS of the spherical OCRED model is plotted in Figure 24. The RCS is plotted versus frequencies ranging from 2 to 18 GHz, for θ =30°, 45°, and 60° off normal and for parallel and perpendicular polarizations. Several features are evident. First, there is a pronounced null in the RCS near 6 GHz at all angles and polarizations. This null is likely associated with the resonant frequency of the TM$_{p11}$ mode of the spherical cavity (see Table 1). The null is shifted about 5% due to the effects of the aperture. (If the aperture were smaller, that is if α in Figure 17(a) were less than 45°, then we would expect the null to be shifted back toward the TM$_{p11}$ resonant

64
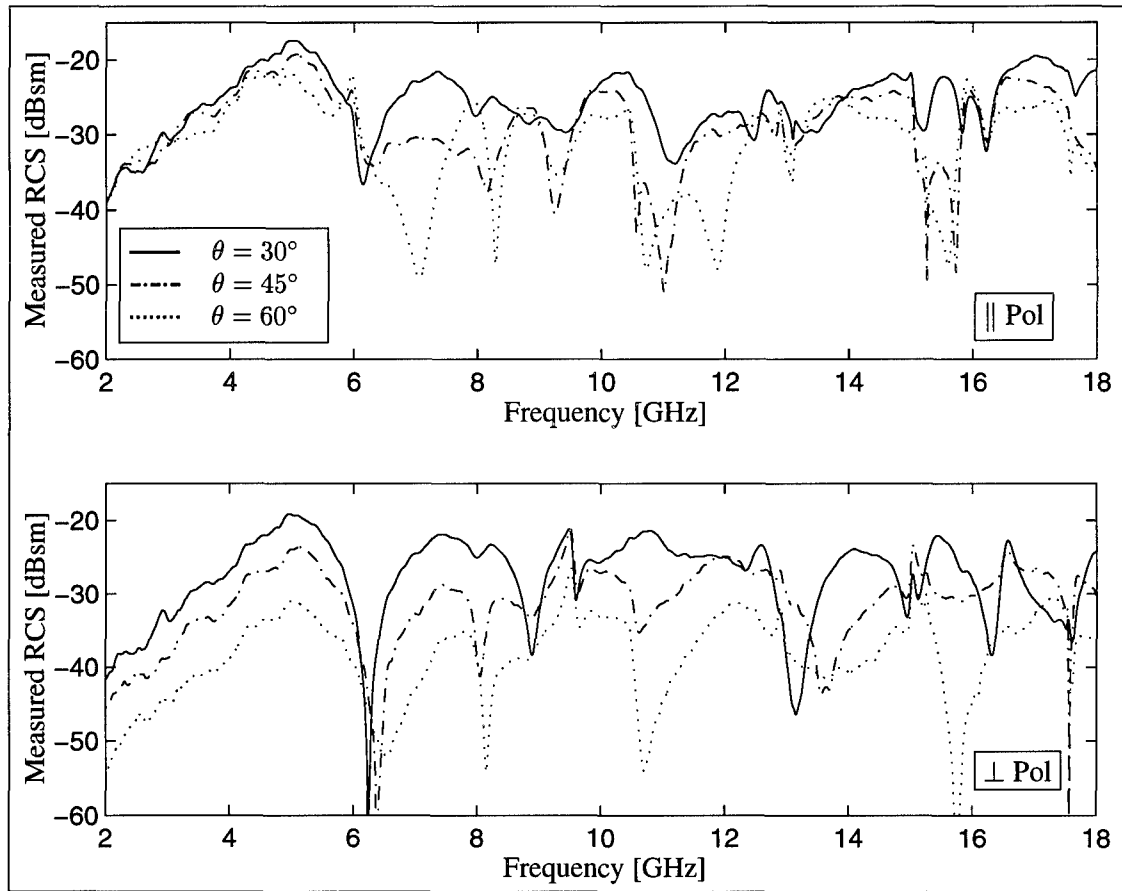
Figure 24   The measured RCS of the spherical OCRED model as a function of frequency.

frequency since the Q of the cavity would be higher). Second, at frequencies above 7 GHz, the RCS at different angles/polarizations appears to be uncorrelated. This behavior is indicative of complex interactions among the higher-order cavity modes which are excited differently with respect to angle and polarization. Third, at frequencies below 5 GHz, the RCS increases nearly monotonically for all angles/polarizations. In fact, it increases proportional to the square of the electrical area of the aperture. For example, if the frequency increases by a factor of 2, then the electrical area of the aperture quadruples and the the OCRED RCS increases by $20 \log 4 = 12$ dB. Indeed, this behavior agrees with Rayleigh scattering [33] in which RCS is proportional to the fourth power of the frequency.

From these observations, we conclude that the spherical OCRED RCS falls into one of three categories, depending on the frequency relative to the lowest resonant frequency f_{r0} of the corresponding spherical cavity. When the frequency is significantly below f_{r0}, then the OCRED

Table 2   Lowest cutoff frequencies of a perfectly conducting cylindrical waveguide with radius of 5/8 inch.

Modes	TE_{11}	TM_{01}	TE_{21}	TM_{11}
Cutoff Frequency [GHz]	5.54	7.23	9.19	11.5

behaves as a Rayleigh scatterer. When the frequency is near f_{r0}, the RCS exhibits a deep null that is nearly independent of angle and polarization. When the frequency is significantly above f_{r0}, multiple cavity modes are excited in the OCRED and they coherently combine to create an RCS that does not follow an easily predictable pattern.

5.2.2   The Deep Cylindrical OCRED.

The second OCRED model to be considered is cylindrical in shape. Its generating arc is shown in Figure 17(b) and described in Section 5.1. For the deep cylindrical cavity, the depth is $d = 3.0$ inches $= 0.0762$ meters. Because the cylindrical OCRED bears a strong resemblance to a cylindrical waveguide, we expect the frequency response of the RCS of the cylindrical OCRED to exhibit singular behavior near the cutoff frequencies of a cylindrical waveguide of the same radius. Using a classical separation of variables approach, the lowest cutoff frequencies of a cylindrical waveguide having a 0.625 inch radius can be determined [21]. These frequencies, and their corresponding modes, are shown in Table 2. The measured RCS of the deep cylindrical OCRED model is plotted in Figure 25. The RCS is plotted versus frequencies ranging from 2 to 18 GHz, for $\theta = 30°$, $45°$, and $60°$ off normal and for parallel and perpendicular polarizations. Several features are evident. First, there are pronounced nulls in the RCS near 5.9 and 6.9 GHz at all angles and polarizations. These nulls are associated with the group velocities of the lowest-order mode of the equivalent cylindrical waveguide (see Table 2), and will be discussed in more detail in Section 5.3.1. Second, at frequencies well above 8 GHz, the RCS at different angles/polarizations appears to be uncorrelated. This behavior is indicative of complex coherent interference among the higher-order waveguide modes which are excited differently with respect to angle and polarization. Third, at frequencies below 5 GHz, the RCS increases nearly monotonically for all angles/polarizations, again displaying the Rayleigh scattering behavior seen with the spherical OCRED.

From these observations, we conclude that the deep cylindrical OCRED RCS falls into one of three categories, depending on the frequency relative to the lowest cutoff frequency f_{c0} of the

66
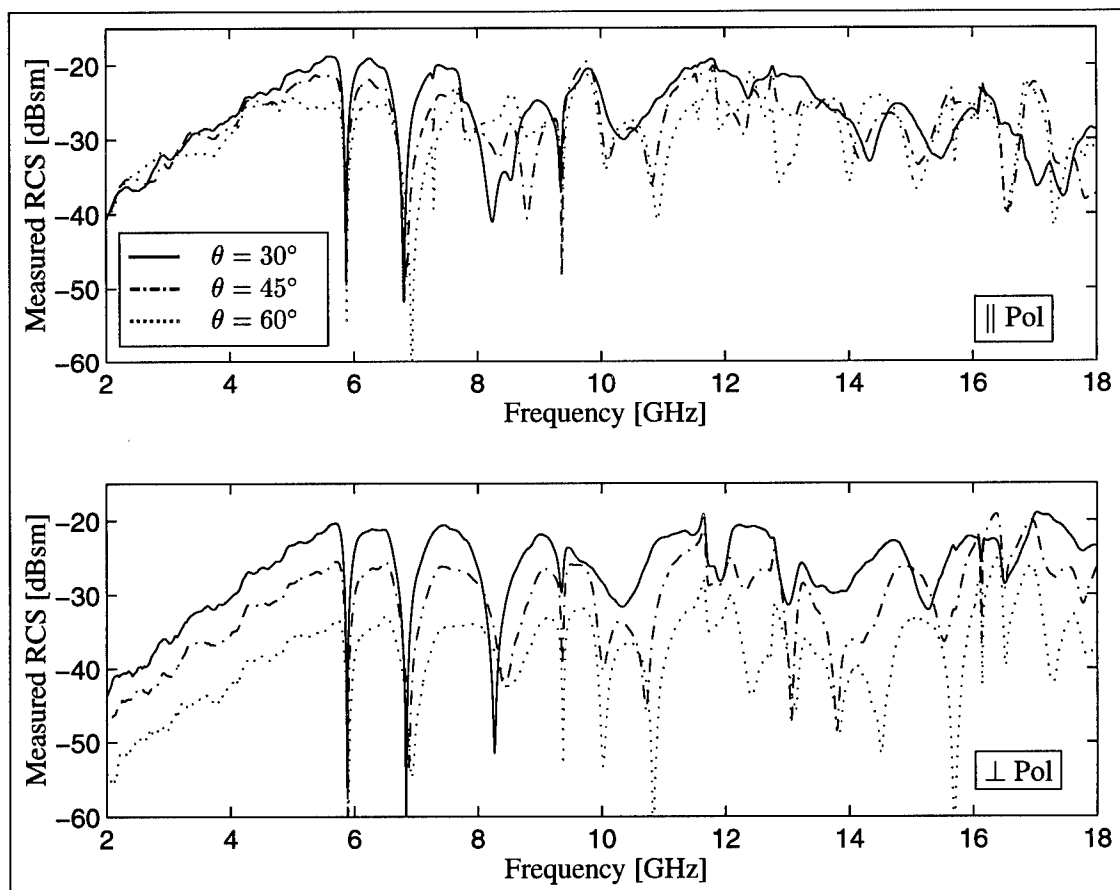
Figure 25   The measured RCS of the deep cylindrical OCRED model as a function of frequency.

corresponding cylindrical waveguide. When the frequency is significantly below f_{c0}, the OCRED behaves as a Rayleigh scatterer. When the frequency is near f_{c0}, the RCS exhibits deep nulls near the cutoff frequencies of the lowest-order cylindrical waveguide modes. These nulls are nearly independent of angle and polarization. When the frequency is significantly above f_{c0}, multiple waveguide modes propagate in the OCRED and coherently combine to create an RCS that does not follow an easily predictable pattern.

5.2.3   The Conical OCRED.

The third OCRED model to be considered is conical in shape. Its generating arc is shown in Figure 17(c) and described in Section 5.1. The measured RCS of the shallow cylindrical OCRED model is plotted in Figure 26. The RCS is plotted versus frequencies ranging from 2 to 18 GHz, for $\theta =30°$, $45°$, and $60°$ off normal and for parallel and perpendicular polarizations. Unlike the previous OCRED geometries, the RCS of the conical
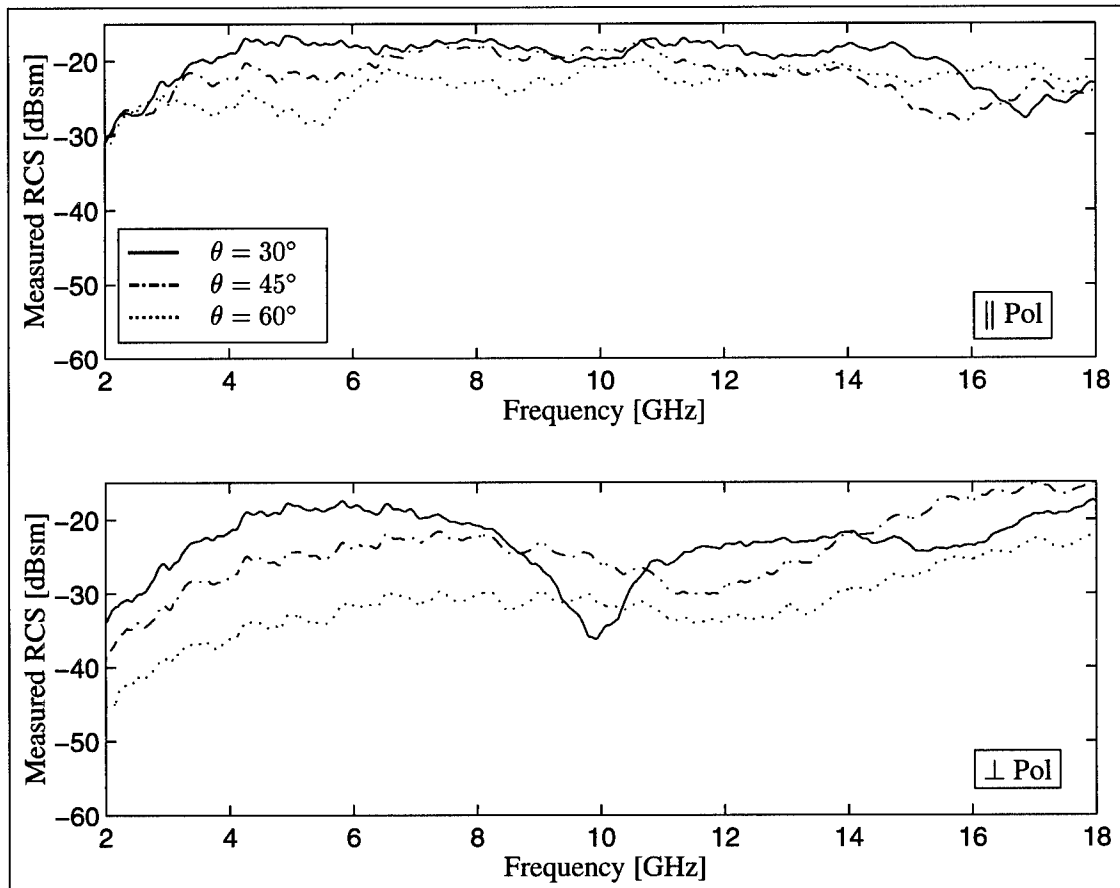
Figure 26   The measured RCS of the conical OCRED model as a function of frequency.

OCRED does not have any pronounced nulls. In the parallel polarization, the RCS of the conical OCRED is remarkably flat, staying within 5 dB of -22 dBsm over nearly all the 2-18 GHz bandwidth. In the perpendicular polarization, the RCS for θ =45° and θ =60° off normal appear smooth and well correlated, while the RCS for θ =30° exhibits a null near 10 GHz. This null is likely caused by the destructive interference between the scattering from the near and far edges of the aperture.

5.2.4   The Shallow Cylindrical OCRED.   The fourth OCRED model to be considered is cylindrical in shape. This OCRED model is the same as the second one, discussed in Section 5.2.2, except the depth is changed to d = 1.5 inches = 0.0381 meters. Like the deep cylindrical OCRED, we expect the frequency response of the RCS of the shallow cylindrical OCRED to exhibit singular

68

behavior near the cutoff frequencies of a cylindrical waveguide of the same radius. These cutoff frequencies are shown in Table 2.
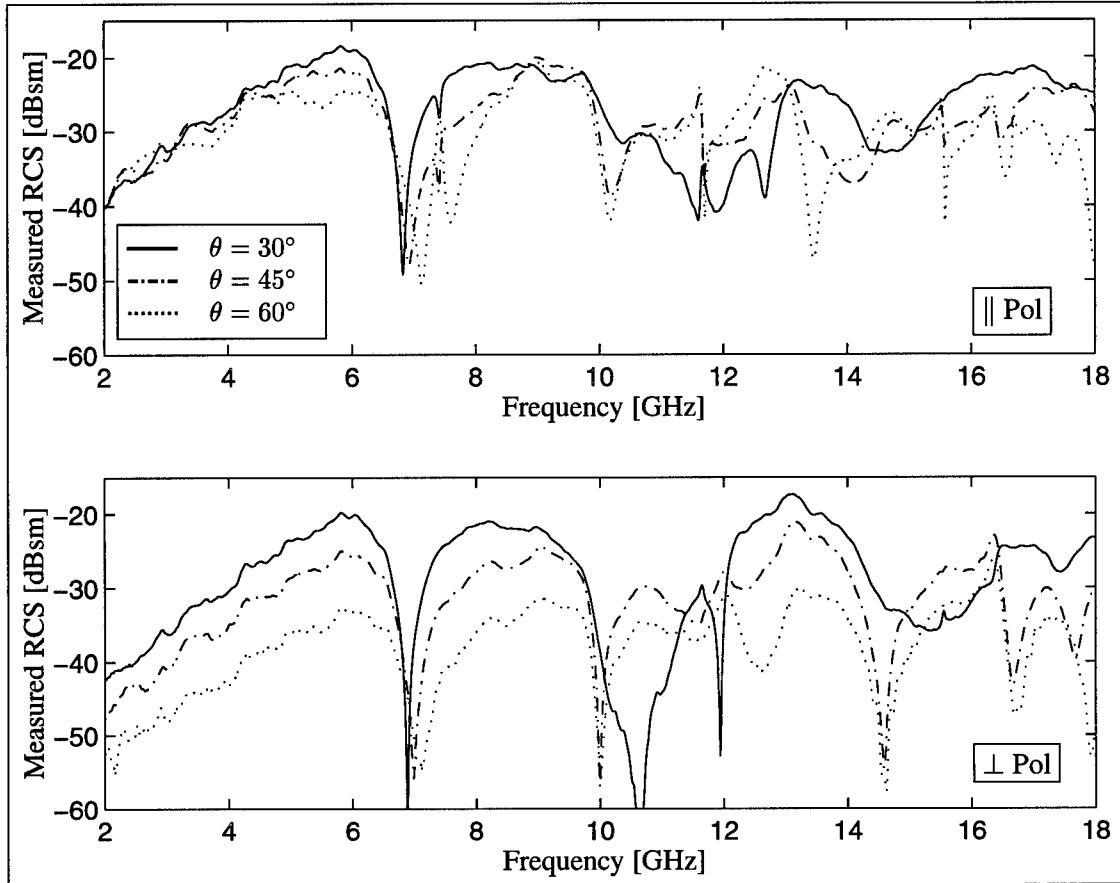
Figure 27   The measured RCS of the shallow cylindrical OCRED model as a function of frequency.

The measured RCS of the shallow cylindrical OCRED model is plotted in Figure 27. The RCS is plotted versus frequencies ranging from 2 to 18 GHz, for θ =30°, 45°, and 60° off normal and for parallel and perpendicular polarizations. We see the similar features as those for the deep cylindrical OCRED, except that the null at approximately 5.9 GHz is absent. It will become clear in Section 5.3.3 why this null is not present, and we shall further learn that the location of the null is a function of cylindrical cavity depth d.

69

5.3 Calculations – RCS

The computer program implementing the numerical algorithm described in Chapter IV was run on the four BOR OCRED geometries described in Section 5.1. Since the algorithm is a frequency-domain one, each computer run generated data for a single frequency, so generating RCS versus frequency plots like those shown in Section 5.2 is impractical. Instead, calculations for each geometry were made at several judiciously chosen frequencies, and the results compared to measurements. In all cases, the moment method solution is calculated using 20 segments per free-space wavelength.

5.3.1 The Spherical OCRED.

The spherical OCRED poses a special challenge in that its generating arc is curved, but the computer program was written to handle only piecewise linear generating arcs. Thus, the curved part of the generating arc has been replaced by a piecewise linear approximation, as shown in Figure 28. Through numerical experiments, it was found that an eleven-segment piecewise linear approximation was adequate for the highest frequency tested (10 GHz), though more segments might be necessary at higher frequencies.
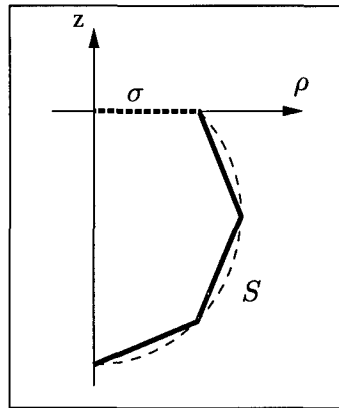
Figure 28   A piecewise linear approximation to the generating arc for the spherical OCRED. As shown, the curved part of the generating arc is approximated by three line segments. In the calculations, eleven line segments are used.

Figure 29 shows the resultant calculated RCS for the spherical OCRED as a function of angle from normal at three discrete frequencies. The corresponding measured RCS values are plotted as well, and good agreement is observed between calculations and measurements at each frequency. The three frequencies chosen are 4, 6.25, and 10 GHz. 4 GHz was chosen because the

70

spherical OCRED behaves as a Rayleigh scatterer at that frequency. 6.25 GHz was chosen because measurements show that the RCS of the spherical OCRED has a null near there (see Figure 24), which implies that the spherical OCRED is near resonance at 6.25 GHz. This is a challenging frequency for the calculations. 10 GHz was chosen to test the accuracy of the moment method program with an electrically large problem.

As can be seen in Figure 29, the measured and calculated values agree quite well at each frequency and polarization. Measured data only exists for angles from $\theta = 30°$ to $\theta = 90°$ from normal. Measured data was not taken at normal or near-normal aspects. (The background-subtraction measurement technique significantly degrades there due to the excessively large physical optics return from the test fixture.) The RCS at 4 GHz is nearly constant with θ in parallel polarization, but falls off rapidly with θ in perpendicular polarization, a direct result of the $\cos\theta$ factors appearing in the incident field, equation (110), and the radiation, equation (39). At 6.25 GHz, the deep null in perpendicular polarization is evident, although it is interesting how narrow in θ it is. The calculations show that the RCS at the two polarizations converge as $\theta \to 0$, as expected. The measured data is significantly corrupted near grazing aspects due to significant interactions between the OCRED and the edges of the test fixture. As expected, this corruption is most evident in parallel polarization and decreases as frequency increases.

Figures 30 and 31 show the measured and calculated RCS of the spherical OCRED as a function of frequency and angle for parallel and perpendicular polarizations, respectively. The frequency varies from 5.9 to 6.5 GHz while the angle varies from 30° to 85° from normal. The deep null in parallel polarization is clearly evident (see Figure 24), and we note that the location of the null in angle varies with frequency. The measured data exhibits contamination near grazing incidence, especially in parallel polarization, as discussed in Section 5.2. This contamination "ripples" with frequency, which is to be expected since the electrical distance between the OCRED model and the edge of the test fixture varies with frequency.

5.3.2 The Deep Cylindrical OCRED. The generating arc (see Figure 17(b)) for the deep cylindrical OCRED is piecewise linear, and thus can be modeled exactly by the computer program. Figure 32 shows the resultant calculated RCS for the deep cylindrical OCRED as a function of angle from normal at four discrete frequencies. The corresponding measured RCS

71

Figure 29   The RCS of the spherical OCRED as a function of aspect angle θ at three discrete frequencies.

values are plotted as well, and good agreement is observed between calculations and measurements at each frequency. The four frequencies chosen are 4, 5.9, 6.9 and 10 GHz. 4 GHz was chosen because the deep cylindrical OCRED behaves as a Rayleigh scatterer at that frequency. 5.9 and 6.9 GHz were chosen because measurements show that the RCS of the deep cylindrical OCRED has nulls near those frequencies (see Figure 25), which implies that the deep cylindrical OCRED is near resonance there. These are challenging frequencies for the calculations since the RCS is very sensitive to the frequency of the incident field. 10 GHz was chosen to test the accuracy of the moment method program with an electrically large problem in which multiple waveguide modes are expected to propagate in the cavity.

As can be seen in Figure 32, the measured and calculated values agree quite well at each frequency and polarization. Measured data only exists for angles from $\theta = 30°$ to $\theta = 90°$ from normal. Measured data was not taken at normal or near-normal aspects. At 4 GHz, the RCS is nearly flat for parallel polarization and decays as $\cos^2 \theta$ for perpendicular polarization. At 5.9

72
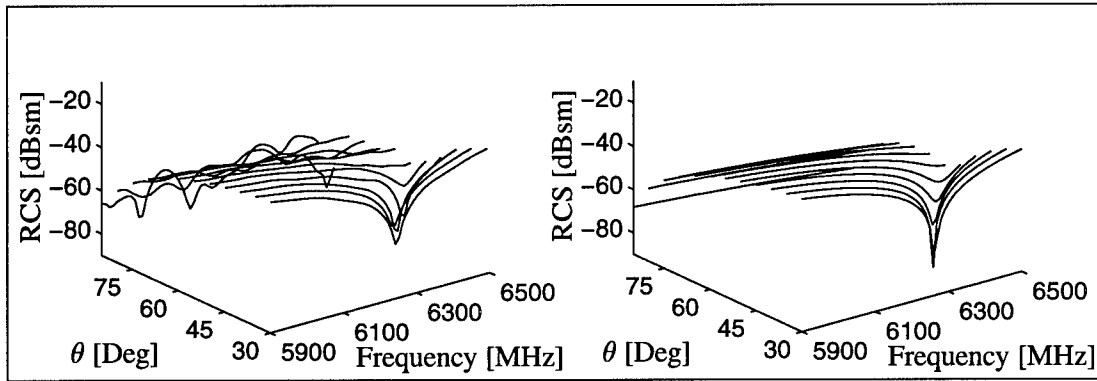
Figure 30 RCS versus angle from normal and frequency for the spherical OCRED for parallel polarization. Measured RCS plotted on left, calculated RCS plotted on right.
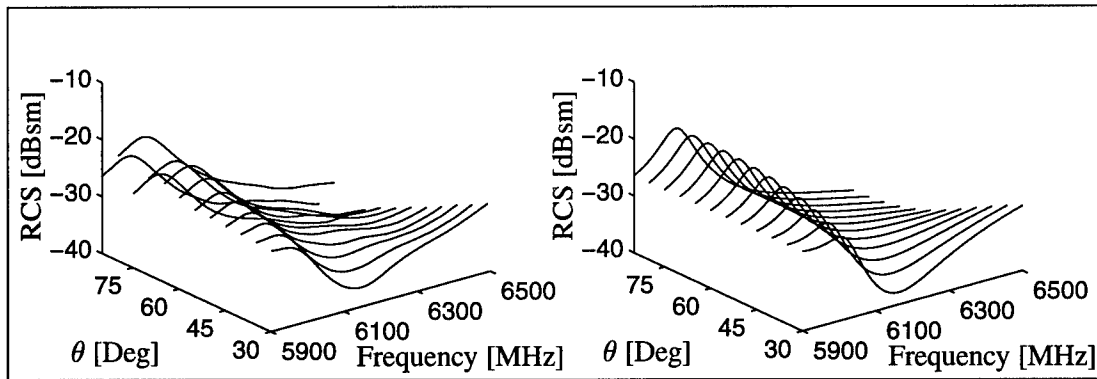
Figure 31 RCS versus angle from normal and frequency for the spherical OCRED for perpendicular polarization. Measured RCS plotted on left, calculated RCS plotted on right.

GHz, both polarizations decay more rapidly with θ than at 4 GHz. At 6.9 GHz, a null appears at $\theta = 55°$ in parallel polarization. At 10 GHz, the roll-off of RCS with θ is nearly monotonic. As was the case for the spherical OCRED, the measured data is significantly corrupted near grazing aspects due to significant interactions between the cavity and the edges of the test fixture, and this corruption is most evident in parallel polarization and decreases as frequency increases.

5.3.3 The Conical OCRED.   The generating arc for the conical OCRED (see Figure 17(c)) is piecewise linear, and thus can be modeled exactly by the computer program. Figure 33 shows the resultant calculated RCS for the conical OCRED as a function of angle from normal at two discrete frequencies. The corresponding measured RCS values are plotted as well, and good agreement is observed between calculations and measurements at each frequency. The two frequencies chosen are 4 and 10 GHz. 4 GHz was chosen to maintain consistency with the

73
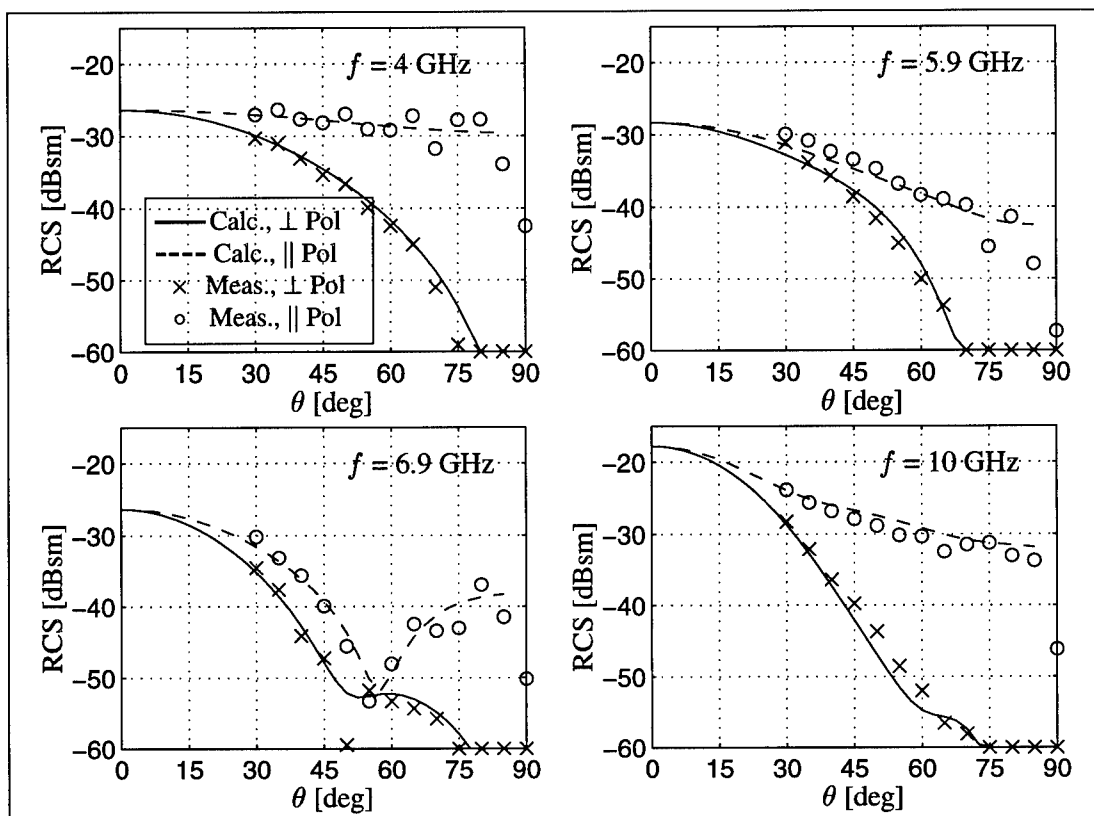
Figure 32   The RCS of the deep cylindrical OCRED as a function of aspect angle θ at four discrete frequencies.

other OCRED geometries. 10 GHz was chosen to test the accuracy of the moment method program with an electrically large problem in which significant field penetration into the cavity is expected.

As can be seen in Figure 33, the measured and calculated values agree quite well at each frequency and polarization. Measured data only exists for angles from θ =30° to θ =90° from normal. Measured data was not taken at normal or near-normal aspects. At 4 GHz, the $\cos^2 \theta$ dependence is evident at perpendicular polarization. The RCS at normal incidence is higher than for the spherical or deep cylindrical OCREDs due to the larger aperture of the conical OCRED. At 10 GHz, there is a fairly pronounced null at 32.5° in perpendicular polarization, indicating possible destructive coherent scattering from the rim and wall of the cavity. As with previous geometries, the measured data is significantly corrupted near grazing aspects due to significant interactions between the OCRED and the edges of the test fixture, and this corruption is most evident in parallel polarization and decreases as frequency increases.

74
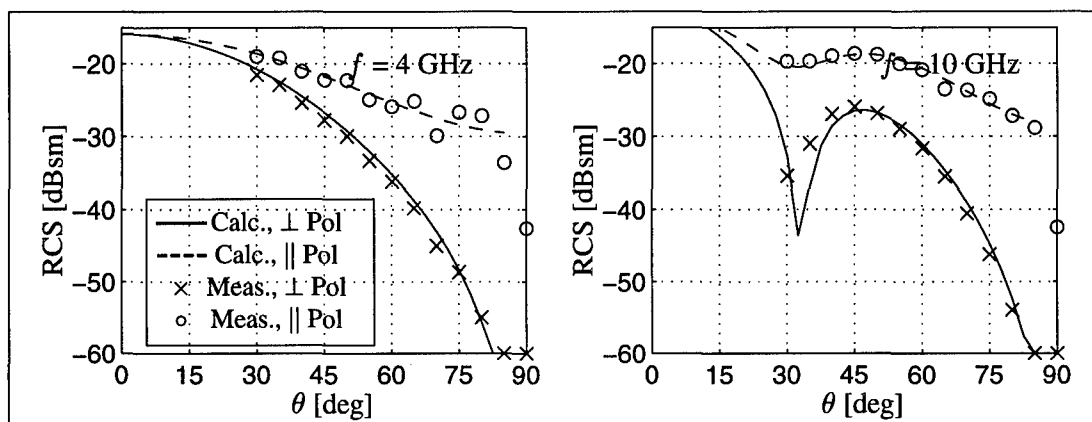
Figure 33   The RCS of the conical OCRED as a function of aspect angle θ at two discrete frequencies.

5.3.4   The Shallow Cylindrical OCRED.

The generating arc for the shallow cylindrical OCRED (see Figure 17(b)) is piecewise linear, and thus can be modeled exactly by the computer program. Figure 34 shows the resultant calculated RCS for the shallow cylindrical OCRED as a function of angle from normal at four discrete fre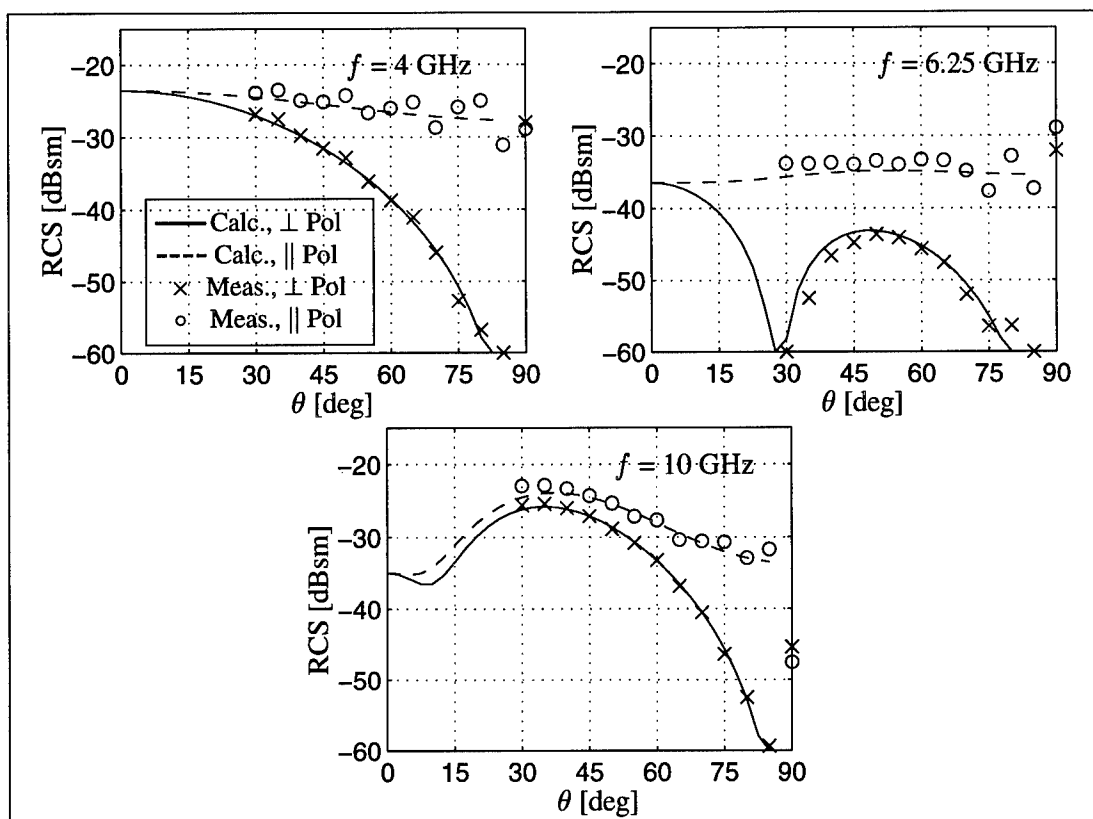quencies. The corresponding measured RCS values are plotted as well, and good agreement is observed between calculations and measurements at each frequency. The four frequencies chosen are 4, 5.9, 6.9 and 10 GHz. 4 GHz was chosen because the shallow cylindrical OCRED behaves as a Rayleigh scatterer at that frequency. 6.9 GHz was chosen because measurements show that the RCS of the shallow cylindrical OCRED has a null near that frequency (see Figure 27), which implies that the shallow cylindrical OCRED is near resonance there. This is a challenging frequency for the calculations. 5.9 GHz was chosen as a comparison with the deep cylindrical OCRED. As noted previously, the deep cylindrical OCRED RCS has a null at 5.9 GHz that is curiously absent in the shallow cylindrical OCRED's RCS. 10 GHz was chosen to test the accuracy of the moment method program with an electrically large problem.

As can be seen in Figure 34, the measured and calculated values agree quite well at each frequency and polarization. Measured data only exists for angles from θ =30° to θ =90° from normal. Measured data was not taken at normal or near-normal aspects. At 4 GHz, the RCS of the shallow cylindrical OCRED is almost identical to that of the deep cylindrical OCRED, suggesting the RCS is independent of cavity depth at that frequency. At 5.9 GHz, the RCS has nearly the same shape as for the deep cylindrical OCRED but is nearly 12 dB higher. At 6.9 GHz, the RCS has
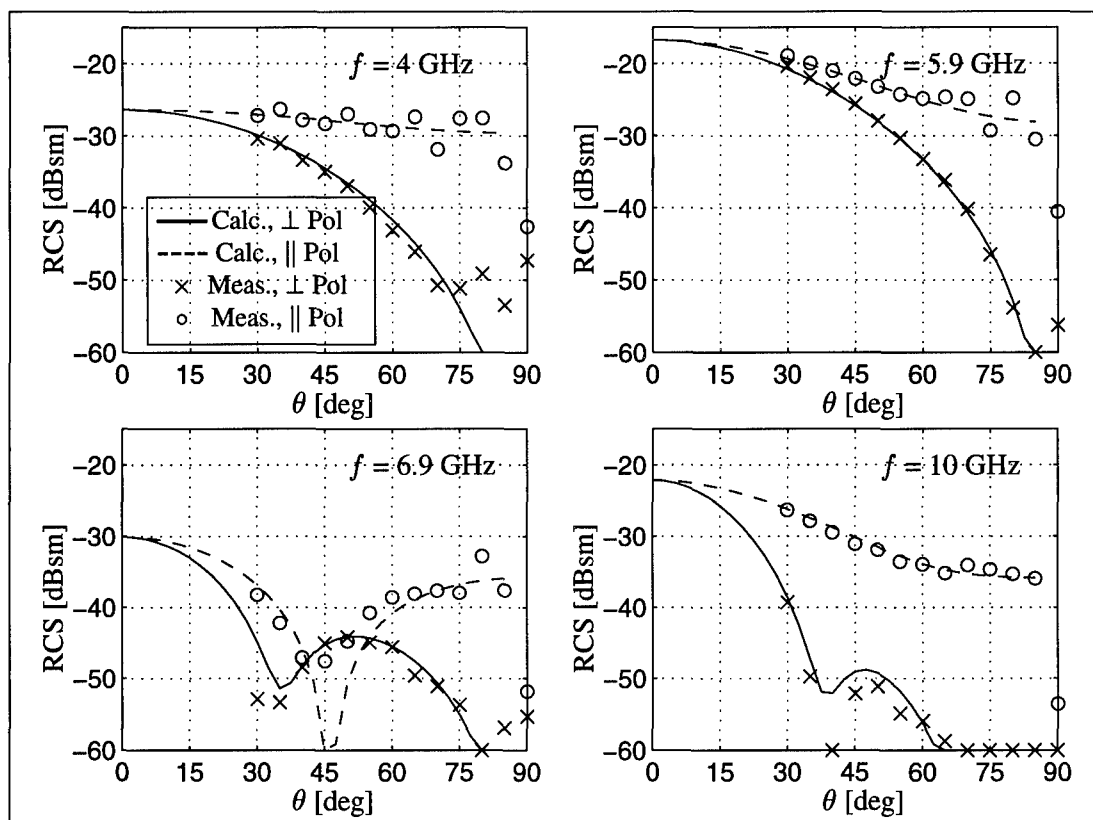
Figure 34   The RCS of the shallow cylindrical OCRED as a function of aspect angle θ at four discrete frequencies.

nulls in both polarizations, but at slightly different angles. At 10 GHz, the RCS rolls off gently in parallel polarization, and has a null in perpendicular polarization.

5.4   Calculations – Other Attributes

In Section 5.3, the ability of the numerical algorithm to accurately model the radar cross section of several BOR OCRED geometries was validated against measurements. However, the RCS is a derived quantity inasmuch as it depends on the electric current density on the cavity surface. Therefore it is prudent to evaluate the quality of the (approximate) electric current density, which is the direct product of the numerical algorithm. Since we have no way to measure the electric current density, we will instead check that the numerical algorithm produces electric current densities $\vec{J}_\sigma$ and $\vec{J}_S$ that satisfy our *a priori* knowledge of those quantities. We will also evaluate the numerical

stability of the moment method matrices used to find $\vec{J}_\sigma$ and $\vec{J}_S$, and investigate which Fourier modes must be included in the solution to produce accurate RCS data.

5.4.1 The Electric Current Density. The electric current density $\vec{J}(\vec{r})$, $\vec{r} \in \sigma \cup S$, will exhibit certain properties. As noted in Chapter III, to satisfy Meixner's edge condition at the aperture rim, the $\hat{\ell}$ component of $\vec{J}(\vec{r})$ must be continuous and bounded as $\vec{r}$ crosses from σ to S, and the $\hat{\phi}$ component of $\vec{J}(\vec{r})$ must be discontinuous and unbounded as $\vec{r}$ crosses from σ to S. At points away from the rim, we expect $\vec{J}(\vec{r})$ to be a smooth function of position.

The electric current density near the center of the aperture is a continuous function of position there, and so can be expressed in a Taylor series about the center as

$$\begin{aligned} \vec{J}(\vec{r}) &= \vec{J}(0) + \mathcal{O}(|\vec{r}|) \\ &= \hat{x}J_x(0) + \hat{y}J_y(0) + \mathcal{O}(|\vec{r}|) \qquad \text{for } |\vec{r}| \to 0 \end{aligned} \tag{123}$$

However, on the portion of the aperture associated with the portion of the generating arc between ℓ_0 and ℓ_1, the current density is expressed as (see equation (47))

$$\begin{aligned} \vec{J}(\vec{r}) &= \sum_{m=-M}^{M} \left[B_{m1}^\ell\, \hat{\ell} + B_{m1}^\phi\, \hat{\phi} \right] e^{jm\phi} \\ &= \sum_{m=-M}^{M} \left\{ \hat{x} \left[B_{m1}^\ell\, \cos\phi - B_{m1}^\phi\, \sin\phi \right] e^{jm\phi} \right. \\ &\qquad \left. \hat{y} \left[B_{m1}^\ell\, \sin\phi - B_{m1}^\phi\, \cos\phi \right] e^{jm\phi} \right\} \qquad \text{for } |\vec{r}| < \ell_1 \end{aligned} \tag{124}$$

Equating equations (123) and (124), we find that B_{m1}^ℓ and B_{m1}^ϕ vanish for $|m| \neq 1$ and that

$$B_{m1}^\ell = jB_{m1}^\phi \qquad \text{for } m = -1 \tag{125a}$$

$$B_{m1}^\ell = -jB_{m1}^\phi \qquad \text{for } m = 1 \tag{125b}$$

These relations are consistent with the symmetry relations of Section 4.6, equation (113). Another way of stating this is that only the first-order Fourier modes do not identically vanish at $\ell = 0$. Using an identical analysis as above near the bottom of the OCRED cavity, we find that only the first-order Fourier modes of $\vec{J}$ do not identically vanish at $\ell = L$.

In the rest of this section, we examine the electric current density as a function of the arc length variable ℓ. We define

$$J_\ell(\ell) = \int_0^{2\pi} \left[\vec{\mathbf{J}}(\ell, \phi) \cdot \hat{\ell} \right] e^{-\jmath m\phi} \, d\phi \tag{126}$$

$$J_\phi(\ell) = \int_0^{2\pi} \left[\vec{\mathbf{J}}(\ell, \phi) \cdot \hat{\phi} \right] e^{-\jmath m\phi} \, d\phi \tag{127}$$

to be the mth Fourier components of the $\hat{\ell}$-directed and $\hat{\phi}$-directed electric current density $\vec{\mathbf{J}}$, respectively.

Figure 35   The electric current density plotted as a function of arc length ℓ for the spherical OCRED: $f = 4$ GHz, $\theta = 30°$. The aperture rim corresponds to $\ell = 1.59$ cm.

The Spherical OCRED. At a frequency of 4 GHz, the spherical OCRED behaves as a Rayleigh scatterer, as can be seen from Figure 24. A characteristic of a Rayleigh scatterer is that its

Figure 36   The electric current density plotted as a function of arc length ℓ for the spherical OCRED: $f = 4$ GHz, $\theta = 60°$, and $m = 1$. The aperture rim corresponds to $\ell = 1.59$ cm.

scattering cross section varies sharply with respect to its electrical size, but not with respect to its shape. This implies that electromagnetic fields inside the cavity are small. This is further suggested by the fact that the frequency is below the lowest resonant frequency of the corresponding closed spherical cavity (see Table 1). Figure 35 shows the magnitude of the electric current density on ∂D for $\theta = 30°$ and Fourier modes m=0, 1, 2, and 3. This shows that all Fourier components of the electric current density are largest near the rim and rapidly decay for $\ell > \ell_{N_a}$. As expected, only the $m = 1$ Fourier component has a non-zero value at $\ell = 0$. Figure 36 shows the magnitude and phase of J_ℓ and J_ϕ for $\theta = 60°$ and $m = 1$. Here we see that J_ℓ is bounded and continuous near $\ell = \ell_{N_a}$. In contrast, the magnitude of J_ϕ peaks strongly near $\ell = \ell_{N_a}$ while the phase of J_ϕ exhibits a 180° phase shift there. This behavior is entirely consistent with the edge condition at the aperture rim.

At 6.25 GHz, the frequency is above the resonant frequency of the lowest-order mode of the corresponding closed spherical cavity. Furthermore, as shown in Figure 24, the spherical OC-RED no longer behaves as a Rayleigh scatterer at 6.25 GHz. This suggests that the fields should significantly penetrate the cavity interior. Figure 37 shows the magnitude of the electric current density components for $\theta = 30°$ and m=0, 1, 2, and 3. The m=0 and m=1 components show that there is indeed significant field penetration into the OCRED interior. However, the m=2 and m=3 (and higher) components do not significantly penetrate the cavity interior, indicating that only the low-order Fourier modes are excited at this frequency. We also see that the necessary conditions

79

Figure 37   The electric current density plotted as a function of arc length ℓ for the spherical OCRED: $f = 6.25$ GHz, $\theta = 30°$. The aperture rim corresponds to $\ell = 1.59$ cm.

are satisfied at $\ell = 0$, $\ell = \ell_{N_a}$, and $\ell = L$. That is, only the $m=1$ Fourier component is non-zero at the aperture center and cavity bottom, and the J_ℓ and J_ϕ components satisfy the edge condition at the aperture rim. Figure 38 shows the magnitude and phase of J_ℓ and J_ϕ for $\theta = 60°$ and $m = 1$. The magnitude and phase of J_ℓ are continuous and bounded at $\ell = \ell_{N_a}$, while the magnitude of J_ϕ is unbounded and the phase of J_ϕ is discontinuous there. Also, note the null and $180°$ phase shift of J_ℓ at $\ell \approx 3.6$ cm; this is suggestive of a standing wave pattern caused by the interference between two spherical cavity modes. This phenomenon is especially likely because there are multiple modes that resonate at f_{r0}, as shown in Table 1. Another interesting feature is the "scalloping" evident in the plot of J_ϕ. This is caused by the eleven-segment piecewise linear approximation to the curved portion of the spherical OCRED generating arc.
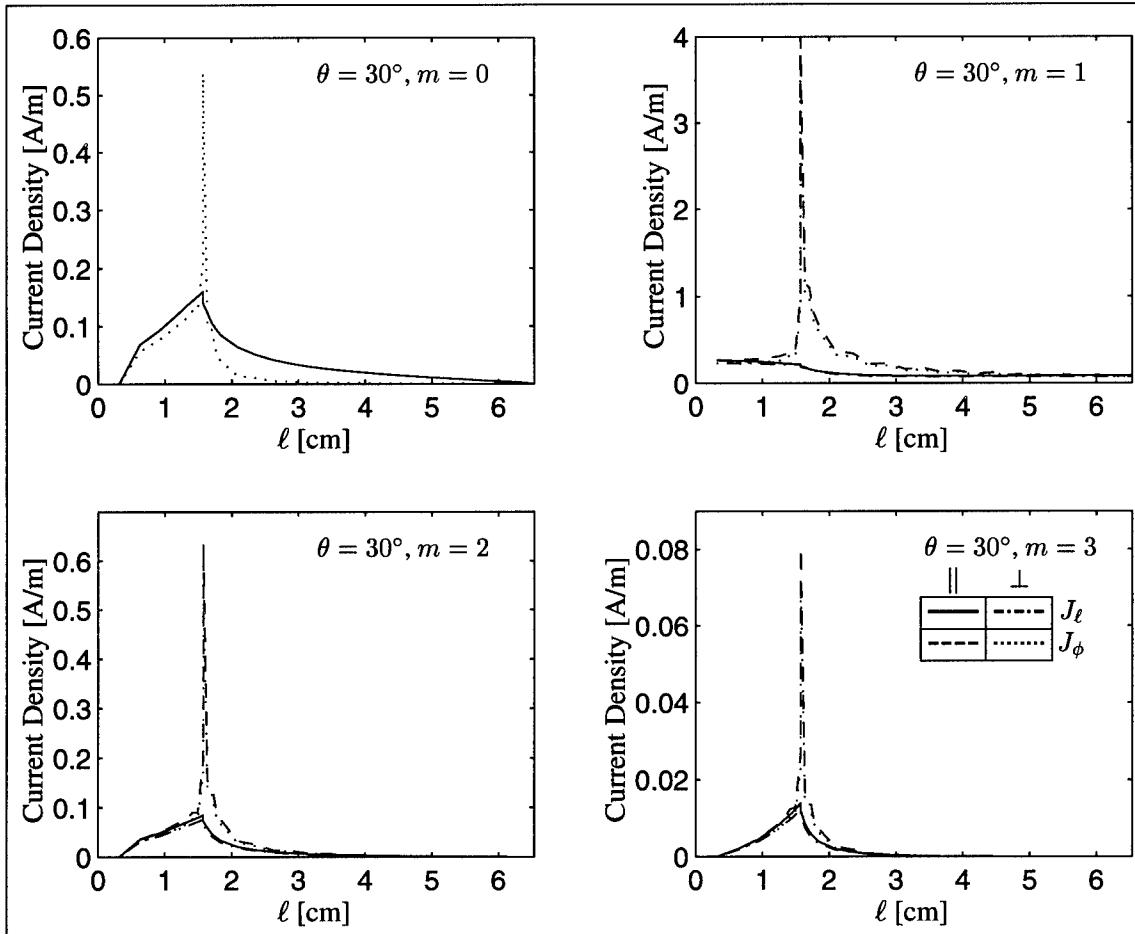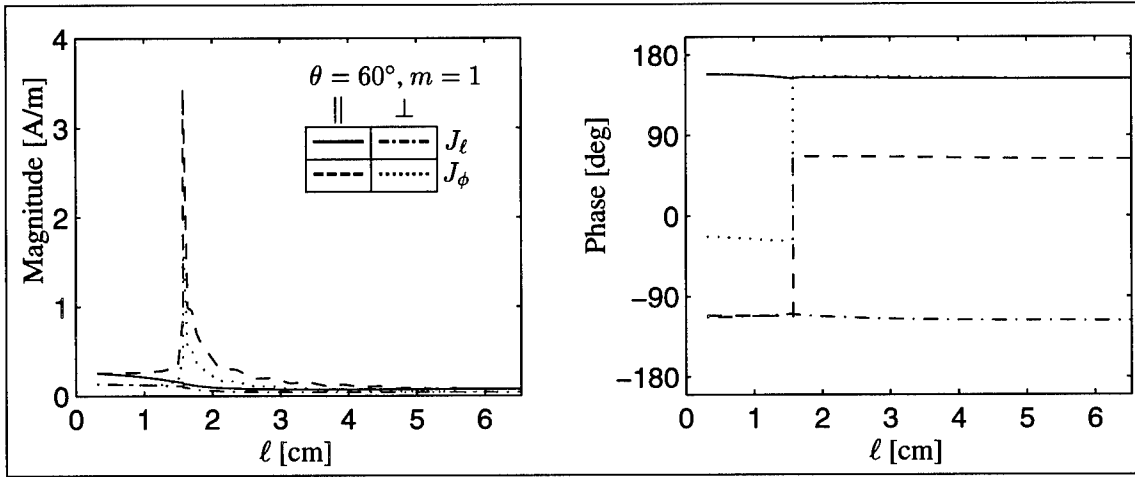
Figure 38   The electric current density plotted as a function of arc length ℓ for the spherical OCRED: $f = 6.25$ GHz, $\theta = 60°$, and $m = 1$. The aperture rim corresponds to $\ell = 1.59$ cm.

At 10 GHz, the frequency is above the resonant frequency of the three lowest-order modes of the corresponding closed spherical cavity (see Table 1). We expect to see a more complex field distribution in the spherical OCRED than was evident at 6.25 GHz when only one cavity mode was active. Figure 39 shows the magnitude of the electric current density components for $\theta = 30°$ and m=0, 1, 2, and 3. The m=0, 1, and 2 Fourier components penetrate the cavity interior, but the m=3 component does not. As was the case at 6.25 GHz, all the necessary conditions are satisfied at $\ell = 0$, $\ell = \ell_{N_a}$, and $\ell = L$. Figure 40 shows the magnitude and phase of J_ℓ and J_ϕ for $\theta = 60°$ and $m = 1$. The magnitude and phase of J_ℓ are continuous and bounded at $\ell = \ell_{N_a}$. We expect J_ϕ to be unbounded at $\ell = \ell_{N_a}$, and, indeed, for perpendicular polarization it is, but not for parallel polarization. However, as shown in Figure 41, J_ϕ is unbounded in magnitude and its phase shifts 180° at $\ell = \ell_{N_a}$ for m=2. Thus we see that the total J_ϕ obeys the edge condition at $\ell = \ell_{N_a}$ although each of its individual Fourier components may not. As was the case at 6.25 GHz, we see the distinctive "scalloping" effect of J_ϕ due to the eleven segment piecewise linear approximation to the curved portion of the spherical OCRED generating arc.

The Deep Cylindrical OCRED. At a frequency of 4 GHz, the deep cylindrical OC-RED behaves as a Rayleigh scatterer, as can be seen from Figure 25. Table 2 shows that the deep cylindrical OCRED will not support a propagating waveguide mode at 4 GHz, and we expect to see little field penetration into the cavity interior. Figure 42 shows the magnitude of the electric of the

81

Figure 39   The electric current density plotted as a function of arc length ℓ for the spherical OCRED: $f = 10$ GHz, $\theta = 30°$. The aperture rim corresponds to $\ell = 1.59$ cm.

electric current density components for $\theta = 30°$ and m=0, 1, 2, and 3. This figure indicates that all of the Fourier components of J_ℓ and J_ϕ decay for $\ell > \ell_{N_a}$. Additionally, all Fourier components obey the edge condition at the aperture rim, and only the m=1 Fourier component does not vanish at $\ell = 0$ and $\ell = L$.

At a frequency of 5.9 GHz, the deep cylindrical OCRED will support the TE_{11} cylindrical waveguide mode and we expect to see significant field penetration into the cavity interior. Figure 44 shows the magnitude of the electric current density for $\theta = 30°$ and m=0, 1, 2, and 3. Each Fourier component decays for $\ell > \ell_{N_a}$, except for the m=1 component which shows considerable penetration into the cavity interior. The electric current density for m=1 is evidently caused by an interference pattern set up by a downward propagating TE_{11} wave and its upward propagating
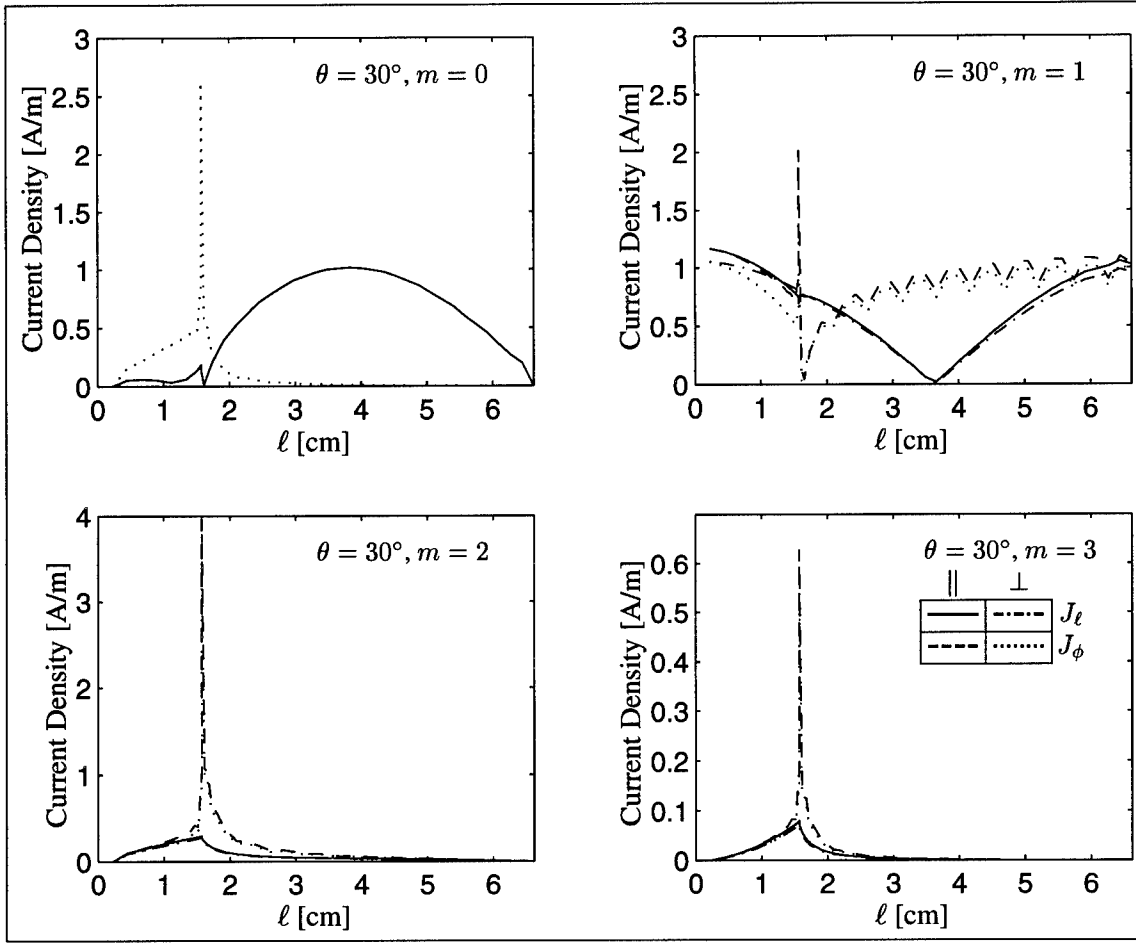
82

Figure 40   The electric current density plotted as a function of arc length ℓ for the spherical OCRED: $f = 10$ GHz, $\theta = 60°$, and $m = 1$. The aperture rim corresponds to $\ell = 1.59$ cm.

Table 3   Longitudinal wavelengths the four lowest-order modes of a perfectly conducting cylindrical waveguide with radius of 5/8 inch at 5.9, 6.9, and 10 GHz. A real value indicates a propagating mode; an imaginary value indicates an evanescent mode.

Mode	λ_z [cm]		
	f=5.9 GHz	f=6.9 GHz	f=10 GHz
TE_{11}	14.7	7.3	3.6
TM_{01}	j7.2	j13.8	4.3
TE_{21}	j4.3	j4.9	7.6
TM_{11}	j3.0	j3.2	j5.2

reflection. At 5.9 GHz, the "longitudinal wavelength" λ_z of the TE_{11} mode is given by $\lambda_z = 2\pi/\sqrt{k^2 - (1.841/R_a)^2} = 14.7$ cm where 1.841 is the first zero of J_1' [21, p. 205]. Table 3 shows the "longitudinal wavelength" for the three lowest-order waveguide modes at 5.9, 6.9 and 10 GHz. This value is very nearly twice the depth of the deep cylindrical OCRED, or, in other words, the OCRED is nearly one-half λ_z at 5.9 GHz. This explains the deep null in Figure 25 there. Figure 45 shows the magnitude and phase of the electric current density for $\theta = 60°$ and m=1. A similar standing-wave pattern is evident, except that the TE_{11} mode is excited more strongly at $\theta = 30°$. Additionally, the J_ℓ and J_ϕ components are nearly $\pm 90°$ out of phase for $\ell > \ell_{N_a}$, with J_ℓ experiencing a 180° phase shift at its null near $\ell = 5.5$ cm.

At 6.9 GHz, the deep cylindrical OCRED still propagates only the TE_{11} cylindrical waveguide mode, so we expect to see a field distribution in the cavity interior similar to that at 5.9 GHz.

83

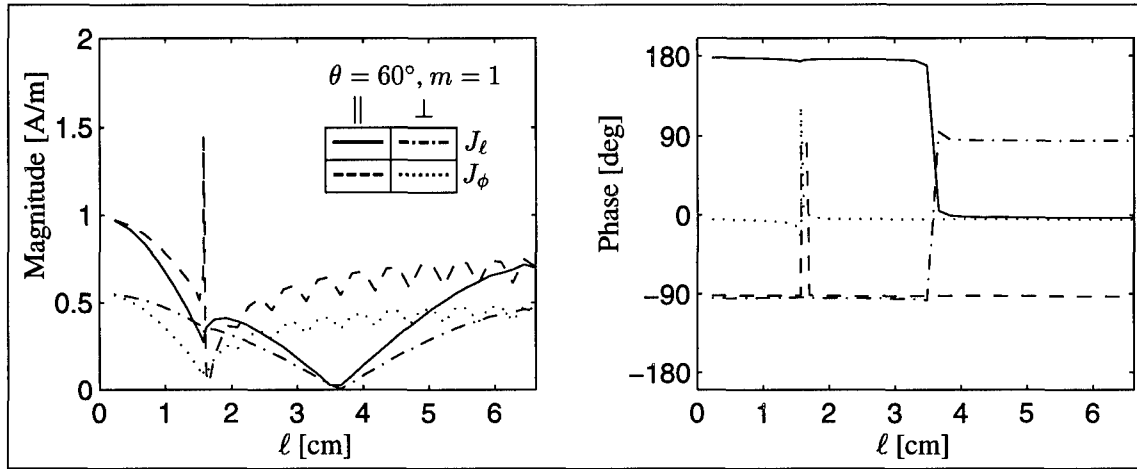Figure 41   The electric current density plotted as a function of arc length ℓ for the spherical OCRED: $f = 10$ GHz, $\theta = 60°$, and $m = 2$. The aperture rim corresponds to $\ell = 1.59$ cm.

Figure 46 shows the magnitude of the electric current density for $\theta = 30°$ and m=0, 1, 2, and 3. These components look very much like those shown in Figure 44 for 5.9 GHz. One obvious difference, however, is the "double hump" pattern of the m=1 Fourier component instead of the "single hump" pattern present at 5.9 GHz. The longitudinal wavelength of the TE_{11} mode at 6.9 GHz is $\lambda_z = 7.3$ cm, nearly half the longitudinal wavelength at 5.9 GHz. This indicates that the deep cylindrical OCRED is nearly one longitudinal wavelength deep at 6.9 GHz, causing the deep null in Figure 25 there. Figure 47 shows the magnitude and phase of the electric current density for $\theta = 60°$ and m=1. The same "double hump" standing-wave pattern is evident. The J_ℓ and J_ϕ components are nearly $\pm 90°$ out of phase for $\ell > \ell_{N_a}$, and both experience a 180° phase shift at their nulls ($\ell \approx 3.8$ and 7.4 cm for J_ℓ, $\ell \approx 5.6$ cm for J_ϕ).

At 10 GHz, the deep cylindrical cavity will support three propagating modes (see Table 2). Figure 48 shows the magnitude of the electric current density for $\theta = 30°$ and m=0, 1, 2, and 3. At this frequency, the three lowest-order waveguide modes (TE_{11}, TM_{01}, and TE_{21}) propagate, each with a different longitudinal wavelength λ_z as given in Table 3. Using this information, we see that the $m = 0$ Fourier component contains the TM_{01} mode, the $m = 1$ Fourier component contains the TE_{11} mode, and the $m = 2$ Fourier component contains the TE_{21} mode. This is evident from the fact that the null-to-null distance in the standing wave patterns correlates to one-half λ_z of these modes. Figure 49 shows the magnitude and phase of the electric current density for $\theta = 60°$, $m = 1$. This figure shows that J_ℓ under parallel polarization does not have a nicely formed lobing
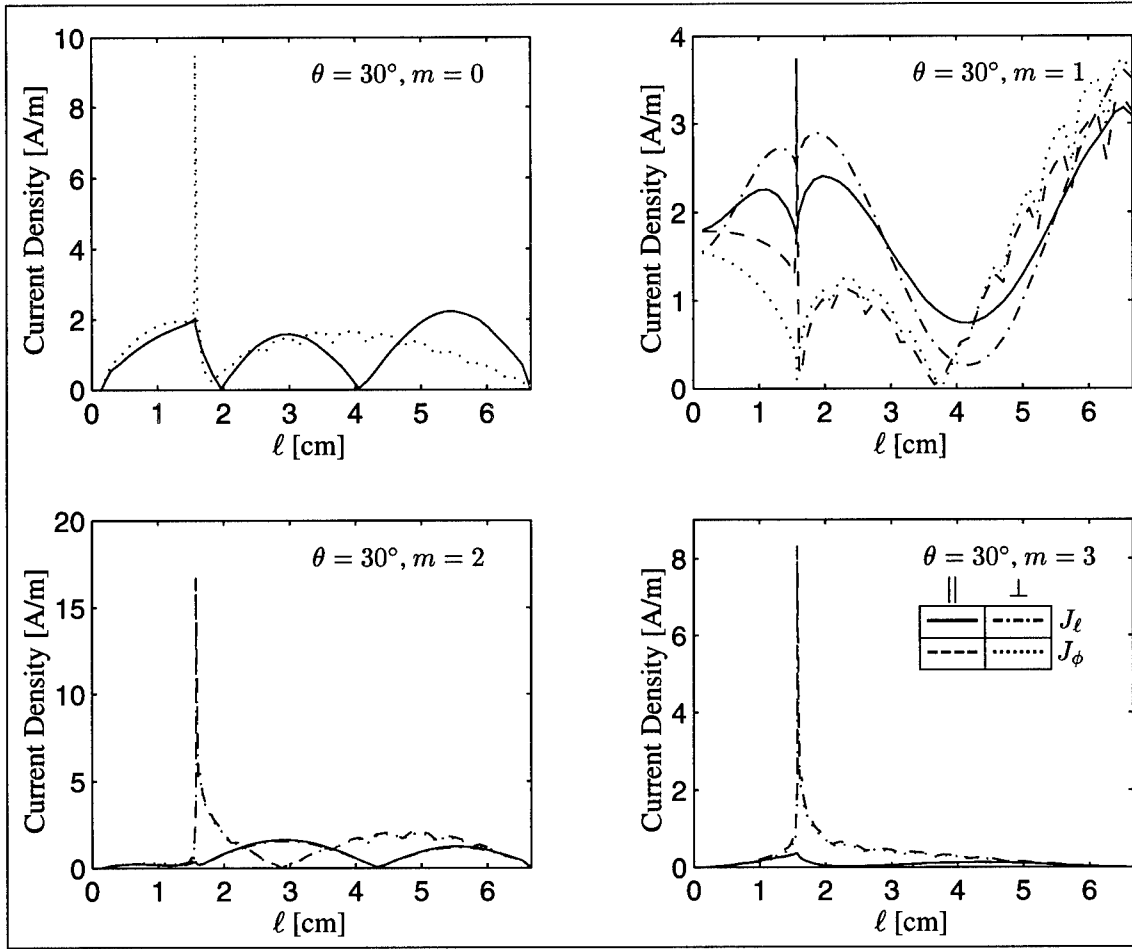
84

Figure 42   The electric current density plotted as a function of arc length ℓ for the deep cylindrical OCRED: $f = 4$ GHz, $\theta = 30°$. The aperture rim corresponds to $\ell = 1.59$ cm.

structure near the top of the OCRED sidewall ($\ell_{N_a} < \ell < \ell_{N_a} + 1$), as it did at $\theta = 30°$. This can be attributed to the TM_{11} waveguide mode, which is weakly evanescent at 10 GHz. (Table 2 shows that the TM_{11} mode cuts on at 11.5 GHz.) Comparing Figures 48 and 49 shows that the TM_{11} mode is excited more strongly at $\theta = 60°$ than at $\theta = 30°$, probably due to the different incident field.

The Conical OCRED.   At a frequency of 4 GHz, the conical OCRED is in transition between the Rayleigh and resonance regimes. This implies that the electromagnetic field does not penetrate as strongly into the cavity as at higher frequencies. Figure 50 shows the magnitude of the electric current density for $\theta = 30°$, *m*=0-3. As expected, none of the Fourier components
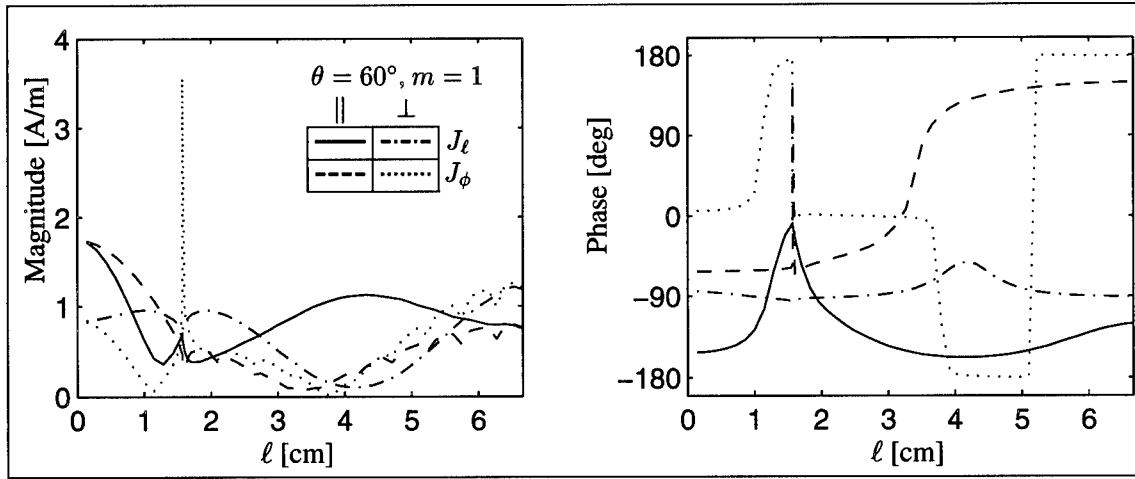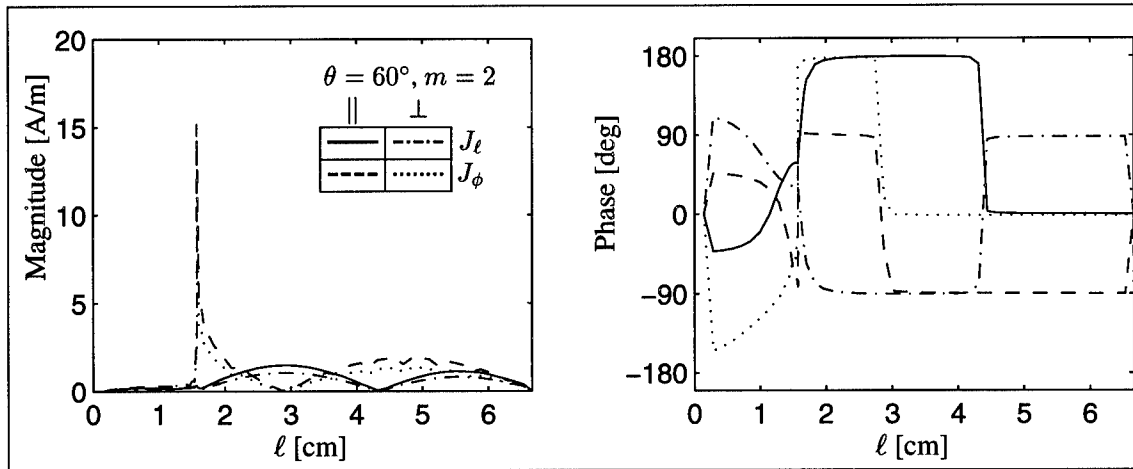
85

Figure 43   The electric current density plotted as a function of arc length ℓ for the deep cylindrical OCRED: $f = 4$ GHz, $\theta = 60°$, and $m = 1$. The aperture rim corresponds to $\ell = 1.59$ cm.

penetrates strongly into the cavity interior, and all of them obey the edge condition at $\ell = \ell_{N_a}$. Furthermore, only the $m = 1$ Fourier component does not vanish at $\ell = 0$.

At 10 GHz, the conical OCRED does not behave as a Rayleigh scatterer, and we expect to see significant field penetration into the interior of the cavity. Figure 52 shows the magnitude of the electric current density for $\theta = 30°$, m=0-3. In contrast to 4 GHz, there is considerable penetration into the cavity interior, especially for the lowest three Fourier components. Figure 53 shows the magnitude and phase of the electric current density for $\theta = 60°$, $m = 1$. Notice the fairly clean null and corresponding 180° phase shifts at $\ell \approx 4.1$ cm and $\ell \approx 5.2$ cm. This is evidence of a well-formed interference pattern, though only for J_ℓ under perpendicular polarization and J_ϕ under parallel polarization. The satisfaction of equation (125) at $\ell = 0$ is quite visible in Figure 53.

The Shallow Cylindrical OCRED.   At a frequency of 4 GHz, the shallow cylindrical OCRED behaves as a Rayleigh scatterer, as can be seen from Figure 27. Table 2 shows that the shallow cylindrical OCRED will not support a propagating waveguide mode at 4 GHz, and we expect to see little field penetration into the cavity interior. Figure 54 shows the magnitude of the electric current density components for $\theta = 30°$ and m=0, 1, 2, and 3. This figure indicates that all of the Fourier components of J_ℓ and J_ϕ decay for $\ell > \ell_{N_a}$. Additionally, all Fourier components obey the edge condition at the aperture rim, and only the m=1 Fourier component does not vanish at $\ell = 0$ and $\ell = L$.

86

Figure 44   The electric current density plotted as a function of arc length ℓ for the deep cylindrical OCRED: $f = 5.9$ GHz, $\theta = 30°$. The aperture rim corresponds to $\ell = 1.59$ cm.

At a frequency of 5.9 GHz, the shallow cylindrical OCRED will support the TE_{11} cylindrical waveguide mode and we expect to see significant field penetration into the cavity interior. Figure 55 shows the magnitude of the electric current density for $\theta = 30°$ and m=0, 1, 2, and 3. Each Fourier component decays for $\ell > \ell_{N_a}$, except for the m=1 component which shows considerable penetration into the cavity interior. The electric current density for m=1 is evidently caused by an interference pattern set up by a downward propagating TE_{11} wave and its upward propagating reflection. Table 3 shows the "longitudinal wavelength" λ_z for the three lowest-order waveguide modes at 5.9 GHz, from which we see that $\lambda_z = 14.7$ cm for the TE_{11} mode. This value is very nearly four times the depth of the shallow cylindrical OCRED, or, in other words, the OCRED is nearly one-quarter λ_z at 5.9 GHz, rather than one-half λ_z as was the case for the deep cylindrical
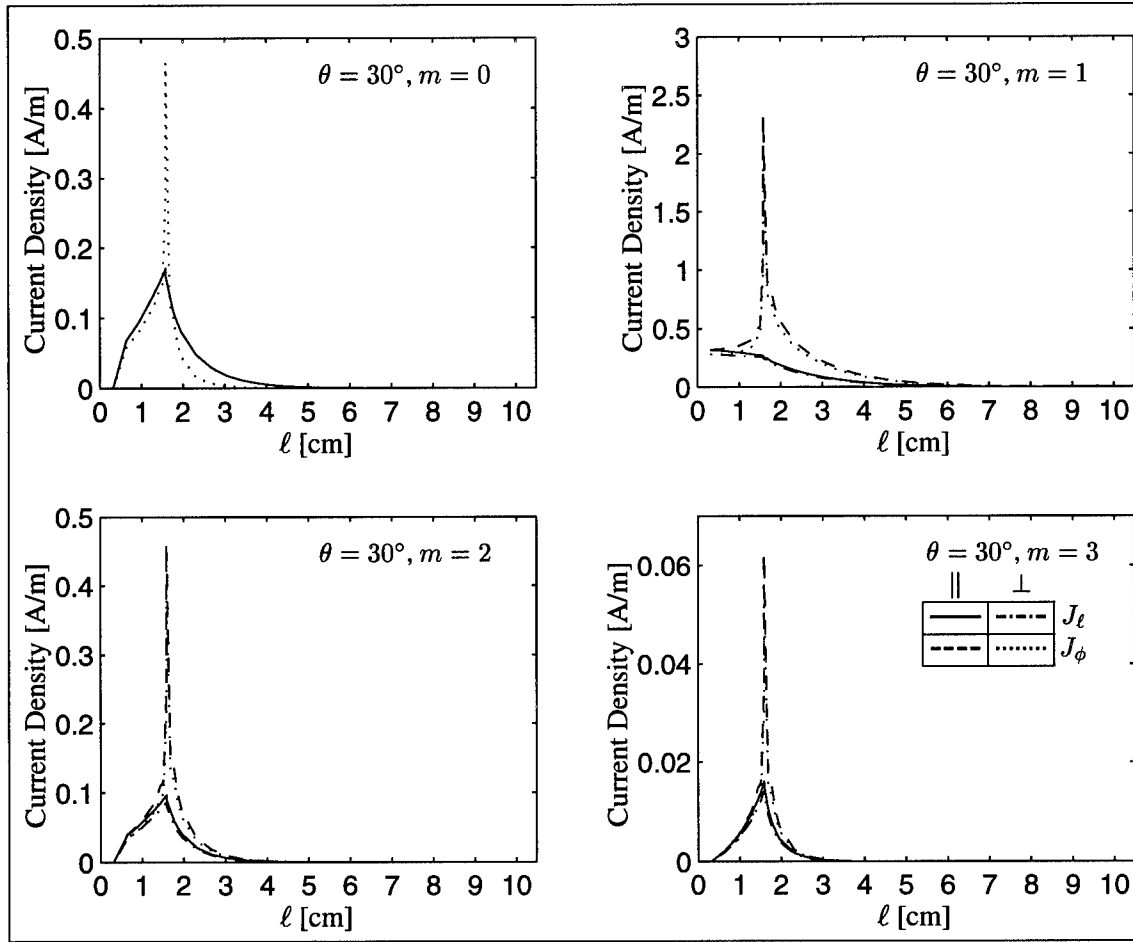
87

Figure 45   The electric current density plotted as a function of arc length ℓ for the deep cylindrical OCRED: $f = 5.9$ GHz, $\theta = 60°$, and $m = 1$. The aperture rim corresponds to $\ell = 1.59$ cm.

OCRED. This explains the absence of a null in Figure 27 there. Figure 56 shows the magnitude and phase of the electric current density for $\theta = 60°$ and $m=1$. The same standing-wave pattern is evident. Additionally, the J_ℓ and J_ϕ components are nearly $\pm 90°$ out of phase for $\ell > \ell_{N_a}$, with J_ℓ experiencing a $180°$ phase shift at its null near $\ell = 5.5$ cm.

At 6.9 GHz, the shallow cylindrical OCRED still propagates only the TE_{11} cylindrical waveguide mode, so we expect to see a field distribution in the cavity interior similar to that at 5.9 GHz. Figure 57 shows the magnitude of the electric current density for $\theta = 30°$ and $m=0$, 1, 2, and 3. These components look very much like those shown in Figure 55 for 5.9 GHz. One obvious difference, however, is the "single hump" pattern of the $m=1$ Fourier component instead of the "half hump" pattern present at 5.9 GHz. The longitudinal wavelength of the TE_{11} mode at 6.9 GHz is $\lambda_z = 7.3$ cm, nearly half the longitudinal wavelength at 5.9 GHz. This indicates that the shallow cylindrical OCRED is nearly one-half longitudinal wavelength deep at 6.9 GHz, causing the deep null in Figure 27 there. Figure 58 shows the magnitude and phase of the electric current density for $\theta = 60°$ and $m=1$. The same "single hump" standing-wave pattern is evident. The J_ℓ and J_ϕ components are nearly $\pm 90°$ out of phase for $\ell > \ell_{N_a}$, and J_ℓ experiences a $180°$ phase shift at its null at $\ell \approx 3.8$ cm.

At 10 GHz, the shallow cylindrical cavity will support three propagating modes (see Table 2). Figure 59 shows the magnitude of the electric current density for $\theta = 30°$ and $m=0$, 1, 2, and 3. At
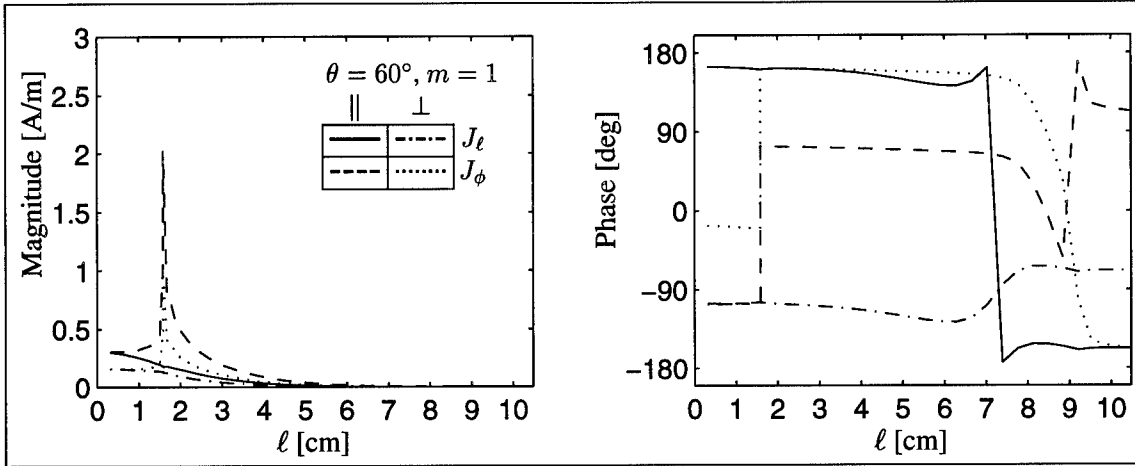
88

Figure 46   The electric current density plotted as a function of arc length ℓ for the deep cylindrical OCRED: $f = 6.9$ GHz, $\theta = 30°$. The aperture rim corresponds to $\ell = 1.59$ cm.

this frequency, the three lowest-order waveguide modes (TE$_{11}$, TM$_{01}$, and TE$_{21}$) propagate, each with a different longitudinal wavelength λ_z as given in Table 3. Using this information, we see that the $m = 0$ Fourier component contains the TM$_{01}$ mode, the $m = 1$ Fourier component contains the TE$_{11}$ mode, and the $m = 2$ Fourier component contains the TE$_{21}$ mode. Figure 60 shows the magnitude and phase of the electric current density for $\theta = 60°$, $m = 1$. This figure shows that J_ℓ under parallel polarization does not have a nicely formed lobing structure near the top of the OCRED sidewall ($\ell_{N_a} < \ell < \ell_{N_a} + 1$), as it did at $\theta = 30°$. This can be attributed to the TM$_{11}$ waveguide mode, which is weakly evanescent at 10 GHz. Comparing Figures 59 and 60 shows that the TM$_{11}$ mode is excited more strongly at $\theta = 60°$ than at $\theta = 30°$, probably due to the different incident field.

89
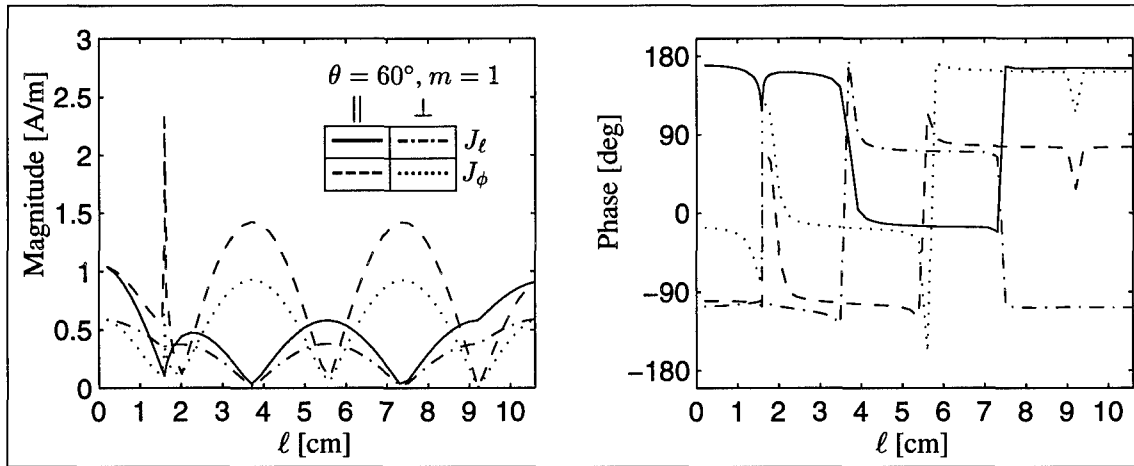
Figure 47   The electric current density plotted as a function of arc length ℓ for the deep cylindrical OCRED: $f = 6.9$ GHz, $\theta = 60°$, and $m = 1$. The aperture rim corresponds to $\ell = 1.59$ cm.
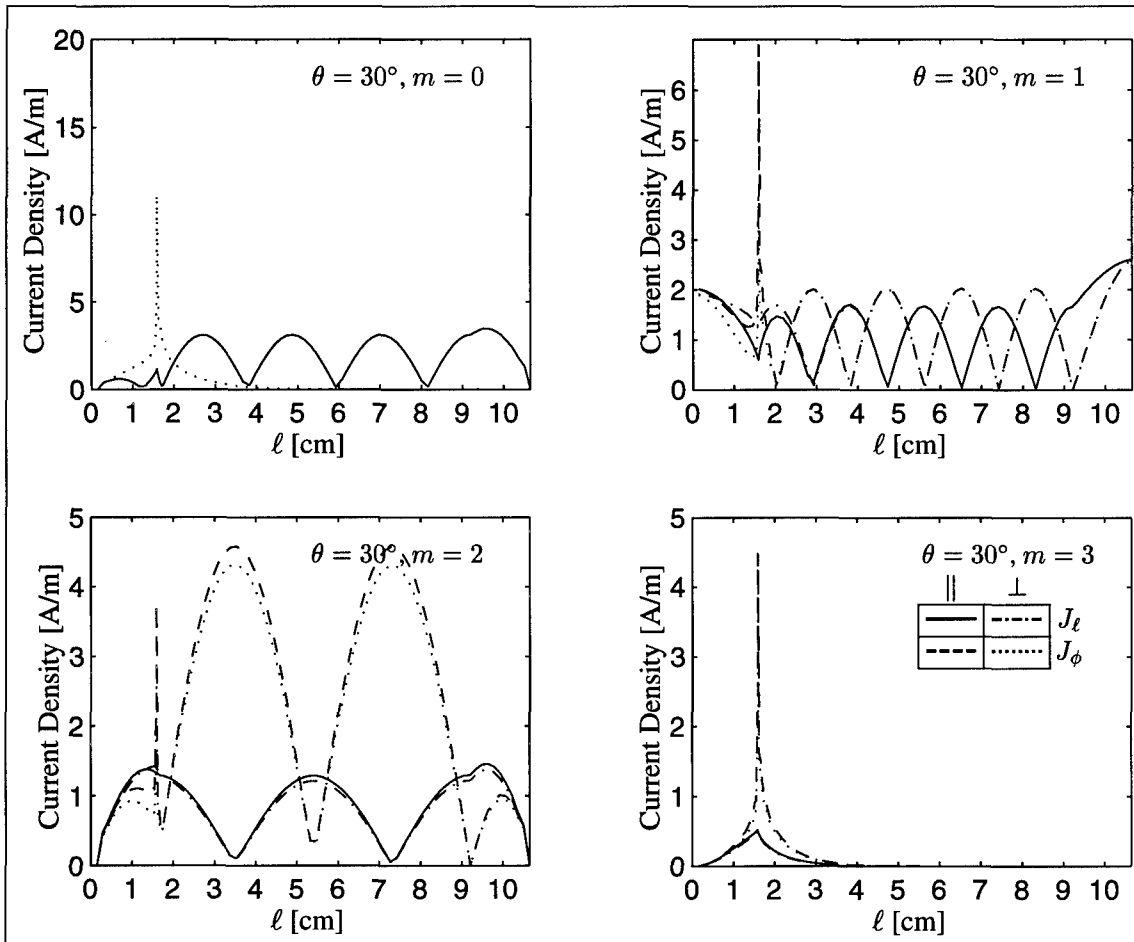
Figure 48   The electric current density plotted as a function of arc length ℓ for the deep cylindrical OCRED: $f = 10$ GHz, $\theta = 30°$. The aperture rim corresponds to $\ell = 1.59$ cm.
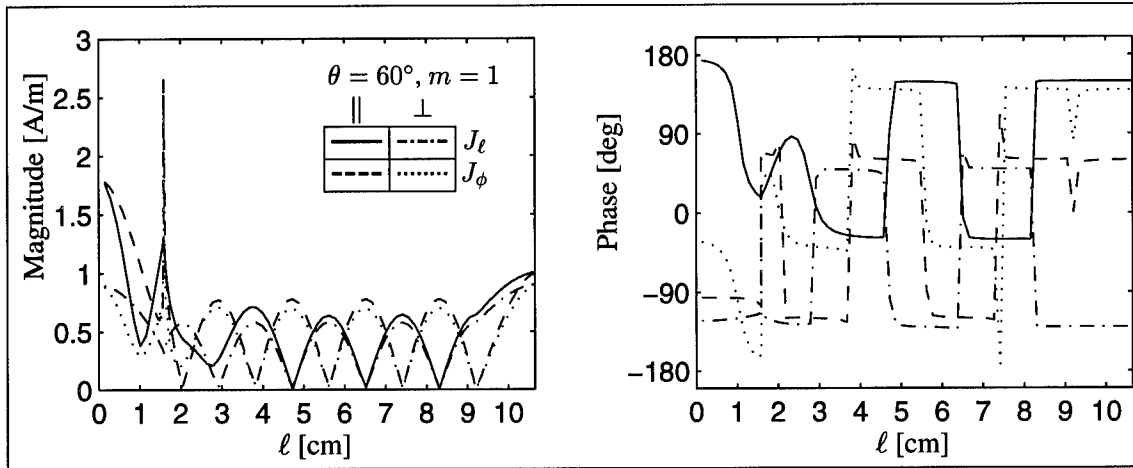
Figure 49   The electric current density plotted as a function of arc length ℓ for the deep cylindrical OCRED: $f = 10$ GHz, $\theta = 60°$, and $m = 1$. The aperture rim corresponds to $\ell = 1.59$ cm.
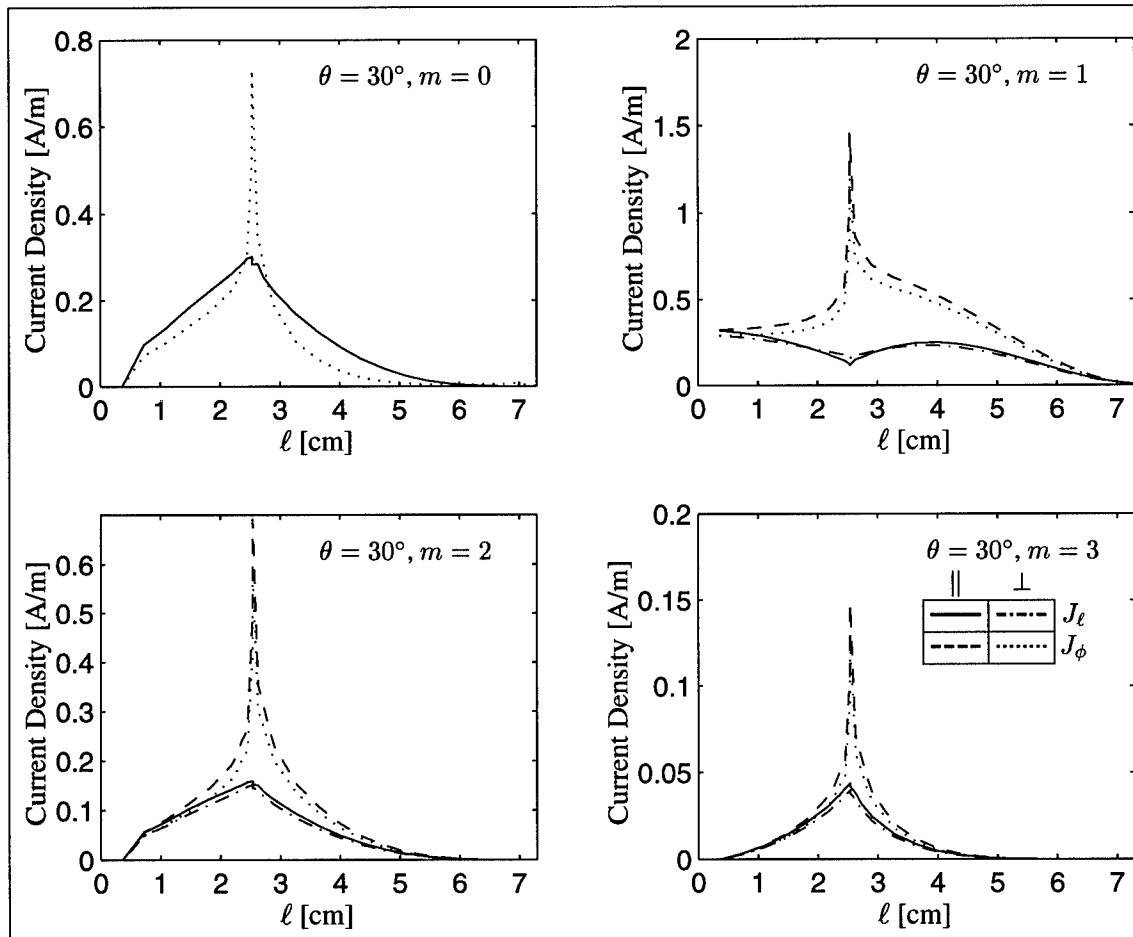
Figure 50   The electric current density plotted as a function of arc length ℓ for the conical OCRED: $f = 4$ GHz, $\theta = 30°$. The aperture rim corresponds to $\ell = 2.54$ cm.

91
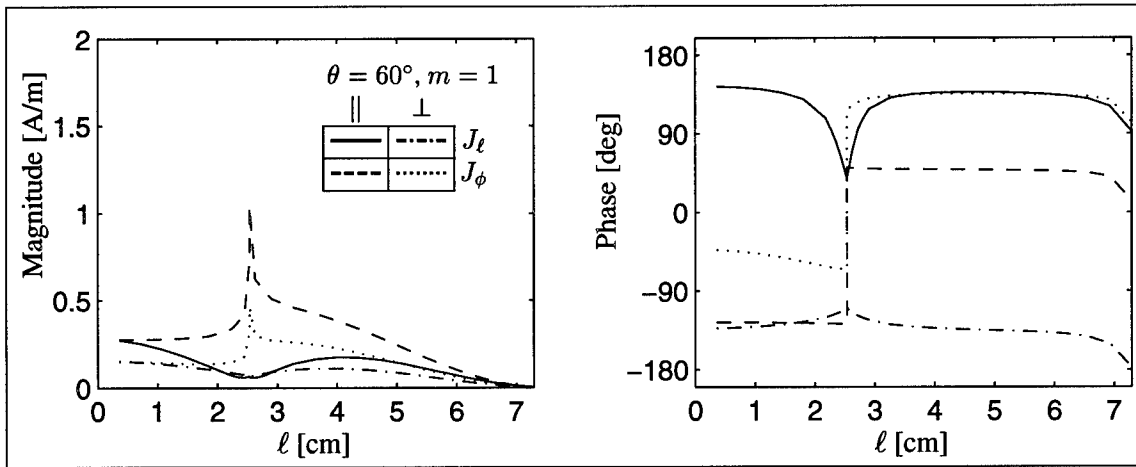
Figure 51   The electric current density plotted as a function of arc length ℓ for the conical OC-RED: $f = 4$ GHz, $\theta = 60°$, and $m = 1$. The aperture rim corresponds to $\ell = 2.54$ cm.
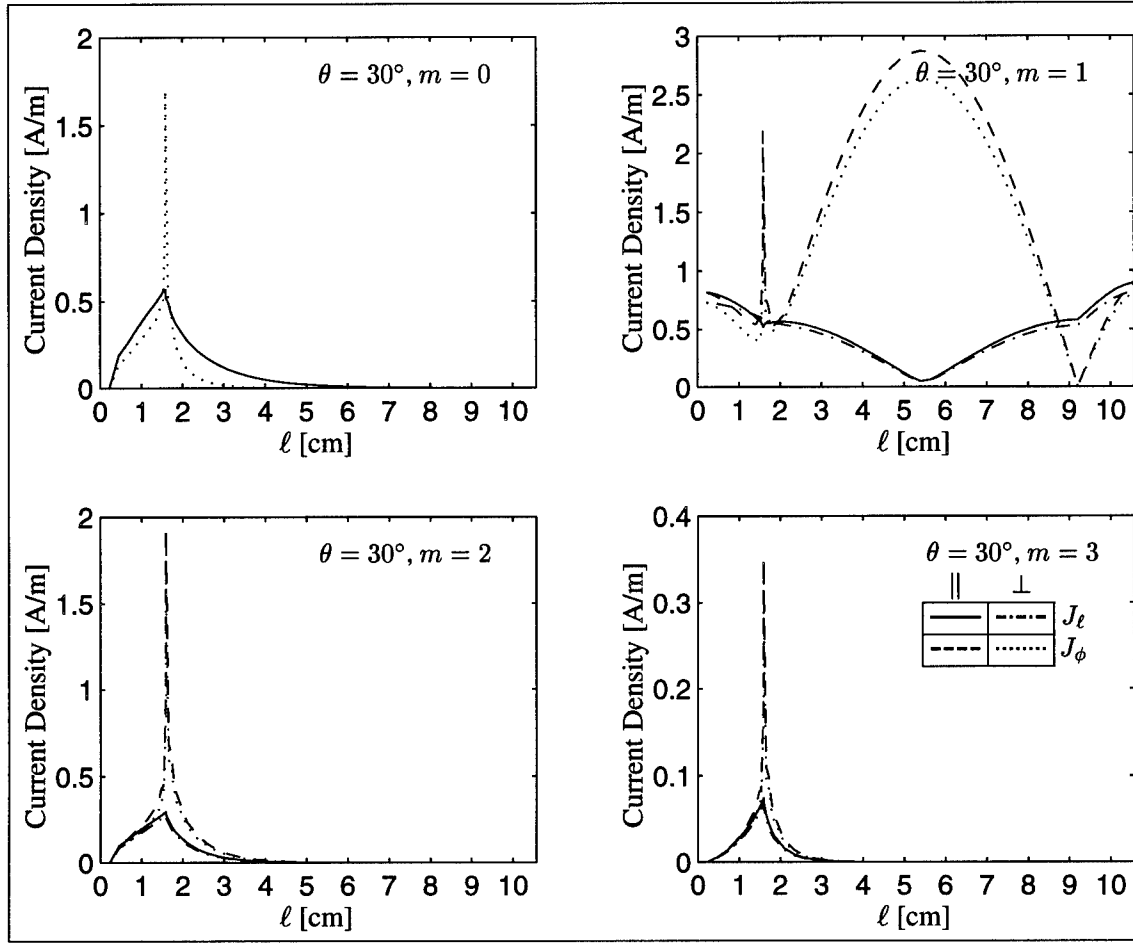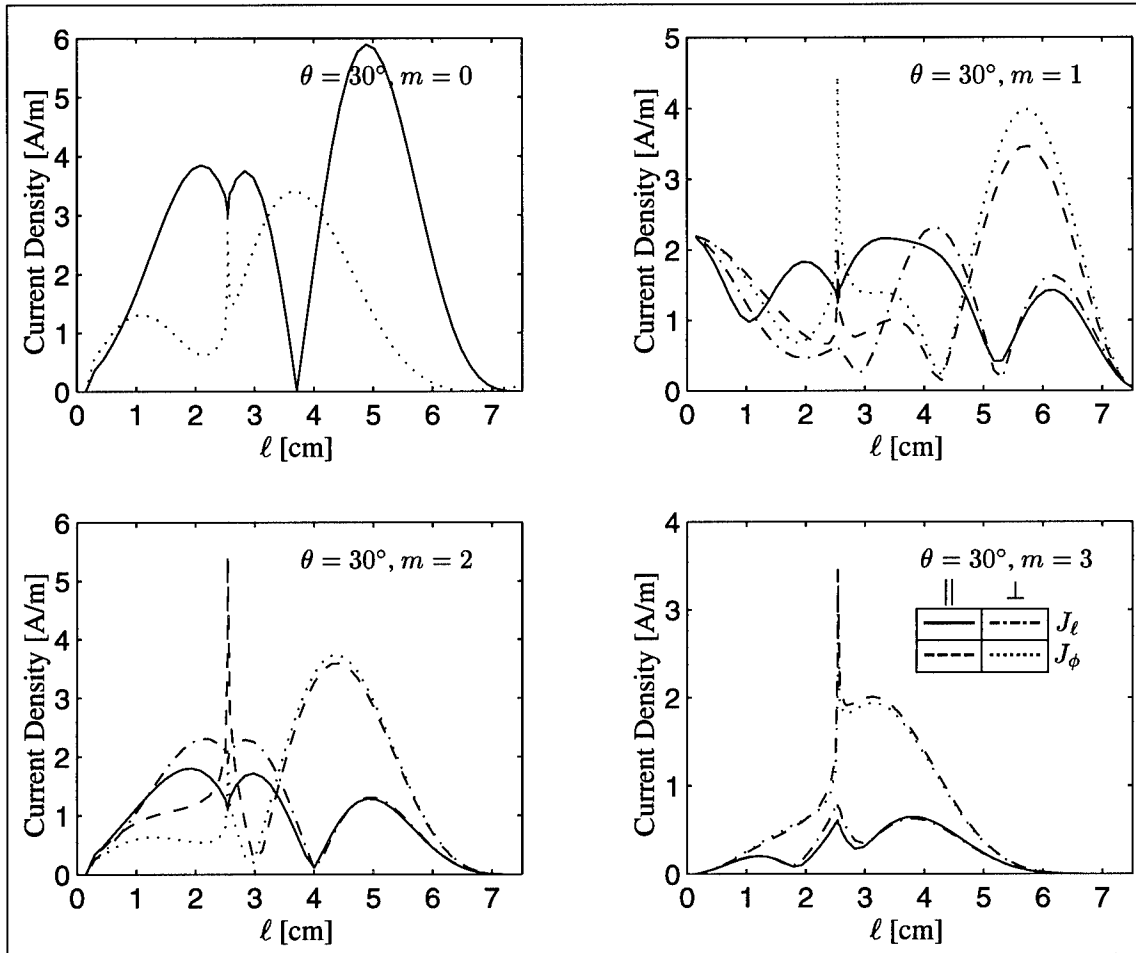

Figure 52   The electric current density plotted as a function of arc length ℓ for the conical OC-RED: $f = 10$ GHz, $\theta = 30°$. The aperture rim corresponds to $\ell = 2.54$ cm.
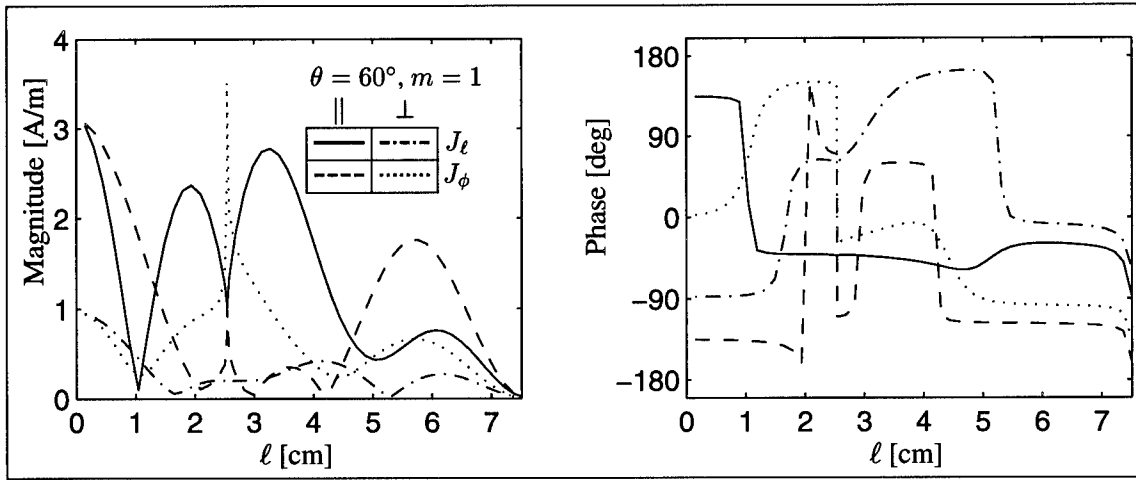
Figure 53   The electric current density plotted as a function of arc length ℓ for the conical OC-RED: $f = 10$ GHz, $\theta = 60°$, and $m = 1$. The aperture rim corresponds to $\ell = 2.54$ cm.
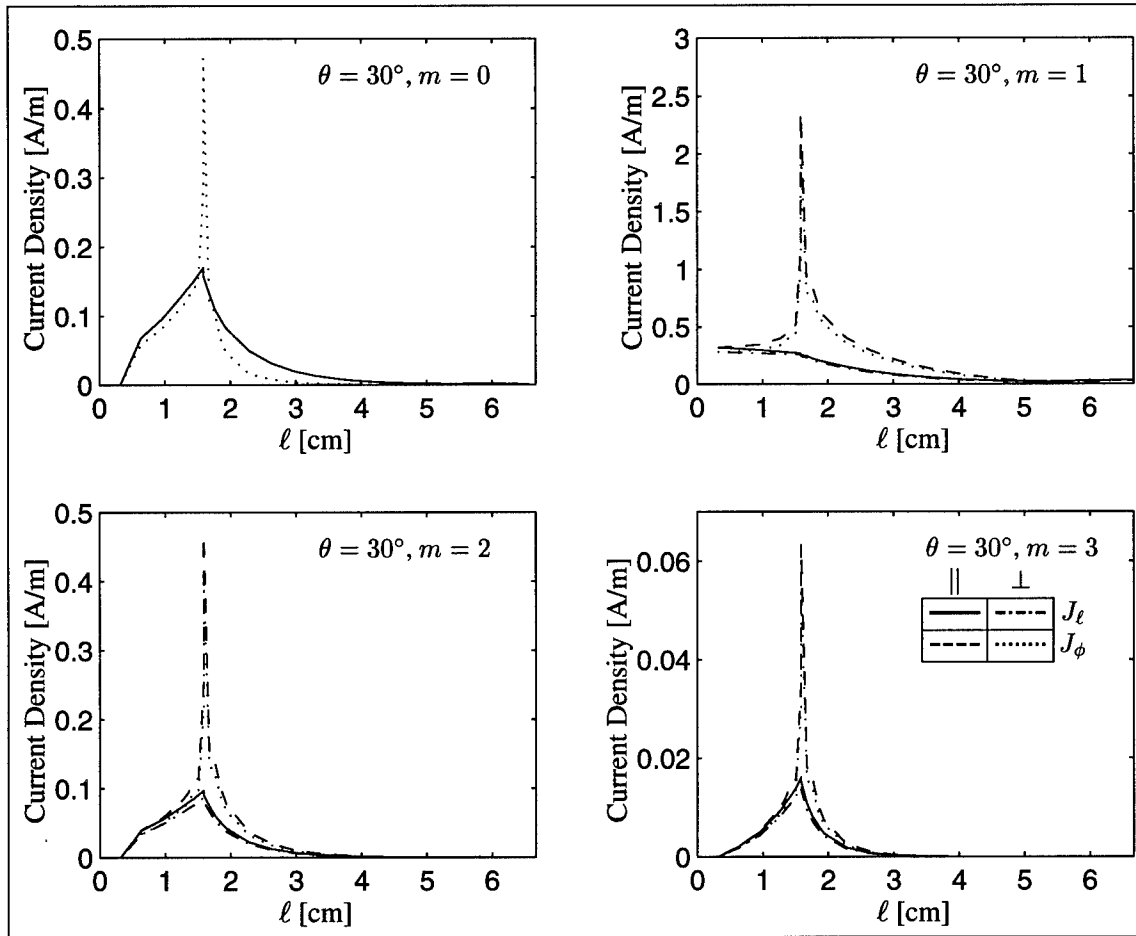
Figure 54   The electric current density plotted as a function of arc length ℓ for the shallow cylindrical OCRED: $f = 4$ GHz, $\theta = 30°$. The aperture rim corresponds to $\ell = 1.59$ cm.

93
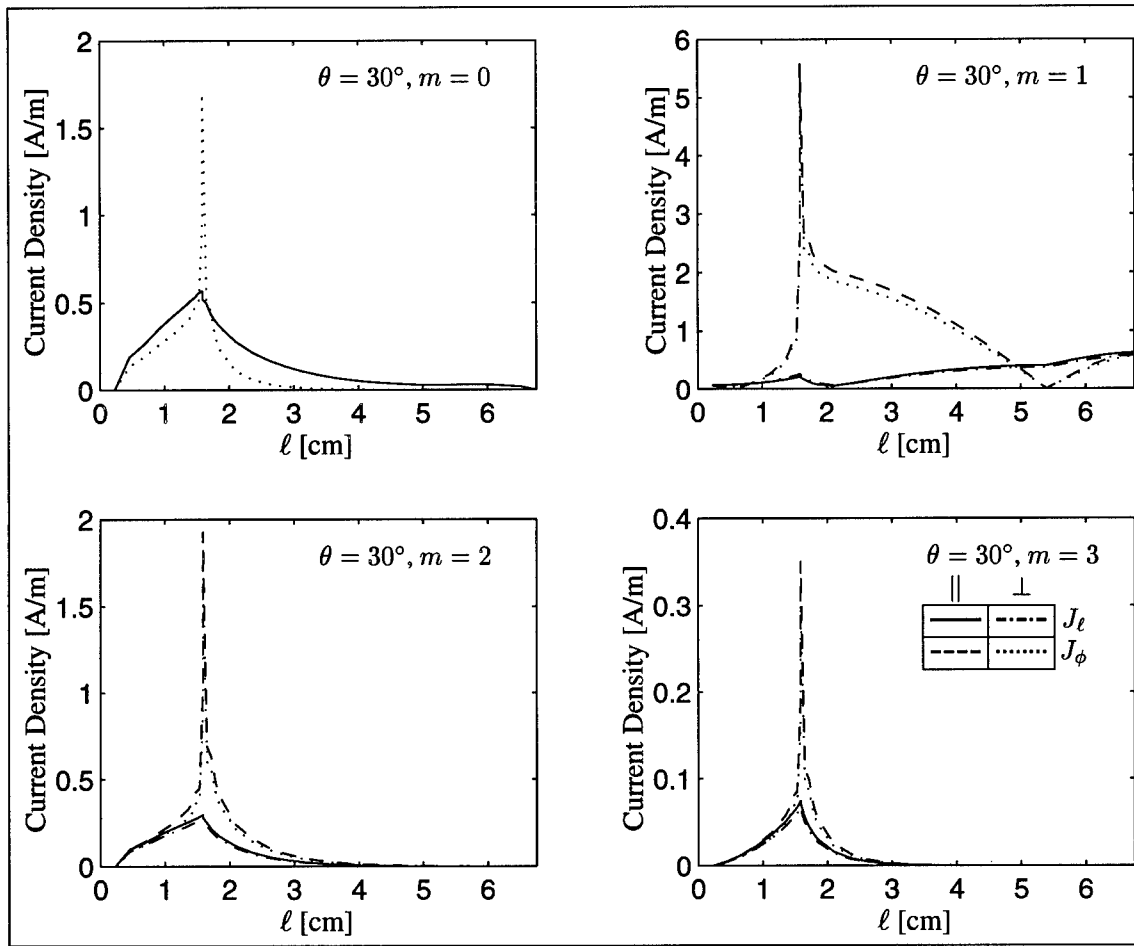
Figure 55   The electric current density plotted as a function of arc length ℓ for the shallow cylindrical OCRED: $f = 5.9$ GHz, $\theta = 30°$. The aperture rim corresponds to $\ell = 1.59$ cm.
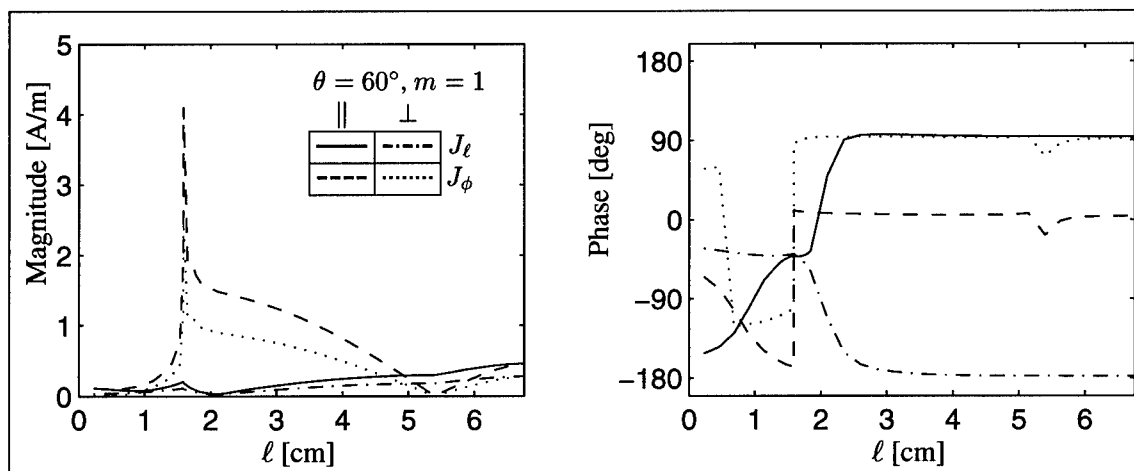
Figure 56   The electric current density plotted as a function of arc length ℓ for the shallow cylindrical OCRED: $f = 5.9$ GHz, $\theta = 60°$, and $m = 1$. The aperture rim corresponds to $\ell = 1.59$ cm.

94
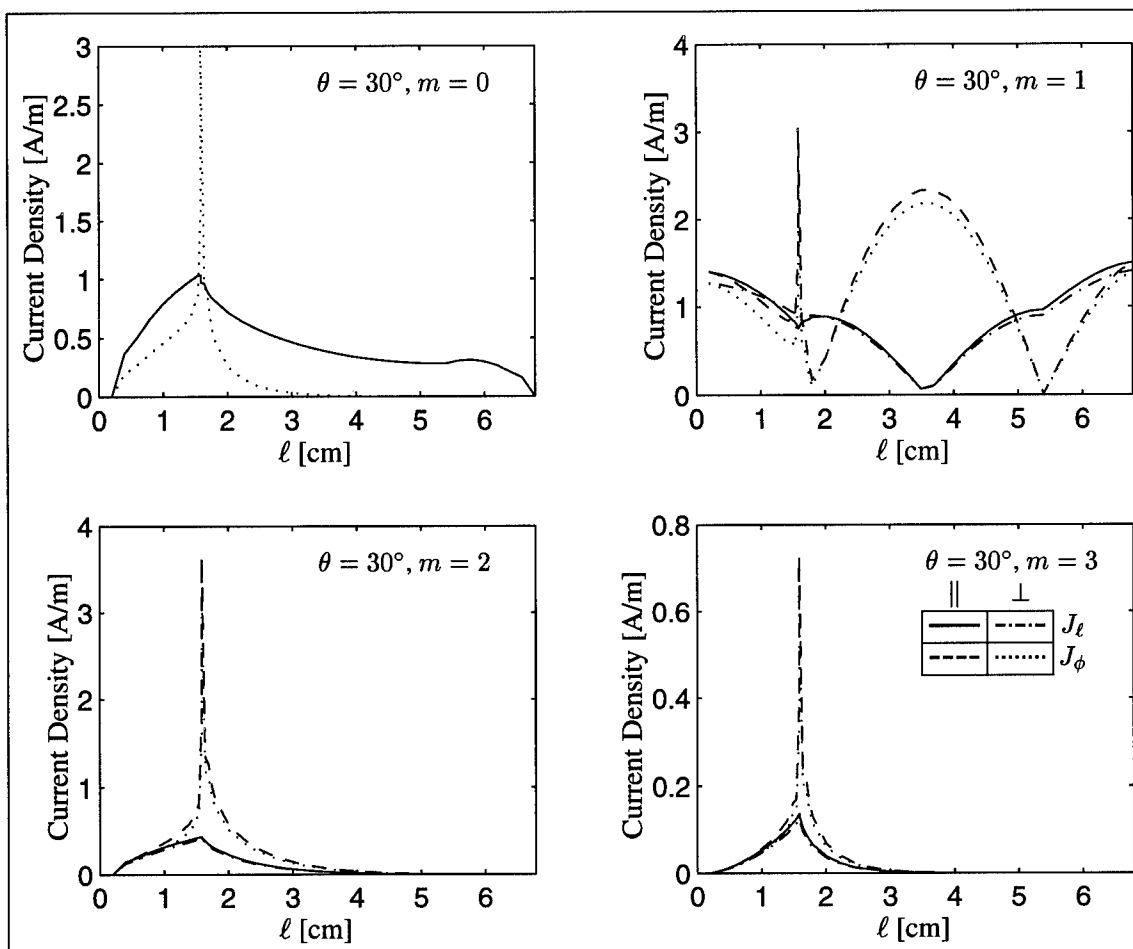
Figure 57   The electric current density plotted as a function of arc length ℓ for the shallow cylindrical OCRED: $f = 6.9$ GHz, $\theta = 30°$. The aperture rim corresponds to $\ell = 1.59$ cm.
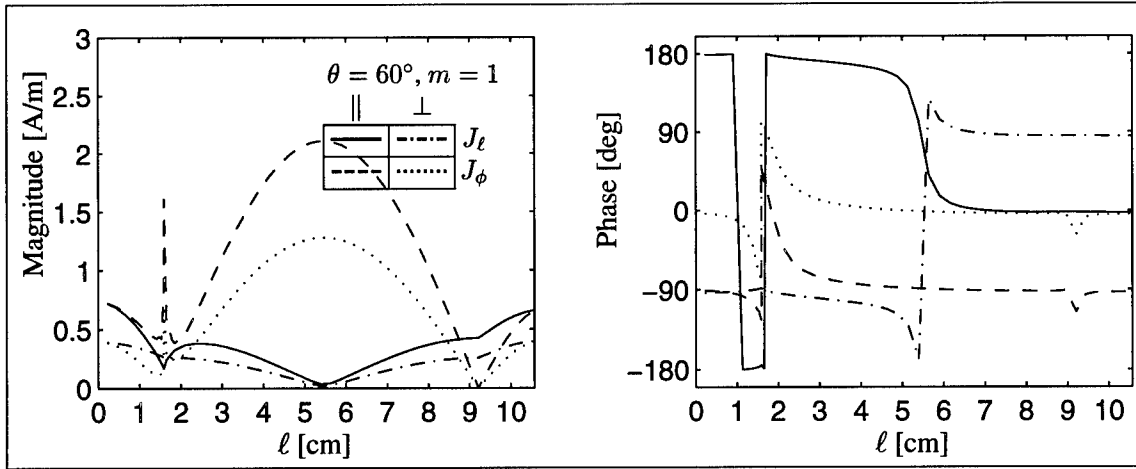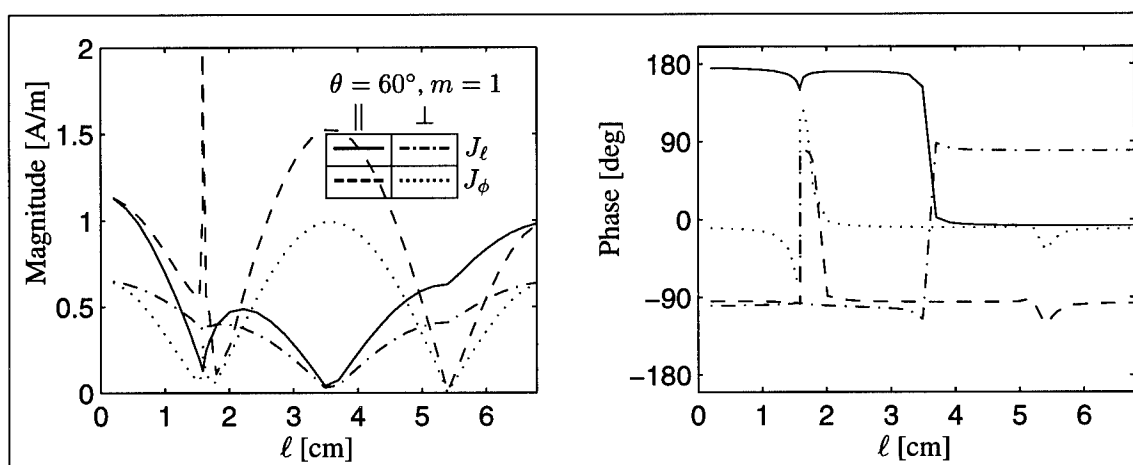

Figure 58   The electric current density plotted as a function of arc length ℓ for the shallow cylindrical OCRED: $f = 6.9$ GHz, $\theta = 60°$, and $m = 1$. The aperture rim corresponds to $\ell = 1.59$ cm.

95
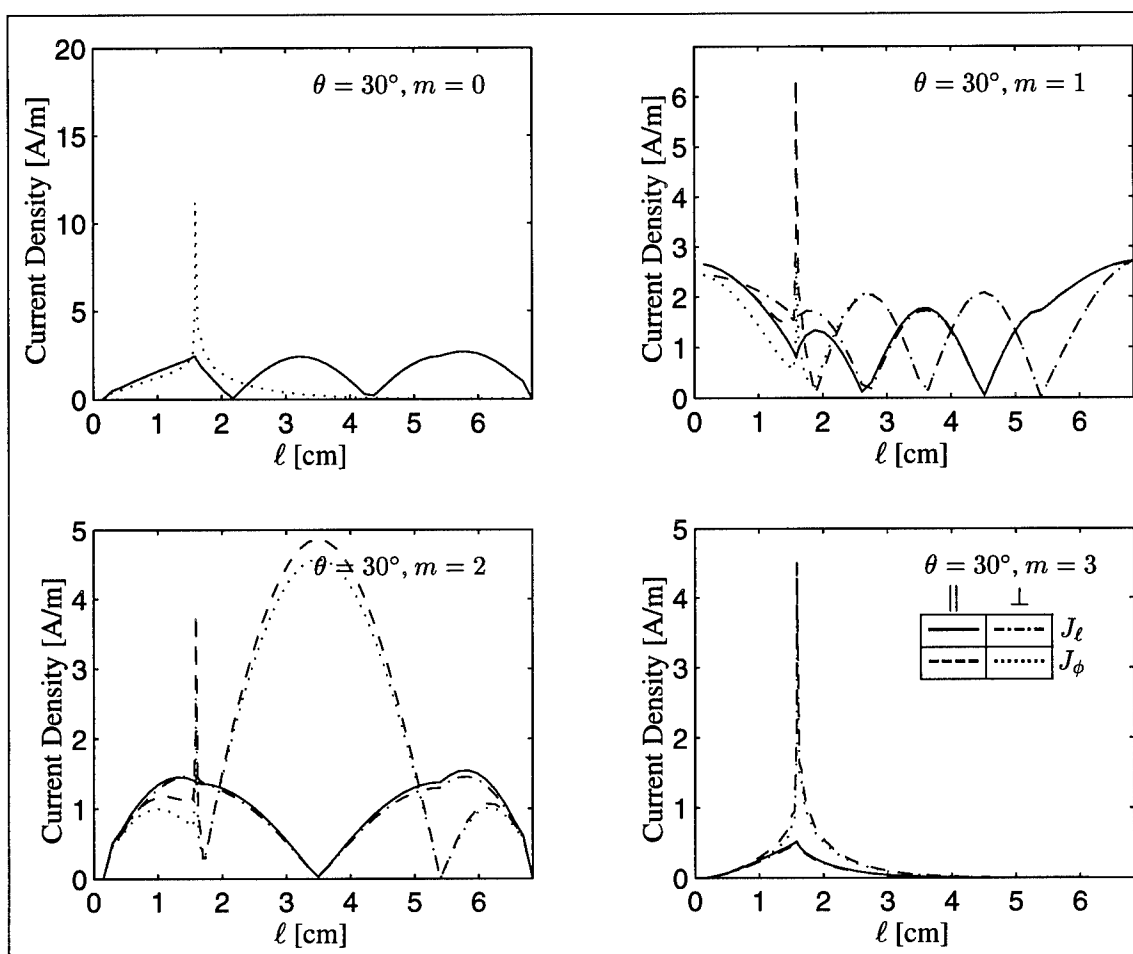
Figure 59   The electric current density plotted as a function of arc length ℓ for the shallow cylindrical OCRED: $f = 10$ GHz, $\theta = 30°$. The aperture rim corresponds to $\ell = 1.59$ cm.
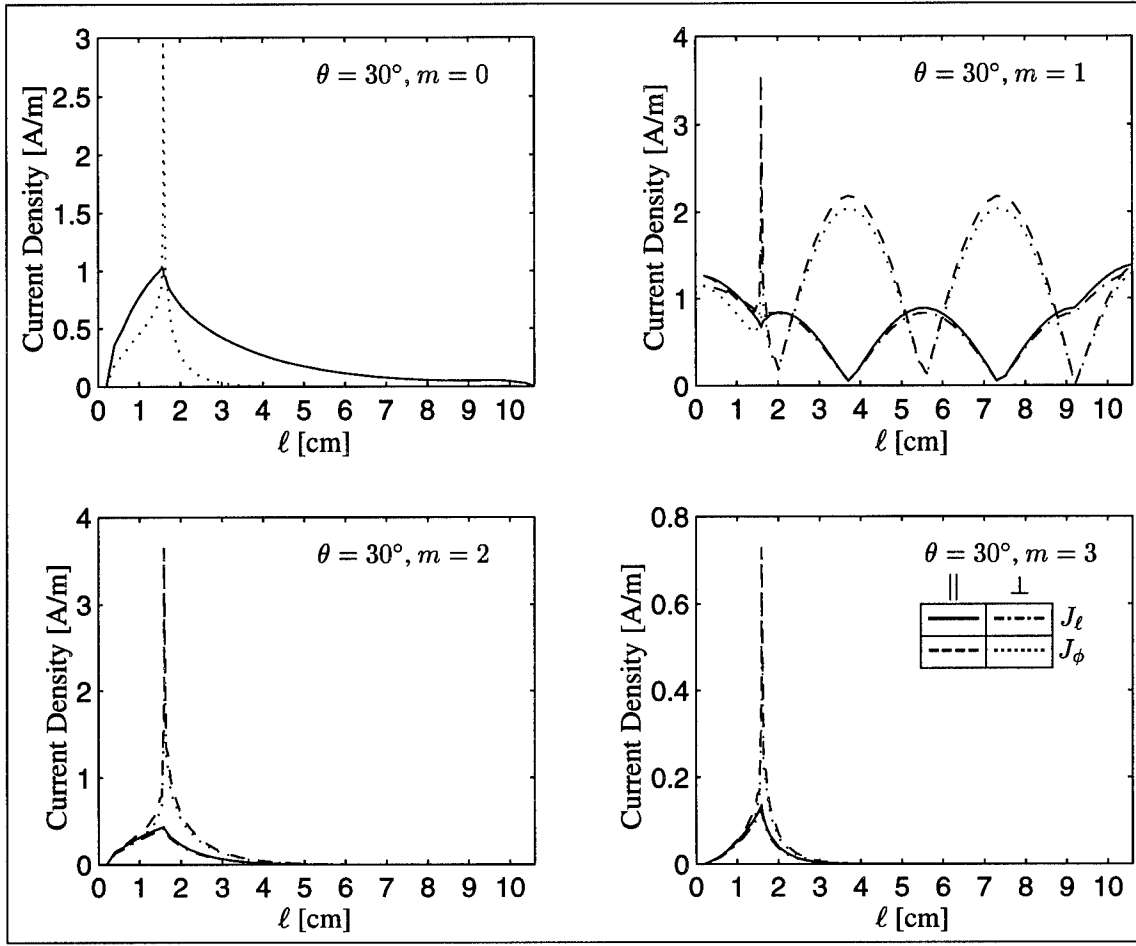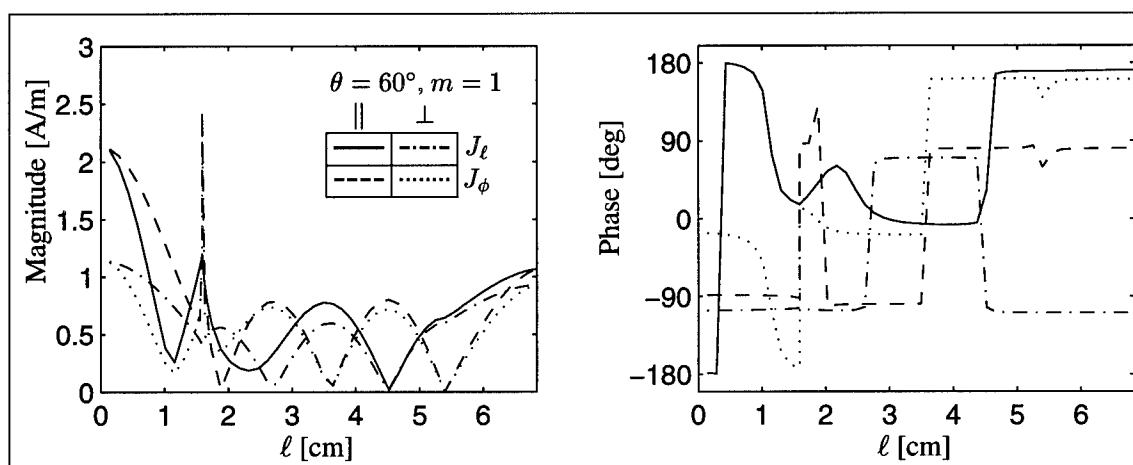

Figure 60   The electric current density plotted as a function of arc length ℓ for the shallow cylindrical OCRED: $f = 10$ GHz, $\theta = 60°$, and $m = 1$. The aperture rim corresponds to $\ell = 1.59$ cm.

5.4.2 The Condition of the Moment Method Matrix.

The effectiveness of the moment method solution technique requires the generalized impedance matrix to be well-conditioned. If the matrix is well-conditioned, then small changes in the forcing vector cause small changes in the solution vector, and the linear transformation defined by the matrix is stable. If the matrix is poorly conditioned, then small changes in the forcing vector may produce large changes in the solution vector, and the linear transformation defined by the matrix is unstable. The condition of the moment method matrix is inherently limited by the integral equations to which the moment method is applied, and a well-conditioned moment method matrix is an indication of a well-conditioned set of integral equations.

The condition of an $N \times N$ matrix is measured by the so-called "condition number" κ. It is a measure of the sensitivity of the linear system $ZI = V$ in the following sense. If the elements of Z and V are in error by some small amount, then the resulting solution I will also be in error, such that

$$(Z + \delta Z)(I + \delta \mathcal{I}) = (V + \delta \mathcal{V}) \tag{128}$$

The error of the solution I is bounded by [18, page 79]

$$\frac{\|\mathcal{I}\|}{\|I\|} \leq \kappa \left[\frac{\|\mathcal{V}\|}{\|V\|} + \frac{\|\mathcal{Z}\|}{\|Z\|} \right] + \mathcal{O}(\delta) \tag{129}$$

The condition number κ is thus dependent on the matrix norm employed. If the 2-norm is chosen, then κ is given by [18]

$$\kappa = \frac{\sigma_N}{\sigma_1} \tag{130}$$

where σ_1 is the smallest singular value of the matrix and σ_N is the largest. (Recall that the singular values of a complex matrix are always real, non-negative, and $\sigma_p \leq \sigma_{p+1}$.) A perfectly conditioned matrix (*e.g.*, the identity matrix) has a condition number $\kappa = 1$, while a condition number much greater than unity reflects a poorly conditioned matrix.

Tables 4–7 show the condition numbers of the moment method matrix used to calculate the electric current density $\vec{\mathbf{J}}(\vec{\mathbf{r}})$ for each combination of OCRED geometry, frequency, and Fourier

Freq [GHz]	N	Fourier Index, m							
		0	1	2	3	4	5	6	7
4	62	111	327	131	131				
6.25	86	172	368	228	201	199	197		
10	114	219	522	368	408	294	278	273	271

Table 4   Condition number κ of $N \times N$ moment method matrix Z_m for the spherical OCRED.

Freq [GHz]	N	Fourier Index, m							
		0	1	2	3	4	5	6	7
4	74	66	191	72	72				
5.9	100	92	241	106	104	103			
6.9	116	110	262	129	125	124	124		
10	186	159	354	198	187	178	176	175	175

Table 5   Condition number κ of $N \times N$ moment method matrix Z_m for the deep cylindrical OCRED.

index. It should be stressed that these condition numbers relate to using the moment method as applied to equations (36) and (37) to find $\vec{J}_\sigma$ and $\vec{J}_S$ since the cavities considered in this chapter are unfilled. Several trends are immediately clear. First, the condition number κ generally increases with frequency, the dependence being nearly linear. Second, the condition number corresponding to $m = 1$ exceeds the condition number for any other Fourier mode, except under special circumstances that will be described later in this section. Third, as the Fourier index m increases past unity, the condition number asymptotically approaches a finite limit. Most importantly, however, in all cases the condition number is quite benign in the sense that it does not vary greatly with geometry, frequency, or Fourier mode. In fact the largest observed κ was 632 while the smallest was 66, a variation of less than a factor of ten.

Figure 61 shows the condition number κ for the spherical OCRED as a function of frequency. Data for the first four Fourier modes ($m = 0 - 3$) are shown. The $m = 0$ Fourier mode shows a peak in its condition number at approximately 6.01 GHz while the condition numbers for the other Fourier modes are nearly constant across the band. The peak in the $m = 0$ Fourier mode can be explained as follows. The lowest-order mode of the corresponding spherical cavity resonates at 5.89 GHz (See Table 1). The presence of the aperture in the spherical OCRED causes two things to happen: the resonant frequency becomes complex due to the radiation losses through the aperture, and the volume of the cavity is reduced by a function of the aperture angle α and the cavity

Freq [GHz]	N	Fourier Index, m											
		0	1	2	3	4	5	6	7	8	9	10	11
4	54	150	244	109	108	108	107						
10	116	377	598	263	261	267	263	257	254	253	253	253	253

Table 6   Condition number κ of $N \times N$ moment method matrix Z_m for the conical OCRED.

Freq [GHz]	N	Fourier Index, m							
		0	1	2	3	4	5	6	7
4	54	69	166	75	75				
5.9	70	92	273	106	104	103			
6.9	80	110	249	129	125	124	124		
10	108	161	353	180	190	181	178	178	177

Table 7   Condition number κ of $N \times N$ moment method matrix Z_m for the shallow cylindrical OCRED.

radius R_s (see Figure 17(a)). In effect, we consider the spherical OCRED to be a perturbation of a spherical cavity. The volume of the corresponding spherical cavity is $V_{\text{cavity}} = \frac{4}{3}\pi R_s^3$, while the volume of the interior of the spherical OCRED is $V_{\text{OCRED}} = \left(\frac{2}{3} + \cos\alpha - \frac{1}{3}\cos^3\alpha\right)\pi R_s^3$. With $\alpha \approx 45.6°$, we find $\frac{V_{\text{OCRED}}}{V_{\text{cavity}}} \approx 0.939$. A spherical cavity having a volume equal to V_{OCRED} would have a radius of approximately equal to $0.979R_s$, and thus would resonate at approximately 5.89/0.979=6.015 GHz. From this we see that the condition number of the $m = 0$ Fourier mode peaks at a frequency corresponding to the resonant frequency of a spherical cavity having *the same volume* as the spherical OCRED interior. We expect this relation to be valid when the aperture angle α is small enough such that the fields inside the OCRED are similar to the fields inside the corresponding spherical cavity. As the aperture angle α is reduced toward zero, we would expect the peak in Figure 61 to become higher and narrower, and to move toward 5.89 GHz.

5.4.3   Relative Importance of Fourier Modes.   The accuracy of the RCS produced by the numerical algorithm is a function of the number of Fourier modes included in the solution. It is not known *a priori* how many Fourier modes must be included to achieve a desired level of accuracy, but a rule-of-thumb [41,44] is to include all Fourier modes up to the Mth, where $M = \lceil 2k\rho_{\text{max}} \rceil$, k is the wavenumber, ρ_{max} is the maximum distance between a point on the generating arc and the axis of rotation and $\lceil x \rceil$ is the least integer greater than x.
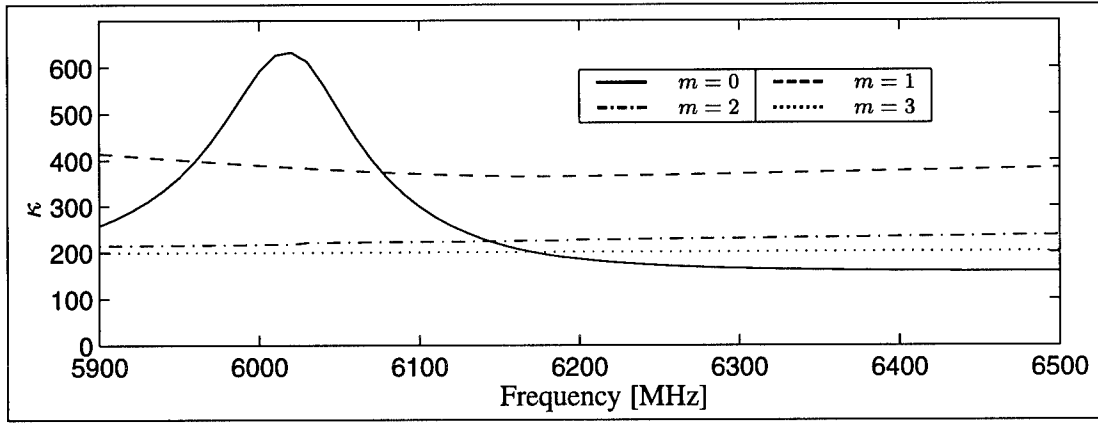
Figure 61 Condition number for the spherical OCRED as a function of frequency. κ for the $m = 0$ Fourier mode is plotted as ———; κ for the $m = 1$ Fourier mode is plotted as - - - -; κ for the $m = 2$ Fourier mode is plotted as -·-·-·; κ for the $m = 3$ Fourier mode is plotted as ········.

We may assess the relative importance of each Fourier mode in the following manner. Instead of looking at the contribution of the mth Fourier mode to the total RCS, we will look at its contribution to the total electric current density $\vec{J}(\vec{r})$. The importance metric we will employ will be the integral of the mth Fourier component of $|\vec{J}(\vec{r})|$, integrated along the generating arc. This can be expressed directly in terms of the expansion coefficients as

$$I_m^{\ell} = \sum_{n=1}^{N_a} |B_{mn}^{\ell}| \frac{\ell_{n+1} - \ell_{n-1}}{2} + \sum_{n=N_a}^{N_a+N_s-1} |C_{mn}^{\ell}| \frac{\ell_{n+1} - \ell_{n-1}}{2} \qquad (131)$$

$$I_m^{\phi} = \sum_{n=1}^{N_a} |B_{mn}^{\phi}| \frac{\ell_{n+1} - \ell_{n-1}}{2} + \sum_{n=N_a}^{N_a+N_s-1} |C_{mn}^{\phi}| \frac{\ell_{n+1} - \ell_{n-1}}{2} \qquad (132)$$

We will normalize this metric by the contribution from the dominant Fourier mode, such that

$$\tilde{I}_m^{\ell} = \frac{I_m^{\ell}}{\max\left\{I_m^{\ell}\right\}_{m=0}^{M}} \qquad (133)$$

$$\tilde{I}_m^{\phi} = \frac{I_m^{\phi}}{\max\left\{I_m^{\phi}\right\}_{m=0}^{M}} \qquad (134)$$

Figures 62–65 show the normalized metric $\tilde{I}_m$ plotted versus Fourier index m for each of the four BOR OCRED geometries. The aspect angle is held constant at $\theta = 45°$, and data is shown for both $\parallel$ and $\perp$ polarizations. Using this metric, we see that the contribution of the Mth Fourier mode

100
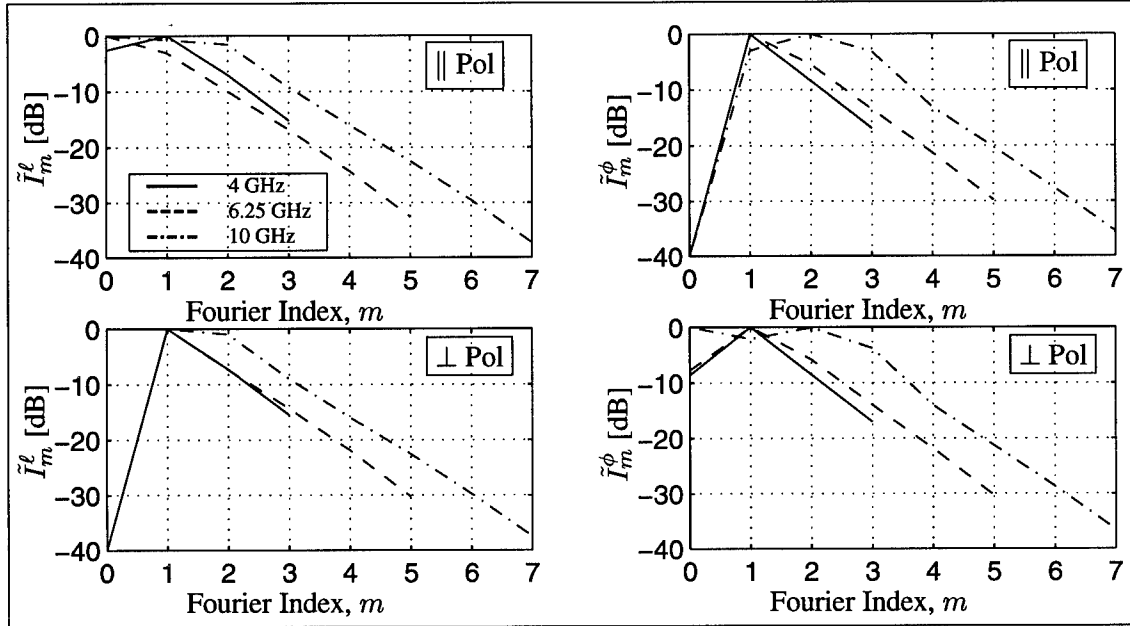
Figure 62   Normalized metric $\tilde{I}_m$ versus Fourier index for the spherical OCRED, $\theta = 45°$. Plots for 4 GHz (solid), 6.25 GHz (dashed), and 10 GHz (dash-dot). $M = \lceil 2k\rho_{\text{max}} \rceil$ is 4 at 4 GHz, 6 at 6.25 GHz, and 10 at 10 GHz.
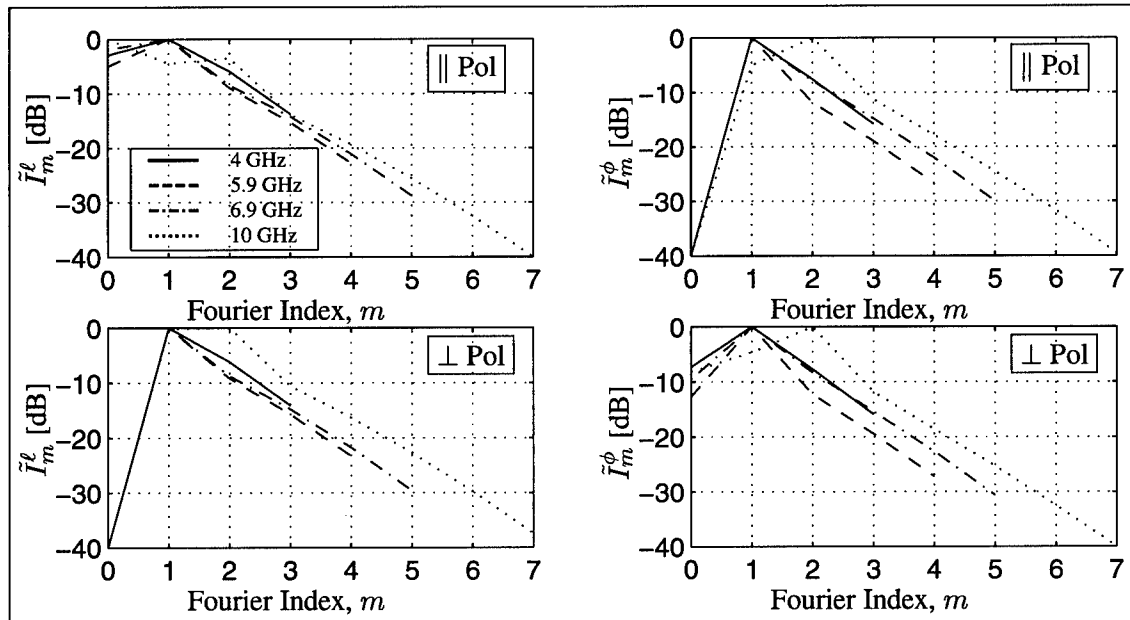
Figure 63   Normalized metric $\tilde{I}_m$ versus Fourier index for the deep cylindrical OCRED, $\theta = 45°$. Plots for 4 GHz (solid), 5.9 GHz (dashed), 6.9 GHz (dash-dot), 10 GHz (dotted). $M = \lceil 2k\rho_{\text{max}} \rceil$ is 3 at 4 GHz, 4 at 5.9 GHz, 5 at 6.9 GHz, and 7 at 10 GHz.

Figure 64   Normalized metric $\tilde{I}_m$ versus Fourier index for the conical OCRED, $\theta = 45°$. Plots for 4 GHz (solid) and 10 GHz (dashed). $M = \lceil 2k\rho_{\max} \rceil$ is 5 at 4 GHz and 11 at 10 GHz.
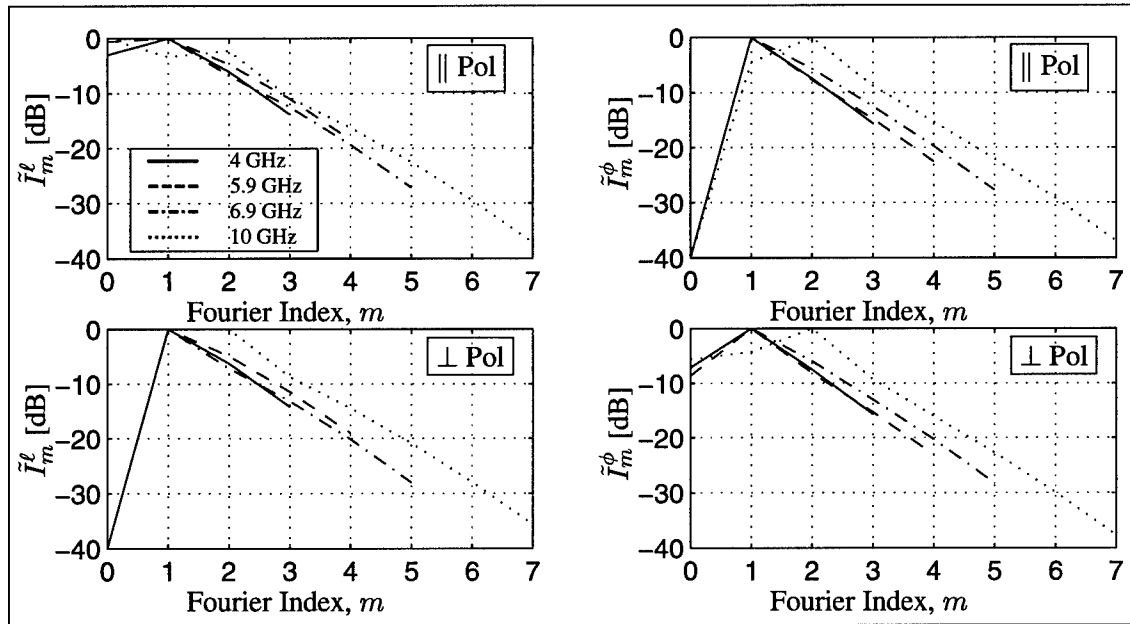
Figure 65   Normalized metric $\tilde{I}_m$ versus Fourier index for the shallow cylindrical OCRED, $\theta = 45°$. Plots for 4 GHz (solid), 5.9 GHz (dashed), 6.9 GHz (dash-dot), 10 GHz (dotted). $M = \lceil 2k\rho_{\max} \rceil$ is 3 at 4 GHz, 4 at 5.9 GHz, 5 at 6.9 GHz, and 7 at 10 GHz.

is several orders of magnitude below the contribution of the dominant mode. Furthermore, for m greater than approximately $M/2$, the integrated current magnitude decays exponentially with m, at a rate of 7–8 dB per unit increase in m. Surprisingly, this rate of decay is nearly independent of geometry and of frequency, suggesting that this may be an intrinsic property of all BOR OCREDs.

VI. Conclusions

This dissertation documents an investigation into the development of an integral equation-based solution for the determination of the electromagnetic scattering from a cavity-backed aperture embedded in an infinite, perfectly conducting ground plane. The cavity may be filled with a homogeneous, isotropic, linear material. Such a geometry is of interest in designing an effective RCS enhancement device to be installed on airborne vehicles while not compromising aerodynamic performance properties. A substantial body of work exists in the open literature documenting research into the scattering properties of open cavities, but none incorporates the integral equation technique developed here. The coupled set of integral equations developed here provides an accurate prediction for the RCS of the open cavity, and the results support the assertion that the integral equations possess a unique solution at all real, positive frequencies.

In the previous chapters, a comprehensive theoretical, numerical, and experimental treatment is presented for the aforementioned scattering problem. Fundamental theorems governing the behavior of the electromagnetic fields in the cavity interior and upper half-space are introduced and proved. These theorems are used to generate a coupled set of three integral equations in which the unknown quantities are the tangential magnetic field on the cavity surface and the tangential electric and magnetic fields on the aperture. It is shown that, for the case of unfilled cavities, the formulation degenerates into a coupled set of two integral equations involving just the tangential magnetic fields. The system excitation is provided by the incident tangential magnetic field on the aperture, which may be radiated by near-field or far-field sources. Integral representations are given for the total fields in the cavity interior, and for the scattered fields in the upper half-space.

A numerical algorithm, based on the method of moments, is presented to find an approximate solution to the set of integral equations for the important case of axisymmetric (body of revolution) cavities. The unknown tangential fields are expanded using piecewise-linear functions and complex exponentials (Fourier modes). Methods to treat the numerical computation of the resultant integrals are given, as well as a novel transformation to reduce the order of the singularity of a dyadic kernel. Various aspects of the resultant approximate solution are discussed. The far-field scattered fields are compared to measurements of several full-scale physical models, and excellent agreement is observed. The approximate tangential fields on the cavity surface and aperture are shown to be

well-behaved and, in particular, to satisfy the edge condition at the aperture rim. The stability of the numerical solution is discussed.

This research represents the first use of this integral equation-based technique to the open cavity problem. The success of the numerical algorithm suggests several areas in which future research might concentrate. First, the numerical algorithm could easily be extended to handle non-axisymmetric cavities. This would necessitate using a different set of basis functions; the so-called "Rao-Wilton-Glisson" [54] basis functions might prove useful here. Such an extension would enable the analysis of several interesting cavity shapes, such as rectangular ones. Second, the numerical algorithm could be verified with dielectric-filled cavities. Such verification should incorporate a measurement program with several types of material fillings and cavity shapes. A two-dimensional version should be verified before a three-dimensional version is attempted. Third, an optimization scheme could be developed to find the "best" open cavity shape for a given set of scattering requirements. This would provide an alternative to the costly "design-fabricate-measure" iterative loop that would currently have to be employed today. Fourth, the integral equations could be generalized to handle radiation from an open cavity using an excitation source inside, or on the surface of, the cavity. This would allow the technique to be used for antenna analysis as well as scattering analysis. Finally, the integral equation technique could be used as part of a larger, hybrid system to handle installation issues in an airborne application. For instance, if an open cavity were embedded in the upper surface of an aircraft wing, the integral equation technique might be used for the cavity and physical optics might be used for the rest of the airframe.

Appendix A. **Proof of the Fundamental Theorems**

In this appendix, we prove the fundamental theorems presented in Chapter III. The proofs employ the classical methods of infinitesimal vector calculus. For Theorem 1, we also show that $\overline{\overline{\Gamma}}(\vec{r}, \vec{r}')$ satisfies a dyadic form of the reduced wave equation in the distributional sense.

Proof of Theorem 1

In this section, we prove Theorem 1 using the classical methods of infinitesimal vector calculus. We recognize that $\overline{\overline{\Gamma}}(\vec{r}, \vec{r}')$ can be expressed as the sum of three components, namely,

$$\overline{\overline{\Gamma}}(\vec{r}, \vec{r}') = \sum_{\ell=1}^{3} \overline{\overline{\Gamma}}^{(\ell)}(\vec{r}, \vec{r}') \tag{135a}$$

$$\overline{\overline{\Gamma}}^{(\ell)}(\vec{r}, \vec{r}') = -jk \, \nabla G(k; \vec{r}, \vec{r}') \times \hat{e}_\ell \hat{e}_\ell \quad \text{for } \ell = 1, 2, 3 \tag{135b}$$

where $\hat{e}_1 = \hat{x}$, $\hat{e}_2 = \hat{y}$, and $\hat{e}_3 = \hat{z}$. Now we introduce Green's Second Identity for mixed vector-dyadic fields [61],

$$\int_V \left[\left(\nabla \times \nabla \times \vec{A} \right) \cdot \overline{\overline{B}} - \vec{A} \cdot \left(\nabla \times \nabla \times \overline{\overline{B}} \right) \right] dv =$$
$$\int_{\partial V} \hat{n} \cdot \left[\vec{A} \times \left(\nabla \times \overline{\overline{B}} \right) + \left(\nabla \times \vec{A} \right) \times \overline{\overline{B}} \right] ds \tag{136}$$

where V is a volumetric region with regular boundary ∂V, $\hat{n}$ is the outward unit normal vector on ∂V, and $\vec{A} \equiv \vec{A}(\vec{r})$ and $\overline{\overline{B}} \equiv \overline{\overline{B}}(\vec{r})$ are arbitrary vector and dyadic functions, respectively, twice-differentiable in V. In particular, we choose $\vec{A}(\vec{r})$ to satisfy the homogeneous wave equation (2) in V, and let $\overline{\overline{B}}(\vec{r}) \equiv \overline{\overline{\Gamma}}^{(\ell)}(\vec{r}, \vec{r}')$ with ℓ and $\vec{r}'$ fixed. It can be shown that $\overline{\overline{\Gamma}}^{(\ell)}(\vec{r}, \vec{r}')$ also satisfies equation (2) for $\vec{r} \neq \vec{r}'$. With these choices, it is easy to see that the volume integral in equation (136) vanishes when $\vec{r}' \notin \overline{V}$, where $\overline{V}$ is the closure of V. Thus

$$\int_{\partial V} \hat{n} \cdot \left[\vec{A} \times \left(\nabla \times \overline{\overline{\Gamma}}^{(\ell)} \right) + \left(\nabla \times \vec{A} \right) \times \overline{\overline{\Gamma}}^{(\ell)} \right] ds = 0 \quad \text{for } \vec{r}' \notin \overline{V} \tag{137}$$

If $\vec{r}' \in V$, we exclude from V a small volume, V_δ, containing $\vec{r}'$ in its interior. We choose V_δ to be a sphere of radius δ centered at $\vec{r}'$, as shown in Figure 66. We apply equation (136) to the
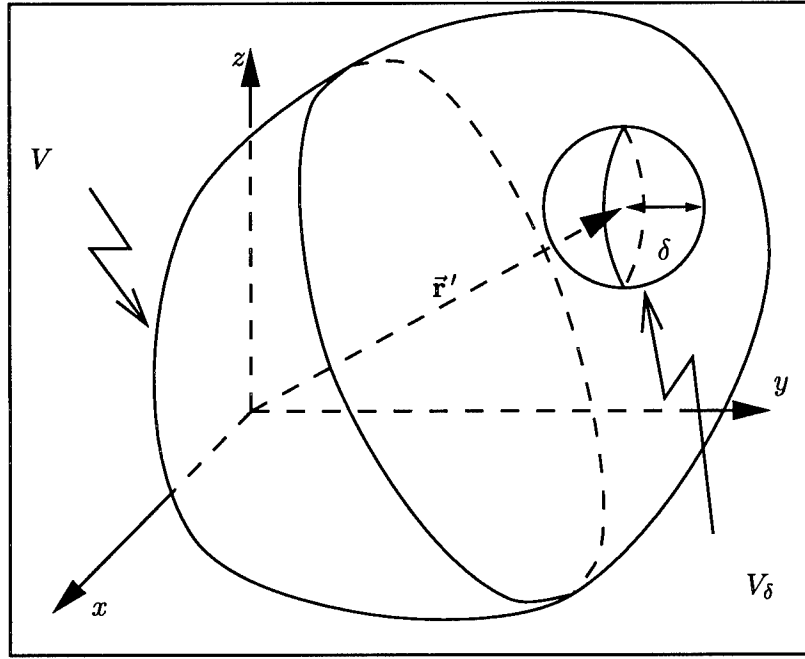
Figure 66   A volume V and volume V_δ. V_δ is spherical with radius δ, centered at $\vec{r}' \in V$.

region $V - V_\delta$. We see that the volume integral in equation (136) vanishes and we have

$$
\int_{\partial V} \hat{\mathbf{n}} \cdot \left[\vec{\mathbf{A}} \times \left(\nabla \times \overline{\overline{\Gamma}}^{(\ell)} \right) + \left(\nabla \times \vec{\mathbf{A}} \right) \times \overline{\overline{\Gamma}}^{(\ell)} \right] \, ds =
$$
$$
- \int_{\partial V_\delta} \hat{\mathbf{n}} \cdot \left[\vec{\mathbf{A}} \times \left(\nabla \times \overline{\overline{\Gamma}}^{(\ell)} \right) \right] \, ds
$$
$$
- \int_{\partial V_\delta} \hat{\mathbf{n}} \cdot \left[\left(\nabla \times \vec{\mathbf{A}} \right) \times \overline{\overline{\Gamma}}^{(\ell)} \right] \, ds, \quad \text{for } \vec{r}' \in V \quad (138)
$$

Now we are in the position to evaluate the right side of equation (138) in the limit as $\delta \to 0$. To do so, we consider the two integrals on the right side of equation (138) separately.

The First Integral.   Consider the first integral on the right side of equation (138),

$$
I_1(\delta) = - \int_{\partial V_\delta} \hat{\mathbf{n}} \cdot \left[\vec{\mathbf{A}}(\vec{r}) \times \left(\nabla \times \overline{\overline{\Gamma}}^{(\ell)}(\vec{r}, \vec{r}') \right) \right] \, ds \qquad (139)
$$

We establish a local spherical coordinate system $(\varrho, \vartheta, \varphi)$ centered at $\vec{r}'$. Without loss of generality, we let $\ell = 3$, so that the "north pole" of the local spherical coordinate system is aligned with $\hat{\mathbf{e}}_3 = \hat{\mathbf{z}}$, as shown in Figure 67. The spherical unit vectors are: $\hat{\varrho} = \sin \vartheta \cos \varphi \hat{\mathbf{x}} + \sin \vartheta \sin \varphi \hat{\mathbf{y}} + \cos \vartheta \hat{\mathbf{z}}$,

107

$\hat{\vartheta} = \cos\vartheta\cos\varphi\hat{\mathbf{x}} + \cos\vartheta\sin\varphi\hat{\mathbf{y}} - \sin\vartheta\hat{\mathbf{z}}$, and $\hat{\varphi} = -\sin\varphi\hat{\mathbf{x}} + \cos\varphi\hat{\mathbf{y}}$. Using the identity [47] $\vec{\mathbf{a}}\cdot(\vec{\mathbf{b}}\times\overline{\overline{\mathbf{c}}}) = -\vec{\mathbf{b}}\cdot(\vec{\mathbf{a}}\times\overline{\overline{\mathbf{c}}}) = (\vec{\mathbf{a}}\times\vec{\mathbf{b}})\cdot\overline{\overline{\mathbf{c}}}$ and noting that $\hat{\mathbf{n}} = -\hat{\varrho}$ on ∂V_δ, we can write

$$I_1(\delta) = \int_{\partial V_\delta} \left[\hat{\varrho}\times\vec{\mathbf{A}}(\vec{\mathbf{r}})\right]\cdot\left[\nabla\times\overline{\overline{\Gamma}}^{(\ell)}(\vec{\mathbf{r}},\vec{\mathbf{r}}')\right]\ ds \tag{140}$$

Since $\vec{\mathbf{A}}(\vec{\mathbf{r}})$ satisfies the homogeneous wave equation in the neighborhood of $\vec{\mathbf{r}}'$, we have that $\vec{\mathbf{A}}(\vec{\mathbf{r}})$ is infinitely differentiable at $\vec{\mathbf{r}} = \vec{\mathbf{r}}'$ and thus can be expanded in a Taylor series about $\vec{\mathbf{r}}'$ in the neighborhood of $\vec{\mathbf{r}}'$. Indeed, expressing $\vec{\mathbf{A}}(\vec{\mathbf{r}})$ in terms of its components in Cartesian coordinates as $\vec{\mathbf{A}}(\vec{\mathbf{r}}) = A_x(x,y,z)\hat{\mathbf{x}} + A_y(x,y,z)\hat{\mathbf{y}} + A_z(x,y,z)\hat{\mathbf{z}}$, we can write

$$\begin{aligned}
\hat{\varrho}\times\vec{\mathbf{A}}(\vec{\mathbf{r}}) = &\ \hat{\varphi}\left[A_x\cos\vartheta\cos\varphi + A_y\cos\vartheta\sin\varphi - A_z\sin\vartheta\right]\\
&+ \hat{\vartheta}[A_x\cos\varphi - A_y\sin\varphi]\\
&+ \delta\,\hat{\varphi}\left[\begin{array}{l}\dfrac{\partial A_x}{\partial x}\cos\vartheta\sin\vartheta\cos^2\varphi + \dfrac{\partial A_x}{\partial y}\cos\vartheta\sin\vartheta\cos\varphi\sin\varphi\\[2mm]
+\dfrac{\partial A_x}{\partial z}\cos^2\vartheta\cos\varphi + \dfrac{\partial A_y}{\partial x}\cos\vartheta\sin\vartheta\cos\varphi\sin\varphi\\[2mm]
+\dfrac{\partial A_y}{\partial y}\cos\vartheta\sin\vartheta\sin^2\varphi + \dfrac{\partial A_y}{\partial z}\cos^2\vartheta\sin\varphi\\[2mm]
-\dfrac{\partial A_z}{\partial x}\sin^2\vartheta\cos\varphi - \dfrac{\partial A_z}{\partial y}\sin^2\vartheta\sin\vartheta - \dfrac{\partial A_z}{\partial z}\cos\vartheta\sin\vartheta\end{array}\right]\\
&+ \delta\,\hat{\vartheta}\left[\begin{array}{l}\dfrac{\partial A_x}{\partial x}\sin\vartheta\cos\varphi\sin\varphi + \dfrac{\partial A_x}{\partial y}\sin\vartheta\sin^2\varphi + \dfrac{\partial A_x}{\partial z}\cos\vartheta\sin\varphi\\[2mm]
-\dfrac{\partial A_y}{\partial x}\sin\vartheta\cos^2\varphi - \dfrac{\partial A_y}{\partial y}\sin\vartheta\cos\varphi\sin\varphi - \dfrac{\partial A_y}{\partial z}\cos\vartheta\cos\varphi\end{array}\right]\\
&+ \mathcal{O}(\delta^2)
\end{aligned} \tag{141}$$

where the field components and their derivatives are evaluated at $\vec{\mathbf{r}} = \vec{\mathbf{r}}'$. Expressed in the same coordinates, the curl of $\overline{\overline{\Gamma}}^{(3)}(\vec{\mathbf{r}},\vec{\mathbf{r}}')$ is

$$\nabla\times\overline{\overline{\Gamma}}^{(3)}(\vec{\mathbf{r}},\vec{\mathbf{r}}') = -\jmath k\frac{e^{-\jmath k\varrho}}{4\pi\varrho^3}\left\{2\left(\jmath k\varrho + 1\right)\cos\vartheta\hat{\varrho} + \left[(\jmath k\varrho)^2 + \jmath k\varrho + 1\right]\sin\vartheta\hat{\vartheta}\right\}\hat{\mathbf{z}} \tag{142}$$

We apply these last two equations to the integral in equation (140). Noting that the differential surface $ds = \delta^2\sin\vartheta\,d\vartheta\,d\varphi$, we find

$$I_1(\delta) = \jmath k\frac{e^{-\jmath k\delta}}{4}\left[(\jmath k\delta)^2 + \jmath k\delta + 1\right]\left(\frac{\partial A_x}{\partial y} - \frac{\partial A_y}{\partial x}\right)\int_0^\pi\sin^3\vartheta\,d\vartheta\hat{\mathbf{z}} + \mathcal{O}(\delta) \tag{143}$$

108
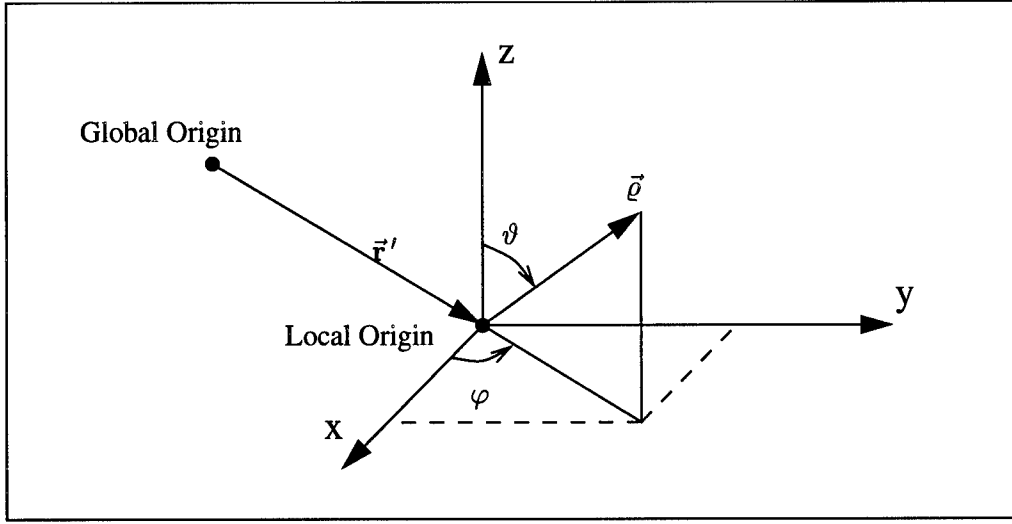
Figure 67   Local spherical coordinate system centered at $\vec{r}'$

Letting $\delta \to 0$, we have

$$\lim_{\delta \to 0} I_1(\delta) = \frac{jk}{3} \nabla' \times \vec{A}(\vec{r}') \cdot \hat{z}\hat{z} \tag{144}$$

The Second Integral.   Consider the second integral on the right side of equation (138),

$$I_2(\delta) = -\int_{\partial V_\delta} \hat{n} \cdot \left[\left(\nabla \times \vec{A}(\vec{r}) \right) \times \overline{\overline{\Gamma}}^{(3)}(\vec{r}, \vec{r}') \right] ds \tag{145}$$

Using the same identities as used in the previous section, $I_2(\delta)$ can be written as

$$I_2(\delta) = -\int_{\partial V_\delta} \left(\nabla \times \vec{A}(\vec{r}) \right) \cdot \left[\hat{\varrho} \times \overline{\overline{\Gamma}}^{(3)}(\vec{r}, \vec{r}') \right] ds \tag{146}$$

where $\hat{\varrho} \times \overline{\overline{\Gamma}}^{(3)}(\vec{r}, \vec{r}')$ is

$$\hat{\varrho} \times \overline{\overline{\Gamma}}^{(3)}(\vec{r}, \vec{r}') = jk \left(jk\varrho + 1 \right) \frac{e^{-jk\varrho}}{4\pi \varrho^2} \sin \vartheta \hat{\vartheta}\hat{z} \tag{147}$$

109

as expressed in the local spherical coordinates. Expanding $\nabla \times \vec{\mathbf{A}}(\vec{\mathbf{r}})$ in a Taylor series about $\vec{\mathbf{r}} = \vec{\mathbf{r}}'$, $I_2(\delta)$ becomes

$$I_2(\delta) = \frac{\jmath k}{2} \int_0^\pi \sin^3 \vartheta \, d\vartheta \left[\nabla' \times \vec{\mathbf{A}}(\vec{\mathbf{r}}') \right] \cdot \hat{\mathbf{z}}\hat{\mathbf{z}} + \mathcal{O}(\delta) \tag{148}$$

Letting $\delta \to 0$, we have

$$\lim_{\delta \to 0} I_2(\delta) = \frac{2\jmath k}{3} \nabla' \times \vec{\mathbf{A}}(\vec{\mathbf{r}}') \cdot \hat{\mathbf{z}}\hat{\mathbf{z}} \tag{149}$$

By taking the limit as V_δ becomes an infinitesimally small sphere (that is, $\delta \to 0$), and incorporating equations (144) and (149) into equation (138), we can write

$$\int_{\partial V} \hat{\mathbf{n}} \cdot \left[\vec{\mathbf{A}} \times \left(\nabla \times \overline{\overline{\Gamma}}^{(3)} \right) + \left(\nabla \times \vec{\mathbf{A}} \right) \times \overline{\overline{\Gamma}}^{(3)} \right] ds = \jmath k \nabla' \times \vec{\mathbf{A}}(\vec{\mathbf{r}}') \cdot \hat{\mathbf{z}}\hat{\mathbf{z}} \quad \text{for } \vec{\mathbf{r}}' \in V \tag{150}$$

Similarly, equation (150) holds for $\overline{\overline{\Gamma}}^{(1)}$ and $\overline{\overline{\Gamma}}^{(2)}$, with $\hat{\mathbf{z}}\hat{\mathbf{z}}$ replaced by $\hat{\mathbf{x}}\hat{\mathbf{x}}$ and $\hat{\mathbf{y}}\hat{\mathbf{y}}$, respectively. Hence we may write

$$\int_{\partial V} \hat{\mathbf{n}} \cdot \left[\vec{\mathbf{A}} \times \left(\nabla \times \overline{\overline{\Gamma}}^{(\ell)} \right) + \left(\nabla \times \vec{\mathbf{A}} \right) \times \overline{\overline{\Gamma}}^{(\ell)} \right] ds = \jmath k \nabla' \times \vec{\mathbf{A}}(\vec{\mathbf{r}}') \cdot \hat{\mathbf{e}}_\ell \hat{\mathbf{e}}_\ell \quad \text{for } \vec{\mathbf{r}}' \in V \tag{151}$$

where $\ell = 1, 2, 3$. By equation (135a), it follows from equation (151) that

$$\int_{\partial V} \hat{\mathbf{n}} \cdot \left[\vec{\mathbf{A}} \times \left(\nabla \times \overline{\overline{\Gamma}} \right) + \left(\nabla \times \vec{\mathbf{A}} \right) \times \overline{\overline{\Gamma}} \right] ds = \jmath k \nabla' \times \vec{\mathbf{A}}(\vec{\mathbf{r}}') \quad \text{for } \vec{\mathbf{r}}' \in V \tag{152}$$

Combining equations (137) and (152), we have

$$\int_B \hat{\mathbf{n}} \cdot \left\{ \vec{\mathbf{A}} \times \left[\nabla \times \overline{\overline{\Gamma}} \right] + \left[\nabla \times \vec{\mathbf{A}} \right] \times \overline{\overline{\Gamma}} \right\} ds = \begin{cases} \jmath k \nabla' \times \vec{\mathbf{A}}(\vec{\mathbf{r}}') & \text{for } \vec{\mathbf{r}}' \in V \\ 0 & \text{for } \vec{\mathbf{r}}' \notin \overline{V} \end{cases} \tag{153}$$

and the proof of Theorem 1 is complete. Notice that Theorem 1 yields no information for the case in which $\vec{\mathbf{r}}' \in \partial V$.

A distributional differential equation satisfied by $\overline{\overline{\Gamma}}$. In this section, we show that $\overline{\overline{\Gamma}}$ satisfies the distributional differential equation

$$\nabla \times \nabla \times \overline{\overline{\Gamma}} - k^2 \overline{\overline{\Gamma}} = -jk\nabla\delta(\vec{r} - \vec{r}') \times \overline{\overline{I}} \tag{154}$$

First, let $I_a(\vec{r}')$ be given by

$$I_a(\vec{r}') = -jk \int_V \vec{A} \cdot \left[\nabla\delta(\vec{r} - \vec{r}') \times \overline{\overline{I}}\right] dv \tag{155}$$

Using the identity $\vec{a} \cdot \left(\vec{b} \times \overline{\overline{I}}\right) = \vec{a} \times \vec{b}$, the above equation becomes

$$I_a(\vec{r}') = -jk \int_V \vec{A} \times \nabla\delta(\vec{r} - \vec{r}') \, dv \tag{156}$$

Noting $\nabla\delta(\vec{r} - \vec{r}') = -\nabla'\delta(\vec{r} - \vec{r}')$, using the vector identity $\nabla' \times (u\vec{a}) = u\nabla' \times \vec{a} - \vec{a} \times \nabla'u$, and noting $\nabla' \times \vec{A}(\vec{r}) = \vec{0}$, we have

$$I_a(\vec{r}') = -jk \int_V \nabla' \times \left[\delta(\vec{r} - \vec{r}')\vec{A}\right] dv \tag{157}$$

The curl operates on primed variables, and can be brought in front of the integral sign, giving us

$$I_a(\vec{r}') = -jk\nabla' \times \int_V \delta(\vec{r} - \vec{r}')\vec{A} \, dv \tag{158}$$

Exploiting the sifting property of the delta function, we have

$$I_a(\vec{r}') = \begin{cases} -jk\nabla' \times \vec{A}(\vec{r}') & \text{for } \vec{r}' \in V \\ 0 & \text{for } \vec{r}' \notin \overline{V} \end{cases} \tag{159}$$

Now, let $I_b(\vec{r}')$ be given by

$$I_b(\vec{r}') = \int_V \vec{A}(\vec{r}) \cdot \left[\nabla \times \nabla \times \overline{\overline{\Gamma}} - k^2\overline{\overline{\Gamma}}\right] dv \tag{160}$$

Noting that $\vec{\mathbf{A}}$ satisfies equation (2),

$$\nabla \times \nabla \times \vec{\mathbf{A}}(\vec{\mathbf{r}}) - k^2 \vec{\mathbf{A}}(\vec{\mathbf{r}}) = 0 \tag{161}$$

we have

$$I_b(\vec{\mathbf{r}}') = \int_V \left[\vec{\mathbf{A}} \cdot \left(\nabla \times \nabla \times \overline{\overline{\Gamma}} \right) - \left(\nabla \times \nabla \times \vec{\mathbf{A}} \right) \cdot \overline{\overline{\Gamma}} \right] dv \tag{162}$$

Using equation (136), we have

$$I_b(\vec{\mathbf{r}}') = -\int_{\partial V} \hat{\mathbf{n}} \cdot \left[\vec{\mathbf{A}} \times \left(\nabla \times \overline{\overline{\Gamma}} \right) + \left(\nabla \times \vec{\mathbf{A}} \right) \times \overline{\overline{\Gamma}} \right] ds \tag{163}$$

and in light of equation (153)

$$I_b(\vec{\mathbf{r}}') = \begin{cases} -\jmath k \nabla' \times \vec{\mathbf{A}}(\vec{\mathbf{r}}') & \text{for } \vec{\mathbf{r}}' \in V \\ 0 & \text{for } \vec{\mathbf{r}}' \notin \overline{V} \end{cases} \tag{164}$$

Comparing equations (159) and (164) we see that $I_a(\vec{\mathbf{r}}') = I_b(\vec{\mathbf{r}}')$ for $\vec{\mathbf{r}}' \notin \partial V$ and, due to the arbitrary nature of $\vec{\mathbf{A}}$ leads to

$$\nabla \times \nabla \times \overline{\overline{\Gamma}} - k^2 \overline{\overline{\Gamma}} = -\jmath k \nabla \delta(\vec{\mathbf{r}} - \vec{\mathbf{r}}') \times \overline{\overline{\mathbf{I}}} \tag{165}$$

Proof of Theorem 2

In this section, we prove Theorem 2. We will make use of some of the intermediate results of the first proof of Theorem 1 as presented in Section A. In particular, we will require the vector function $\vec{\mathbf{A}}(\vec{\mathbf{r}})$ and the dyadic function $\overline{\overline{\Gamma}}(\vec{\mathbf{r}}, \vec{\mathbf{r}}')$ to satisfy the same requirements as in Section A.

Examination of equations (14a) and (14b) along with equation (135b) reveals that we can write the auxiliary dyadic functions as

$$\overline{\overline{\Gamma}}_1(\vec{\mathbf{r}}, \vec{\mathbf{r}}') = \overline{\overline{\Gamma}}^{(1)}(\vec{\mathbf{r}}, \vec{\mathbf{r}}') + \overline{\overline{\Gamma}}^{(2)}(\vec{\mathbf{r}}, \vec{\mathbf{r}}') + \overline{\overline{\Gamma}}^{(3)}(\vec{\mathbf{r}}, \vec{\mathbf{r}}')$$
$$+ \overline{\overline{\Gamma}}^{(1)}(\vec{\mathbf{r}}, \vec{\mathbf{r}}_i') + \overline{\overline{\Gamma}}^{(2)}(\vec{\mathbf{r}}, \vec{\mathbf{r}}_i') - \overline{\overline{\Gamma}}^{(3)}(\vec{\mathbf{r}}, \vec{\mathbf{r}}_i') \tag{166}$$

112

Let V be regular volumetric region and V_i be its image with respect to the xy-plane. Let $V \cup V_i$ be empty; that is, V lies completely on one side of the xy-plane. Then we can consider three cases.

Case 1: $\vec{\mathbf{r}}' \in V$. Applying equation (151) in a straightforward manner to equation (166) allows us to write

$$\int_{\partial V} \hat{\mathbf{n}} \cdot \left\{ \vec{\mathbf{A}} \times \left[\nabla \times \overline{\overline{\Gamma}}_1 \right] + \left[\nabla \times \vec{\mathbf{A}} \right] \times \overline{\overline{\Gamma}}_1 \right\} \, ds = \jmath k \nabla' \times \vec{\mathbf{A}}(\vec{\mathbf{r}}') \qquad \text{for } \vec{\mathbf{r}}' \in V \qquad (167)$$

Case 2: $\vec{\mathbf{r}}_i' \in V$. Equation (151) does not apply directly to the present case in which $\vec{\mathbf{r}}_i' \in V$. Replacing z by $-z$ in the development of equation (151), we can derive the related equation

$$\int_{\partial V} \hat{\mathbf{n}} \cdot \left[\vec{\mathbf{A}} \times \left(\nabla \times \overline{\overline{\Gamma}}^{(\ell)} \right) + \left(\nabla \times \vec{\mathbf{A}} \right) \times \overline{\overline{\Gamma}}^{(\ell)} \right] \, ds$$
$$= \jmath k \nabla_i' \times \vec{\mathbf{A}}(\vec{\mathbf{r}}_i') \cdot \hat{\mathbf{e}}_\ell \hat{\mathbf{e}}_\ell \quad \text{for } \vec{\mathbf{r}}_i' \in V \qquad (168)$$

where

$$\nabla_i \times \vec{\mathbf{A}} = \left(\frac{\partial A_z}{\partial y} + \frac{\partial A_y}{\partial z} \right) \hat{\mathbf{x}} + \left(-\frac{\partial A_x}{\partial z} - \frac{\partial A_z}{\partial x} \right) \hat{\mathbf{y}} + \left(\frac{\partial A_y}{\partial x} - \frac{\partial A_x}{\partial y} \right) \hat{\mathbf{z}} \qquad (169)$$

Applying equation (168) to equation (166) allows us to write

$$\int_{\partial V} \hat{\mathbf{n}} \cdot \left\{ \vec{\mathbf{A}} \times \left[\nabla \times \overline{\overline{\Gamma}}_1 \right] + \left[\nabla \times \vec{\mathbf{A}} \right] \times \overline{\overline{\Gamma}}_1 \right\} \, ds = \jmath k \nabla_i' \times \vec{\mathbf{A}}(\vec{\mathbf{r}}_i') \cdot (\hat{\mathbf{x}}\hat{\mathbf{x}} + \hat{\mathbf{y}}\hat{\mathbf{y}} - \hat{\mathbf{z}}\hat{\mathbf{z}})$$
$$= \jmath k \left[\nabla_i' \times \vec{\mathbf{A}}(\vec{\mathbf{r}}_i') \right]_i \quad \text{for } \vec{\mathbf{r}}_i' \in V \qquad (170)$$

Case 3: $\vec{\mathbf{r}}' \notin \overline{V}$, $\vec{\mathbf{r}}_i' \notin \overline{V}$. When neither $\vec{\mathbf{r}}$ nor $\vec{\mathbf{r}}_i$ lie in the interior of V, then it is clear from equations (151), (168), and (166) that the surface integral on the boundary of V vanishes. That is,

$$\int_{\partial V} \hat{\mathbf{n}} \cdot \left\{ \vec{\mathbf{A}} \times \left[\nabla \times \overline{\overline{\Gamma}}_1 \right] + \left[\nabla \times \vec{\mathbf{A}} \right] \times \overline{\overline{\Gamma}}_1 \right\} \, ds = 0 \quad \text{for } \vec{\mathbf{r}}' \notin \overline{V} \text{ and } \vec{\mathbf{r}}_i' \notin \overline{V} \qquad (171)$$

Combining these three cases, we can write the single equation,

$$
\int_{\partial V} \hat{\mathbf{n}} \cdot \left\{ \vec{\mathbf{A}} \times \left[\nabla \times \bar{\bar{\Gamma}}_1 \right] + \left[\nabla \times \vec{\mathbf{A}} \right] \times \bar{\bar{\Gamma}}_1 \right\} \, ds
$$

$$
= \begin{cases} \jmath k \nabla' \times \vec{\mathbf{A}}(\vec{\mathbf{r}}') & \text{for } \vec{\mathbf{r}}' \in V \\ \jmath k \left[\nabla_i' \times \vec{\mathbf{A}}(\vec{\mathbf{r}}_i') \right]_i & \text{for } \vec{\mathbf{r}}' \in V_i \\ 0 & \text{for } \vec{\mathbf{r}}' \notin \overline{V} \text{ and } \vec{\mathbf{r}}' \notin \overline{V_i} \end{cases} \tag{172}
$$

and the proof of Theorem 2 is complete.

Proof of Theorem 3

The proof of Theorem 3 is exactly the same as the proof of Theorem 2 except that $\bar{\bar{\Gamma}}_1$ is replaced by $\bar{\bar{\Gamma}}_2$. This leads to

$$
\int_{\partial V} \hat{\mathbf{n}} \cdot \left\{ \vec{\mathbf{A}} \times \left[\nabla \times \bar{\bar{\Gamma}}_2 \right] + \left[\nabla \times \vec{\mathbf{A}} \right] \times \bar{\bar{\Gamma}}_2 \right\} \, ds
$$

$$
= \begin{cases} \jmath k \nabla' \times \vec{\mathbf{A}}(\vec{\mathbf{r}}') & \text{for } \vec{\mathbf{r}}' \in V \\ -\jmath k \left[\nabla_i' \times \vec{\mathbf{A}}(\vec{\mathbf{r}}_i') \right]_i & \text{for } \vec{\mathbf{r}}' \in V_i \\ 0 & \text{for } \vec{\mathbf{r}}' \notin \overline{V} \text{ and } \vec{\mathbf{r}}' \notin \overline{V_i} \end{cases} \tag{173}
$$

Appendix B. **Application of the Fundamental Theorems**

In this appendix, we present the results of applying Theorems 1, 2, and 3 to the OCRED geometry. Each application represents a choice of one from each of the following three sets:

- Theorem 1, Theorem 2, or Theorem 3.

- V is the cavity volume, D, or the upper half space (UHS), $z > 0$.

- $\vec{A}$ is the electric or magnetic field.

The table at the bottom of this page provides an index and gives the equation number corresponding to each combination. Significant algebraic manipulations are needed to arrive at the equations that follow, and will not be given here. The interested reader can verify any equation by exploiting vector and dyadic identities (all of which can be found in [62]), along with the boundary conditions satisfied by $\vec{E}$ on S and σ^c, and the boundary conditions satisfied by $\overline{\overline{\Gamma}}_1$ and $\overline{\overline{\Gamma}}_2$ on σ (see equations (15)–(16)).

Theorem 1, $V = D$, $\vec{A} = \vec{E}$:

$$
\int_\sigma \left[\hat{z} \times \vec{E}(\vec{r}) \right] \cdot \nabla \times \overline{\overline{\Gamma}}(k_1, \vec{r}, \vec{r}') \, d\sigma - jk_1 Z_1 \int_{S \cup \sigma} \left[\hat{n} \times \vec{H}(\vec{r}) \right] \cdot \overline{\overline{\Gamma}}(k_1, \vec{r}, \vec{r}') \, ds
$$

$$
= \begin{cases} k_1^2 Z_1 \vec{H}(\vec{r}') & \text{for } \vec{r}' \in D \\ 0 & \text{for } z' > 0 \end{cases} \tag{174}
$$

Table 8   Equation index for application of the fundamental theorems to the OCRED problem.

	Theorem 1	Theorem 2	Theorem 3
$V = D$, $\vec{A} = \vec{E}$	(174)	(178)	(182)
$V = D$, $\vec{A} = \vec{H}$	(175)	(179)	(183)
$V = \text{UHS}$, $\vec{A}^s = \vec{E}^s$	(176)	(180)	(184)
$V = \text{UHS}$, $\vec{A}^s = \vec{H}^s$	(177)	(181)	(185)

Theorem 1, $V = D$, $\vec{\mathbf{A}} = \vec{\mathbf{H}}$:

$$\int_\sigma \left[\hat{\mathbf{z}} \times \vec{\mathbf{E}}(\vec{\mathbf{r}}) \right] \cdot \overline{\overline{\Gamma}}(k_1, \vec{\mathbf{r}}, \vec{\mathbf{r}}') \, d\sigma + \frac{1}{\jmath k_1 Y_1} \int_{S \cup \sigma} \left[\hat{\mathbf{n}} \times \vec{\mathbf{H}}(\vec{\mathbf{r}}) \right] \cdot \nabla \times \overline{\overline{\Gamma}}(k_1, \vec{\mathbf{r}}, \vec{\mathbf{r}}') \, ds$$
$$= \begin{cases} \jmath k_1 \vec{\mathbf{E}}(\vec{\mathbf{r}}') & \text{for } \vec{\mathbf{r}}' \in D \\ 0 & \text{for } z' > 0 \end{cases} \quad (175)$$

Theorem 1, $V = UHS$, $\vec{\mathbf{A}} = \vec{\mathbf{E}}$:

$$\int_\sigma \left[\hat{\mathbf{z}} \times \vec{\mathbf{E}}(\vec{\mathbf{r}}) \right] \cdot \nabla \times \overline{\overline{\Gamma}}(k_0, \vec{\mathbf{r}}, \vec{\mathbf{r}}') \, d\sigma - \jmath k_0 Z_0 \int_{\sigma \cup \sigma^c} \left[\hat{\mathbf{z}} \times \vec{\mathbf{H}}^s(\vec{\mathbf{r}}) \right] \cdot \overline{\overline{\Gamma}}(k_0, \vec{\mathbf{r}}, \vec{\mathbf{r}}') \, d\sigma$$
$$= \begin{cases} 0 & \text{for } \vec{\mathbf{r}}' \in D \\ -k_0^2 Z_0 \vec{\mathbf{H}}^s(\vec{\mathbf{r}}') & \text{for } z' > 0 \end{cases} \quad (176)$$

Theorem 1, $V = UHS$, $\vec{\mathbf{A}} = \vec{\mathbf{H}}$:

$$\int_\sigma \left[\hat{\mathbf{z}} \times \vec{\mathbf{E}}(\vec{\mathbf{r}}) \right] \cdot \overline{\overline{\Gamma}}(k_0, \vec{\mathbf{r}}, \vec{\mathbf{r}}') \, d\sigma + \frac{1}{\jmath k_0 Y_0} \int_{\sigma \cup \sigma^c} \left[\hat{\mathbf{z}} \times \vec{\mathbf{H}}^s(\vec{\mathbf{r}}) \right] \cdot \nabla \times \overline{\overline{\Gamma}}(k_0, \vec{\mathbf{r}}, \vec{\mathbf{r}}') \, d\sigma$$
$$= \begin{cases} 0 & \text{for } \vec{\mathbf{r}}' \in D \\ -\jmath k_0 \vec{\mathbf{E}}^s(\vec{\mathbf{r}}') & \text{for } z' > 0 \end{cases} \quad (177)$$

Theorem 2, $V = D$, $\vec{\mathbf{A}} = \vec{\mathbf{E}}$:

$$2 \int_\sigma \left[\hat{\mathbf{z}} \times \vec{\mathbf{E}}(\vec{\mathbf{r}}) \right] \cdot \nabla \times \overline{\overline{\Gamma}}(k_1, \vec{\mathbf{r}}, \vec{\mathbf{r}}') \, d\sigma - \jmath k_1 Z_1 \int_S \left[\hat{\mathbf{n}} \times \vec{\mathbf{H}}(\vec{\mathbf{r}}) \right] \cdot \overline{\overline{\Gamma}}_1(k_1, \vec{\mathbf{r}}, \vec{\mathbf{r}}') \, ds$$

$$= \begin{cases} k_1^2 Z_1 \vec{\mathbf{H}}(\vec{\mathbf{r}}') & \text{for } \vec{\mathbf{r}}' \in D \\ k_1^2 Z_1 \vec{\mathbf{H}}_i(\vec{\mathbf{r}}_i') & \text{for } \vec{\mathbf{r}}' \in D_i \\ 0 & \text{for } \vec{\mathbf{r}}' \in D_f \end{cases} \quad (178)$$

Theorem 2, $V = D$, $\vec{\mathbf{A}} = \vec{\mathbf{H}}$:

$$2 \int_\sigma \left[\hat{\mathbf{z}} \times \vec{\mathbf{H}}(\vec{\mathbf{r}}) \right] \cdot \nabla \times \overline{\overline{\Gamma}}(k_1, \vec{\mathbf{r}}, \vec{\mathbf{r}}') \, d\sigma + \int_S \left[\hat{\mathbf{n}} \times \vec{\mathbf{H}}(\vec{\mathbf{r}}) \right] \cdot \nabla \times \overline{\overline{\Gamma}}_1(k_1, \vec{\mathbf{r}}, \vec{\mathbf{r}}') \, ds$$

$$= \begin{cases} -k_1^2 Y_1 \vec{\mathbf{E}}(\vec{\mathbf{r}}') & \text{for } \vec{\mathbf{r}}' \in D \\ -k_1^2 Y_1 \vec{\mathbf{E}}_i(\vec{\mathbf{r}}_i') & \text{for } \vec{\mathbf{r}}' \in D_i \\ 0 & \text{for } \vec{\mathbf{r}}' \in D_f \end{cases} \quad (179)$$

Theorem 2, $V = UHS$, $\vec{\mathbf{A}} = \vec{\mathbf{E}}^s$:

$$\int_\sigma \left[\hat{\mathbf{z}} \times \vec{\mathbf{E}}(\vec{\mathbf{r}}) \right] \cdot \nabla \times \overline{\overline{\Gamma}}(k_0, \vec{\mathbf{r}}, \vec{\mathbf{r}}') \, d\sigma = \begin{cases} \frac{-k_0^2 Z_0}{2} \vec{\mathbf{H}}_i^s(\vec{\mathbf{r}}_i') & \text{for } \vec{\mathbf{r}}' \in D \\ \frac{-k_0^2 Z_0}{2} \vec{\mathbf{H}}^s(\vec{\mathbf{r}}') & \text{for } z' > 0 \end{cases} \quad (180)$$

Theorem 2, $V = UHS$, $\vec{\mathbf{A}} = \vec{\mathbf{H}}^s$:

$$\int_{\sigma \cup \sigma^c} \left[\hat{\mathbf{z}} \times \vec{\mathbf{H}}^s(\vec{\mathbf{r}}) \right] \cdot \nabla \times \overline{\overline{\Gamma}}(k_0, \vec{\mathbf{r}}, \vec{\mathbf{r}}') \, d\sigma = \begin{cases} \frac{k_0^2 Y_0}{2} \vec{\mathbf{E}}_i^s(\vec{\mathbf{r}}_i{}') & \text{for } \vec{\mathbf{r}}' \in D \\[2mm] \frac{k_0^2 Y_0}{2} \vec{\mathbf{E}}^s(\vec{\mathbf{r}}') & \text{for } z' > 0 \end{cases} \tag{181}$$

Theorem 3, $V = D$, $\vec{\mathbf{A}} = \vec{\mathbf{E}}$:

$$2 \int_\sigma \left[\hat{\mathbf{z}} \times \vec{\mathbf{H}}(\vec{\mathbf{r}}) \right] \cdot \overline{\overline{\Gamma}}(k_1, \vec{\mathbf{r}}, \vec{\mathbf{r}}') \, d\sigma + \int_S \left[\hat{\mathbf{n}} \times \vec{\mathbf{H}}(\vec{\mathbf{r}}) \right] \cdot \overline{\overline{\Gamma}}_2(k_1, \vec{\mathbf{r}}, \vec{\mathbf{r}}') \, ds$$

$$= \begin{cases} \jmath k_1 \vec{\mathbf{H}}(\vec{\mathbf{r}}') & \text{for } \vec{\mathbf{r}}' \in D \\[2mm] -\jmath k_1 \vec{\mathbf{H}}_i(\vec{\mathbf{r}}_i{}') & \text{for } \vec{\mathbf{r}}' \in D_i \\[2mm] 0 & \text{for } \vec{\mathbf{r}}' \in D_f \end{cases} \tag{182}$$

Theorem 3, $V = D$, $\vec{\mathbf{A}} = \vec{\mathbf{H}}$:

$$2 \int_\sigma \left[\hat{\mathbf{z}} \times \vec{\mathbf{E}}(\vec{\mathbf{r}}) \right] \cdot \overline{\overline{\Gamma}}(k_1, \vec{\mathbf{r}}, \vec{\mathbf{r}}') \, d\sigma + \frac{1}{\jmath k_1 Y_1} \int_S \left[\hat{\mathbf{n}} \times \vec{\mathbf{H}}(\vec{\mathbf{r}}) \right] \cdot \nabla \times \overline{\overline{\Gamma}}_2(k_1, \vec{\mathbf{r}}, \vec{\mathbf{r}}') \, ds$$

$$= \begin{cases} \jmath k_1 \vec{\mathbf{E}}(\vec{\mathbf{r}}') & \text{for } \vec{\mathbf{r}}' \in D \\[2mm] -\jmath k_1 \vec{\mathbf{E}}_i(\vec{\mathbf{r}}_i{}') & \text{for } \vec{\mathbf{r}}' \in D_i \\[2mm] 0 & \text{for } \vec{\mathbf{r}}' \in D_f \end{cases} \tag{183}$$

Theorem 3, $V = UHS$, $\vec{\mathbf{A}} = \vec{\mathbf{E}}^s$:

$$\int_{\sigma \cup \sigma^c} \left[\hat{\mathbf{z}} \times \vec{\mathbf{H}}^s(\vec{\mathbf{r}}) \right] \cdot \overline{\overline{\Gamma}}(k_0, \vec{r}, \vec{r}') \, d\sigma = \begin{cases} \frac{\jmath k_0}{2} \vec{\mathbf{H}}_i^s(\vec{\mathbf{r}}_i{}') & \text{for } \vec{r}' \in D \\ \frac{-\jmath k_0}{2} \vec{\mathbf{H}}^s(\vec{\mathbf{r}}') & \text{for } z' > 0 \end{cases} \tag{184}$$

Theorem 3, $V = UHS$, $\vec{\mathbf{A}} = \vec{\mathbf{H}}^s$:

$$\int_{\sigma \cup \sigma^c} \left[\hat{\mathbf{z}} \times \vec{\mathbf{E}}(\vec{\mathbf{r}}) \right] \cdot \overline{\overline{\Gamma}}(k_0, \vec{r}, \vec{r}') \, d\sigma = \begin{cases} \frac{-\jmath k_0}{2} \vec{\mathbf{E}}_i^s(\vec{\mathbf{r}}_i{}') & \text{for } \vec{r}' \in D \\ \frac{\jmath k_0}{2} \vec{\mathbf{E}}^s(\vec{\mathbf{r}}') & \text{for } z' > 0 \end{cases} \tag{185}$$

Appendix C. Regularization of a Singular Integral

When formulating the expressions for the elements of Z_m^{12} and Z_m^{13}, we must deal with an iterated surface integral of the form

$$I = \int_{S_1} \int_{S_2} \vec{A}(\vec{r}') \cdot \hat{n}' \times \left[\vec{B}(\vec{r}) \cdot \nabla \nabla G(k; \vec{r}, \vec{r}') \right] ds \, ds' \tag{186}$$

where S_1 and S_2 are regular surfaces, $\vec{A}(\vec{r}')$ is defined on S_1, $\vec{B}(\vec{r})$ is defined on S_2, $\hat{n}'$ is the unit normal vector on S_1 at the point defined by $\vec{r}'$, and $\hat{n}$ has a similar relationship with S_2 and $\vec{r}$. The unit normal vectors vary continuously almost everywhere on their domains. We further suppose that $\hat{n}' \cdot \vec{A}(\vec{r}') = 0$ on S_1 and that $\hat{n} \cdot \vec{B}(\vec{r}) = 0$ on S_2; that is, $\vec{A}$ and $\vec{B}$ have only tangential components on their respective domains. The kernel of equation (186) is $\nabla \nabla G(k; \vec{r}, \vec{r}')$, which can be written as

$$\nabla \nabla G(k; \vec{r}, \vec{r}') = \left\{ \left[3 + 3jkR + (jkR)^2 \right] \hat{R} \hat{R} - (1 + jkR) \bar{\bar{I}} \right\} \frac{e^{-jkR}}{4\pi R^3} \tag{187}$$

where $R = |\vec{r} - \vec{r}'|$ and $\hat{R} = (\vec{r} - \vec{r}') / R$. From equation (187) we see that

$$\nabla \nabla G(k; \vec{r}, \vec{r}') \sim \left(3\hat{R}\hat{R} - \bar{\bar{I}} \right) \frac{1}{4\pi R^3} \quad \text{for } \vec{r} \to \vec{r}' \tag{188}$$

Let $R_{\min}$ be the minimum value of R for any $\vec{r}' \in S_1$ and $\vec{r} \in S_2$. If S_1 and S_2 do not overlap, then $R_{\min} > 0$, $\nabla \nabla G(k; \vec{r}, \vec{r}')$ is bounded, and the integral in equation (186) exists and is uniformly convergent. However, if $R_{\min}$ is small, then the absolute value of the kernel of equation (186) will be $\mathcal{O}(R_{\min}^{-3})$ when $\vec{r}'$ is near $\vec{r}$, and numerical integration techniques may have poor convergence properties. If S_1 and S_2 overlap, then the integral in equation (186) must be treated very carefully. We may consider the overlapping case to be the limit of a non-overlapping case as $R_{\min} \to 0$. Wilson [65] establishes the existence of this integral, but its numerical evaluation is cumbersome and computationally expensive. We now show a method by which equation (186) may be transformed into a form that is much more amenable to numerical computation.

Let S_1 and S_2 be two regular surfaces that do not overlap, as shown in Figure 68. Also, let $\vec{A}(\vec{r}')$ and $\vec{B}(\vec{r})$ be continuous, differentiable vector functions defined on S_1 and S_2, respectively.
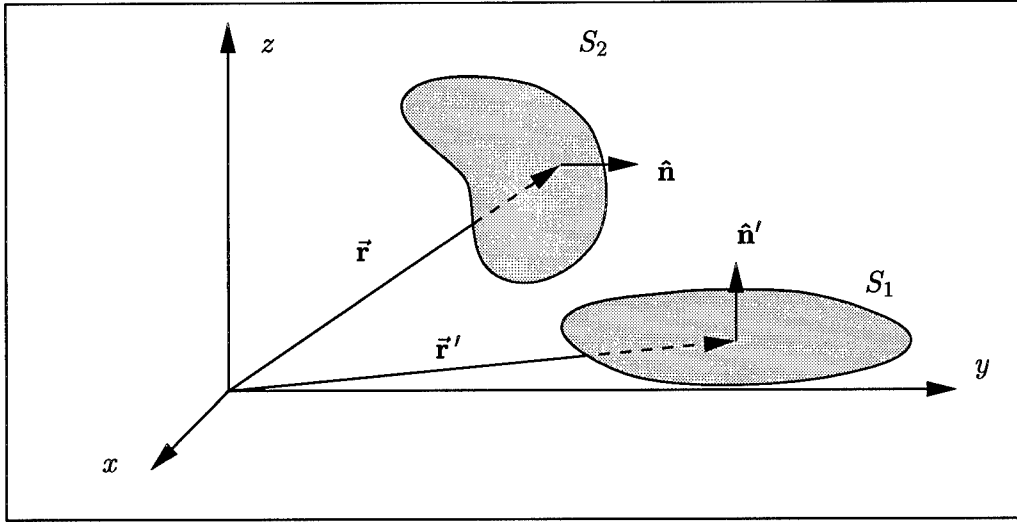
Figure 68   Geometry used in regularization procedure. Regular surfaces S_1 and S_2 do not overlap. $\vec{r} \in S_2$ and $\hat{n}$ is the unit normal on S_2 at $\vec{r}$. $\vec{r}' \in S_1$ and $\hat{n}'$ is the unit normal on S_1 at $\vec{r}'$.

Because the surface integrals in equation (186) are uniformly convergent, we may write

$$I = \int_{S_1} \vec{A}(\vec{r}') \cdot \hat{n}' \times \vec{C}(\vec{r}') \, ds' \tag{189a}$$

where

$$\vec{C}(\vec{r}') = \int_{S_2} \vec{B}(\vec{r}) \cdot \nabla\nabla G(k; \vec{r}, \vec{r}') \, ds \tag{189b}$$

Since $\vec{B}(\vec{r})$ is everywhere tangent to S_2, then $\vec{B}(\vec{r}) = \hat{n} \times \left[\vec{B}(\vec{r}) \times \hat{n} \right]$ so that

$$\vec{C}(\vec{r}') = \int_{S_2} \left\{ \hat{n} \times \left[\vec{B}(\vec{r}) \times \hat{n} \right] \right\} \cdot \nabla\nabla G(k; \vec{r}, \vec{r}') \, ds \tag{190}$$

Using the identity $\left(\vec{a} \times \vec{b} \right) \cdot \overline{\overline{c}} = \vec{a} \cdot \left(\vec{b} \times \overline{\overline{c}} \right)$ with $\vec{a} = \hat{n}$, $\vec{b} = \vec{B}(\vec{r}) \times \hat{n}$ and $\overline{\overline{c}} = \nabla\nabla G(k; \vec{r}, \vec{r}')$, equation (190) becomes

$$\vec{C}(\vec{r}') = \int_{S_2} \hat{n} \cdot \left\{ \left[\vec{B}(\vec{r}) \times \hat{n} \right] \times \nabla\nabla G(k; \vec{r}, \vec{r}') \right\} \, ds \tag{191}$$

121

Using another identity, namely $\nabla \times \left(\vec{a}\vec{b} \right) = (\nabla \times \vec{a})\,\vec{b} - \vec{a} \times \nabla\vec{b}$ with $\vec{a} = \vec{B}(\vec{r}) \times \hat{n}$ and $\vec{b} = \nabla G(k; \vec{r}, \vec{r}')$, equation (191) becomes

$$\vec{C}(\vec{r}') = \int_{S_2} \hat{n} \cdot \nabla \times \left[\vec{B}(\vec{r}) \times \hat{n} \right]\, \nabla G(k; \vec{r}, \vec{r}')\, ds$$
$$- \int_{S_2} \hat{n} \cdot \nabla \times \left\{ \left[\vec{B}(\vec{r}) \times \hat{n} \right] \nabla G(k; \vec{r}, \vec{r}') \right\}\, ds \qquad (192)$$

We introduce a dyadic form of Stokes' Theorem:

$$\int_S \hat{n} \cdot \nabla \times \bar{\bar{a}}\, ds = \oint_{\partial S} d\vec{c} \cdot \bar{\bar{a}} \qquad (193)$$

where the line integral is traversed in the positive sense with respect to the unit normal vector $\hat{n}$ (i.e., in accordance with the right-hand rule). Applying equation (193) to the second integral in equation (192), we have

$$\vec{C}(\vec{r}') = \int_{S_2} \hat{n} \cdot \nabla \times \left[\vec{B}(\vec{r}) \times \hat{n} \right]\, \nabla G(k; \vec{r}, \vec{r}')\, ds$$
$$- \oint_{\partial S_2} \nabla G(k; \vec{r}, \vec{r}') \left[\vec{B}(\vec{r}) \times \hat{n} \right] \cdot d\vec{c} \qquad (194)$$

The first integral in equation (194) may be simplified by noting that

$$\hat{n} \cdot \nabla \times \left[\vec{B}(\vec{r}) \times \hat{n} \right] = -\nabla_s \cdot \vec{B}(\vec{r}) \qquad (195)$$

where "$\nabla_s \cdot$" is the surface divergence operator [62, page 501]. Then equation (194) becomes

$$\vec{C}(\vec{r}') = - \int_{S_2} \nabla_s \cdot \vec{B}(\vec{r})\, \nabla G(k; \vec{r}, \vec{r}')\, ds$$
$$- \oint_{\partial S_2} \nabla G(k; \vec{r}, \vec{r}') \left[\vec{B}(\vec{r}) \times \hat{n} \right] \cdot d\vec{c} \qquad (196)$$

Combining equation (196) with equation (189a), and noting $\nabla' G(k; \vec{r}, \vec{r}') = -\nabla G(k; \vec{r}, \vec{r}')$, we obtain

$$I = \int_{S_1} \int_{S_2} \vec{A}(\vec{r}') \cdot \left[\hat{n}' \times \nabla' G(k; \vec{r}, \vec{r}') \right] \ \nabla_s \cdot \vec{B}(\vec{r}) \ ds \ ds'$$
$$+ \int_{S_1} \oint_{\partial S_2} \vec{A}(\vec{r}') \cdot \left[\hat{n}' \times \nabla' G(k; \vec{r}, \vec{r}') \right] \ \left[\vec{B}(\vec{r}) \times \hat{n} \right] \cdot d\vec{c} \ ds' \qquad (197)$$

or

$$I = \int_{S_2} D(\vec{r}) \ \nabla_s \cdot \vec{B}(\vec{r}) \ ds + \oint_{\partial S_2} D(\vec{r}) \ \left[\vec{B}(\vec{r}) \times \hat{n} \right] \cdot d\vec{c} \qquad (198a)$$

with

$$D(\vec{r}) = \int_{S_1} \vec{A}(\vec{r}') \cdot \hat{n}' \times \nabla' G(k; \vec{r}, \vec{r}') \ ds' \qquad (198b)$$

Using the identity $\vec{a} \cdot \left(\vec{b} \times \vec{c} \right) = \vec{b} \cdot (\vec{c} \times \vec{a})$, equation (198b) becomes

$$D(\vec{r}) = \int_{S_1} \hat{n}' \cdot \left[\nabla' G(k; \vec{r}, \vec{r}') \times \vec{A}(\vec{r}') \right] \ ds' \qquad (199)$$

Using another vector identity, namely $\nabla' \times (\phi \vec{a}) = \nabla' \phi \times \vec{a} + (\nabla' \times \vec{a}) \phi$ with $\phi = G(k; \vec{r}, \vec{r}')$ and $\vec{a} = \vec{A}(\vec{r}')$, equation (199) becomes

$$D(\vec{r}) = \int_{S_1} \hat{n}' \cdot \nabla' \times \left[G(k; \vec{r}, \vec{r}') \vec{A}(\vec{r}') \right] \ ds'$$
$$- \int_{S_1} \hat{n}' \cdot \nabla' \times \vec{A}(\vec{r}') \ G(k; \vec{r}, \vec{r}') \ ds' \qquad (200)$$

Using a vector form of Stokes' Theorem,

$$\int_{S} \hat{n}' \cdot \nabla' \times \vec{a}(\vec{r}') \ ds' = \oint_{\partial S} \vec{a}(\vec{r}') \cdot d\vec{c}' \qquad (201)$$

equation (200) may be written as

$$D(\vec{r}) = \oint_{\partial S_1} G(k;\vec{r},\vec{r}') \, \vec{A}(\vec{r}') \cdot d\vec{c}' - \int_{S_1} \hat{n}' \cdot \nabla' \times \vec{A}(\vec{r}') \, G(k;\vec{r},\vec{r}') \, ds' \qquad (202)$$

The second integral in equation (202) may be simplified by noting that $\vec{A}(\vec{r}')$ is everywhere tangent to S_1, so that $\vec{A}(\vec{r}') = \left[\hat{n}' \times \vec{A}(\vec{r}') \right] \times \hat{n}'$. Then, incorporating equation (195), equation (202) becomes

$$D(\vec{r}) = \oint_{\partial S_1} G(k;\vec{r},\vec{r}') \, \vec{A}(\vec{r}') \cdot d\vec{c}' + \int_{S_1} G(k;\vec{r},\vec{r}') \, \nabla'_s \cdot \left[\hat{n}' \times \vec{A}(\vec{r}') \right] \, ds' \qquad (203)$$

Finally, we combine equation (203) with equation (198a) to get

$$\begin{aligned} I = & \int_{S_1} \int_{S_2} G(k;\vec{r},\vec{r}') \, \nabla_s \cdot \vec{B}(\vec{r}) \, \nabla'_s \cdot \left[\hat{n}' \times \vec{A}(\vec{r}') \right] \, ds \, ds' \\ & + \int_{S_2} \oint_{\partial S_1} G(k;\vec{r},\vec{r}') \, \nabla_s \cdot \vec{B}(\vec{r}) \, \vec{A}(\vec{r}') \cdot d\vec{c}' \, ds \\ & + \int_{S_1} \oint_{\partial S_2} G(k;\vec{r},\vec{r}') \, \nabla'_s \cdot \left[\hat{n}' \times \vec{A}(\vec{r}') \right] \, \left[\vec{B}(\vec{r}) \times \hat{n} \right] \cdot d\vec{c} \, ds' \\ & + \oint_{\partial S_1} \oint_{\partial S_2} G(k;\vec{r},\vec{r}') \, \left[\vec{B}(\vec{r}) \times \hat{n} \right] \cdot d\vec{c} \, \vec{A}(\vec{r}') \cdot d\vec{c}' \end{aligned} \qquad (204)$$

This proves Theorem 5.

If we compare equation (204) with equation (186), we see that the order of the singularity of the integrand has been reduced from R^{-3} to R^{-1}. This has been accomplished at the cost of requiring that the vector functions $\vec{A}$ and $\vec{B}$ have bounded derivatives everywhere on their domains and evaluating additional integrals on the boundaries of S_1 and S_2. These additional integrals need not always be numerically evaluated. They must be considered only if $\vec{A}(\vec{r}')$ has a non-vanishing tangential component on ∂S_1, or if $\vec{B}(\vec{r}) \times \hat{n}$ has a non-vanishing tangential component on ∂S_2.

The advantage of equation (204) over equation (186) can be illustrated by the following numerical example. Let S_1 be a 1λ-radius disk in the xy-plane, centered at the origin. Let S_2 be a 1λ-radius disk parallel to S_1, centered at $(0, 0, \delta)$, $\delta > 0$. This geometry is shown in Figure 69.
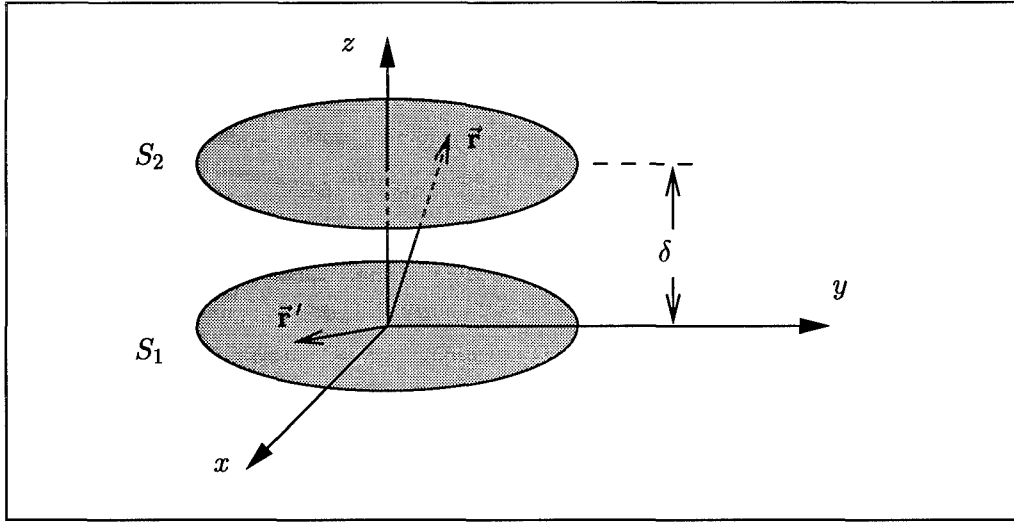
Figure 69   Geometry for numerical example. S_1 is a 1λ-radius disk centered at $(0,0,0)$. S_2 is a 1λ-radius disk centered at $(0,0,\delta)$. Both are parallel to the xy-plane. The vectors are such that $\vec{r}' \in S_1$ and $\vec{r} \in S_2$.

Define $\vec{A}(\vec{r}')$ and $\vec{B}(\vec{r})$ as

$$\vec{A}(\vec{r}') = \frac{1 - |2\rho' - 1|}{\rho'}\, e^{j\phi'}\, \hat{\phi}' \tag{205a}$$

$$\vec{B}(\vec{r}') = \frac{1 - |2\rho - 1|}{\rho}\, e^{j\phi}\, \hat{\rho}' \tag{205b}$$

with $\rho' = |\vec{r}'|$, $\rho = |\vec{r} - \delta\hat{z}|$, $\hat{\phi}' = -\hat{x}\sin\phi' + \hat{y}\cos\phi'$, $\hat{\rho} = \hat{x}\cos\phi + \hat{y}\sin\phi$. Since both $\vec{A}(\vec{r}')$ and $\vec{B}(\vec{r})$ vanish on the boundaries of their respective domains, only the first integral in equation (204) survives. The surface divergences are

$$\nabla_s' \cdot \left[\hat{n}' \times \vec{A}(\vec{r}')\right] = \pm\frac{2}{\rho'}\, e^{j\phi'} \tag{206a}$$

$$\nabla_s \cdot \vec{B}(\vec{r}') = \pm\frac{2}{\rho}\, e^{j\phi} \tag{206b}$$

where the positive sign is taken when ρ' or ρ is less than 0.5λ and the negative sign is taken otherwise. A computer program was written to calculate I using the formulation of equation (186) and of equation (204). Figure 70 shows the results for various values of the separation distance δ and the Gauss-Legendre quadrature order N_g. With δ held constant the formulation of equation (186) converges very slowly as N_g increases, and with N_g held constant it diverges as δ decreases. In

125

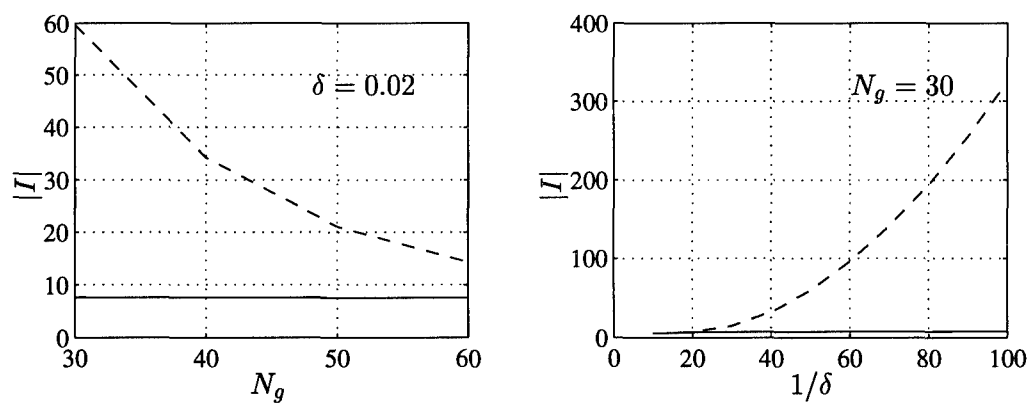Figure 70   Magnitude of I for as a function of quadrature order N_g with $\delta = 0.02$, and as a function of δ with $N_g = 30$. Equation (186) formulation is plotted as a dashed line; equation (204) formulation is plotted as a solid line.

contrast, the formulation of equation (204) is quite well-behaved. Thus, equation (204) requires far fewer computational resources to evaluate than equation (186).

Bibliography

1. Asvestas, J.S. "Scattering by an indentation satisfying a dyadic impedance boundary condition," *IEEE Transactions on Antennas and Propagation*, *45*(1):28–33 (January 1997).

2. Asvestas, J.S. and Kleinman, R.E. "Electromagnetic scattering by indented screens," *IEEE Transactions on Antennas and Propagation*, *42*(1):22–30 (January 1994).

3. Barkeshli, K. "Scattering from loaded grooves," *International Journal of Infrared and Millimeter Waves*, *13*(2):171–96 (February 1992).

4. Barkeshli, K. and Volakis, J. L. "Electromagnetic scattering from an aperture formed by rectangular cavity recessed in a ground plane," *Journal of Electromagnetic Waves and Applications*, *5*(7):715–734 (1991).

5. Blume, S. and Klinkenbusch, L. "Scattering of a plane electromagnetic wave by a spherical shell with an elliptical aperture," *IEEE Transactions on Electromagnetic Compatibility*, *34*(3):308–314 (August 1992).

6. Burden, R.L. and Faires, J.D. *Numerical Analysis* (Third Edition). Boston: Prindle, Weber & Schmidt, 1985.

7. Burkholder, R.J. "Two ray shooting methods for computing the EM scattering by large open-ended cavities," *Computer Physics Communications*, *68*(1-3):353–65 (November 1991).

8. Butler, C. M., et al. "Electromagnetic penetration through apertures in conducting surfaces," *IEEE Transactions on Antennas and Propagation*, *26*(1):82–93 (January 1978).

9. Chou, R.-C. "The modelling and the electromagnetic scattering from bifurcated open-ended cavities," *International Journal of Numerical Modelling: Electronic Networks, Devices and Fields*, *7*(3):167–77 (May-June 1994).

10. Collin, R.E. "Rayleigh scattering and power conservation," *IEEE Transactions on Antennas and Propagation*, *AP-29*(5):795–798 (September 1981).

11. Colton, D. L. and Kress, R. *Integral Equation Methods in Scattering Theory*. Wiley, 1983.

12. Crispin, J.W. and Siegel, K.M., editors. *Methods of Radar Cross-Section Analysis*. New York: Academic Press, 1968.

13. Dominek, A.K. "RCS measurement of small circular holes," *IEEE Transactions on Antennas and Propagation*, *36*(10):1495–1497 (October 1988).

14. Fairbanks, R. *Coupled Integral Equation Solution for Two-Dimensional Bistatic TE Scatter from a Conducting Cavity-Backed Infinite Plane*. MS thesis, Air Force Institute of Technology, Wright-Patterson Air Force Base, OH, December 1988.

15. Garcia-Pino, A. "Scattering from conducting open cavities by generalized ray expansion (GRE)," *IEEE Transactions on Antennas and Propagation*, *41*(7):989–92 (July 1993).

16. Gedney, S.D. and Mittra, R. "A hybrid method for the solution of the electromagnetic scattering by an inhomogeneously filled trough or slit in thick conducting screen." *1990 International*

Symposium Digest. Antennas And Propagation. Institute of Electrical and Electronics Engineers. Merging Technologies for the 90's (Cat. No. 90CH2776-3)4. 1730–3. 1990.

17. Goggans, P. M. and Shumpert, T. H. "CFIE MM solution for TE and TM incidence on a 2-D conducting body with dielectric filled cavity," *IEEE Transactions on Antennas and Propagation, 38*(10):1645–1649 (October 1991).

18. Golub, G.H. and Van Loan, C.F. *Matrix Computations* (Second Edition). The Johns Hopkins University Press, 1989.

19. Gradshteyn, I.S. and Ryzhik, I.M. *Table of Integrals, Series, and Products* (Fourth Edition). San Diego, CA: Academic Press, Inc, 1980.

20. Hansen, T. B. and Yaghjian, A. D. "Low-frequency scattering from two-dimensional perfect conductors," *IEEE Transactions on Antennas and Propagation, 40*(11):1389–1402 (November 1992).

21. Harrington, R.F. *Time-Harmonic Electromagnetic Fields.* New York: McGraw-Hill, 1961.

22. Harrington, R.F. *Field Computation by Moment Methods.* New York: Macmillan, 1968.

23. Harrington, R.F and Mautz, J.R. "A generalized network formulation for aperture problems," *IEEE Transactions on Antennas and Propagation,* 870–873 (November 1976).

24. Jeng, S.-K. "Scattering from a cavity-backed slit in a ground plane – TE case," *IEEE Transactions on Antennas and Propagation, 38*(10):1523–9 (October 1990).

25. Jeng, S.-K. and Tzeng, S.-T. "Scattering from a cavity-backed slit in a ground plane – TM case," *IEEE Transactions on Antennas and Propagation, 39*(5):661–663 (May 1991).

26. Jin, J.-M. and Volakis, J.L. "TM scattering by an inhomogeneously filled aperture in thick conducting plane," *IEE Proceedings. H, Microwaves, Antennas, and Propagation, 137*(3):153 (June 1990).

27. Jin, Jian-Ming and Volakis, John L. "A finite-element-boundary integral formulation for scattering by three-dimensional cavity-backed apertures," *IEEE Transactions on Antennas and Propagation, 39*(1):97–104 (January 1991).

28. Jin, Jian-Ming and Volakis, John L. "Electromagnetic scattering by and transmission through a three-dimensional slot in a thick conducting plane," *IEEE Transactions on Antennas and Propagation, 39*(4):543–550 (April 1991).

29. Jin, J.M. and Volakis, J.L. "TE scattering by an inhomogeneously filled aperture in thick conducting plane," *IEEE Transactions on Antennas and Propagation, 38*(8):1280 (August 1990).

30. Jones, D. S. *Methods in Electromagnetic Wave Propagation* (Second Edition). Oxford: Clarendon Press, 1994.

31. Jones, D.S. *The Theory of Electromagnetism.* New York: MacMillan, 1964. QC670.J63.

32. Kempel, L. C. and Senior, T. B. A. "Scattering by a small cavity-backed hole," *IEEE Transactions on Antennas and Propagation, 41*(8):1115–1121 (August 1993).

33. Knott, E.F., et al. *Radar Cross Section.* Norwood, MA: Artech House, 1985.

128

34. Lee, R. and T.-T. Chia. "Analysis of electromagnetic scattering from a cavity with a complex termination by means of a hybrid ray-FDTD method," *IEEE Transactions on Antennas and Propagation, 41*(11):1560–9 (1993).

35. Liang, C.-H. and Cheng, D. "Electromagnetic fields coupled into a cavity with a slot-aperture under resonant conditions," *IEEE Transactions on Antennas and Propagation, 30*(4):664–672 (July 1982).

36. Ling, H. "High-frequency RCS of open cavities with rectangular and circular cross sections," *IEEE Transactions on Antennas and Propagation, 37*(5):648–654 (1989).

37. Ling, H. "Shooting and bouncing rays: calculating the RCS of an arbitrarily shaped cavity," *IEEE Transactions on Antennas and Propagation, 37*(2):194–205 (February 1989).

38. Ling, H, et al. "Shooting and bouncing rays: calculating the RCS of an arbitrarily shaped cavity," *IEEE Transactions on Antennas and Propagation, 37*(2):194–205 (February 1989).

39. Luebbers, R. and Penney, C. "Scattering from apertures in infinite ground planes using FDTD," *IEEE Transactions on Antennas and Propagation, 42*(5):731 (May 1994).

40. Maue, A.W. "On the formulation of a general scattering problem by means of an integral equation," *Z. Phys., 126*(7):601–618 (1949).

41. Mautz, J.R. and Harrington, R.F. "Radiation and scattering from bodies of revolution," *Applied Scientific Research, 20*(6):405–435 (June 1969).

42. Mautz, J.R. and Harrington, R.F. "H-field, E-field, and combined-field solutions for conducting bodies of revolution," *Archiv fur Elektronik Ubertragungstechnik (Electron. Commun.), 32*(4):157–164 (1978). OCLC 1481946.

43. Mautz, J.R. and Harrington, R.F. "A combined-source solution for radiation and scattering from a perfectly conducting body," *IEEE Transactions on Antennas and Propagation, 27*:445–454 (July 1979).

44. Medgyesi-Mitschang, L.N. and Putnam, J.M. "Electromagnetic scattering from axially inhomogeneous bodies of revolution," *ieee-tap, AP–32*(8):797–806 (August 1984).

45. Meixner, J. "The behavior of electromagnetic fields at edges," *IEEE Transactions on Antennas and Propagation, 20*(4):442–446 (July 1972).

46. Monegato, G. "Numerical evaluation of hypersingular integrals," *Journal of Computational and Applied Mathematics, 50*:9–31 (1994).

47. Morse, P. M. and Feshbach, H. *Methods of Theoretical Physics.* New York: McGraw-Hill, 1953.

48. Müller, C. *Foundations of the Mathematical Theory of Electromagnetic Waves.* Springer-Verlag, 1969.

49. Pathak, P.H. "High-frequency electromagnetic scattering by open-ended waveguide cavities," *Radio Science, 26*(1):211–18 (Jan.-Feb. 1989).

50. Penney, C.W. and Luebbers, R.J. "Input impedance, radiation pattern, and radar cross section of spiral antennas using FDTD," *IEEE Transactions on Antennas and Propagation, 42*(9):1328–32 (1994).

51. Peterson, A.F. "The "interior resonance" problem associated with surface integral equations of electromagnetics: numerical consequences and a survey of remedies," *Electromagnetics*, *10*:293–312 (1990).

52. Plocharski, J., et al. "Conductivity of doped polyacetylenes and their morphology," *Synthetic Metals, 37*(s 1-3):7 (August 1990).

53. Rahman, B. M. A. "Penalty function improvement of waveguide solution by finite elements," *IEEE Transactions on Microwave Theory and Techniques, 32*:922–928 (August 1984).

54. Rao, S.M., et al. "Electromagnetic scattering by surfaces of arbitrary shape," *IEEE Transactions on Antennas and Propagation, AP-30*(3):409–418 (May 1982).

55. Ruck, G.T. *et al. Radar Cross Section Handbook.* Plenum, 1970.

56. Said, R. A. and Hamid, M. "Scattering by a thin multicoated perfectly conducting spherical shell with a circular aperture," *Canadian Journal of Physics, 70*:164–172 (February 1992).

57. Saunders, W. K. "On solutions of Maxwell's equations in an exterior region," *Proc. Natl. Acad. Sci., 38*(4):342–348 (1952).

58. Senior, T.B.A. and Desjardins, G.A. "Electromagnetic field penetration into a spherical cavity," *IEEE Transactions on Electromagnetic Compatibility, 16*(4):205–208 (1974).

59. Stratton, J. A. *Electromagnetic Theory.* New York: McGraw-Hill, 1941.

60. Sun, D., et al. "Spurious modes in finite-element methods," *IEEE Antennas and Propagation Magazine, 37*(5):12–24 (October 1995).

61. Tai, C.-T. *Dyadic Green Functions in Electromagnetic Theory* (Second Edition). IEEE Press, 1994.

62. Van Bladel, J. *Electromagnetic Fields* (Revised Printing Edition). Hemisphere, 1985.

63. Wang, T., et al. "Electromagnetic scattering from and transmission through arbitrary apertures in conducting bodies," *IEEE Transactions on Antennas and Propagation, 38*(11):1805 (November 1990).

64. Webb, J. P. "Finite element analysis of dispersion in waveguides with sharp metal edges," *IEEE Transactions on Microwave Theory and Techniques, 36*:1819–1824 (December 1988).

65. Wilson, G., et al. *Coated Quadrilateral Flat Plate: E–M Scattering Computations: Method of Moments Solution Using Pulse and Physical Basis.* Final Rreport MRC-R-DN-90-009, Dayton, OH: Mission Research Corporation, November 1990.

66. Wood, A. Stuart. "Conductivity: powerful polymers emerge from the lab," *Modern Plastics, 68*(8):47 (August 1991).

67. Woodworth, M.B. and Yaghjian, A.D. "Derivation, application and conjugate gradient solution of dual-surface integral equations for three-dimensional multi-wavelength perfect conductors." *Progress in Electromagnetics Research 5*, edited by Sarkar, T.K., chapter 4, 103–129, Elsevier, 1991.

68. Yaghjian, A.D. "Augmented electric and magnetic-field integral equations," *Radio Science, 16*:987–1001 (Nov–Dec 1981).

69. Ziolkowski, R. W. and W. A. Johnson. "Electromagnetic scattering of an arbitrary plane wave from a spherical shell with a circular aperture," *Journal of Mathematical Physics*, 28(6):1293–1314 (1987).

Vita

Captain William D. Wood, Jr., ██████████████████████████ After graduating from W.T.Woodson High School in 1981, he attended the University of Arizona, receiving the B.S.E.E. degree in 1985. Upon graduation, he was commissioned as a Second Lieutenant in the United States Air Force and assigned to the Avionics Laboratory, Wright-Patterson AFB, OH. He attended the Air Force Institute of Technology during 1989-90, receiving the M.S.E.E. degree. He was then assigned to the Aeronautical Systems Center, Wright-Patterson AFB, OH, where he served as an engineer in the F-22 System Program Office. In 1993, he returned to AFIT to pursue a doctorate in electrical engineering. Capt Wood is a member of IEEE, Eta Kappa Nu, and Tau Beta Pi.

REPORT DOCUMENTATION PAGE

1. AGENCY USE ONLY *(Leave blank)*	2. REPORT DATE	3. REPORT TYPE AND DATES COVERED
	April 1997	Doctoral Dissertation

4. TITLE AND SUBTITLE

ELECTROMAGNETIC SCATTERING FROM A CAVITY IN A GROUND PLANE: THEORY AND EXPERIMENT

5. FUNDING NUMBERS

6. AUTHOR(S)

William D. Wood, Jr., Captain USAF

7. PERFORMING ORGANIZATION NAME(S) AND ADDRESS(ES)

Air Force Institute of Technology, 2950 P Street, WPAFB OH 45433-7765

8. PERFORMING ORGANIZATION REPORT NUMBER

AFIT/DS/ENG/96-16

9. SPONSORING/MONITORING AGENCY NAME(S) AND ADDRESS(ES)

Mr. Jeffrey Hughes, Technical Specialist
Wright Laboratory, Target Modeling Branch (WL/AACT)
Wright-Patterson AFB OH 45433-7001

10. SPONSORING/MONITORING AGENCY REPORT NUMBER

11. SUPPLEMENTARY NOTES

12a. DISTRIBUTION/AVAILABILITY STATEMENT

APPROVED FOR PUBLIC RELEASE; DISTRIBUTION UNLIMITED

12b. DISTRIBUTION CODE

13. ABSTRACT *(Maximum 200 words)*

The electromagnetic scattering from an arbitrarily shaped open cavity embedded in a perfectly conducting, infinite ground plane is examined. The cavity is filled with a linear, isotropic, homogeneous material. The fields in the cavity interior and above the ground plane are expressed in terms of the tangential fields on the cavity surface and aperture. A coupled set of three integral equations is developed governing the tangential fields on the aperture and cavity surface. The support of the unknown tangential fields is finite. A moment-method based algorithm to approximate the solution to the integral equations for axisymmetric geometries is developed. The unknown tangential fields are expanded using piecewise-linear functions in the elevation plane and complex exponentials in the azimuth plane. Orthogonality is exploited to reduce the size of the matrix. The algorithm yields a well-conditioned numerical solution. The solution obeys the edge condition at the aperture rim. The integral equations are uniquely solvable at frequencies where other integral equation-based techniques admit spurious solutions. Radar cross section calculations are compared to experimental measurements of full-scale physical models. Results show that an open cavity can serve as an effective radar cross section enhancement device.

14. SUBJECT TERMS

Electromagnetic Scattering, Cavity Scattering, Integral Equations, Radar Cross Section, Radar Cross Section Enhancement, Radar Cross Section Measurement, Dyadic Green's Functions, Body of Revolution

15. NUMBER OF PAGES

145

16. PRICE CODE

17. SECURITY CLASSIFICATION OF REPORT	18. SECURITY CLASSIFICATION OF THIS PAGE	19. SECURITY CLASSIFICATION OF ABSTRACT	20. LIMITATION OF ABSTRACT
UNCLASSIFIED	UNCLASSIFIED	UNCLASSIFIED	UL

GENERAL INSTRUCTIONS FOR COMPLETING SF 298

The Report Documentation Page (RDP) is used in announcing and cataloging reports. It is important that this information be consistent with the rest of the report, particularly the cover and title page. Instructions for filling in each block of the form follow. It is important to *stay within the lines* to meet *optical scanning requirements*.

Block 1. Agency Use Only *(Leave blank)*.

Block 2. Report Date. Full publication date including day, month, and year, if available (e.g. 1 Jan 88). Must cite at least the year.

Block 3. Type of Report and Dates Covered. State whether report is interim, final, etc. If applicable, enter inclusive report dates (e.g. 10 Jun 87 - 30 Jun 88).

Block 4. Title and Subtitle. A title is taken from the part of the report that provides the most meaningful and complete information. When a report is prepared in more than one volume, repeat the primary title, add volume number, and include subtitle for the specific volume. On classified documents enter the title classification in parentheses.

Block 5. Funding Numbers. To include contract and grant numbers; may include program element number(s), project number(s), task number(s), and work unit number(s). Use the following labels:

C	-	Contract	PR -	Project
G	-	Grant	TA -	Task
PE	-	Program Element	WU -	Work Unit Accession No.

Block 6. Author(s). Name(s) of person(s) responsible for writing the report, performing the research, or credited with the content of the report. If editor or compiler, this should follow the name(s).

Block 7. Performing Organization Name(s) and Address(es). Self-explanatory.

Block 8. Performing Organization Report Number. Enter the unique alphanumeric report number(s) assigned by the organization performing the report.

Block 9. Sponsoring/Monitoring Agency Name(s) and Address(es). Self-explanatory.

Block 10. Sponsoring/Monitoring Agency Report Number. *(If known)*

Block 11. Supplementary Notes. Enter information not included elsewhere such as: Prepared in cooperation with...; Trans. of...; To be published in.... When a report is revised, include a statement whether the new report supersedes or supplements the older report.

Block 12a. Distribution/Availability Statement. Denotes public availability or limitations. Cite any availability to the public. Enter additional limitations or special markings in all capitals (e.g. NOFORN, REL, ITAR).

DOD	-	See DoDD 5230.24, "Distribution Statements on Technical Documents."
DOE	-	See authorities.
NASA	-	See Handbook NHB 2200.2.
NTIS	-	Leave blank.

Block 12b. Distribution Code.

DOD	-	Leave blank.
DOE	-	Enter DOE distribution categories from the Standard Distribution for Unclassified Scientific and Technical Reports.
NASA	-	Leave blank.
NTIS	-	Leave blank.

Block 13. Abstract. Include a brief *(Maximum 200 words)* factual summary of the most significant information contained in the report.

Block 14. Subject Terms. Keywords or phrases identifying major subjects in the report.

Block 15. Number of Pages. Enter the total number of pages.

Block 16. Price Code. Enter appropriate price code *(NTIS only)*.

Blocks 17. - 19. Security Classifications. Self-explanatory. Enter U.S. Security Classification in accordance with U.S. Security Regulations (i.e., UNCLASSIFIED). If form contains classified information, stamp classification on the top and bottom of the page.

Block 20. Limitation of Abstract. This block must be completed to assign a limitation to the abstract. Enter either UL (unlimited) or SAR (same as report). An entry in this block is necessary if the abstract is to be limited. If blank, the abstract is assumed to be unlimited.